UC Davis
UC Davis Electronic Theses and Dissertations

Title
Using Type II Supernovae to Study their Massive Star Progenitors

Permalink
https://escholarship.org/uc/item/0ds4d2dt

Author
Bostroem, Kyra

Publication Date
2021

Peer reviewed|Thesis/dissertation

eScholarship.org Powered by the California Digital Library
University of California

Using Type II Supernovae to Study their Massive Star Progenitors

By

KYRA AZALEE BOSTROEM

DISSERTATION

Submitted in partial satisfaction of the requirements for the degree of

DOCTOR OF PHILOSOPHY

in

PHYSICS

in the

OFFICE OF GRADUATE STUDIES

of the

UNIVERSITY OF CALIFORNIA

DAVIS

Approved:

Stefano Valenti, chair

Maruša Bradač

Andrew Wetzel

Committee in Charge

2021

© K. Azalee Bostroem, 2021. All rights reserved.

To my champions

Contents

Abstract v

Acknowledgments vi

Chapter 1. Introduction 1

1.1. Massive Star Evolution 1

1.2. Massive Star Supernovae 3

1.3. Challenges of Studying Massive Stars 4

1.4. Open Questions 5

Chapter 2. SN 2018ivc Observations and Properties 8

2.1. Observations and Data Reduction 9

2.2. Supernova Parameters 15

2.3. Host Properties 16

2.4. Evolution of SN 2018ivc 18

Chapter 3. ASASSN-15oz Observations and Properties 28

3.1. Observations and Data Reduction 28

3.2. Supernova Parameters 35

3.3. Light Curve Evolution of ASASSN-15oz 39

3.4. Spectroscopic Analysis 41

3.5. Comparison to other SNe 44

Chapter 4. Mass Loss in Massive Stars 48

4.1. Evidence for Interaction in SN 2018ivc 49

4.2. Evidence for CSM Interaction in ASASSN-15oz 51

4.3. Conclusions 65

Chapter 5. Progenitors of SN 2018ivc and ASASSN-15oz 66
5.1. The Progenitor Mass of SN 2018ivc 68
5.2. The Progenitor Mass of ASASSN-15oz 73
5.3. Conclusions 74

Chapter 6. Progenitor Masses from Nebular Spectra 78
6.1. Comparing Observations to Models 78
6.2. ^{56}Co Luminosity 79
6.3. [O I] Luminosity 82
6.4. Sample Selection and Analysis 86
6.5. Conclusions 90

Chapter 7. Conclusions 92
7.1. Future Work 93

Appendix A. Tables of Photometric and Spectroscopic Observations of SN 2018ivc 95
A.1. Tables of Observations SN 2018ivc 95

Appendix B. Supplementary Materials for ASASSN-15oz Analysis 110
B.1. Line Identification and Fitting Details 110
B.2. Tables of Observations 113

Appendix C. Table of Spectroscopic Observations of Literature Sample Used in Nebular Spectra Analysis 139
C.1. Nebular Spectra Observations from the Literature 139

Bibliography 143

Abstract

Although massive stars have a profound influence on the Universe at every scale, the answers to key questions about their mass loss and explodability are unknown. This is because massive stars are rare and the final phases of their evolution and explosions, as supernovae, occur on very short time scales. Over the last 5 years, wide-field surveys have greatly increased the number of supernovae discovered, opening a new window onto massive star evolution. In this thesis I will present the extensive studies of ASASSN-15oz and SN 2018ivc, two hydrogen rich supernovae with linearly declining light curves. In both of these supernovae we find evidence of circumstellar interaction, through radio detections and light curve modeling for ASASSN-15oz and the X-ray detection and uncharacteristic light curve of SN 2018ivc. These observations show that just prior to explosion, red supergiants may undergo eruptive mass loss events typically associated with more massive progenitors. Additionally, through the modeling of pre-explosion observations, the supernova light curve, and nebular spectra, we find that zero-age main sequence mass of the progenitors of these supernovae were less than 17 $M_{\odot}$. Finally, we analyze progenitor masses from the nebular spectra of 24 supernovae found in the literature. Consistent with progenitor masses determined from pre-explosion observations, we again do not find any high mass red supergiant progenitors from this independent technique, implying that a theoretical explanation may be needed to explain the lack of high mass progenitors.

Acknowledgments

Many thanks to my advisor Stefano Valenti for research guidance and teaching me about supernovae. To Sarah Loebman and Curtis McCully, you are my mentors and champions and this work would not exist without your belief in me, consistent support of all facets of my identity, and thoughtful conversations. To the Carpentries, and especially Greg Wilson, for constantly reminding me that there is a world outside of academia and that I am a valued member and leader in a vibrant and inclusive community. To Claudio Salusso for perfectly capturing my essence and writing it down so that I could remind myself of who I am at my core on the days that this was obscured by the values of academia. To my family - my original champions - it has been a gift to live nearby and visit often. Your constant love and support have fed my spirit throughout this process.

CHAPTER 1

Introduction

Massive stars ($M \lesssim 8$ $M_\odot$) play a key role in many areas of astrophysics, spanning size scales from nuclei to galaxies and time scales from days to gigayears [see for example Hirschi, 2017, Hopkins et al., 2018]. Nucleosynthesis throughout their evolution is responsible for the creation of most of the elements in the periodic table, including those necessary for life. These elements enrich the interstellar medium through stellar winds, eruptive mass-loss events, supernova (SN) explosions, and kilonovae [Kobayashi et al., 2020, and references therein]. Additionally, the energy from massive stars and their SN explosions is important for galaxy formation and evolution. Cosmological simulations have shown that stellar feedback and in particular massive star SNe have a significant effect on galaxy masses, metallicities, rotation curves, morphologies, and star formation histories [e.g. Hopkins et al., 2018, Vogelsberger et al., 2014, Wang et al., 2015]. Therefore, to understand stellar evolution, galaxy formation, and chemical enrichment, it is necessary to understand how these stars evolve, how they lose mass, and which stars explode as SNe.

1.1. Massive Star Evolution

Star formation occurs when a giant molecular cloud (GMC) is disturbed, initiating a gravitational collapse. As the GMC fragments and contracts, denser and denser regions form until eventually, in each region, the critical temperature and density is reached for the fusion of hydrogen into helium. The energy released in the form of photons from hydrogen fusion halts the gravitational collapse and the star enters the main sequence phase of its life. Massive stars spend most of their lifetimes on the main sequence, fusing hydrogen into helium in their cores.

Eventually there is not enough hydrogen in the core for fusion to occur and, unsupported again, the star begins to contract. For most of the star, this contraction is halted by the fusion of a layer of hydrogen around an inert helium core. The core continues to contract until eventually helium fusion begins. The contraction of the core during shell burning expands the envelope, increasing

the stars radius and cooling its surface. Observationally, this has the effect of making the star brighter and redder, leading to stars in this phase being called red supergiants (RSG).

During the RSG phase this process is repeated with successively heavier and heavier elements. With each contraction, the process becomes less efficient, requiring more fuel to halt the gravitational collapse and leading to successively shorter and shorter phases. Simultaneously, this process repeats itself in the layers above the core, with different shells of material reaching the temperature and density for the fusion of its most common element. This leads to a hydrogen envelope encircling shells of successively heavier elements. This process continues until an iron core is formed. As the element with the smallest binding energy, no further energy can be gained from the fusion of iron leading to an inert core. The iron core accumulates and continues to contract. The collapse is accelerated to near free-fall as the high temperature and density causes two processes which remove pressure support: electron capture and photo-disintegration. Eventually, the core reaches nuclear densities and electron capture by protons turns the core material into a neutron star. At this time, neutron degeneracy pressure halts the gravitational collapse and creates a stiff surface off of which the layers just outside bounce, creating a shock wave. The creation of neutrons also creates a huge number of neutrinos, which invigorate the shock, allowing it propagate through the remaining layers of the star and unbind the material, creating a SN.

The nucleosynthesis of elements during the supernova explosion occurs due to two processes: the heating of the ejecta by the shock and the interaction of the neutrinos (and anti-neutrinos) released during the creation of the neutron star with the ejecta [Woosley and Heger, 2007, Woosley et al., 1990]. As the shock passes through the ejecta, the high temperatures it creates unbind atoms into nucleons and α particles in the inner regions of the ejecta. As the ejecta expands and cools, these nucleons and α particles reassemble into heavy elements through the capture of protons via the p-process and νp-process and the capture of neutron via the s-process. These processes create both stable and unstable nuclei of primarily alpha elements above Si and Fe-group elements [Thielemann et al., 2018]. Additionally, Type Ia SNe contribute significantly to the abundance of Fe-group elements in the Universe. Although this is an active area of research, massive star evolution and core-collapse SNe are not thought to be the primary origin of elements above Mo and Ru [Eichler et al., 2018].

1.2. Massive Star Supernovae

SNe are observationally classified into those which show hydrogen in their spectra, called Type II SNe, and those that do not show hydrogen, called Type I SNe. Type I SNe from massive star are thought to have lost their hydrogen envelopes either through strong stellar winds or through mass loss to a binary companion. Type II SNe, on the other hand, have maintained their hydrogen envelopes. As more massive stars have stronger winds due to their higher luminosities, it is thought that the progenitors of Type II SNe are stars with masses between ~ 8 and ~ 30 $M_{\odot}$, while more massive stars form Type I SNe. This thesis focuses on the study of Type II SNe.

Type II SNe can be further divided based on the shape of their light curves. Although no strict definitions exist, Type IIP SNe typically show a period of ∼80-120 days over which their brightness is constant - creating a plateau after which they are named. Type IIL SNe, on the other hand, typically decline linearly (in magnitude) over approximately this same period. With small samples, some authors have found a distinction between Type IIP and Type IIL SN light curves (with various definitions) [e.g. Arcavi et al., 2012, Faran et al., 2014]. However, recent analyses of large samples of SNe by Anderson et al. [2014], Galbany et al. [2016b], Sanders et al. [2015], Valenti et al. [2016], and Rubin and Gal-Yam [2016] show a continuum between the archetypical IIP and IIL light curves. Given the continuum of light curves observed, we will use IIP-like to denote SNe at the IIP end of the spectrum and IIL-like to denote SNe at the IIL end of the spectrum.

The light curves of Type II SNe are divided into four main evolutionary phases which are governed by the physical mechanisms powering the light curve. A SN begins to shine at shock breakout, when the photons from the SN shock break through the dense outer layers of the star. As the shocked material and photosphere expand, the brightness of the SN increases and the light curve rises to its peak brightness. At peak, the material has cooled enough for the outer edge of the ionized hydrogen envelope to begin to recombine. The photosphere follows the recombination front through the hydrogen envelope, staying at constant temperature and approximate radius, leading to a near constant brightness for ~ 100 days. This phase is referred to as the plateau, although as mentioned above, the brightness can also decline linearly and thus we will prefer the term photospheric phase. As the photosphere reaches the inner edge of the hydrogen envelope, it quickly recedes through inner layers of the star, creating a rapid drop in brightness ($1 - 3$ mags

in ~ 20 days). This phase is referred to as the fall from plateau. The final evolutionary phase is the radioactive decay tail. ^{56}Ni, created from the iron core during collapse produces gamma-rays as it radioactively decays from $^{56}\mathrm{Ni} \rightarrow {}^{56}\mathrm{Co} \rightarrow {}^{56}\mathrm{Fe}$. These gamma-rays are reprocessed by the hydrogen envelope generating the optical photons that are observed during this phase of linear decline.

Spectroscopically, Type II SNe show a blue featureless continuum during their light curve rise due to their ejecta being very hot and fully ionized. Around peak brightness, broad hydrogen lines begin to appear with P-Cygni profiles. At this time the photosphere has begun to recombine leaving an neutral hydrogen layer expanding above the photosphere which scatters the emitted photons. Photons emitted with any velocity component towards the observer are scattered out of the line of sight creating an absorption feature from rest wavelengths blueward. Other photons are scattered into the line of sight having been emitted in all directions (except directly behind the photosphere) creating an emission profile centered at the rest wavelength of the feature. The superposition of these two profiles is called a P-Cygni profile. As the SN ejecta slows down, these lines get narrower over time. At the fall from plateau, the spectra undergo a marked change, from blackbody continuum with P-Cygni profiles, to nebular emission, with no continuum and pure emission lines. Nebular spectra are observed for the remainder of radioactive tail.

1.3. Challenges of Studying Massive Stars

A variety of factors make massive stars challenging to study directly. In a given burst of star formation, the number of stars formed with a given mass decreases with mass as a power law, meaning that few massive stars form. Those that do form, often form in clusters, limiting the distance at which they can be individually resolved. Finally, more massive stars have shorter life times giving us a shorter observational window. This is especially true of the later RSG evolutionary stages which occur on time scales that range from days to months to years compared to the main sequence time scales of tens of Myrs.

SNe on the other hand, occur one at a time and are very luminous, allowing them to be individually resolved out to great distances. Additionally, the SN explosion itself alerts us to the end of the RSG phase and the subsequent evolution of the SN allows us to look backwards in

time, both via the interaction of the SN with mass lost during the progenitor's lifetime and via the recession of the photosphere through the star. Observations of SNe combined with analytic and numerical modeling can be used to constrain key aspects of massive stars, overcoming many of these limitations. Analytic models of the rise of the SN light curve constrain the radius of the progenitor with larger radii progenitors cooling more slowly than more compact progenitors [Rabinak and Waxman, 2011, Sapir and Waxman, 2017]. Detailed modeling of spectroscopy at different phases of evolution can be used to understand the composition of different layers of the ejecta as well as the geometry of the explosion [e.g. Maguire et al., 2012, and references therein]. Modelling of nebular phase spectra can also be used to determine progenitor mass. The interaction of the SN shock with material lost during the RSG lifetime produces a number of observational signatures which probe the density, time, and speed of the mass loss (see Section 1.4). Finally, numerical modeling of the full light curve can be used to determine progenitor radius and mass as well as mass-loss parameters such as density and radial extent.

1.4. Open Questions

This thesis focuses on two broad open questions in astrophysics: how do the stars that explode as Type II SNe lose mass and what stars actually explode as Type II SNe? Mass-loss rates for RSGs are not well understood theoretically and are extremely difficult to characterize with observations due to both the short period of this phase as well as the rarity of high mass stars. Thus the mass-loss rates for RSG are uncertain, with typical mass-loss rate estimates between $10^{-6} - 10^{-4}$ $M_{\odot}yr^{-1}$ and wind velocities between $10 - 100$ km s^{-1} [Mauron and Josselin, 2011].

Over the course of its lifetime, the material lost via winds from the progenitor star leads to a substantial amount of circumstellar material (CSM). The configuration of the CSM and its density depend on the time of the mass loss, the rate of the mass loss (which could be steady or episodic), and the symmetry of the mass loss. While interaction has been observed in Type IIP/IIL SNe at the edge of the light curve distribution in terms of decline rate (steep) and absolute magnitude (bright; e.g. SN 1979C: Blinnikov and Bartunov 1993; SN 1980K: Chugai 1992; SN 1998S: Chugai 2001), it is often assumed to be negligible.

Historically, CSM was identified in SNe either through narrow lines produced by unshocked, photoionized CSM, intermediate-width lines created by shocked CSM, radio and/or X-ray detections, or by light curves that deviated from the typical Type IIP/IIL shape and color. Recently, signs of interaction have been identified beyond these traditional diagnostics. CSM interaction has been seen in Type IIP/IIL SNe at late phases [Andrews et al., 2010, Mauerhan et al., 2017], early CSM interaction has been invoked to explain the early-time light curve of most Type IIP/IIL SNe [Morozova et al., 2017, 2018], and the presence of CSM material very close to the progenitor has been used to explain early, narrow, high-ionization features ("flash spectroscopy" lines) in several Type II SNe [e.g., Gal-Yam et al., 2014, Hosseinzadeh et al., 2018, Khazov et al., 2016, Quimby et al., 2006, Smith et al., 2015]. Each of these signatures of interaction occurs during a specific phase of evolution and could be missed without continuous and frequent observations from explosion through the nebular phase. With high-cadence optical surveys, SNe are being discovered closer to explosion leading to well-sampled light curves throughout their evolution, spectroscopy at key phases, and X-ray and radio observations. These observations present evidence of interaction and indicate that mass loss should be considered in the interpretation of IIP/IIL SNe. However, even in this golden age of SN discovery and follow up, a complete picture of how each of these diagnostics fits into RSG mass loss is missing.

Another incomplete picture is which stars explode as Type II SNe. Stellar evolution theory predicts that single stars between 8 and 30 $M_{\odot}$, become RSGs and eventually explode as hydrogen-rich core-collapse SNe. However, searches for the progenitor systems of these SNe in serendipitously observed, archival, pre-explosion images have only found stars below 16 $M_{\odot}$. With the current pre-explosion sample size of 45 SNe, we should have observed 13 high mass (¡18 $M_{\odot}$) progenitors [Smartt, 2015]. It is not understood if the discrepancy between the predicted and observed number of high mass progenitors is due to theory incorrectly determining which stars explode or observations incorrectly determining progenitor masses.

An observational explanation put forth by Davies and Beasor [2018] is that RSGs are enshrouded in more dust as they approach explosion than is accounted for by the current analysis [see also Walmswell and Eldridge, 2012]. For this reason, the progenitor luminosity we derive from pre-explosion observations, and therefore the mass that we infer, is systematically low. On the other

hand, by carefully modeling the neutrino effects in 1D SN explosions, Sukhbold and Adams [2020] show that 16 $M_\odot$ corresponds to the transition between convective and radiative carbon burning. This influences the compactness of the pre-SN core, causing most stars above 16 $M_\odot$ to implode rather than explode. This theoretical explanation predicts that only a small fraction of stars over 16 $M_\odot$ explode and therefore a larger observational sample is needed to see these SNe from high mass progenitors. However, this hypothesis has not been confirmed with observations, nor the dust hypothesis disproved.

One way to determine whether the high mass progenitors are missing due to observational bias or incorrect theory is to derive progenitor mass from a different set of observations. Using independent observations and models, we can verify the masses determined from pre-explosion observations for a few SNe per year. Two independent, post-explosion methods for determining progenitor mass are hydrodynamic modeling of the light curve and non-local thermodynamic equilibrium modeling of the nebular phase spectra. The application of these techniques to individual objects [see for example: Bersten et al., 2011, Morozova and Stone, 2018] and small samples [Jerkstrand et al., 2015, Morozova et al., 2018, Valenti et al., 2016] show consistency between methods. However, there has not been a statistical sample built that is comparable in size to (or larger than) the direct detection sample and it remains an open question whether stars between 16-30 $M_\odot$ explode as Type II SNe.

This thesis will examine both the mass loss and progenitor mass of two Type IIL-like SNe, SN 2018ivc and ASASSN-15oz, in detail. Observations and general properties of the SNe and their hosts are presented in Chapters 2 (SN 2018ivc) and 3 (ASASSN-15oz). Also included in these chapters is their photometric and spectroscopic evolutions. Chapter 4 discusses the mass loss inferred from these observations. An analysis of the progenitor masses of ASASSN-15oz and SN2018ivc is presented in Chapter 5. Finally, in Chapter 6, the progenitor masses of a sample nebular spectra are derived. Chapter 7 summarizes the results.

CHAPTER 2

SN 2018ivc Observations and Properties

SN 2018ivc is a Type IIL-like supernova (SN) that exploded in a complex circumstellar environment in the well-studied Seyfert 2 galaxy NGC 1068 (M77; see Figure 2.1), and was discovered by the $D < 40$ Mpc Supernova Survey [DLT40; Tartaglia et al., 2018]. We adopt a distance of $D = 10.1$ Mpc [$\mu = 30.02$ mag; Tully et al., 2008] and a recessional velocity of 1037 km s^{-1} (z=0.003793; Huchra et al. 1999) for NGC 1068 in this work. Our near-daily observations of the SN show the presence of several rapid changes, both in the spectra and in the light curve, which could be easily missed in undersampled observations of other Type IIL-like SNe.

2.0.1. SN 2018ivc Discovery and Rapid Follow-up Observations. The initial DLT40 discovery image of SN 2018ivc (which was given an internal DLT40 designation of DLT18aq) was taken 2018 Nov. 24.04 (UT dates are used throughout this thesis) by the PROMPT5 telescope on CTIO, with a magnitude of $r = 14.65 \pm 0.02$. The DLT40 machine-learning algorithm identified a strong SN candidate in the initial image of the NGC 1068 field, and an email alert was sent out two minutes later. A second observation taken 14 min after the discovery image confirmed the transient. We then took a sequence of PROMPT5 images of the field over the next ~ 2.5 hr, during which the SN brightened from the initial $r = 14.65$ mag to 14.61 mag. During this time period, we reported the SN candidate to the community [Valenti et al., 2018] and also triggered the Las Cumbres Observatory network of robotic telescopes to obtain multiband observations ($UBVgri$) as soon as possible (first images on 2018 Nov. 24.11, 2 hr after discovery). We obtained our first spectrum with the FLOYDS spectrograph on 2018 Nov. 24.28 and a second spectrum with the BFOSC spectrograph on 2018 Nov. 24.70 [Zhang et al., 2018].

The last nondetection in the NGC 1068 field by the DLT40 team was on 2018 Nov. 19. The field of NGC 1068 had not been observed in the days just prior to the discovery of SN 2018ivc owing to the lunar angle constraint DLT40 places on its target fields ($\theta_{\rm Moon} > 25^\circ$).

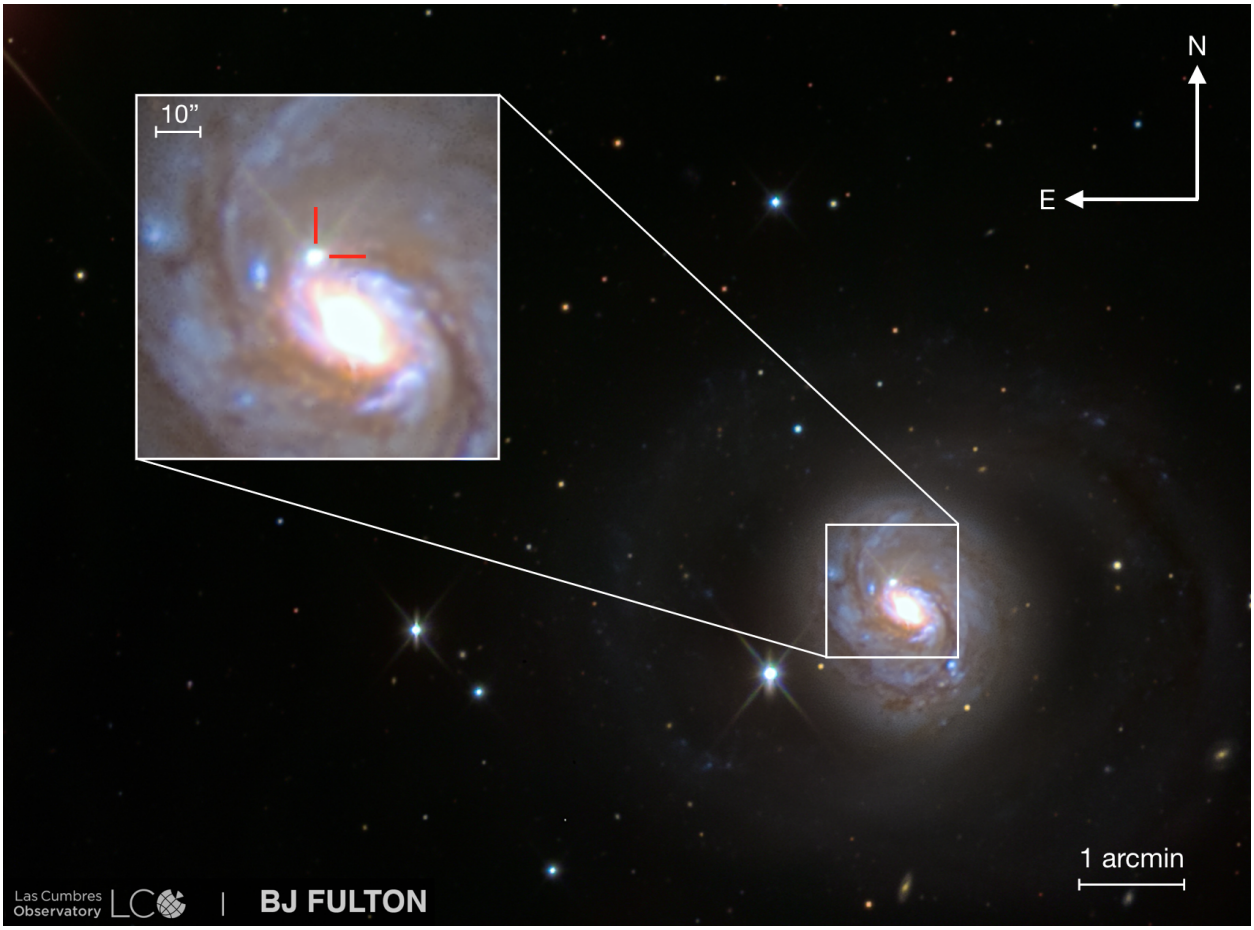

Figure 2.1 A color image of SN 2018ivc and its host galaxy NGC 1068 composed of multiband observations obtained with Las Cumbres Observatory. The inset shows a close-up image of the nuclear region of NGC 1068. SN 2018ivc is indicated with the red guider lines northeast of the nucleus.

2.1. Observations and Data Reduction

The photometric and spectroscopic follow-up observations of SN 2018ivc were obtained and coordinated through Las Cumbres Observatory's Global Supernova Project (GSP; PI: D. A. Howell), a key project to collect densely sampled optical light curves and spectra of nearby and bright SNe [e.g., Andrews et al., 2019, Szalai et al., 2019].

In addition to the extensive optical dataset, we also obtained early UV and near-infrared (NIR) photometry and NIR spectroscopy throughout the first $\sim$ 50 days, and an early X-ray observation[1].

[1]We also obtained Giant Metrewave Radio Telescope observations. However, we found issues with the calibration which rendered the observations unusable.

2.1.1. Photometry. Starting within hours of discovery, high-cadence optical photometric data from the Las Cumbres Observatory telescope network were acquired in the $UBVgri$ bands for SN 2018ivc; all data were reduced using the `lcogtsnpipe` software suite [Valenti et al., 2016] on difference images. Photometric monitoring with the Las Cumbres Observatory was stopped when we were no longer able to detect the SN against the bright host background, on 2019 Jan. 21.18 (day 60). These observations were supplemented with high-cadence photometry from the DLT40 survey, observed with the Open/Clear filters and calibrated to the r band. The DLT40 observations were reduced using the `DLT40 pipeline` [Tartaglia et al., 2018] and photometry was performed on difference images. DLT40 monitoring was stopped when the SN disappeared behind the Sun.

We augment these observations with data from the 1.04 m Sampurnanand Telescope (ST) in the $BVRI$ bands [Sagar, 1999], the 1.3 m Devasthal Fast Optical Telescope in the $BVRI$ bands [Sagar et al., 2012], the 2.01 m Himalayan Chandra Telescope (HCT) in the $BVRI$ bands [Prabhu and Anupama, 2010], the Mont4K instrument on the 1.55 m Kuiper Telescope in the UBV bands, and the 0.6 m Super-LOTIS telescope [Williams et al., 2008] in the $BVRI$ bands. Point-spread-function (PSF) photometry was performed on the original images using the `DAOPhot` [Stetson, 1987] `PyRAF`[2] package. As the photometry of these observations was not performed on difference images, imperfect background subtraction produces more scatter in the light curves. The optical light curve is presented in Figure 2.2.

Late-time optical observations were obtained with *HST* on 2019 July 1 using the Wide Field Camera 3 (WFC3) UVIS channel (F555W and F814W), as part of the ToO program GO-15151 (PI: S. Van Dyk). We used `Dolphot` [Dolphin, 2016, 2000] to extract the photometry from the `*_flc.fits` frames. A list of all photometric observations are listed in Table A.2 and the first few rows are shown in Table 2.1.

SN 2018ivc was also observed with the Neil Gehrels *Swift* Observatory [Gehrels et al., 2004]. Observations with the Ultra-Violet Optical Telescope (UVOT; Roming et al., 2005) were reduced and analyzed using the pipeline for the *Swift* Optical Ultraviolet Supernova Archive (SOUSA; Brown et al., 2014), which includes an arithmetic subtraction of the underlying host-galaxy flux measured from pre-explosion imaging. The magnitudes use the updated calibration from Breeveld

[2] `PyRAF` is a product of the Space Telescope Science Institute, which is operated by AURA, Inc., for NASA

et al. [2010] and are on the UVOT/Vega system. Optical magnitudes are not reported because the underlying host galaxy was too bright to correct for the coincidence loss. Upper limits in *uvw2* and *uvm2* and detections in *uvw1* are included in Table 2.1 and plotted in Figure 2.2.

Table 2.1 An example of the photometric observations of SN 2018ivc. A complete machine readable table is included in Appendix A.

Observation Date UT	MJD	Phase (day)	Source	Filter	Magnitude (mag)	Magnitude Error (mag)
2018-11-13 02:16:15.16	58435.09	-9.16	CTIO-Prompt5	Open	< 15.26	-
2018-11-14 02:33:08.64	58436.11	-8.14	CTIO-Prompt5	Open	< 15.29	-
2018-11-15 02:24:00.86	58437.10	-7.15	CTIO-Prompt5	Open	< 15.79	-
2018-11-15 05:56:24.00	58437.25	-7.00	ZTF	g	< 19.82	-
2018-11-15 07:29:16.80	58437.31	-6.94	ZTF	g	< 20.16	-
2018-11-16 03:03:18.72	58438.13	-6.12	CTIO-Prompt5	Open	< 15.66	-
2018-11-17 02:50:24.57	58439.12	-5.13	CTIO-Prompt5	Open	< 15.75	-
2018-11-18 02:02:48.19	58440.09	-4.16	CTIO-Prompt5	Open	< 15.57	-
2018-11-19 02:39:18.43	58441.11	-3.14	CTIO-Prompt5	Open	< 19.36	-
2018-11-20 10:14:52.00	58442.43	-1.82	ATLAS	o	< 18.60	-
2018-11-24 00:52:16.32	58446.04	1.79	CTIO-Prompt5	Open	14.65	0.01
2018-11-24 01:14:37.24	58446.05	1.80	CTIO-Prompt5	Open	14.66	0.01
2018-11-24 01:06:45.50	58446.05	1.80	CTIO-Prompt5	Open	14.68	0.01
2018-11-24 01:33:23.90	58446.06	1.81	CTIO-Prompt5	Open	14.63	0.01
2018-11-24 02:14:47.04	58446.09	1.84	LCO LSC 1m	U	14.35	0.02

The *UVW1*, *UVW2*, *UVM2*, *U*, *B*, and *V* filters are given in the Vega magnitude system; the *g*, *r*, and *i* filters are given in the AB magnitude system.

2.1.2. Spectroscopy. Spectroscopic observations from a variety of telescopes and instruments were obtained almost daily in the optical, starting within 5 hr of discovery and continuing through day 35. Less frequent monitoring with larger telescopes was performed until SN 2018ivc disappeared behind the Sun $\sim$ 80 days post-discovery. A single nebular spectrum was obtained with Keck/DEIMOS on day 279 (see Figure 2.3).

Similarly, NIR observations began on day 3 and continued almost weekly through day 53. A selection of spectra is shown in Figure 2.4 and all spectroscopic observations are listed in Appendix A. All of the spectra presented in this work were obtained at the parallactic angle to minimize atmospheric refraction [Filippenko, 1982]. These spectra are available on WISeREP[3] [Yaron and Gal-Yam, 2012].

[3]http://wiserep.weizmann.ac.il

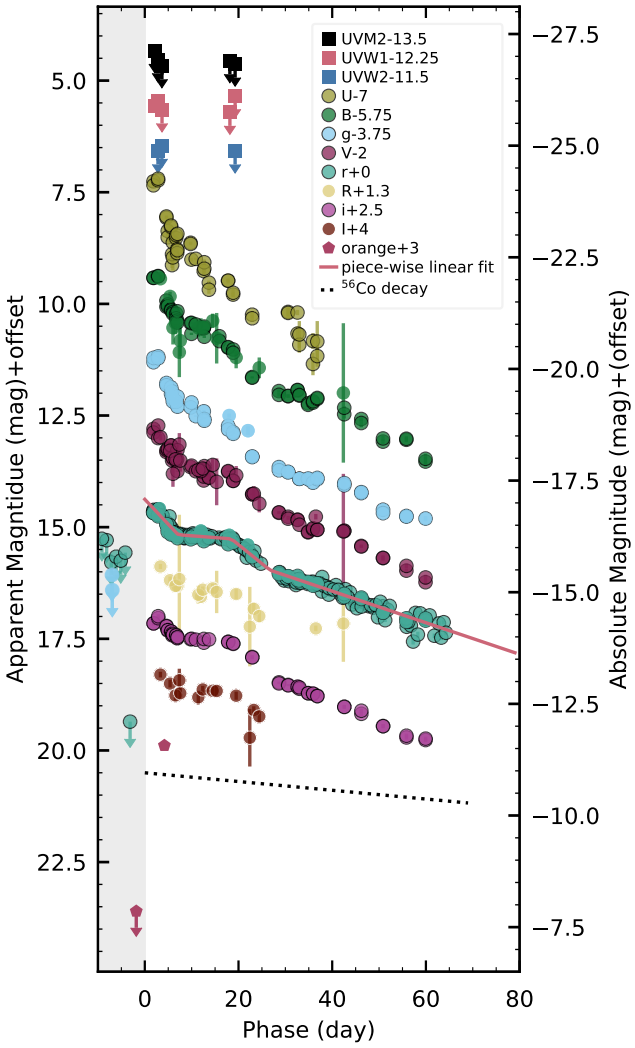

Figure 2.2 The light curve of SN 2018ivc at UV (square symbols) and optical (circles and pentagons) wavelengths. Difference-image photometry is indicated by a black outline. Upper limits are denoted with arrows. All phases are calculated with respect to the inferred explosion epoch (2018 Nov. 22.25; see Section 2.2) and the period prior to this time shaded in gray. The piecewise linear fit of the DLT40 r-band light curve is shown in pink. Individual filters have been offset by a constant (denoted in the legend) for ease of viewing. The black dashed line shows the V-band slope expected if the light curve is fully powered by the radioactive decay of ^{56}Co.

Optical spectra were reduced using standard techniques, including bias subtraction, flat fielding, and cosmic-ray rejection. SN 2018ivc is embedded in NGC 1068; given this complex background, local sky subtraction was very important for the spectral extraction. Despite the care taken, some

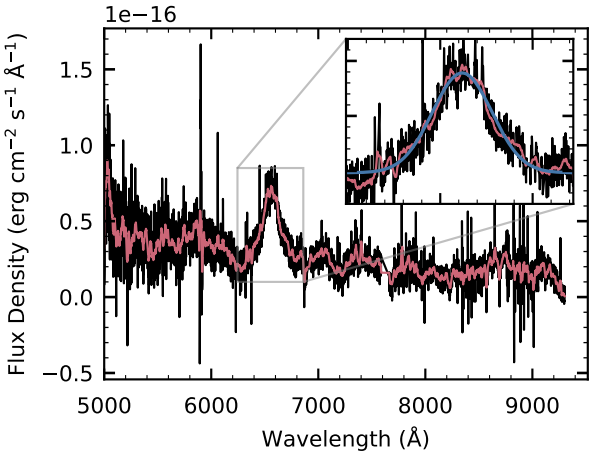

Figure 2.3 The Keck/DEIMOS nebular spectrum, observed on day 279 (black; pink is smoothed by 25 pixels) with a zoom-in on the H α region in the inset. A single Gaussian fit is shown in the inset in blue. Although the spectrum has a low signal-to-noise ratio, there is no evidence of multiple components in the H α feature.

narrow emission lines are still visible in the final reduced spectra. In these cases, after visual inspection of two-dimensional spectra and our highest resolution data (see Section 2.4.2 for a detailed discussion), we believe these originate from the host galaxy.

Flux calibration was performed using standard-star observations. For the NIR spectra, the data were reduced in a similar manner as by Hsiao et al. [2019], using the standard ABBA technique; observations were taken of nearby A0V stars adjacent to the science exposures to facilitate telluric corrections and flux calibration [e.g., Vacca et al., 2003].

2.1.3. X-ray Observations. The *Chandra* X-ray Observatory observed SN 2018ivc on 2018 Dec. 05.7 for 10.0 ks (ObsID 20306) with the telescope aimpoint on the Advanced CCD Imaging Spectrometer (ACIS) S3 chip as part of a program to follow up possible X-ray detections from other facilities (PI: D. Pooley). The host galaxy, NGC 1068, has been observed many times previously with *Chandra*, often but not always with the High Energy Transmission Gratings (HETG) in place. For a straightforward comparison to our observation, we selected the longest ACIS-S3 observation with no grating in the *Chandra* data archive: ObsID 344 (PI: A. Wilson) began on 2000 Feb 21.7 and had an exposure time of 47.4 ks. Data reduction was performed with the `chandra_repro` script, part of the `Chandra Interactive Analysis of Observations (CIAO) software` [Fruscione et al., 2006]. We used `CIAO` version 4.11 and calibration database (CALDB) version 4.8.3.

The source is clearly detected (Figure 2.5) with 207 total counts recorded in a $1\farcs5$ radius source extraction region in the 0.5–8 keV band. The background contribution to this X-ray flux is non-negligible but difficult to estimate given the non-spatially-uniform X-ray emission immediately surrounding the location of SN 2018ivc in its host galaxy. One estimate of the background comes from an annular background region of inner radius $2''$ and outer radius $4''$ centered on the SN. Based on the 80 counts in this background region, there are 192 ± 14 net counts from SN 2018ivc in the 0.5–8 keV band.

To assess the spectral properties of the SN and determine its X-ray flux, we extract and simultaneously fit source and background spectra in the 0.5–8 keV band using `Sherpa` [Freeman et al., 2001] with the modified Cash [1979] statistic cstat and the simplex optimization method. Our model components in all cases are absorbed hot plasmas (APEC model). We use the Tuebingen-Boulder Interstellar Medium absorption model [Wilms et al., 2000] with a minimum column density equal to the Galactic value of $n_{\rm H} = 1.55 \times 10^{19}$ cm^{-2}. We separately use two options for the background spectrum: the first is the annulus mentioned above in the SN observation and the second is a $1\farcs5$ radius circle (identical to the source extraction region) in the observation taken prior to explosion.

The first choice of background spectrum is well fit by two hot plasmas (temperatures of $kT_1 = 0.01$ keV and $kT_2 = 0.85$ keV) absorbed by a column of density 3.2×10^{20} cm^{-2}. The second choice of background spectrum is also well fit by two hot plasmas (temperatures of $kT_1 = 0.21$ keV and $kT_2 = 0.95$ keV) absorbed by a column of density 1.6×10^{19} cm^{-2}. Using each of these background spectra separately, we fit the SN spectrum with an absorbed plasma.

With the first choice of background, we obtain a good fit (reduced cstat of 0.63) with best-fit parameters for the SN of $n_{\rm H} = (4.4^{+0.7}_{-0.9}) \times 10^{22}$ cm^{-2} and $kT = 17^{+63}_{-7}$ keV with the upper limit representing the model maximum. All uncertainties are 68% confidence intervals. The intrinsic X-ray flux of the SN in this model is $(8.2 \pm 0.8) \times 10^{-13}$ erg cm^{-2} s^{-1}. For a distance of 10.1 Mpc, this corresponds to a luminosity of $L_{\rm x} = (1.0 \pm 0.1) \times 10^{40}$ erg s^{-1}.

With the second choice of background, we also obtain a good fit (reduced cstat of 0.59) with best-fit parameters for the SN of $n_{\rm H} = (3.6^{+0.8}_{-0.6}) \times 10^{22}$ cm^{-2} and $kT = 43^{+37}_{-31}$ keV with the upper limit representing the model maximum. The intrinsic X-ray flux of the SN in this model is

$(7.5 \pm 0.7) \times 10^{-13}$ erg cm^{-2} s^{-1}. For a distance of 10.1 Mpc, this corresponds to a luminosity of $L_{\rm x} = (9.2 \pm 0.9) \times 10^{39}$ erg s^{-1}.

Although the different choices for background extraction give slightly different results, they are consistent with each other within the uncertainties. In each case, the reported fluxes are integrated from the unabsorbed models. Uncertainties on those fluxes are calculated as the 68%-confidence bounds of the integrated, unabsorbed fluxes from Monte Carlo realizations (1000 samples) of the best-fit models, taking into account the uncertainties in the best-fit parameters (using the `sample_flux` command in Sherpa)

2.2. Supernova Parameters

The DLT40 survey identified SN 2018ivc on 2018 Nov. 24.07, 4.96 days after the last observation of the field on 2018 Nov. 19.11. After the DLT40 team's prompt reporting of the SN to TNS, the Asteroid Terrestrial-impact Last Alert System (ATLAS) identified a more recent nondetection in their data on 2018 Nov. 20.42 with a limiting magnitude of 18.6 mag in the orange-ATLAS filter. As an explosion epoch we adopt 2018 Nov. 22.25 ± 1.8, the midpoint of the last nondetection (by ATLAS) and the first detection (by DLT40).

We adopt Milky Way extinction values of $E(B-V) = 0.0289 \pm 0.0004$ mag from Schlafly and Finkbeiner [2011]. Unfortunately, SN 2018ivc exploded in a region of high extinction within NGC 1068, which prevented us from deriving the extinction in the host galaxy from the Na I D lines [Poznanski et al., 2012]. Instead, we estimate an extinction of $E(B-V) = 0.5 \pm 0.15$ mag by matching the color evolution of SN 2018ivc over the first 20 days with that of other Type II SNe (SN 1980K: Barbon et al. 1982, Buta 1982, Tsvetkov 1983; SN 1998S: Fassia et al. 2000, Li et al. 2011, Liu et al. 2000, Pozzo et al. 2004; SN 1996al: Benetti et al. 2016; SN 2012A: Tomasella et al. 2013, SN 2013by: Valenti et al. 2015, SN 2013ej: Valenti et al. 2014). While the light curves of these SNe have varying slopes, the colors are consistent during the first 20 days, which is why we choose this period to constrain the extinction. A conservative error of 0.15 mag is adopted to take into account the large uncertainty of the method. This is consistent with the extinction derived in the next section from spectroscopy of the parent H II region and we adopt it as the host-galaxy

extinction for our analysis. Throughout this thesis, unless otherwise noted, we use the extinction law of Cardelli et al. [1989] with $R_V = 3.1$.

In Type IIP/IIL SNe, the amount of ^{56}Ni synthesized in the explosion can be calculated from the luminosity of the SN after the fall from plateau ($\sim$ 80–100 days post explosion), when the light curve is powered by the radioactive decay of $^{56}\mathrm{Ni} \rightarrow {}^{56}\mathrm{Co} \rightarrow {}^{56}\mathrm{Fe}$. We measure the pseudo-bolometric luminosity of SN 2018ivc from the *HST* observations on day 220.9 by first transforming the *F555W* filter and the *F814W* filter to the Landolt V and I filters, respectively, using the relations of Harris [2018]. This first step is necessary as SN 1987A was not observed in the WFC3 *F555W* and *F814W* filters. Following Valenti et al. [2008], we find the pseudo-bolometric luminosity by integrating the apparent magnitude at the effective wavelength of each filter, using the trapezoid rule. We calculate the pseudo-bolometric luminosity for SN 1987A from the V and I filters in the same way. Then, following Spiro et al. [2014], we calculate the nickel mass as $M(^{56}\mathrm{Ni}) = 0.075\,M_{\odot} \times L_{18\mathrm{ivc}}(t)/L_{87\mathrm{A}}(t)$. We find $M(^{56}\mathrm{Ni}) = 0.0056^{+0.0036}_{-0.0022}\,\mathrm{M}_{\odot}$. Uncertainties in the nickel mass were calculated using a Monte Carlo simulation taking into account gaussian uncertainties in the explosion epoch, distance modulus, Galactic extinction, host galaxy extinction, and apparent magnitude of SN 2018ivc and SN 1987A. We caution that to calculate this value we assumed that there was complete gamma-ray trapping, that we could convert *HST* filter magnitudes to Landolt filter magnitudes using relations derived from stellar spectral energy distributions (SEDs), and that SN 1987A and SN 2018ivc have the same SED. The uncertainties associated with each of these assumptions are not included in the reported uncertainties.

2.3. Host Properties

We searched in the ESO Science Portal[4] for MUSE integral field unit (IFU) observations of SN 2018ivc's host galaxy, NGC 1068. It was observed on 2014 Dec. 14 under program 094.B-0298(A), in four pointings which we combined for a total exposure time of 1180 s. All observations were reduced with the standard MUSE pipeline [Weilbacher et al., 2014] using default parameters through `reflex` [Freudling et al., 2013].

[4]http://archive.eso.org/scienceportal/home

For each spaxel, we performed a similar analysis to that of Galbany et al. [2014, 2016a,c]. Briefly, using a modified version of STARLIGHT (Cid Fernandes et al. 2005, López Fernández et al. 2016, priv. comm.), we model the stellar component of the continuum by estimating the fractional contribution of simple stellar populations (SSP) from the Bruzual [2007] base adding dust attenuation effects as a foreground screen with a Fitzpatrick [1999] reddening law and $R_V = 3.1$. Our basis set is composed of 66 SSPs with 17 ages, ranging from 1 Myr to 18 Gyr, and four different metallicities (0.2, 0.4, 1.0, and 2.5 $Z_\odot$).

By subtracting the best SSP fit from each observed spectrum, we obtained a pure gas emission spectrum for each spaxel. From the pure gas spectrum, we estimated the flux of the most prominent emission lines after correcting for dust content with a correction derived from the Balmer decrement (assuming case B recombination; Osterbrock and Ferland 2006, the same extinction law, and $R_V = 3.1$). From the pure gas models for each spaxel, we create an extinction-corrected H α map.

We use our extinction-corrected H α map to identify the H II region containing SN 2018ivc (its "parent" region) and derive environmental and progenitor properties. Following Galbany et al. [2016a, 2018], the H α maps are used to select star-forming H II regions across the galaxy with a modified version of HIIEXPLORER[5] [Sánchez et al., 2012], a package that detects clumps of higher intensity in a map by aggregating adjacent pixels. This procedure selected 1801 H II clumps with an average radius of 140 pc. Once the H II regions were identified, the same analysis described above was performed on the extracted spectra. The observed spectrum and the best-fit STARLIGHT spectrum of the H II region containing SN 2018ivc can be seen in the bottom-left panel of Figure 2.6. From this analysis and using the Cardelli et al. [1989] extinction law, we find $E(B-V) = 0.37 \pm 0.04$ mag for the parent region of SN 2018ivc, consistent with the value derived in the previous section.

We use oxygen abundance as a proxy for metallicity as oxygen is produced at the beginning of the enrichment process by massive stars and, by mass, comprises 50% of the heavy elements in the Universe [López-Sánchez et al., 2012]. Using the pure gas emission spectrum of the H II region, we determine metallicity from the O3N2 empirical calibrator [Pettini and Pagel, 2004]. This same spectrum is used to find the equivalent width of H α (EWH α). The upper-left panel of Figure

[5]http://www.caha.es/sanchez/HII_explorer/

2.6 shows the EWH α values for each H II region in NGC 1068. We find the metallicity to be $12 + \log_{10}(\mathrm{O/H}) = 8.6 \pm 0.26$ and the EWH $\alpha = 38.58 \pm 0.26$ Å.

2.4. Evolution of SN 2018ivc

The detailed evolution of SN 2018ivc was caught in the almost daily photometric and spectroscopic observations. These revealed a rapidly evolving SN with a steeply declining light curve and spectra with broad emission.

2.4.1. Light-Curve Evolution. The light curve of SN 2018ivc rose rapidly, peaking around day 3, only 5 days after the last nondetection. It then showed a rapid, linear decline typical of Type IIL-like SNe. Figure 2.7 displays a comparison of SN 2018ivc and other well-studied SNe with a variety of slopes. While the global trend is linear with a similar decline rate to SNe 1979C and 1980K, our high-cadence observations quickly revealed that there are, in the first 50 days, several changes in the slope rarely seen in other Type IIL-like SNe. SN 2018ivc is also relatively faint compared to other SNe with similar slopes.

The light curve of SN 2018ivc changes slope approximately every 10 days over the first 30 days. We fit a continuous piecewise linear function to the r-band observations, leaving the slopes, initial intercept, and breakpoints as free parameters (8 free parameters). This fit is shown in Figure 2.2. The initial decline ending at day 7.57 ± 0.41 has a slope of 0.1068 ± 0.0094 mag day^{-1}. This is followed by a plateau until day 18.07 ± 0.45 with a slope of 0.0056 ± 0.0031 mag day^{-1}. The light curve begins to decline steeply on day 18.07, with a slope of 0.0811 ± 0.0077 mag day^{-1}. After day 27.55 ± 1.37, the slope changes again to 0.0355 ± 0.0014 mag day^{-1}. At no point is the slope of SN 2018ivc consistent with the slope expected for cobalt decay (0.008 mag day^{-1} in R). Searching among other Type IIP/IIL SNe, we were only able to find one light curve in the literature that resembled the evolution (although ~ 1 mag brighter): that of SN 1996al [Benetti et al., 2016].

We searched the DLT40 difference images in the months leading up to SN 2018ivc for a pre-explosion outburst similar to SN 2009ip ($M_r \approx -14.5$ mag; Foley et al. 2011, Margutti et al. 2014, Mauerhan et al. 2013, Pastorello et al. 2013). However, these observations do not reveal any hint of a pre-outburst eruption, with ~ 90 images of the field take in the ~ 150 days prior to the SN explosion, with a typical limiting magnitude of $r \approx 19.3$ ($M_r \approx -12$ mag).

2.4.2. Spectroscopic Evolution. The spectroscopic evolution of SN 2018ivc shows strong H and He I emission and very shallow (if any) absorption. The full evolution can be seen in Figure 2.4, where prominent spectroscopic features are labeled.

The optical and NIR spectra obtained at 2.04 and 2.95 days (respectively) show a featureless blue continuum. By day 5, broad H α and He I λ5876 emission begin to develop with similar profiles. While the presence of H β in absorption cannot be completely ruled out (because of possible contamination from other lines), an absorption component is clearly missing from both H α and He I λ5876. This is typical of Type IIn SNe and some Type IIL-like SNe [Gutiérrez et al., 2014]. Although the physical mechanism for the lack of absorption is still unclear, possible explanations include a low-density (possibly low-mass) envelope and scattering off of circumstellar material [Schlegel, 1996].

The Ca II $\lambda\lambda$8498, 8542, 8662 emission triplet begins to develop at day 12 and strengthens through day 78. On day 30 the He I λ7065 line begins to show in emission. By day 75, the He I λ6678 line is visible in the red wing of the H α emission; this feature may be blended in earlier spectra. The shape of the emission around H α in the two spectra from days 75 and 78 is very boxy, which we will discuss more in later sections. We obtained a low signal-to-noise ratio (S/N) spectrum at day 279 which shows a broad H α profile, similar to that seen on day 78.

The NIR spectra are dominated by hydrogen and He I emission features. The blue continuum at day 3 gives way to Paschen emission features by day 10. The He I λ10830 line is blended in the P γ feature. In both the optical and the NIR, the widths of the emission lines decrease with time as the speed of the ejecta decreases.

The spectra of SN 2018ivc show potential narrow emission lines on top of the broad H α emission. This region is heavily contaminated by the host-galaxy emission which is challenging to separate from the H α SN emission in all but the highest resolution observations. We searched for a SN component in our highest resolution spectrum: the MMT/Binospec observation from 2018 Dec. 14. In this spectrum we fit a Gaussian profile to night-sky lines, galaxy emission lines, and H α. We find the full width at half-maximum intensity (FWHM) of the narrow H α emission ($\sim$ 130 km s^{-1}) to be consistent with that of the other galaxy emission lines ([N II] $\lambda\lambda$6548, 6583; [S II] $\lambda\lambda$6716, 6731) (see Figure 2.8).

We measure the velocity evolution using the half width at half-maximum intensity (HWHM) of Gaussian fits to the H α, He I λ5876, and P β emission lines and the minimum of the Fe II and H β absorption features. The velocities are shown in Figure 2.9, with velocities measured from emission features in the left panel and velocities measured from absorption features in the right panel. We note that while there is asymmetry, substructure, and host contamination in individual features, the trends are consistent across features, giving us confidence in the overall velocity evolution. However, we caution that there may be significant scatter in individual measurements. The H α velocity can be compared to the average of 112 Type IIP/IIL SNe, calculated by Gutiérrez et al. [2017]. We find that the velocities are similar to those found in Type IIP/IIL SNe and higher than the velocities of SN 1996al. However, the evolution is more rapid, with the initial velocity higher than average and the final velocities lower than average. The Fe II lines are also broadly consistent with the average Type IIP/IIL evolution although there is considerable scatter. We simultaneously fit Fe II $\lambda\lambda$4924, 5018, but we were unable to simultaneously fit Fe II $\lambda\lambda$4924, 5018, 5169 and therefore fit Fe II λ5169 separately. Velocities from both fits are shown in Figure 2.9.

On day 18 an emission feature begins to develop in the blue wing of the emission-line profile of H α, H β, He I λ5876, Ca II triplet, He I λ10830, and P β (see the first five panels of Figure 2.10). This feature gains strength until day $\approx$ 35, after which it fades until it is barely visible on day 78. We identify the emission line that appears blueward of the rest wavelength of these features as a high-velocity (HV) component owing to its presence at the same velocity in each feature (see right panel of Figure 2.10). From the blueshifted peak of the emission we find the velocity of the emitting material to be $\sim$ 9000 km s^{-1} at day 18, slowing down to $\sim$ 7000 km s^{-1} by day 78. Although SN 2018ivc displays many characteristics typical of a type IIL-like SN, its rapidly changing light curve and strong emission features are atypical. The implications of these observations for both the mass-loss history of the progenitor star and its mass will be explored in Chapters 4 and 5.

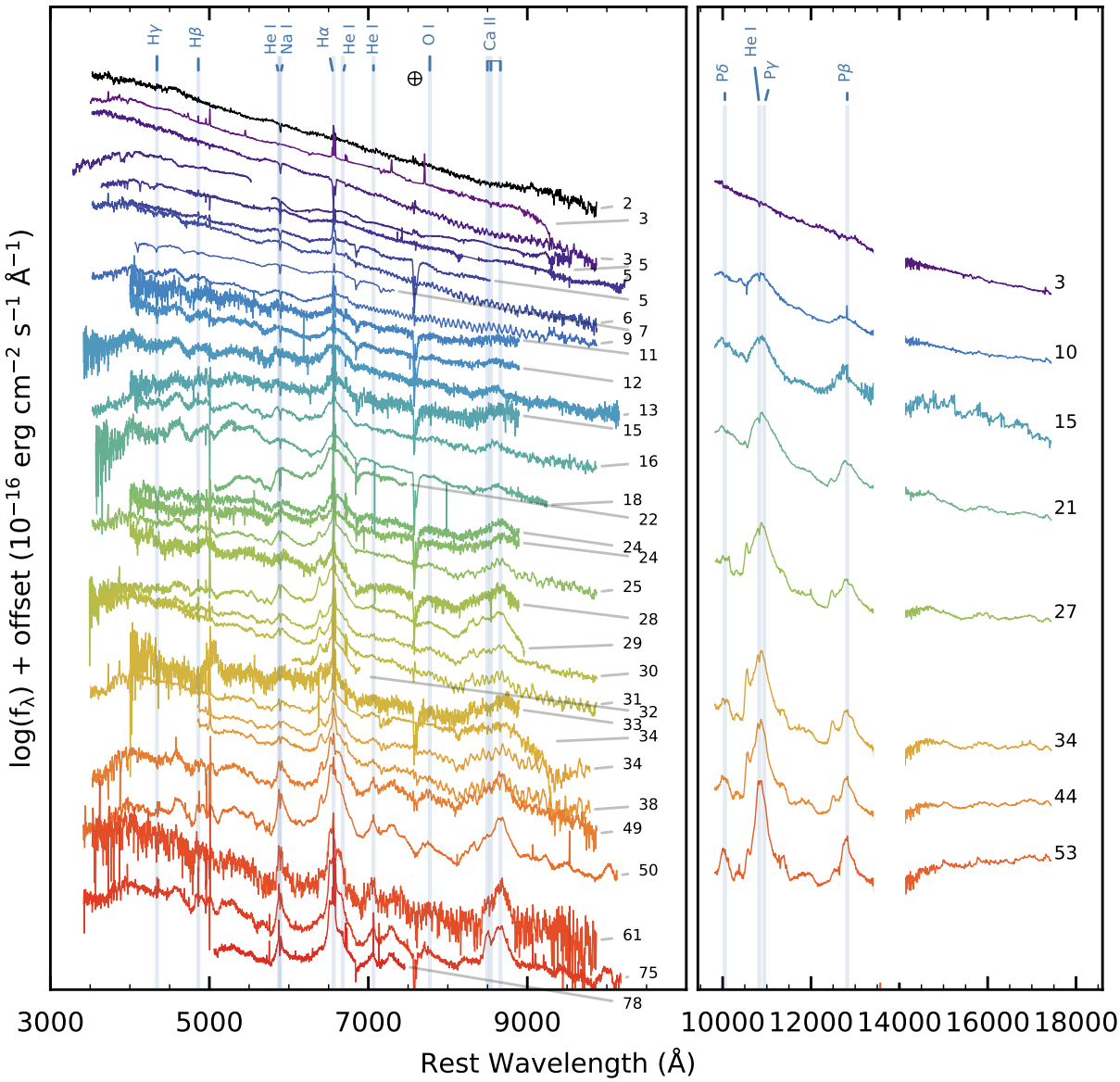

Figure 2.4 *Left*: the spectroscopic evolution of SN 2018ivc at optical wavelengths. SN 2018ivc shows strong emission lines and very little absorption. Imperfect background subtraction may create artificially blue continua and/or strong narrow lines in the broad H α emission. The phase of each spectrum is given on the right. High resolution observations are resampled with `SpectRes` [Carnall, 2017] to 2Å resolution to improve the signal-to-noise ratio. *Right*: the NIR spectroscopic evolution with the phase of the spectrum given on the right. The strong telluric absorption between 13450 Å and 14000 Å is masked in all NIR spectra. At the top of each panel prominent lines are identified, and in the left panel a prominent telluric feature is marked with a cross.

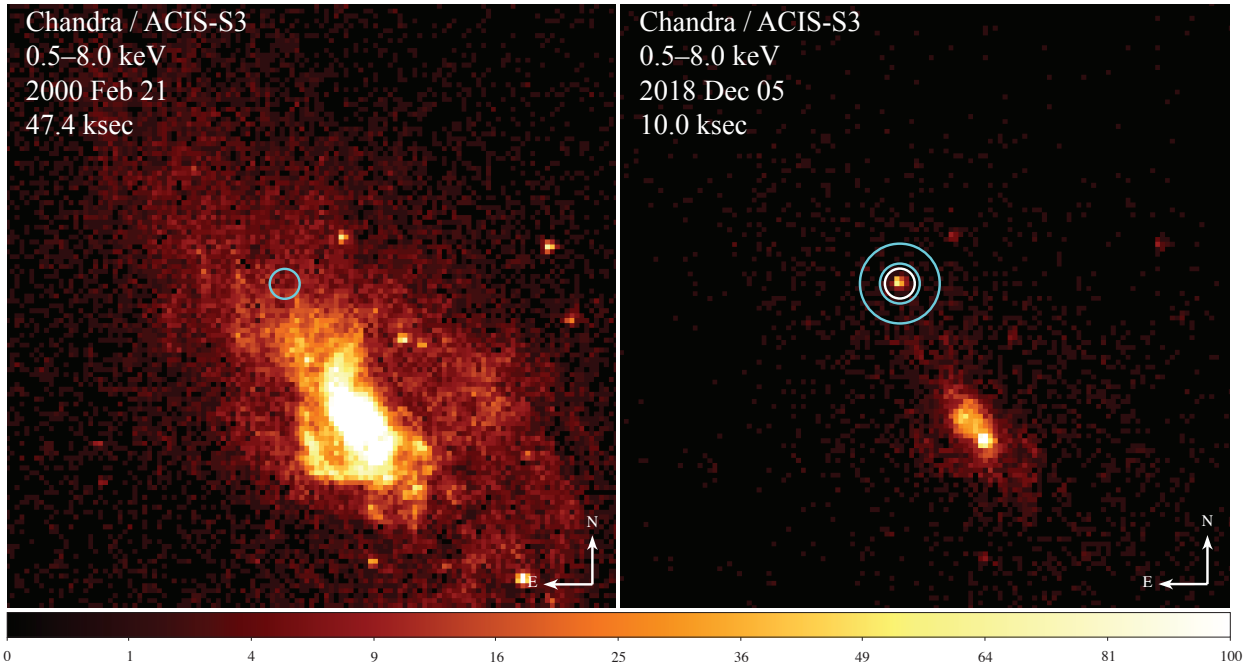

Figure 2.5 Pre-SN (*left*) and post-SN (*right*) images of NGC 1068 taken with *Chandra*/ACIS-S3. Each image is 1′ on a side. The white circle on the right is 1.″5 in radius centered on SN 2018ivc and is used to extract the source spectrum. Note the non-uniform extended emission surrounding the SN. The cyan circle on the left (identical to the source region) and the cyan annulus on the right were each used to extract background spectra. See text for details.

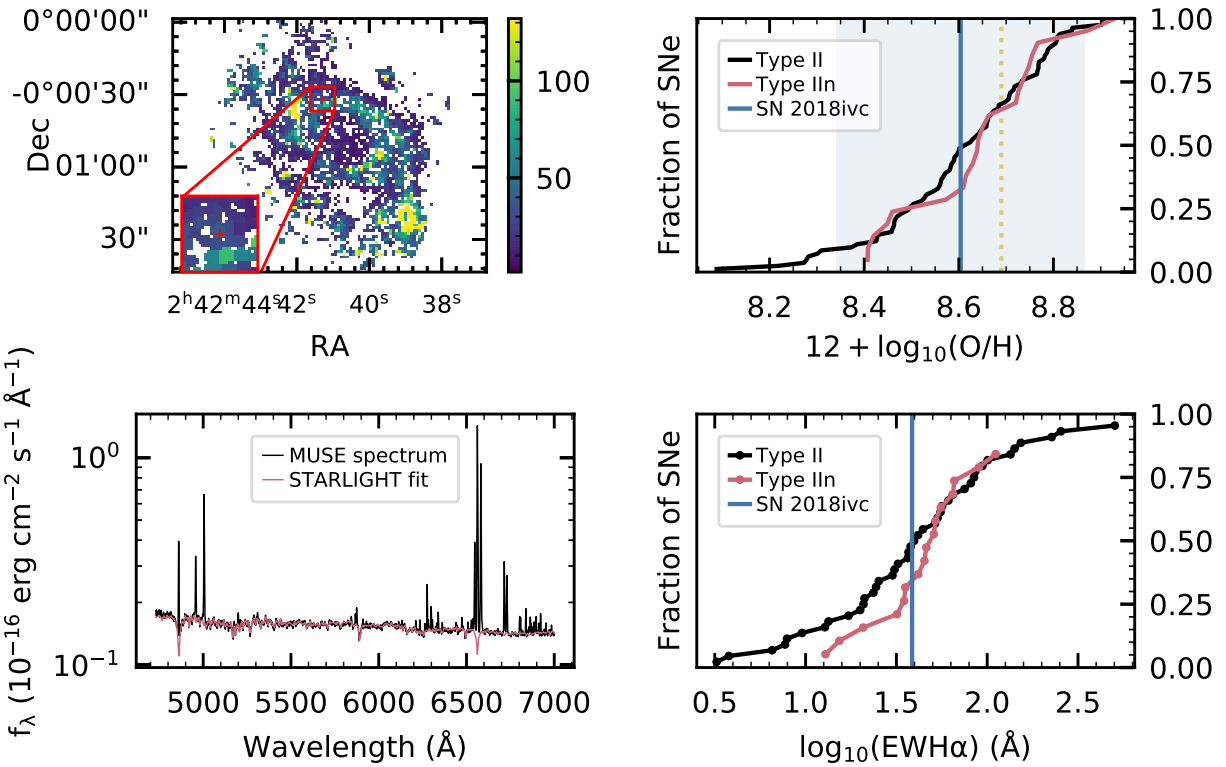

Figure 2.6 *Upper left*: the map of the H II regions in NGC 1068 identified by HIIEXPLORER; the parent H II region of SN 2018ivc is marked with a red point. The map is colored by H α equivalent width (EWH α), which is a proxy for regions with young stellar populations. A close-up view of a 10″region around the SN is shown in the inset. *Lower left*: the MUSE spectrum of the parent H II region of SN 2018ivc (black) and the STARLIGHT fit to the spectrum in pink. *Upper right*: the cumulative fraction of SNe from the PISCO sample [Galbany et al., 2018] as a function of metallicity for Type IIP/IIL SNe (black) and Type IIn SNe (pink). The metallicity of the parent H II region of SN 2018ivc is marked with a blue vertical line and the uncertainty in this value is denoted with the light blue shaded region. Solar metallicity (8.69; Asplund et al. 2009) is plotted as a dotted yellow line. *Lower right*: the cumulative fraction of SNe as a function of EWH α of their parent H II region. The fraction of Type IIP/IIL SNe is shown in black, the fraction of Type IIn SNe in pink, and the EWH α of SN 2018ivc is marked with the blue vertical line.

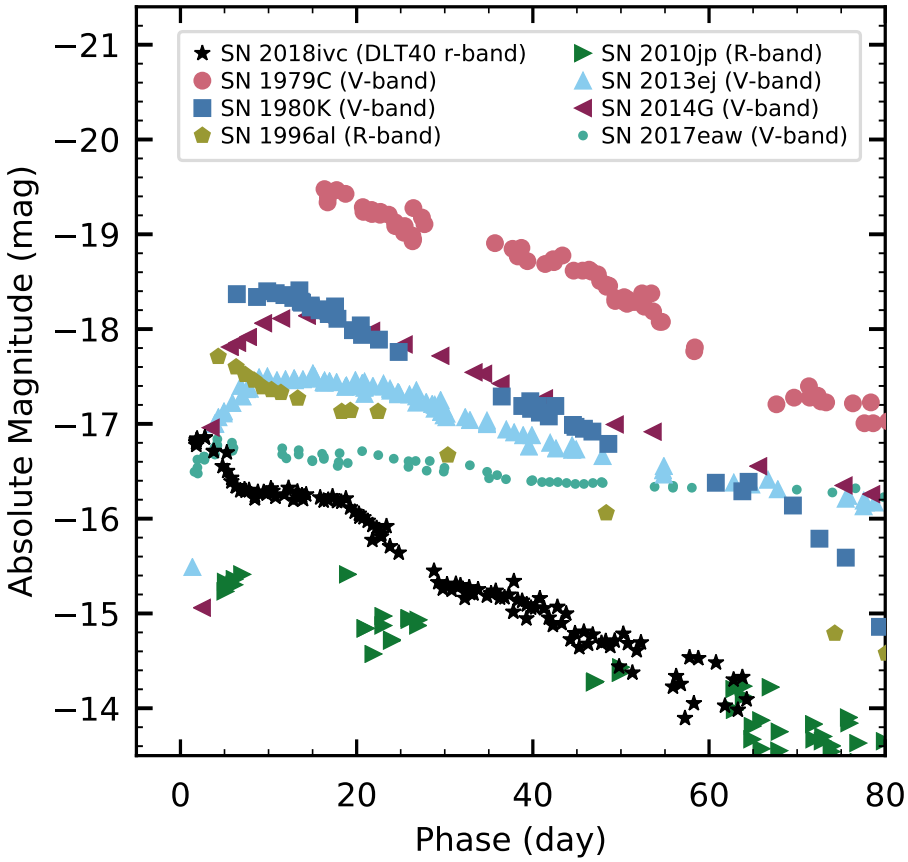

Figure 2.7 The light curve of SN 2018ivc (black stars; DLT40 r band) compared to a sample of well-studied SNe. SNe with a variety of slopes are represented with an emphasis on Type IIL-like SNe. The best-observed filter is shown for each SN. SN 1979C [pink circles, V band; Balinskaia et al., 1980, Barbon et al., 1982, de Vaucouleurs et al., 1981] and SN 1980K [blue squares, V band; Barbon et al., 1982, Buta, 1982, Tsvetkov, 1983] represent the historical Type IIL-like class. SN 2017eaw [sea foam green points, V band; Szalai et al., 2019] represents the Type IIP-like SNe. SN 2013ej [light blue triangles, V band; Valenti et al., 2014] and SN 2014G [maroon arrows, V band; Terreran et al., 2016] are transitional Type IIL-like objects, with a clear fall from the plateau onto the radioactive decay tail. We plot two SNe that will be discussed later in the text in comparison to SN 2018ivc: SN 2010jp [green arrows, R band; Smith et al., 2012] and SN 1996al [yellow pentagons, R band; Benetti et al., 2016].

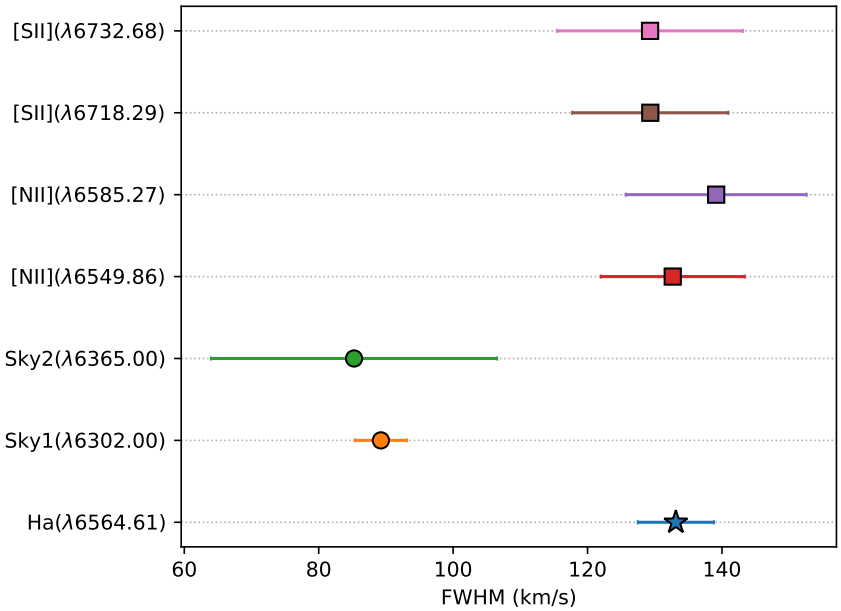

Figure 2.8 A comparison of the FWHM (km s^{-1}) for sky lines, galactic emission lines, and H α. The sky lines are significantly narrower than the galaxy lines demonstrating that we are fully resolving the galaxy lines and H α. The FWHM of H α is comparable to the other galaxy lines indicating that if a SN emission feature exists, it is likely lost in the galactic H α.

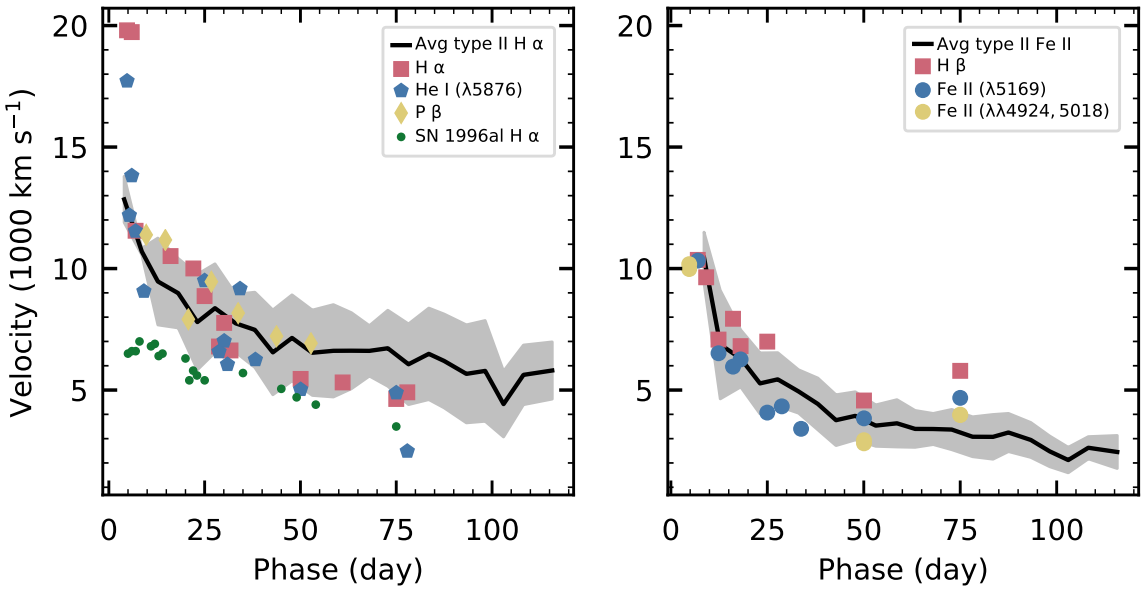

Figure 2.9 *Left*: the expansion velocity evolution of SN 2018ivc found using the HWHM of emission lines H α (pink squares), He I (blue pentagons), and P β (yellow diamonds). The H α velocity of SN 1996al is shown as green circles. The velocity of SN 2018ivc is similar to that of other Type IIP/IIL SNe, although it evolves more rapidly than most, including SN 1996al. *Right*: the expansion velocity evolution of SN 2018ivc found using the minimum wavelength of the absorption features H β (pink squares) and Fe II (blue and yellow circles). The average H α velocity (left) and Fe II (right) of the Gutiérrez et al. [2017] sample of Type IIP/IIL SNe is shown in black with the standard deviation in gray.

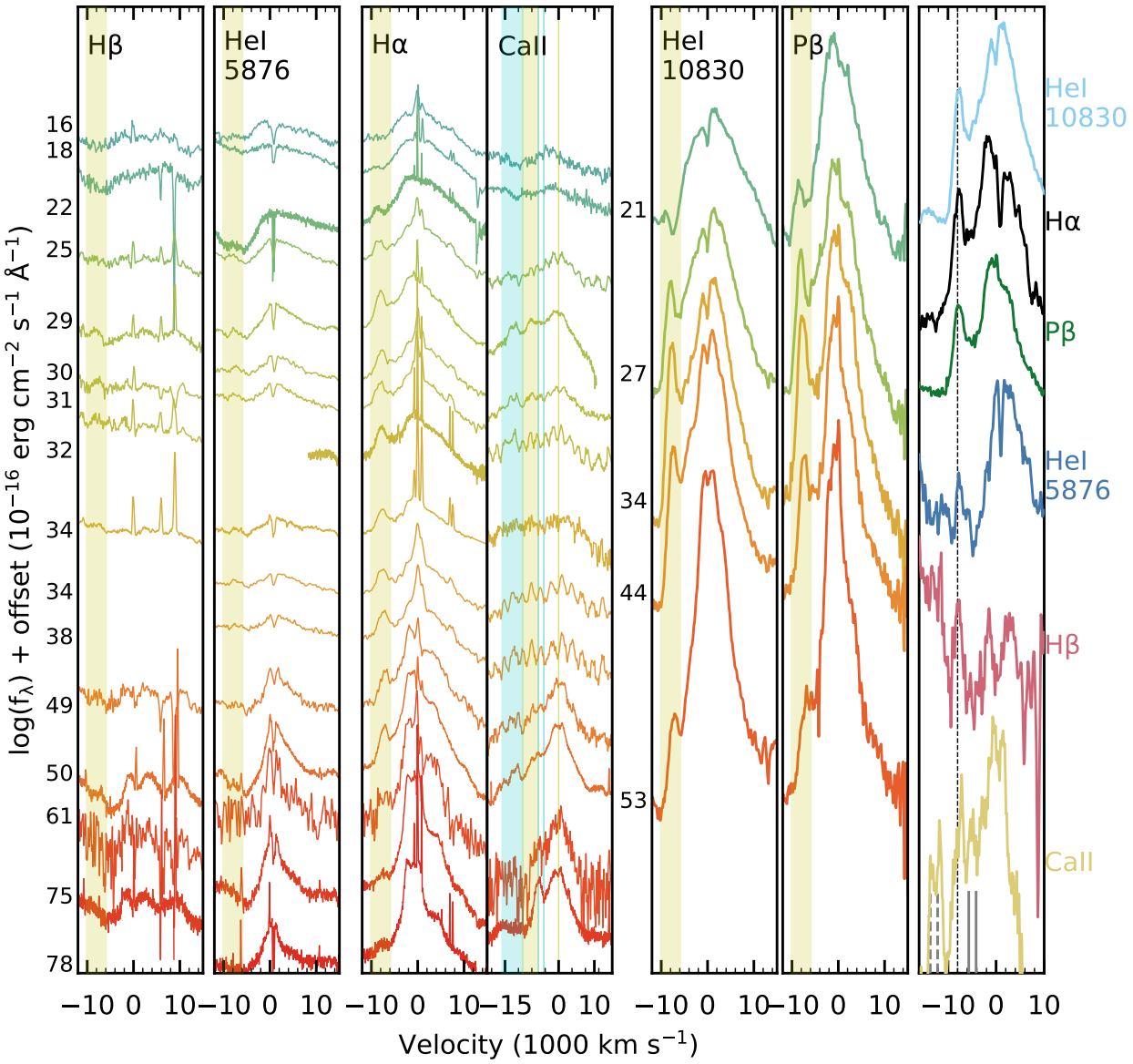

Figure 2.10 The evolution of the high-velocity (HV) features in hydrogen (H α, H β, P β), helium (λ5876, λ10830), and the Ca II triplet from day 18 through day 78 in the optical and day 21 through day 53 in the NIR. The feature is most prominent in H α, P β, and He I λ10830. The panels are labeled in the upper-left corner with the feature they present. The yellow shaded region marks $-10,000$ to -6000 km s^{-1}. The phases of the optical spectra are marked to the left of the first panel, and the NIR phases are marked to the left of the He I λ10830 panel. The Ca II panel is centered on the λ8662 component of the triplet (marked in yellow at both rest wavelengths and shaded in yellow at HV). The two blue components are marked at rest wavelength with vertical cyan lines and at high velocity with a shaded cyan region. The last panel shows the optical features on day 30 and the NIR features on day 34 for all emission lines in which the HV feature is seen. The HV feature is marked with a dashed line at -8000 km s^{-1} and each emission feature is labeled to the right of the panel. The bluest two Ca II triplet features that are offset in velocity space are marked with a solid line gray at the velocity corresponding to their rest wavelengths and dashed gray line for the HV features.

CHAPTER 3

ASASSN-15oz Observations and Properties

ASASSN-15oz was discovered by the All-Sky Automated Survey for SuperNovae (ASAS-SN) survey in HIPASS J1919-33 and was the closest Type II supernova (SN) in 2015. We use the Hubble flow distance modulus to the host galaxy, HIPASS J1919-33, $\mu = 32.3 \pm 0.2$ mag, with H $_0$=73 km s^{-1} Mpc^{-1} corrected for Virgo infall [1]. As a Type IIL-like SN with an extensive set of data, ranging from X-ray to radio wavelengths, ASASSN-15oz is a great candidate to search for evidence of mass loss and to test different methods for determining progenitor mass.

3.1. Observations and Data Reduction

ASASSN-15oz was the closest Type II SN of 2015 and was observed extensively at all wavelengths. The majority of our observations are provided by the Las Cumbres Observatory (LCO; Brown et al. 2013) Supernova Key Project (2014-2017) and the Public ESO Spectroscopic Survey for Transient Objects (PESSTO). We supplemented these with observations in the X-ray, ultraviolet (UV), optical, near infra-red (NIR), and radio. The photometric and spectroscopic data reduction is described in this section. A complete list of photometric and spectroscopic observations is given in Appendix B. All photometric data can be obtained from the SNDAVIS database[2] and all spectroscopic data can be found on WISeREP[3].

3.1.1. Optical. The optical light curve was closely monitored by the LCO from discovery through day 400 in the filters *B, V, g, R, r, I* and *i*. Unfortunately, the SN passed behind the sun around day 80, leaving a gap in the observations from day 87 to day 179, most notably missing the fall from plateau. Figure 3.1 shows the complete multi-band light curve. LCO observations were reduced with the LCO imaging pipeline, `lcogtsnpipe` [Valenti et al., 2016]. This pipeline

[1]The NASA/IPAC Extragalactic Database (NED) is operated by the Jet Propulsion Laboratory, California Institute of Technology, under contract with the National Aeronautics and Space Administration.
[2]http://dark.physics.ucdavis.edu/sndavis/transient
[3]https://wiserep.weizmann.ac.il

employs PSF photometry, removing background contamination by fitting a low order polynomial to the host galaxy. Instrumental magnitudes were converted to apparent magnitudes using stars in the the APASS[4], Sloan, and Landolt catalogs. Apparent magnitudes for the *U, B, V, R,* and *I* filters are given in the Vega magnitude system and apparent magnitudes for the *g, r,* and *i* filters are given in the AB magnitude system.

Extensive optical spectroscopy was obtained during the photospheric phase with the FLOYDS spectrograph [Brown et al., 2013] on the 2m LCO telescope at Siding Springs, Australia and the EFOSC2 spectrograph [Buzzoni et al., 1984] on the 3.6 m NTT telescope at La Silla, Chile during the photospheric and nebular phase. One-dimensional spectra were extracted and calibrated using the `FLOYDS pipeline` [Valenti et al., 2014] and the EFOSC tasks in the `PESSTO pipeline` [Smartt et al., 2015]. Both of these pipelines combine `IRAF` tasks to bias subtract and flat field the data and locate, extract, wavelength calibrate, and flux calibrate the one-dimensional spectrum.

Data were also taken using the X-Shooter echelle spectrograph [Vernet et al., 2011] on the 8.2m Very Large Telescope (VLT) at the European Southern Observatory (ESO). X-Shooter has three arms (UVB, VIS, NIR) which combined provide continuous wavelength coverage over $3000 - 24800$ Å. For our data, we used slit widths of 1.0, 0.9, and 0.9 arcsec in the UVB, VIS, and NIR arms, corresponding to resolutions of R $\sim$5400, 8900, and 5600, respectively. The UVB and VIS data were reduced via a modified version of the `EsoReflex` pipeline [Freudling et al., 2013], with improvements to the sky-subtraction and rebinning procedure on the highly dispersed echelle spectrum.

Figure 3.2 shows the evolution of the optical spectra over time. The progression starts with a blue spectrum with broad hydrogen lines at the top of the figure. Over time (moving down the figure), the spectra develop metal features such as iron and scandium as the velocities decrease and the line widths narrow.

We obtained late time spectra from the Gemini South Observatory through program GS-2016A-Q-75-25 (PI: Valenti). The Gemini spectra of ASASSN-15oz were taken on day 287 (2016 Jun 09), day 288 (2016 Jun 10), and day 290 (2016 Jun12) using the Gemini Multi-Object Spectrograph (GMOS) [Hook et al., 2004]. Data were taken with a blue setting with the B600 grating, no filter, a 1.0″slit, and 2x2 binning, and a red setting with the R400 grating, OG515 order blocking filter,

[4]https://www.aavso.org/apass

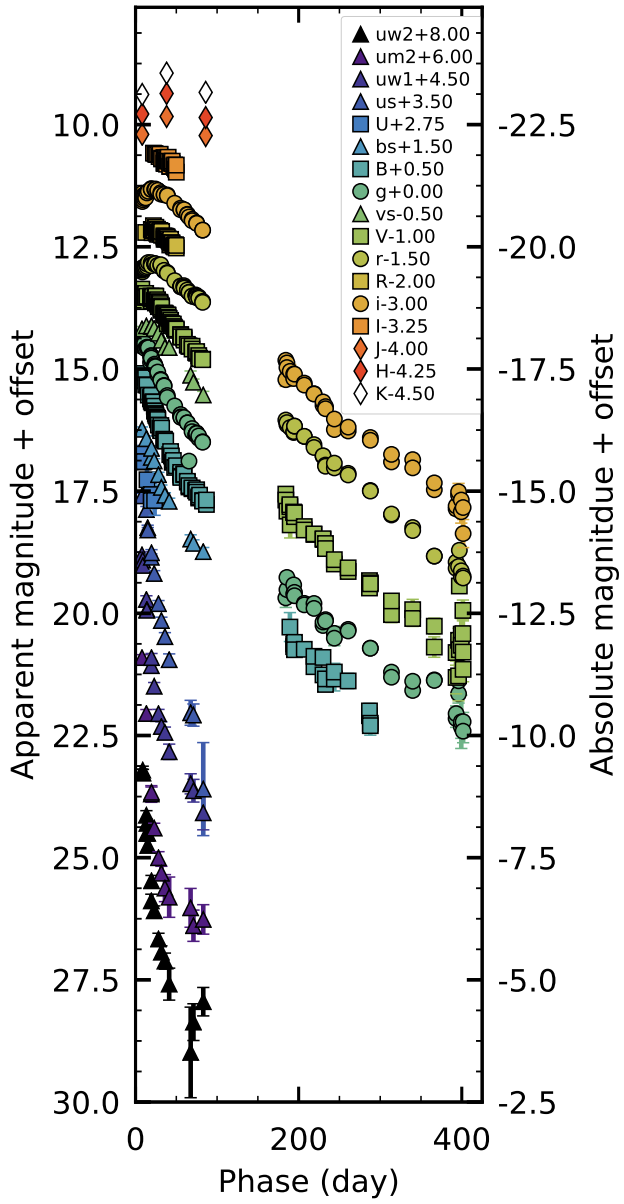

Figure 3.1 The complete UV, optical, and NIR light curve of ASASSN-15oz expressed in terms of days since explosion. Apparent magnitude (+offset) is plotted on the left and absolute magnitude (+offset) is plotted on the right. Each color corresponds to a single filter, labeled in the legend. The optical *Swift* filters are denoted with an "s" in the name (e.g. us) and plotted with the triangle symbol. NIR observations are shown with the diamond symbol. To differentiate the *U, B, V, R,* and *I* filters and the *g, r,* and *i* filters, we use a square symbol for the former and a circle for the later. Each filter has been shifted by a global offset (denoted in the legend) for viewing purposes.

a 1.0″slit, and 2x2 binning. These settings provide a wavelength range 3630 - 6830 Å with a dispersion of 1.0 Å pixel^{-1} in the blue and a wavelength range 5030 - 9800 Å with a dispersion of 1.3Å pixel^{-1} in the red. We used the `Gemini iraf` package for GMOS to process our data. The raw two-dimensional images were bias subtracted, overscan corrected, flat-fielded, wavelength calibrated using CuAr emission lamps, cleaned of cosmic rays, and background subtracted prior to extraction of the 1D target spectra. The spectra were then calibrated using a sensitivity function derived from a standard star observed for the program.

3.1.2. UV and X-Ray Observations. UV and X-Ray imaging observations were obtained concurrently with *Swift* from day 9 (2015 Sep 05) through day 83 (2015 Nov 18). In addition to the imaging observations, two epochs were observed with the *Swift* grism under program 1114241 (PI: Valenti). Imaging observations were processed with aperture photometry following Brown et al. [2009] and employing the updated zeropoints of Breeveld et al. [2010]. UV grism observations were taken at two roll angles and extracted using the `UVOTPY` pipeline[5] [Kuin et al., 2015]. There is a nearby star coincident with the SN at one roll angle and just above it at the other roll angle. Although we tried custom extractions using different extraction box height and template subtraction using `TRUVOT` [Smitka, 2015] we were unable to produce a better calibration than the default pipeline. Due to the distance of the ASASSN-15oz, only the first of the two spectroscopic epochs has sufficient S/N to be extracted. These spectra are shown in Figure 3.3.

X-ray upper limits were calculated using the `SOSTA` command in the `HEAsoft` package `ximage`. Count rates were converted to flux units using `PIMMS` [Mukai, 1993] assuming a power-law model with a photon index of two for an input and output energy range of 0.5-8 keV. There were no X-ray detections at any epoch.

3.1.3. NIR Observations. ASASSN-15oz was observed in the NIR with the SOFI instrument on the NTT telescope through the PESSTO collaboration, the SpeX instrument [Rayner et al., 2003] on the 3.0-m NASA Infrared Telescope Facility (IRTF), and the NIR arm of the X-Shooter spectrograph. The data reduction of the NIR arm of the X-Shooter spectrum is described with the UV and VIS arms in Section 3.1.1.

[5]Kuin [2014]

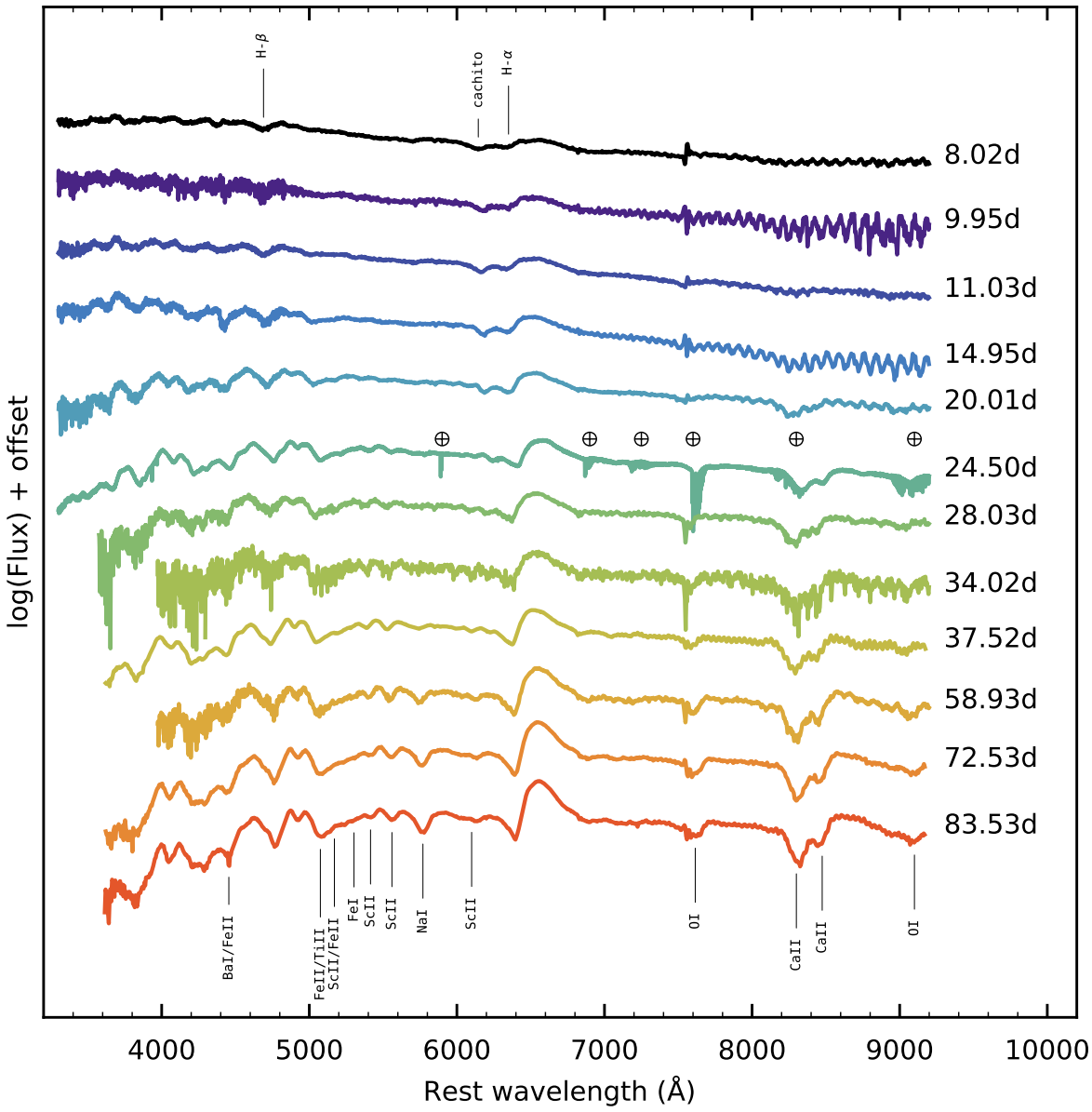

Figure 3.2 A time series of the photospheric spectra of ASASSN-15oz at rest wavelengths. The phase of each spectrum is marked on the right. Potential telluric contamination is marked with crossed circles above the day 24.5 spectrum. The first spectrum taken near maximum light shows hydrogen features (identified at the top of the figure). At this early phase, the cachito feature (see Section 4.2.2) is already visible. Over time the cachito feature fades while the hydrogen emission grows and metal lines become visible and grow in strength. These lines are identified in the bottom spectrum.

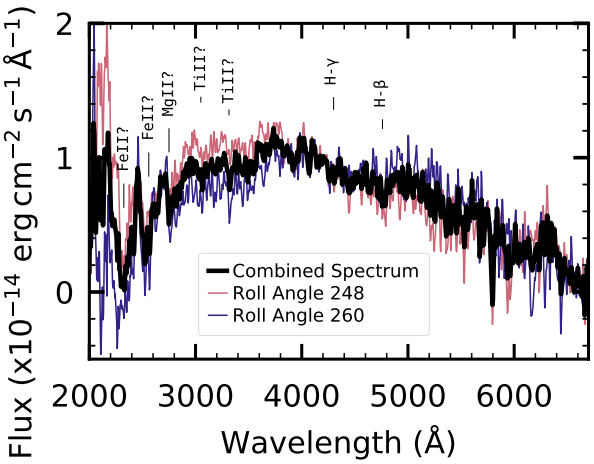

Figure 3.3 The *Swift* UV spectra from day 9 (2015 Sep 05), boxcar smoothed with a kernel of three pixels. The spectrum taken with a roll angle of PA = 248° is in pink, the spectrum taken with a roll angle of PA = 260° in indigo, and average flux is in black. We tentatively identify UV FeII, TiII, and MgII features as well as mark the Balmer lines. These spectra are not template subtracted, therefore they show residuals from zeroth order light. These features can be identified as being in the spectrum of one roll angle but not the other. The lack of narrow line emission indicates a lack of strong interaction.

The SOFI spectroscopic data were reduced with the `PESSTO package` [Smartt et al., 2015]. Photometric measurements were performed with the `QUBA pipeline` [Valenti et al., 2011], which performs DAOPHOT-based [Stetson, 1987] point-spread-function fitting photometry on the SN and on the selected reference stars. *J, H,* and K photometry was then calibrated to the 2MASS magnitude system.

The SpeX data were taken in so-called SXD mode, where the spectrum is cross-dispersed to obtain wavelength coverage from ∼0.8–2.4 μm in a single exposure, spread over six orders. All observations were taken with the slit aligned along the parallactic angle, and we employed a classic ABBA technique for improved sky subtraction. HD 177074, an A0V star, was observed adjacent in time to the science observations for flux and telluric calibration. The spectrum was reduced in a standard way using the publicly available SpeXtool software package [Cushing et al., 2004] and corrections for telluric absorption utilized XTELLCOR [Vacca et al., 2003] and the A0V star observations.

The three photometric observations from day 8 (2015 Sep 04), day 38 (2015 Oct 04), and day 86 (2015 Nov 21) are shown in Figure 3.1. Spectroscopic observations from SOFI (day nine; 2015

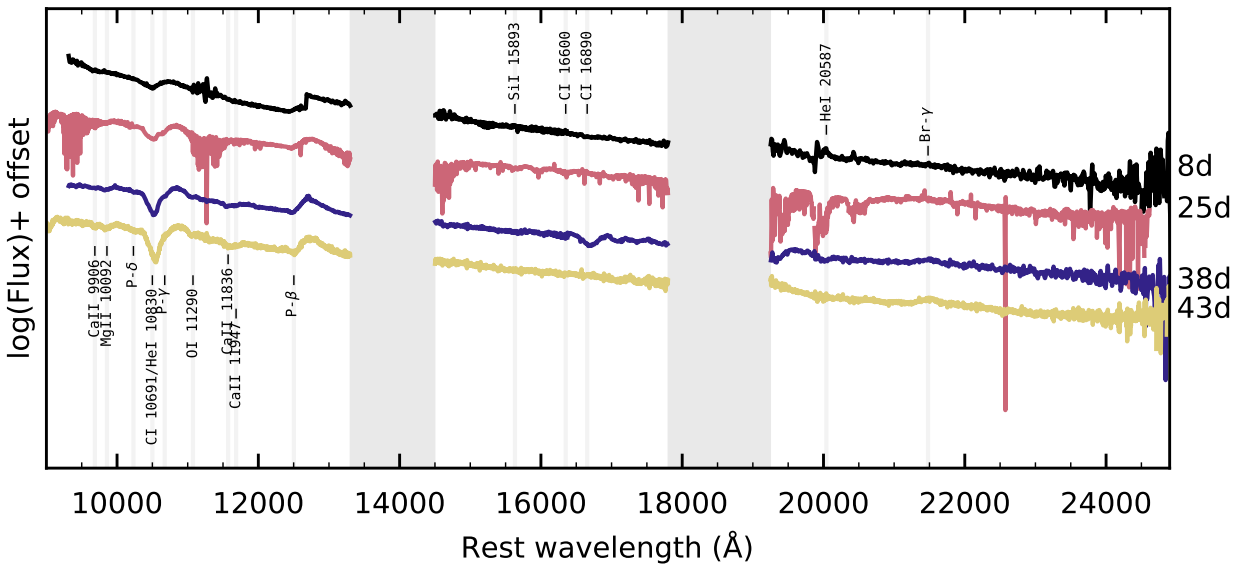

Figure 3.4 The evolution of the infrared spectra at rest wavelengths during the photospheric phase. The spectral evolution in the IR mirrors the optical evolution, with broad hydrogen features narrowing and metal lines developing over time. The first spectrum (black) taken eight days post-explosion shows broad hydrogen features. The later spectra at day 38 (indigo) and 43 (yellow) reveal the development metal lines. Although contaminated with narrow telluric features, the high resolution X-Shooter spectrum (pink) shows an intermediate phase. Regions of severe sky contamination are marked with grey boxes and are masked out of the spectra.

Sep 05 and day 39; 2015 Oct 05), X-Shooter (day 26; 2015 Sep 21), and SpeX (day 44; 2015 Oct 10) are shown in Figure 3.4.

3.1.4. Radio Observations. We observed ASASSN-15oz using the NSF's Karl G. Jansky Very Large Array (VLA) (VLA/15B-362, PI: Valenti) on day 28 (2015 Sep 24) and day 42 (2015 Oct 08). In both of the observations we used J1924-2914 and 3C48 as a phase calibrator and a flux calibrator, respectively. We used the Common Astronomy Software Applications (CASA) standard packages and pipelines to perform the data calibration and imaging. The SN was detected in both observations with the following flux measurements: September 24: $120 \pm 23\,\mu$Jy at 4.8 GHz (C-band) and a $3\,\sigma$ non-detection limit at 22 GHz (K-band); October 08: $210 \pm 21\,\mu$Jy at 4.8 GHz (C-band) and a $80 \pm 17\,\mu$Jy at 15 GHz (KU-band).

3.2. Supernova Parameters

ASASSN-15oz was discovered by the ASAS-SN team on 2015 Aug 31.09 (JD 2457265.59; V = 14.6 mag; RA = 19:19:33.55, Dec=-33:46:01.2) and announced on 2015 Sep 03 (JD 2457268; Brown et al. 2015). The next day, 2015 Sep 04 (JD 2457270.0), LCO classified it as a Type II SN one week after explosion [Hosseinzadeh et al., 2015]. Figure 3.5 shows the Digital Sky Survey (DSS) image of the low luminosity host galaxy, HIPASS J1919-33, prior to explosion (top panel) and our first *V*-band image of ASASSN-15oz taken on day 8 (2015 Sep 04). Imaging of the host galaxy, HIPASS J1919-33, from 2015 Aug 23 (JD 2457257.56) does not show any evidence of ASASSN-15oz (V > 17.8; Brown et al. 2015). We take this date to be a lower limit on the explosion epoch and define the mid-point between the non-detection and the detection as explosion date: t_{expl} = 2015 Aug 27 ±4 days (JD 2457261.5). This is in agreement with the value used in Gutiérrez et al. [2018].

When non-detection observations are not available, other methods can be used to determine the explosion epoch. Gutiérrez et al. [2017] found that the explosion epoch can be determined, with an average errors of 4.9 days, by fitting the blue part of the first spectrum with SNID[6] [Blondin and Tonry, 2007] and using the explosion epoch of the best fit template. This method relies on the existence of a template SN that is similar in both phase and type to the object being fit. ASASSN-15oz is a IIL-like SN. SNID has very few templates for IIL-like SNe, even after adding the new templates provided by Gutiérrez et al. [2017]. Therefore, in addition to the Gutiérrez et al. [2017] templates, we add templates for two well observed SNe with well constrained explosion epochs: SN 2012A [Tomasella et al., 2013], and SN 2013ej [Childress et al., 2016, Dhungana et al., 2016, Smartt et al., 2015, Valenti et al., 2014] [7]. With these templates, we confirm our explosion epoch by fitting the first spectrum (2015 Sep 04) using SNID v. 5.0. The five best fit spectra imply an explosion epoch of 2015 Aug 22±4.9 (JD 2457256.5), consistent with the range we propose based on non-detections. Interestingly, the hydrodynamic light curve modeling also places the best fit explosion epoch earlier than 2016 Aug 27 (see Section 3.3). As the uncertainties of both these methods are greater than that of the non-detection, throughout this thesis we adopt the

[6]Blondin and Tonry [2011]

[7]SNID templates for SN 2012A and SN 2013ej can be found at https://github.com/abostroem/snid_templates

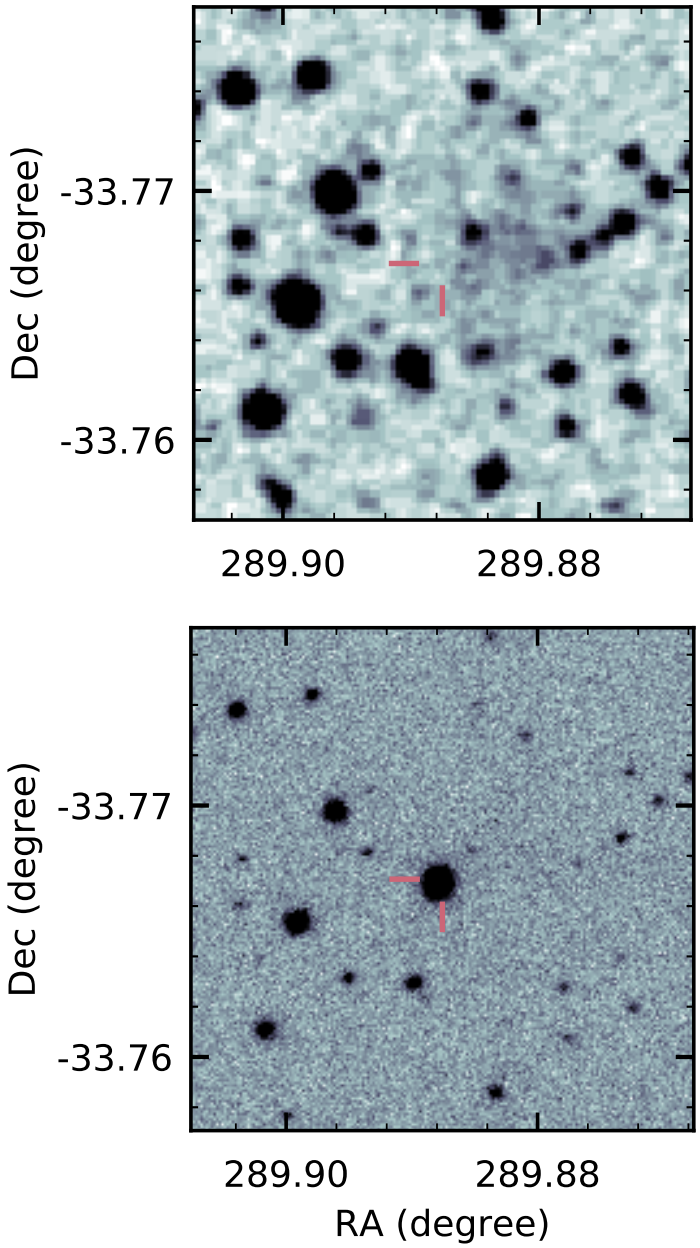

Figure 3.5 Top: The host galaxy of ASASSN-15oz, HIPASS J1919-33, taken prior to the SN explosion by DSS. Bottom: *V*-band image of ASASSN-15oz taken by LCO eight days post explosion (2015 Sep 04). The location of the ASASSN-15oz is marked by the pink ticks in both images.

value determined by the non-detection as the explosion epoch, t_{expl} = 2015 Aug 27 ±4 days (JD 2457261.5), unless otherwise specified.

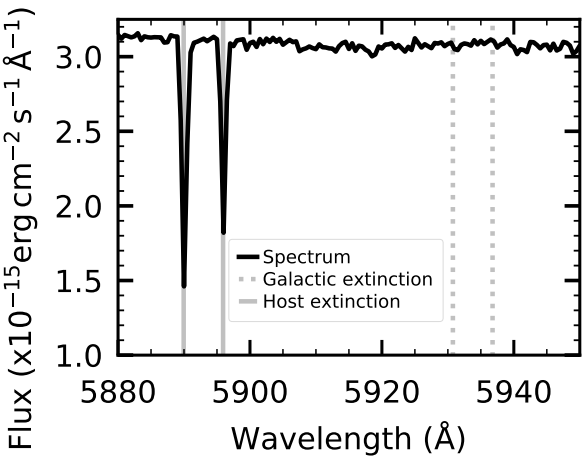

Figure 3.6 The galactic (solid gray lines) and host (dashed gray lines) Na I D1 and D2 lines in the high resolution X-shooter spectrum from day 26; (2015 Sep 21). The galactic profiles are consistent with the galactic extinction of Schlafly and Finkbeiner [2011] while the absence of absorption at the host redshift indicates a lack of dust in the host galaxy.

We use the VIS arm of the X-shooter spectrum (R ∼8900) to constrain the host galaxy reddening and to confirm the galactic reddening using the equivalent widths of the Na I D1 and D2 lines (λ5890, λ5896) [Poznanski et al., 2012]. We find no evidence of Na I absorption at the host redshift and therefore assume no host reddening (see Figure 3.6). By fitting gaussian profiles to the galactic Na I absorption we find $\mathrm{E(B-V)} = 0.12 \pm 0.07$ mag, consistent with the value given by Schlafly and Finkbeiner [2011]. We adopt the Schlafly and Finkbeiner [2011] value of $\mathrm{E(B-V)} = 0.08$ mag for the analysis in this chapter and use the extinction law of Cardelli et al. [1989] with $\mathrm{R_V} = 3.1$.

The pseudo-bolometric luminosity is computed following Valenti et al. [2008]. To summarize the method, the apparent magnitudes are corrected for galactic extinction. We use the *U, B, g, V, r, R, i,* and *I*-bands to calculate the pseudo-bolometric luminosity at the *V*-band cadence. The flux density is calculated from the apparent magnitude at the effective wavelength of each filter and integrated using the trapezoid rule. Finally, the flux is converted to a luminosity using the distance modulus. When *V*-band observations extended either earlier or later than a filter, we use the color with the neighboring filter to extrapolate the flux.

3.2.1. Nickel mass determination. The amount of ^{56}Ni synthesized during the explosion can be inferred using the late time (> 150 days) photometry. At this time, the energy output

is powered by the radioactive decay of ^{56}Ni $\rightarrow$ ^{56}Co $\rightarrow$ ^{56}Fe which produces gamma rays that are reprocessed by the ejecta producing optical light. Assuming that the SN has the same SED as the extremely well characterized SN 1987A, the ^{56}Ni mass synthesized in the SN explosion can be found by scaling the pseudo-bolometric luminosity of SN when it is powered by ^{56}Co to that of SN 1987A with the following equation [Spiro et al., 2014]:

$$M(^{56}Ni) = 0.075 M_{\odot} \times \frac{L_{SN}(t)}{L_{87A}(t)} \tag{3.1}$$

where M(^{56}Ni) is the synthesized ^{56}Ni mass, $L_{SN}(t)$ is the pseudo-bolometric luminosity of the SN at time t, and $L_{87A}(t)$ is the pseudo-bolometric luminosity of SN 1987A at time t using the same filters as were used to compute the pseudo-bolometric luminosity of the SN.

This scaling can be performed at any time, as long as the slope is the same as that of SN 1987A, i.e. consistent with the complete trapping of gamma-rays. As the SN ages, the optical depth of the gamma-rays decreases. Thus a SN is most likely to have complete trapping immediately after the fall from plateau. Unfortunately, for ASASSN-15oz, there is not complete trapping for any part of the observed radioactive decay tail and there are no observations of the period immediately after the fall from plateau. We therefore consider the maximum and minimum ^{56}Ni mass allowed by the observations, under the assumption that there is complete trapping immediately following the fall from plateau. For both cases we also assume that the fall from plateau takes 20 days, based on light curve fits presented in Valenti et al. [2016]. An upper limit on the ^{56}Ni mass is obtained by assuming ASASSN-15oz fell from plateau immediately after the last photospheric point (see upper panel of Figure 3.7). Scaling the pseudo-bolometric luminosity of 1987A at 102 days to that of ASASSN-15oz at the same time, we calculate a ^{56}Ni mass of 0.11 $M_{\odot}$. To find the lower limit, we estimate a conservative value of the time to the middle of the fall from plateau (t_{pt}) to be 125 days using Figure 5a in Valenti et al. [2016]. Using this t_{pt} we calculate the fall from plateau to end 135 days after explosion and extrapolate the tail fit to this phase (see lower panel of Figure 3.7). We compute a ^{56}Ni mass of 0.08 $M_{\odot}$ by scaling the pseudo-bolometric luminosities at 135 days. In both panels of Figure 3.7, the observations are represented with black circles, the s_2 slope with a pink line, the fall from plateau with a indigo line, the tail slope with a yellow line, and the

Table 3.1 The best-fit slope to the V-band light curve of ASASSN-15oz measured between the start and end phase listed in the table. All slopes are measured in units of magnitudes per 50 days.

Slope Type	Slope [mag $(50\text{days})^{-1}$]	Slope Error [mag $(50\text{days})^{-1}$]	Start Phase [day]	End Phase [day]
s_1	1.21	0.066	21.0	38.0
s_2	0.99	0.021	45.0	78.0
s_{50V}	1.09	0.014	18.4	78.0
s_{tail}	0.70	0.029	206.9	368.0

expected tail slope from complete trapping is marked with a dashed green line. The time that is used to scale SN 1987A to ASASSN-15oz is marked with a cyan star.

3.3. Light Curve Evolution of ASASSN-15oz

The light curve of ASASSN-15oz reaches peak brightness in the *V*-band 8.25 days after explosion, one day after the start of our observations, reaching an above average absolute magnitude of -18.05 ± 0.025 mag. The early light curve rises until around day 20 in the redder filters, flattening in the *V*-band and falling in the blue bands during this same period. It then falls in all bands for the remainder of the observations, changing slope around day 40 and again sometime after day 85, as it enters the radioactive decay phase, following the fall from plateau. Following Anderson et al. [2014], we use the *V*-band light curve to fit a slope to the first steep initial decline after maximum (s_1) and to the second shallower slope prior to the fall from plateau (s_2). We also fit a global decline rate, s_{50V} from soon after maximum to prior to the fall from plateau. During the nebular phase we fit a slope to the radioactive decay tail (s_{tail}[8]). The slopes we fit as well as the details of the fit are summarized in Table 3.1 and plotted on top of the *V*-band light curve in Figure 3.8. Both the high slopes and bright maximum luminosity of ASASSN15oz are similar to those of other IIL-like SNe. The slope of the radioactive decay tail is steeper than expected from the radioactive decay of $^{56}\text{Ni} \rightarrow {}^{56}\text{Co} \rightarrow {}^{56}\text{Fe}$ implying that the ejecta is not fully trapping and reprocessing the gamma-rays produced by the radioactive decay.

[8] this is equivalent to s_3 in Anderson et al. [2014]

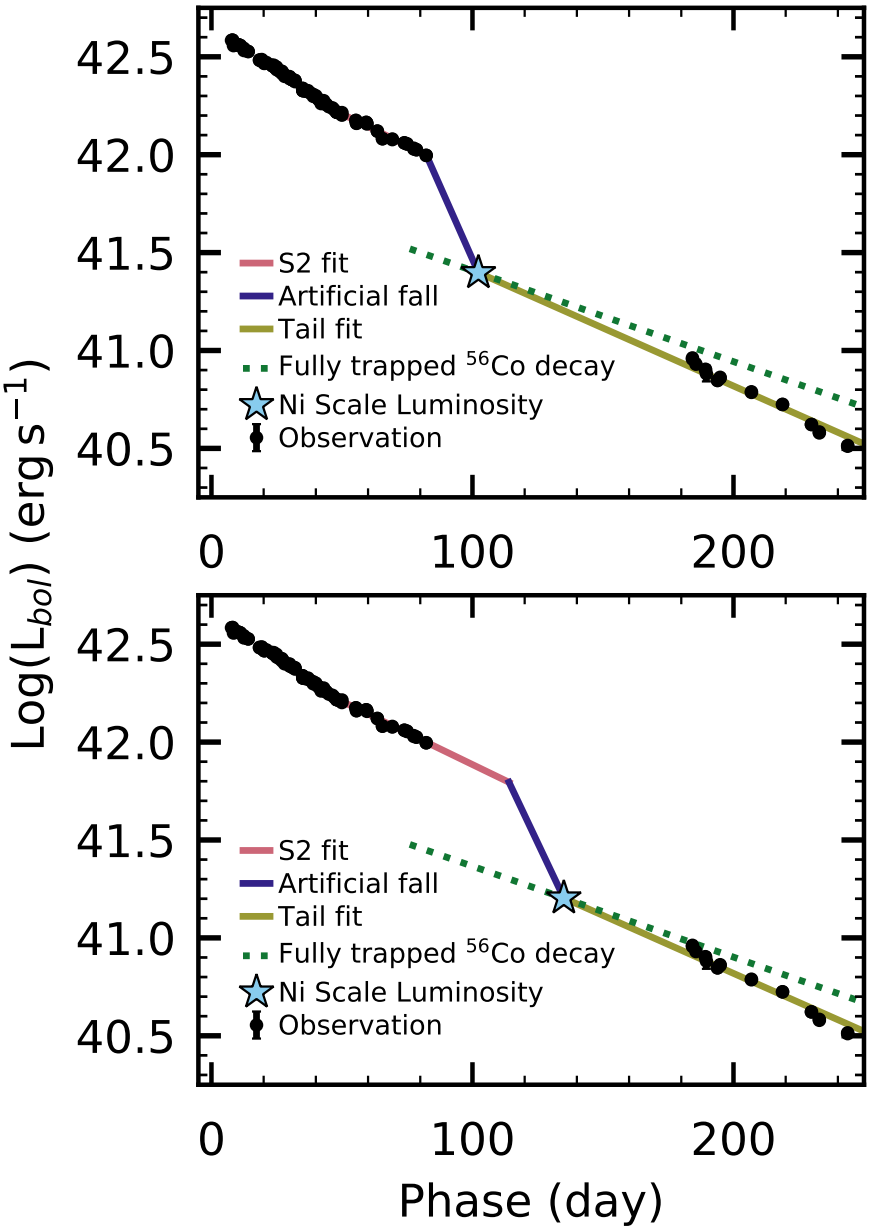

Figure 3.7 The artificial light curve of ASASSN-15oz for the shortest (top) and longest (bottom) plateau lengths. The black points plot the bolometric luminosity while the pink line represents a fit to the s2 data, the indigo line is the artificial fall from plateau, and the yellow line is a fit to the radioactive decay tail. The cyan star marks the point to which the light curve of SN 1987A is scaled to derive a ^{56}Ni mass. Plotted as a green dashed line is the slope of the radioactive decay tail if there was complete trapping. An upper limit on the ^{56}Ni mass of 0.11 $M_{\odot}$ is derived from the light curve in the top panel while a lower limit of 0.08 $M_{\odot}$ is derived from the lower panel.

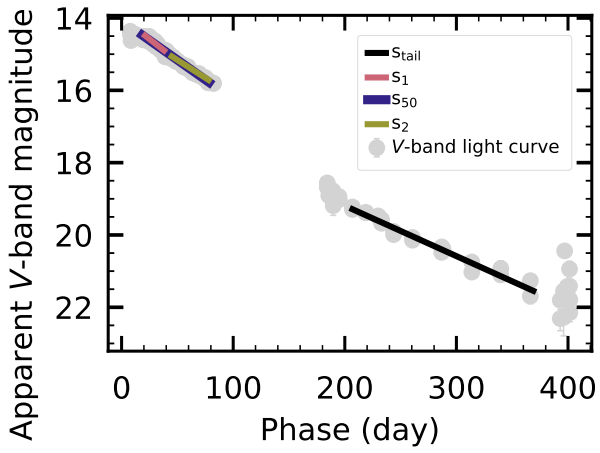

Figure 3.8 The s_1 (pink), s_2 (yellow), s_{50V} (indigo), and s_{tail} (black) fits plotted over the period used to derive the relation. The *V*-band light curve is plotted in gray. Although errors in the apparent magnitude are plotted, in many cases these are smaller than the points.

3.4. Spectroscopic Analysis

The spectroscopic evolution of a SN during the photospheric phase provides insight into details of the SN ejecta. The changes in velocity and the individual line profiles describe the geometry and energetics of the ejecta. The presence of different species at different times gives information about the chemical composition, temperature, and density of the ejecta. In this section we analyze optical and NIR spectra.

3.4.1. Optical Evolution. Initial line identification was performed by comparing the spectra to that of SN 1999em [Leonard et al., 2002]. Identification was confirmed using the spectrum synthesis code `SYN++` [9](Thomas et al. 2011; parameter details in Appendix B). The results of the `SYN++` fit can be seen in Figure 3.9.

We use two methods to find the velocity of lines for which individual components can be resolved, one for blended features, and one for individual features. For lines that are not blended or that are dominated by the absorption of one ion (e.g. Sc II λ 5526, 5662, 6262), we employ the method presented in Silverman et al. [2012]. For blended features we fit a multi-component gaussian to the feature. We use this method to fit H α (λ 6561), O I (λ 7774), FeII (λ 5169), and Ca II ($\lambda\lambda\lambda$ 8498, 8542, 8662). Details of both fitting procedures are given in Appendix B.1. Rather

[9]Thomas [2013]

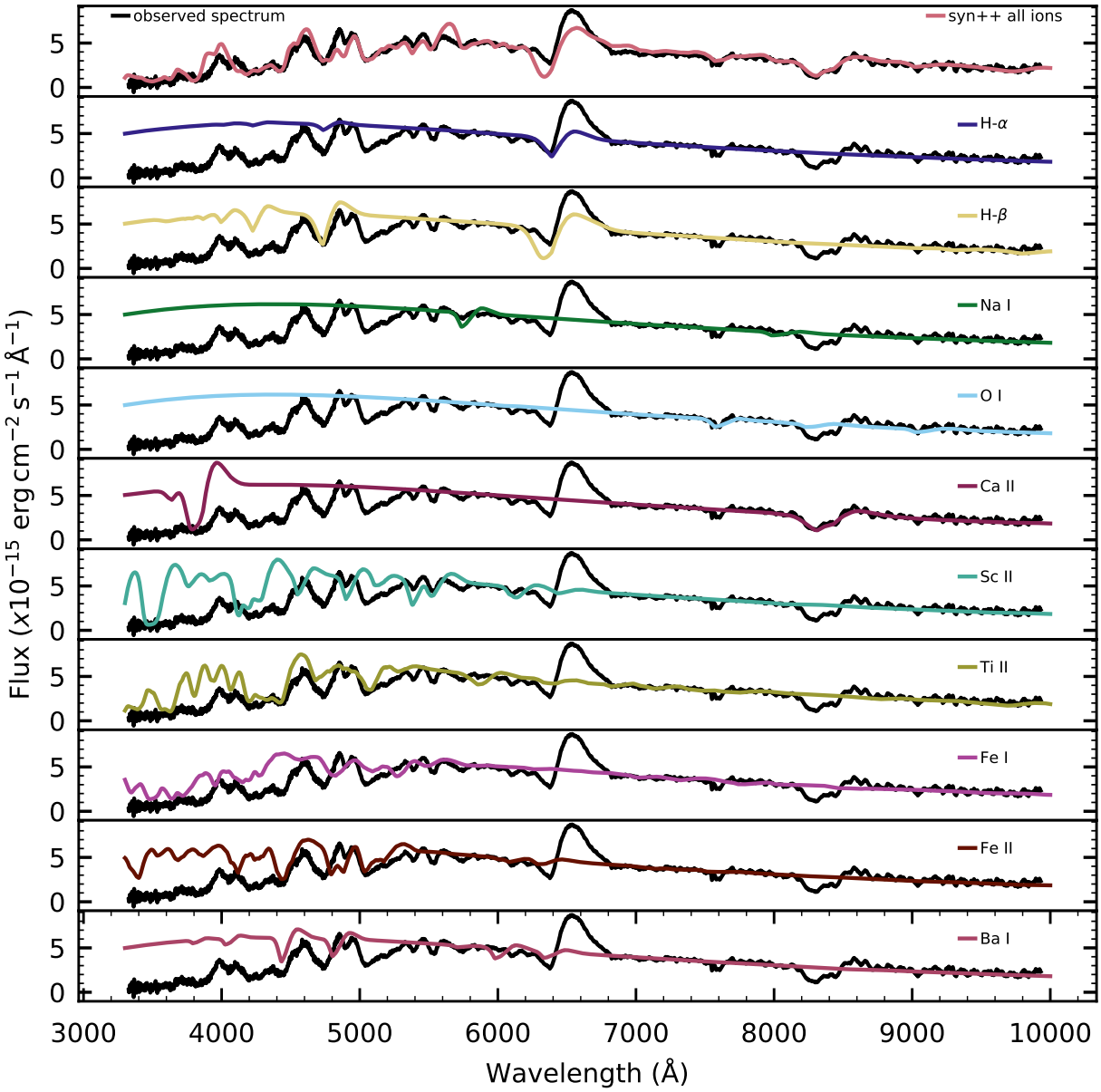

Figure 3.9 A comparison of the model spectra produced by Syn++ (colored lines) and the observed spectrum (black) from day 40 (2015 Oct 06). The top panel shows the best fit with all elements while the remaining panels show the fit for each element individually. We fit H α and H β separately as H α is not well modeled by the pure resonance scattering assumed in Syn++. The H β fit is used in the combined spectrum in the top panel.

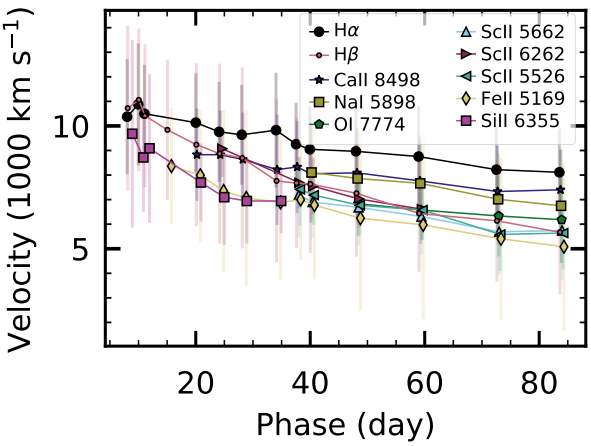

Figure 3.10 The evolution of the velocity of H α, H β, Na I, O I, Ca II, Sc II, and Fe II over time. The points represents the minimum of the feature showing the velocity with the largest optical depth while the bars plot the range of velocities found in the line forming region. The coincidence of velocities of different species, especially at late times, indicates that mixing may have been important for ASASSN-15oz.

than expressing an uncertainty on the fit, we calculate the range of velocities that encompass 68.2% of the integrated (continuum subtracted) flux around the feature minimum. Because each line is formed in an extended region of the ejecta, this represents the range of velocities at which each line forms.

Figure 3.10 shows the measured velocities. The distribution of velocities is typical of other IIP/IIL SNe representing the distribution of elements throughout the ejecta. A comparison of the velocities derived in this chapter to the average values of 122 IIP/IIL SNe described in Gutiérrez et al. [2017] is shown in Figure 3.11. The shaded regions represent the standard deviation of the sample. We find above average velocities throughout the ejecta.

3.4.2. Infrared Evolution. Line identification was performed by comparing the NIR SOFI and SpeX spectra to those in Valenti et al. [2015] and Tomasella et al. [2018]. Figure 3.4 shows the NIR spectra with prominent features labeled. Like the optical, the first spectrum, taken eight days post explosion (2018 Sep 05), is dominated by hydrogen features. The later spectra also mirror the optical evolution, developing metal lines as the ejecta slows and cools. We use the IR spectra to search for evidence of interaction via a high velocity He I feature (see Section 4.2.2).

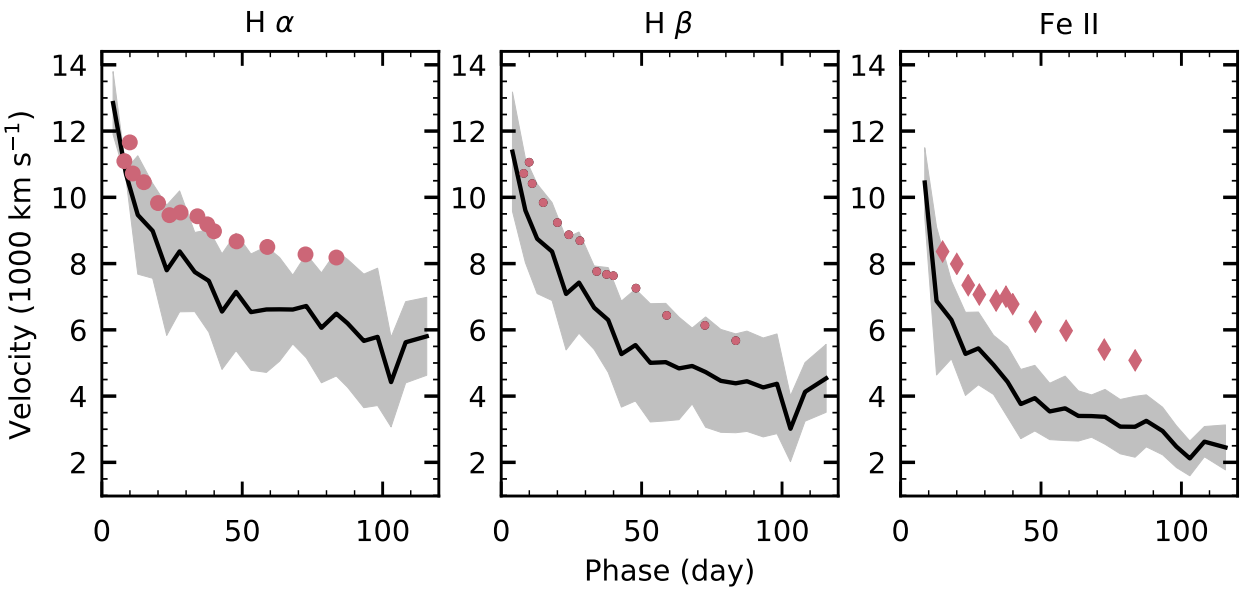

Figure 3.11 A comparison of the velocity of ASASSN-15oz (pink) to the mean velocity of 122 IIP/IIL SNe [Gutiérrez et al., 2017] (black) for H α (left), H β (middle), and Fe II (λ5169; right). The gray regions represent the standard deviations of the mean velocities. The velocity of ASASSN-15oz is $> 1\sigma$ above average for all three ions. Each of these line originates in a different part of the ejecta indicating that this is a global trend and the explosion energy is above average. Following [Silverman et al., 2012] we select velocity errors of 2 Å. These are contained within the symbols and so are not plotted.

3.5. Comparison to other SNe

It is useful to compare observations of ASASSN-15oz to those of other IIP/IIL SNe to understand if it is a typical IIL-like SN or a unique event. Although they are part of a continuous class, IIL-like SNe typically have higher velocity ejecta, are brighter, and have steeper light curve slopes than IIP-like SN. In Section 3.4.1, we showed that ASASSN-15oz has above average ejecta velocity. Here we examine the light curve slope and absolute magnitude in the context of a sample of IIP/IIL SNe.

Population studies of IIP/IIL SNe have found that SNe with steeper light curves are brighter [Anderson et al., 2014, Li et al., 2011, Sanders et al., 2015, Valenti et al., 2016], due to a larger explosion energy, a larger progenitor, interaction with circumstellar material, or a combined effect. The left panel of Figure 3.12 shows the V-band light curve of ASASSN-15oz compared to nine other well studied SNe with a range of s_{50V}. ASASSN-15oz is brighter and more steeply declining than

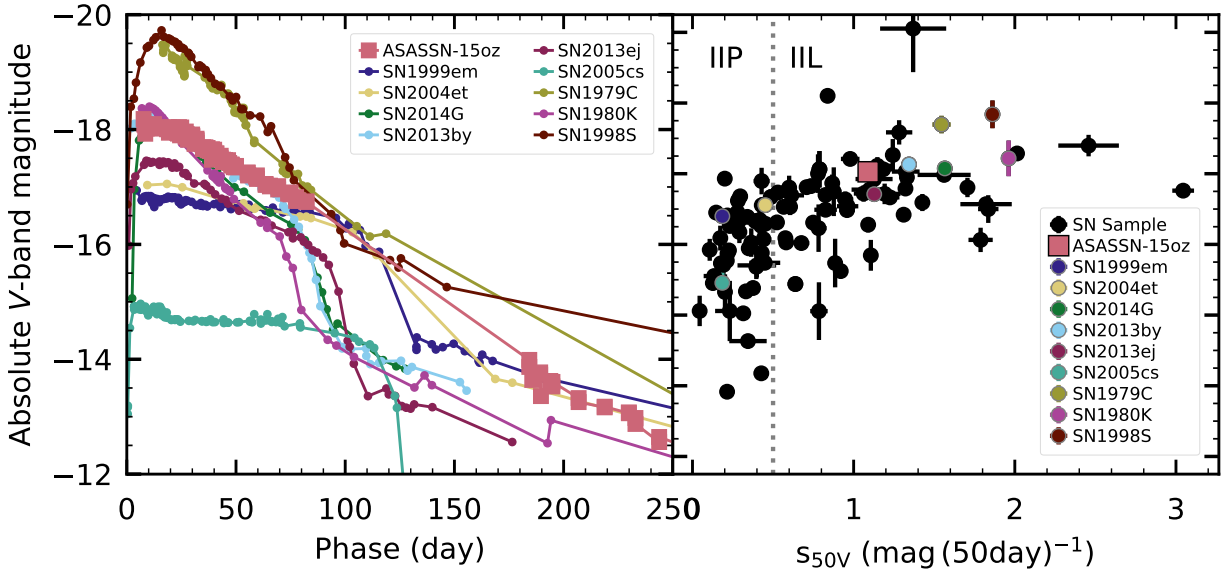

Figure 3.12 Left: the absolute V-band magnitude of ASASSN-15oz and nine well studied SNe that span the IIP/IIL like decline rates (1979C: Balinskaia et al. [1980], Barbon et al. [1982], de Vaucouleurs et al. [1981], 1980K: Barbon et al. [1982], Buta [1982], Tsvetkov [1983], 1998S: Fassia et al. [2000], Li et al. [2011], Liu et al. [2000], Pozzo et al. [2004], 1999em: Elmhamdi et al. [2003], 2004et: Maguire et al. [2010], 2005cs: Pastorello et al. [2009], 2013by: Valenti et al. [2015], 2013ej: Valenti et al. [2014], 2014G: Terreran et al. [2016]). ASASSN-15oz is both bright and steeply declining when compared with this sample of classic SNe. Also visible in this plot, is the steeper decline of the radioactive decay tail of ASASSN-15oz when compared with other objects. Right: the absolute V-band magnitude compared to s_{50V} for a sample of public SNe from the SNDAVIS database (black circles). The trend seen by Anderson et al. [2014] and Valenti et al. [2016] of brighter SNe to have steeper slopes is apparent. ASASSN-15oz (pink square) follows this relationship. The SNe whose light curves are shown on the left are also plotted on the right for reference. The gray dashed line denotes the separation between IIP-like and IIL-like SNe. This separation is poorly defined in the literature. The value we adopt is similar to that used by Faran et al. [2014] and Li et al. [2011].

the classic IIP-like SNe 1999em and 2014et. We also note that the slope of the radioactive tail of ASASSN-15oz is steeper than other objects plotted here.

We use our database of publicly available light curves, SNDAVIS, to compare ASASSN-15oz to a larger sample of objects. In the right panel of Figure 3.12 we plot the s_{50V} and the absolute V-band magnitude for 105 SNe. As a bright IIL-like SN, ASASSN-15oz is consistent with the sample correlation.

We also compare s_{50V} and the radioactive decay slope for ASASSN-15oz with all SNe in our database for which both slopes are measured in Figure 3.13. The steepness of s_{50V} in a IIP/IIL SN

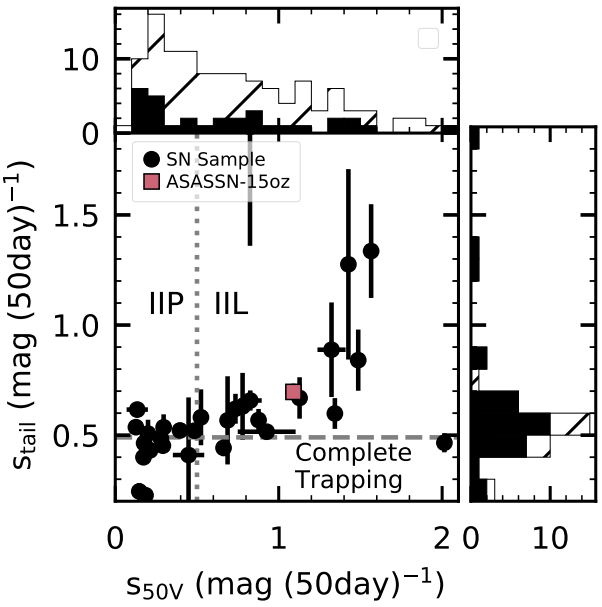

Figure 3.13 Center: the slope of the light curve at late times, during the radioactive decay phase compared to s_{50V} for a sample of publicly available SN light curves. ASASSN-15oz is plotted in pink. Top (Right): A histogram of the radioactive decay (photometric) phase slopes. All measured slopes from this phase are included in the hatched sample. The objects for which there is both a decay phase slope and s_{50V} are plotted in black. The comparison of the full slope sample (hatch) to the combined slope sample (black) gives us confidence that points we plot in the center are representative of the full sample. The dashed grey line marks the radioactive tail slope corresponding to complete trapping with a slope of $s_{tail} = 0.5$ mag (50 day)$^{-1}$. The dotted grey line represents the approximate separation between IIP and IIL SNe with a slope of $s_{50V} = 0.5$ mag (50 day)$^{-1}$.

light curve can be explained by the hydrogen recombination front receding faster than the ejecta expansion, implying a progenitor with a smaller hydrogen envelope. The slope of the radioactive decay tail is determined by the fraction of gamma-rays trapped and reprocessed by this same hydrogen envelope. A lower fraction of trapped gamma-rays can result either from a smaller hydrogen envelope or by external mixing of ^{56}Ni. Given the possible dependence of both s_{50V} and the radioactive decay slope on the hydrogen envelope, the correlation between them, seen in Figure 3.13, is unsurprising. ASASSN-15oz, having relatively steep slopes at both phases, lies at the IIL end of this relationship. This correlation was presented in Anderson et al. [2014] and is supported here with a larger sample.

Overall, we find ASASSN-15oz to be a typical type IIL-like SNe both photometrically and spectroscopically. This allows us to use this extensive dataset (in both wavelength and time) to study the progenitors and mass-loss of type IIL-like SNe in the subsequent chapters.

CHAPTER 4

Mass Loss in Massive Stars

Massive stars stars lose a significant fraction of their zero age main sequence mass over the course of their lifetimes, more than half of which occurs after they evolve off the main sequence. The canonical picture of the RSG mass-loss mechanism is that radiation pressure on dust formed in the cool, low gravity environment of the RSG surface creates stellar winds. Mass-loss prescriptions for this effect have been derived empirically from observations of the circumstellar environment of tens of RSGs [Levesque, 2017]. However different relations predict different mass-loss rates, spanning two orders of magnitude [Mauron and Josselin, 2011], due in part to scatter in the observed mass loss rates. With such a small number of observations, it is unclear if this scatter is intrinsic or systematic. Additionally, although observations of some RSG [e.g. VY Canis Majoris Smith et al., 2001] show episodic outbursts, this wind is most often modeled as constant weak mass loss. Different mass-loss prescriptions have profound implications for the evolution of RSGs with enhanced mass loss leading to stars making excursions into the blue part of the Hertzsprung Russell diagram [Meynet et al., 2015].

SNe provide a complementary tool to study mass loss in massive stars. At the time of explosion, the mass loss history of a star is present as circumstellar material around the star, with earlier mass loss at larger radii. Photons generated by the SN shock wave as well as the SN ejecta itself interacts with this circumstellar material, producing a variety of observational signatures depending on the density of the circumstellar material (CSM). As the shock travels through larger radii, different phases of mass loss are observed. Thus time series observations of a SN represent a rapid reverse mass-loss history of the RSG.

In IIP-like SNe, the plateau is the result of the recession of the photosphere due to hydrogen recombination matching the expansion of the SN ejecta. The linear decline of the light curves of IIL-like SNe is then explained by the photosphere receding faster than the ejecta's expansion. The photosphere's recession is governed by the hydrogen density profile. Although there are a number of

ways to alter the density profile (e.g. mixing of the H and He envelopes; Utrobin and Chugai 2017), one possibility is that mass loss during the last stage of stellar evolution produces a shallow density profile. In this scenario Type IIL-like SNe should undergo more mass loss than Type IIP-like SNe thereby exploding with smaller hydrogen envelopes [Blinnikov and Bartunov, 1993, Grassberg et al., 1971, Young and Branch, 1989]. The shallow H α absorption troughs in IIL-like SNe, possibly due to less absorbing material, support this picture [Gutiérrez et al., 2014, Schlegel, 1996]. SN 2018ivc and ASASSN-15oz are both Type IIL-like SNe with high-cadence optical photometric and spectroscopic observations and multiwavelength data. This chapter presents the evidence for mass loss in these two SNe.

4.1. Evidence for Interaction in SN 2018ivc

Although the declining light curve indicates that this is a Type IIL-like SN, there is evidence that the progenitor is more complicated than that of the typical Type IIL-like SN. The strong He I lines, not always visible in Type IIL-like SNe, could indicate that the progenitor lost most of its hydrogen envelope. The rapidly declining light curve corroborates this picture of mass loss. The frequent change in slope suggests that, in addition to the linear decay of the small hydrogen envelope, the shock is encountering shells of different densities that were ejected from the star during its lifetime. This would imply that some interaction between the SN and the CSM is also partially powering the light curve of SN 2018ivc, even though narrow lines typical of some interacting SNe (IIn) are not detected.

The narrow lines ($\sim 10^2$ km s^{-1}) of Type IIn SNe are formed by the recombination of unshocked CSM that has been ionized by photons from the forward-shock front. CSM can also produce intermediate-width lines ($\sim 10^3$ km s^{-1}) from the recombination of gas after the shock wave has passed through it. In SN 2018ivc, we observe broad emission from the SN ejecta and narrow emission from the host galaxy, but find no evidence that a narrow line SN component exists (see Section 3.4). This lack of narrow lines may indicate a clumpy CSM that has been enveloped by the SN ejecta [Andrews and Smith, 2018, Smith et al., 2015]. We note, however, that Type IIn SNe do not always exhibit narrow lines at all epochs and it is possible that we do not have a high-resolution observation during the time that narrow lines were visible. Additionally, it is possible

that the narrow lines from the CSM are not strong enough to show above broad lines of the ejecta or are too narrow and weak to be distinguished from the significant host contamination.

Despite the lack of narrow lines, there are several other indications that the ejecta of SN 2018ivc are interacting with CSM. The boxy profiles of the H α and He I λ6678 complex could also be indicative of interaction with a shell of CSM [Andrews et al., 2010, Inserra et al., 2011]. The strong X-ray detection likely originates from the shocked CSM. Together, the light curve and spectroscopic observations demonstrate the presence of interaction in SN 2018ivc.

The HV features seen in SN 2018ivc are unusual. The presence of these features indicates that hot, dense, asymmetric material is moving with the speed of the ejecta (if the material is in the line of sight) or faster. Given that the HV features are present in hydrogen, helium, and calcium emission, this feature may be due to material that was ejected in the explosion. It is possible that a bullet of ^{56}Ni was ejected early in the explosion at high speed and that its the radioactive decay powers these features.

Searching the literature, we find that while multicomponent hydrogen features are seen in Type IIP/IIL SNe, they are most often during the nebular phase and at significantly lower velocity. Two notable exceptions to this are SN 2014G [Terreran et al., 2016] and SN 2010jp [Smith et al., 2012]. SN 2014G was a Type IIL-like SN which showed narrow flash spectroscopic features during the first 10 days of evolution. Around day 100, SN 2014G developed a narrow feature blueward of H α that could not be associated with any other species and thus was identified as a HV hydrogen feature, with an initial velocity of $\sim$ 7600 km s^{-1}. Terreran et al. [2016] explain this feature as being caused by the spherically symmetric SN ejecta interacting with a bipolar lobe CSM with a 40° angle between the CSM axis and the observer's line of sight. SN 2010jp was a low luminosity, linearly declining Type IIn SN which showed a triple-peaked H α emission line. The red and blue H α peaks ($-12,000$ and 15,000 km s^{-1}, respectively) are explained by a jet-powered explosion. The HV features in SN 2018ivc, at comparable speeds to those of SN 2014G and SN 2010jp, could originate from a disk or jet-like structure.

4.2. Evidence for CSM Interaction in ASASSN-15oz

ASASSN-15oz, a Type IIL-like SN with photometric and spectroscopic observations from the X-ray through the radio is the ideal SN on which to study the importance of mass loss for IIP-like and IIL-like SNe. The different epochs and wavelengths probe different periods of mass loss allowing for the characterization of the mass-loss history of the progenitor. In this section we analyze the evidence for interaction at different wavelengths. We note that we cannot search for flash ionization features as there are no spectroscopic observations until near maximum.

4.2.1. UV and X-ray. ASASSN-15oz is not detected in any of the *Swift* X-ray observations. The flux limits were converted to luminosity limits assuming Galactic absorption of $6.18\text{x}10^{20}$ cm^{-2} [Kalberla et al., 2005] and a distance of 28.83 Mpc.

We compare these upper limits to the model of SN 1999em [Chugai et al., 2007] which has similar progenitor and explosion parameters. They model the interaction as an infinitely thin double-shock structure [Chevalier, 1982, Nadyozhin, 1985] composed of a forward shock propagating into the surrounding gas and reverse shock propagating backwards into the SN ejecta, towards its core. Chugai et al. [2007] find that the reverse shock dominates the X-ray observations for a pre-explosion mass loss rate of 10^{-6} M$_\odot$ yr^{-1} and a wind velocity of 10 km s^{-1} producing luminosities between 10^{38} and 10^{39} erg s^{-1}. The forward shock produces luminosities comparable to the reverse shock in the first 10 days and decreasing to below 10^{34} erg s^{-1} by day 100. Our non-detections are above the upper limit of this range, making it plausible that if there is X-ray emission, it is below our detection limits.

We use `SYN++` to model and tentatively identify absorption features from Fe II, Ti II, and Mg II features in the first *Swift* UV grism spectrum (see Figure 3.3). This spectrum shows no sign of the narrow emission lines typically associated with strong interaction ($\dot{\text{M}} > 10^{-4}$ g cm^{-1}; Kiewe et al. 2012)

4.2.2. Optical Spectroscopy. Chugai et al. [2007] proposed a high velocity hydrogen and helium line are produced by interaction of the SN ejecta with the stellar wind. According to their model, a notch on the blue side of the H α profile should appear 40-80 days post explosion. Although they could construct a model with the introduction of a cold dense shell in which a similar notch

was visible in H β their simplest model did not show H β due to its low opacity in the wind. They do however, predict absorption in He I λ10830 20-60 days post explosion, a line that is only excited when wind is present.

A feature blueward of H α is often present in Type II SNe, however, it is unclear if this feature is due to high velocity hydrogen or to Si II (λ6355) and it has thus been named the cachito feature to avoid association with a particular species [Gutiérrez et al., 2017]. Building on the analysis of smaller samples (e.g. Leonard et al. 2002, Inserra et al. [2013], Valenti et al. 2014), Gutiérrez et al. [2017] searched for this feature in 122 IIP/IIL SNe. They find the cachito feature in 70 SNe in their sample and divide the detections in early phase detections (phase $<$ 40 days) and late phase detections (phase $>$ 40 days). The velocities of the cachito feature observed in the early sample are most often well matched to the Fe II velocity if interpreted as Si II. For this reason, they interpret the cachito feature in the early sample as Si II and at late times as high velocity hydrogen. Figure 4.1 shows the time evolution of the region surrounding H α (left panel), H β (middle panel), and He I (right panel). H α and H β are marked with a brick dotted line in the left and middle panels, respectively. The dashed line in the left panel marks the location of the cachito feature and in the middle panel, the expected location of the cachito feature in H β. The time of expected CSM interaction is marked in grey. ASASSN-15oz shows a strong cachito feature in the first spectrum, eight days post explosion. This feature strengthens until about day 15 and then fades until it is no longer visible at day 60. We find no evidence for a high velocity feature in H β. The He I feature is fully blended with C I (λ10691) and Paschen-γ and if it is present, it is impossible to deblend and identify. A comparison of the cachito velocity, when interpreted as Si II, and the Fe II velocity is plotted in Figure 4.2. We find excellent agreement between the two velocities strengthening our conclusion that this feature is due to Si II rather than high velocity hydrogen.

The H α emission profiles in the nebular spectra of ASASSN-15oz are asymmetric (see Figure 4.3). In addition to emission at the rest wavelength of H α, there is evidence of both blueshifted and redshifted emission at 2200 kms^{-1} and 800 kms^{-1}, respectively. This feature is strongest in the first spectrum at day 228 (2016 Apr 11), becoming weaker in the subsequent spectra. Asymmetric H α emission has been seen in a few IIP/IIL SNe (e.g. 1999em: Leonard et al. 2002; SN 2004dj: Chugai et al. 2005; SN 2013ej: Utrobin and Chugai 2017). Leonard et al. [2002] explain the shape of the

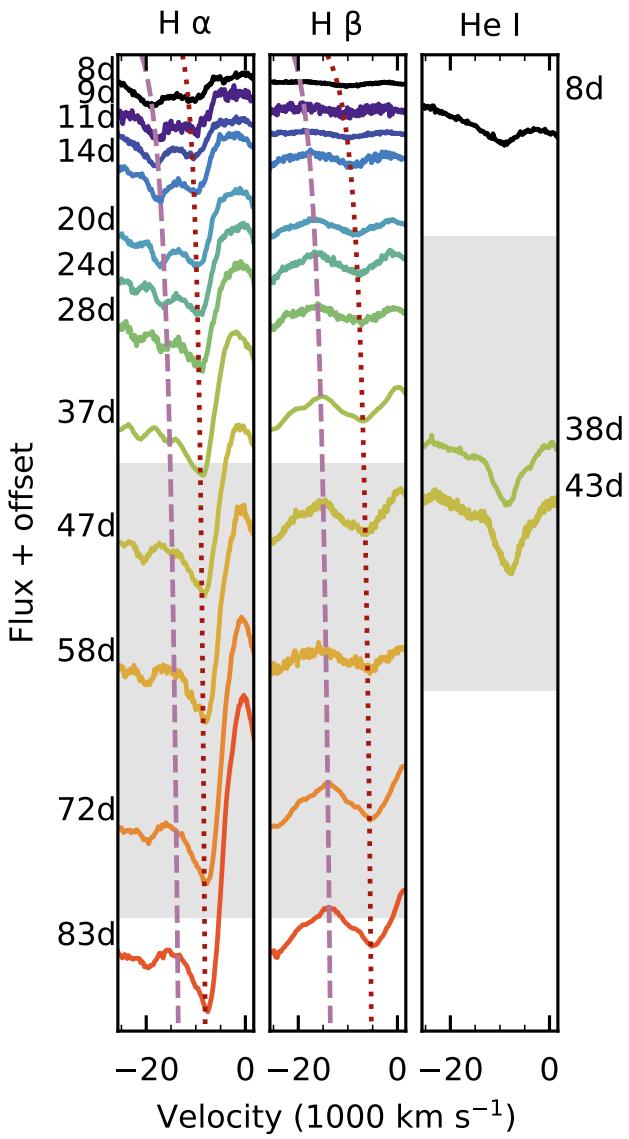

Figure 4.1 The evolution of the cachito feature (left panel; dashed line) over time. The feature is visible bluewards of H α (left panel; dotted line) in the first spectrum, eight days post explosion. It increases in strength for the next 10 days, then decreases until it is barely visible at 60 days post explosion. This evolution is counter to the evolution described in Chugai et al. [2007] in which the high velocity hydrogen feature becomes visible around day 40, making it unlikely that it is high velocity hydrogen. There is no evidence of a high velocity hydrogen feature in H β (center panel; H β marked with dotted line; cachito velocity marked with dashed line) although this is not surprising given the low opacities predicted by Chugai et al. [2007]. The high velocity He I ($\lambda = 10830$) feature (right panel) also predicted by the models of Chugai et al. [2007] is too heavily blended with the Paschen-γ and C I lines to be identifiable.

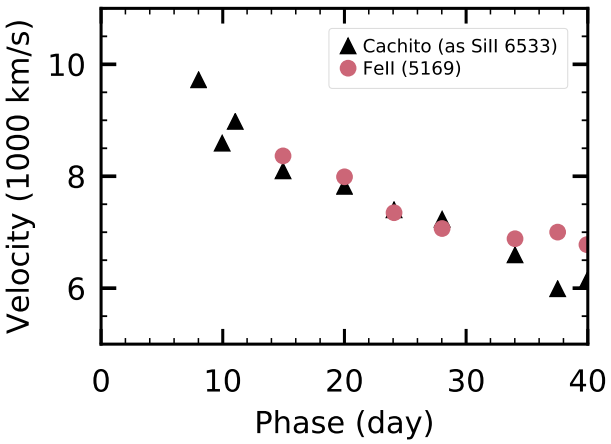

Figure 4.2 A comparison of the velocity of the cachito feature if it is Si II (λ6355) (black triangles) and the velocity of the metals in the ejecta as characterized by the Fe II λ5169 lines (pink circles). The velocities are the same indicating that this line is likely due to Si II rather than high velocity hydrogen in the circumstellar medium.

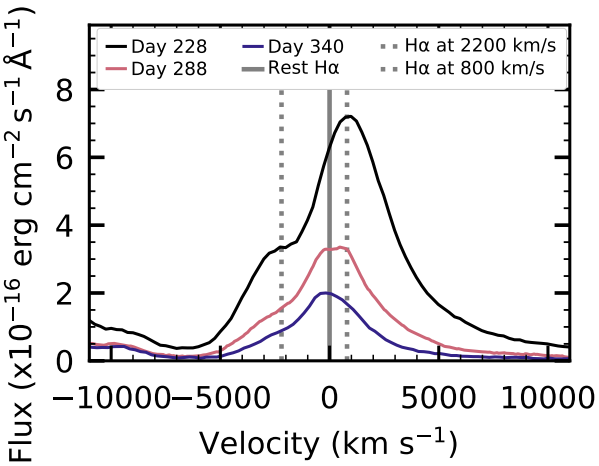

Figure 4.3 The asymmetric H α emission in the nebular spectra of ASASSN-15oz. The spectrum shows H α emission at rest (solid gray line), blueshifted by 2200 km s^{-1} and redshifted by 800 km s^{-1} (dashed gray lines). Although the asymmetry is visible in all of the spectra, it is most prominent in the earliest nebular spectrum on day 228 (2016 Apr 11) and could be a sign of interaction with CSM. However such strong asymmetry would required an high level of interaction not visible by other probes.

H α emission as either due to an asymmetric line-emitting region or due to interaction between the ejecta and the CSM while Chugai et al. [2005] and Utrobin and Chugai [2017] attribute this feature to a bipolar ^{56}Ni ejecta.

4.2.3. Radio. The origin of radio emission from SNe can be explained by the interaction of the SN ejecta with the CSM. This interaction leads to a shockwave traveling via the CSM that in turn accelerates electrons and enhances magnetic fields and thus synchrotron emission ensues [Chevalier, 1982, 1998, Chevalier and Fransson, 2006, Weiler et al., 2002]. It has been shown over the last decade that in most observed SNe, the optically thick part of the observed radio spectrum can be modeled by synchrotron self absorption (SSA; e.g. Horesh et al. 2013, Soderberg et al. 2012). We use the Chevalier [1998] SSA formalism to model the radio measurements of ASASSN-15oz. In such a model the radio emission peaks at a frequency below which the emission is strongly absorbed by SSA. Above that frequency the emission becomes optically thin. As the shockwave progress outwards to lower CSM densities, the SSA optical depth drops and the peak of the radio emission moves to lower and lower frequencies. We use Equation 1 from Chevalier [1998] to model the radio dataset (see Figure 4.4). We use the standard equipartition assumption and set the microphysical parameters, $\epsilon_{\rm e} = \epsilon_{\rm B} = 0.1$ [Chevalier and Fransson, 2006]. We also set the electron power-law distribution to p = 3, leaving the CSM density and shockwave velocity as free parameters. We find the shockwave velocity (assuming constant velocity) is $\sim 1.4 \times 10^4$ km s^{-1} (which is the typical average value observed in SNe; e.g. Chevalier and Fransson 2006). Assuming the CSM surrounding the SN is created by a stellar wind from the progenitor prior to explosion, we model the density profile of the CSM as:

$$\rho(r) = \frac{\dot{M}}{4\pi r^2 v_{wind}} = \frac{K}{r^2} \tag{4.1}$$

where $\dot{M}$ is the wind mass-loss rate and v_{wind} is the wind velocity. We find K = 4.51×10^{11} g cm^{-1}. With a wind velocity between 10-100 km s^{-1}, this implies a mass-loss rate between $\dot{\rm M} \approx 0.9 - 9 \times 10^{-7}$ M$_\odot$ yr^{-1}.

4.2.4. Light Curve Modeling with SNEC. We fit the light curve of ASASSN-15oz using the Supernova Explosion Code (SNEC) [Morozova et al., 2015]. SNEC is an open source Lagrangian 1D radiation hydrodynamic code that employs flux-limited radiation diffusion and assumes local thermodynamic equilibrium (LTE). SNEC uses a Paczyński equation of state [Paczynski, 1983] solving for the ionization fractions using the Saha equations in the non-degenerate approximation [Zaghloul et al., 2000]. Opacities are drawn from OPAL type II opacity tables [Iglesias and Rogers,

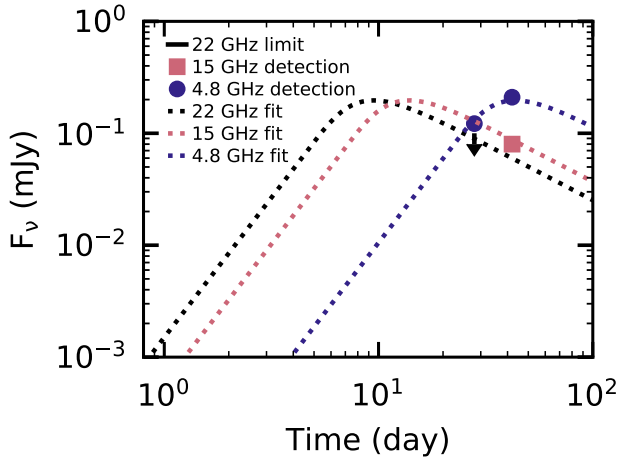

Figure 4.4 The best fit SSA model (dotted lines) plotted over the observations (symbols) at 22 GHz (black), 15 GHz (pink), and 4.8 GHz (indigo). These data are best fit by a shock velocity of $\sim 1.4 \times 10^4$ km s^{-1} and a density of K $= 4.51 \times 10^{11}$ g cm^{-1}

1996] at high temperatures (T $= 10^{4.5} - 10^{8.7}$ K) and tables of Ferguson et al. [2005] at low temperatures (T $= 10^{2.7} - 10^{4.5}$ K) supplemented with an opacity floor of 0.01 cm^{2}g^{-1}. The mixing of isotopes due to the explosion is modeled by boxcar smoothing the progenitor composition profile with a kernel of 0.4 M$_\odot$.

In the past, hydrodynamic SN models that used progenitors evolved with stellar evolution codes (referred to as evolutionary progenitors for the remainder of this thesis; e.g. *Kepler* code, Sukhbold and Woosley 2014, Sukhbold et al. 2016, Weaver et al. 1978, Woosley and Heger 2007, 2015; *MESA*, Paxton et al. 2018) failed to reproduce the shape of the early observed light curves of Type II SNe. Some authors have solved this issue by using hydrostatic progenitor models with extended envelopes and density profiles that are set to match observations rather than calculated by stellar evolution codes (referred to as non-evolutionary progenitors for the remainder of this thesis; e.g. Utrobin and Chugai 2008, Utrobin and Chugai 2017). However, adding a dense CSM ejected just before the explosion to progenitors evolved with stellar evolution codes has resolved the discrepancy between the early observed light curves and the light curves modeled using physically derived progenitors (e.g. Förster et al. 2018, Gezari et al. 2015, Morozova et al. 2018). The presence of this CSM is corroborated by other observations of IIP/IIL SNe (e.g. Bullivant et al. 2018, Yaron et al. 2017).

For the progenitor models, we use a set of non-rotating solar metallicity RSGs parameterized by the M_{ZAMS}, evolved with the *Kepler* code and described in Sukhbold et al. [2016]. Note that the stellar evolution calculations made with *Kepler* take into account the regular steady winds observed in RSGs, in the way prescribed by Nieuwenhuijzen and de Jager [1990] and Wellstein and Langer [1999]. For this reason, the final pre-SN masses of the models may be up to several $M_\odot$ smaller than their initial M_{ZAMS}. Both the M_{ZAMS} and pre-SN masses of the models used are given in Table 4.1. However, for the typical mass loss rates of $\lesssim 10^{-6}$ $M_\odot$ yr^{-1}, the density in these regular steady winds is too low to have any noticeable effect on the post-explosion optical light curves, and these winds are not included in the progenitor profiles.

We explore variations in CSM due to enhanced mass loss by adding a steady-state wind above the RSG models with the density profile expressed in Equation 4.1. This approximation allows us to parameterize the CSM with two parameters, K and R_{ext}, the radial extent of the CSM. In reality, the late enhanced mass loss does not have to be in the form of a steady wind with constant $\dot{M}$ and may instead represent one or several eruptive outbursts. However, in our experience, the early optical light curve depends weakly on the exact slope of the CSM profile, being more sensitive to the total CSM mass.

Recently, Paxton et al. [2018] demonstrated that Type IIP/IIL SNe are well characterized by the radiation diffusion approximation from shock breakout through the fall from plateau. At the same time, they have shown that the assumption of LTE is not well satisfied at the photosphere location of the Type IIP/IIL SNe models. For this reason, SNEC color light curves generally rise faster than the light curves obtained from more sophisticated multi-group radiation-hydrodynamics codes, like STELLA [Paxton et al., 2018]. However, this fact makes the case for introducing a CSM surrounding the RSG before its explosion even stronger. In this view, the total CSM mass derived in our analysis may be considered as a lower limit, while the values obtained with more advanced codes should be comparable, or in some cases larger [Moriya et al., 2017, Paxton et al., 2018].

To account for the formation of the neutron star, we excise the inner $1.4\,M_\odot$ of the progenitor models prior to the explosion. After that, we model the explosion of ASASSN-15oz using a thermal bomb with explosion energy E_{exp} lasting for one second in the inner 0.02 $M_\odot$. When computing the amount of energy injected in the form of a thermal bomb, SNEC automatically takes into

Table 4.1 The grid of parameters used by SNEC. The values that best fit the data are in bold. The pre-explosion masses are taken from Table 2 of Sukhbold et al. [2016].

Parameter	Values
Progenitor ZAMS Mass (M_{ZAMS}; $M_\odot$)	11, 13, 14, 16, **17**, 18, 21
Final Pre-SN Mass ($M_\odot$)	10.688, 11.567, 12.079, 13.145, **14.301**, 14.936, 16.119
Pre-SN Radius (100 $R_\odot$)	5.7, 7.0, 7.8, 8.9, **9.1**, 9.7, 11.2
Explosion Energy (E_{exp}; 10^{51} ergs)	0.5, 0.8, 1.1, **1.4**, 1.7, 2.0
CSM Density (K; 10^{17} g cm^{-1})	0, 10, 20, 30, 35, **40**, 50, 60
CSM Extent (R_{ext}; 100 $R_\odot$)	0, 15, **18**, 21, 24, 27, 30, 33
Ni Mass ($M_\odot$)	**0.08**, 0.09, 0.11

account the total initial (negative, mostly gravitational) energy of the models. Therefore, by the explosion energy E_{exp} in our analysis we mean the total energy of the models after explosion, which is conserved in the code to better than 1% accuracy and eventually mainly transformed into the kinetic energy of the expanding envelope.

SNEC does not model nuclear reaction networks, but rather takes as input a mass of ^{56}Ni. We use a grid of ^{56}Ni masses informed by our analysis in Section 3.2. While SNEC allows for the ^{56}Ni to be mixed out to different values of mass coordinate, Morozova et al. [2017] find that the progenitor masses and explosion energies derived from fitting the IIP/IIL SN light curves are not very sensitive to the degree of ^{56}Ni mixing. Therefore, in our study we choose to keep this parameter fixed and mix the ^{56}Ni up to 5.0 $M_\odot$.

We use SNEC to find the best progenitor parameters varying the progenitor mass, explosion energy, ^{56}Ni mass, CSM density, and CSM extent. Table 4.1 gives the set of parameters used, resulting in over 5000 model light curves. Morozova et al. [2018] find the best fit model with and without CSM as a two step process. First they modeling the second half of the light curve, characterized by the s2 slope without CSM to determine the best progenitor mass and explosion energy. Then, fixing the explosion energy and progenitor mass, they explore the CSM parameter space. This is computationally less intensive than modeling the full parameter space and allows them to explore a finer grid of parameters. Given the complexity of the parameter space, we choose to model the best light curve with CSM, exploring the full set of parameters simultaneously.

For ease of comparison with observations, SNEC uses the photospheric temperature at each time step to compute a blackbody spectrum, which it combines with different filter throughputs to output a light curve in Sloan filters *u, g, r,* and *i*, Bessel filters *U, B, V, R,* and *I* and PanSTARRS

Table 4.2 The best fit SNEC model parameters for the simultaneous fits to *g, r,* and *i*-bands and to the bolometric luminosity with and without CSM.

	Fit to *g, r, i*-bands		Fit to Bolometric Luminosity	
Parameter	With CSM	Without CSM	With CSM	Without CSM
Progenitor ZAMS Mass (M_{ZAMS}; $M_\odot$)	17	18	18	17
Final Pre-SN Mass ($M_\odot$)	14.301	14.936	14.936	14.301
Pre-SN Radius (100 $R_\odot$)	9.1	9.7	9.7	9.1
Explosion Energy (E_{exp}; 10^{51} ergs)	1.4	2.0	1.4	2.0
CSM Density (K; 10^{17} g cm^{-1})	40	0	60	0
CSM Extent (R_{ext}; 100 $R_\odot$)	18	0	15	0
Ni Mass ($M_\odot$)	0.083	0.083	0.083	0.083
Total CSM Mass ($M_\odot$)	1.5	0	1.4	0

filter *z*. During the rise and plateau phase, a blackbody should be a good approximation to the longer wavelengths. However, line blanketing may cause the bluer filters to be a poor representation of the observed spectrum [Dessart and Hillier, 2005, Kasen and Woosley, 2009]. For this reason the best fit model is determined using the *g, r,* and *i* filters. While we do have a *V*-band light curve, the throughput heavily overlaps with the *g*- and *r*-bands and its inclusion would give more weight to these wavelengths without providing new information. The best fit model is determined by interpolating the well-sampled model to the observed wavelengths and computing a chi-square minimization across all three filters. Given the uncertainty in the explosion time, we shift the model spectrum by ±4 days and treat this offset as a free parameter (t_{offset}). Parameters for the best fit models with and without CSM are given in Table 4.2. These models are shown with (solid lines) and without (dashed lines) CSM interaction in the top panel of Figure 4.5. Integrating the CSM density over it radial extent, we find a total CSM mass of 1.5 $M_\odot$.

As a sanity check, we derive the bolometric luminosity by fitting a blackbody to the photometric observations and find the best fit SNEC model with and without CSM. The parameters for these models are given in Table 4.2 and are plotted over the bolometric luminosity in the bottom panel of Figure 4.5. The explosion energy and ejecta masses are similar to those derived from a simultaneous fit of the *g, r,* and *i* bands. Although the individual CSM parameters vary, these are highly degenerate and the total CSM mass, which our model is a better measure of, is very similar. The difference in the total CSM mass from the two different methods can be seen as an indication of the uncertainty in this value.

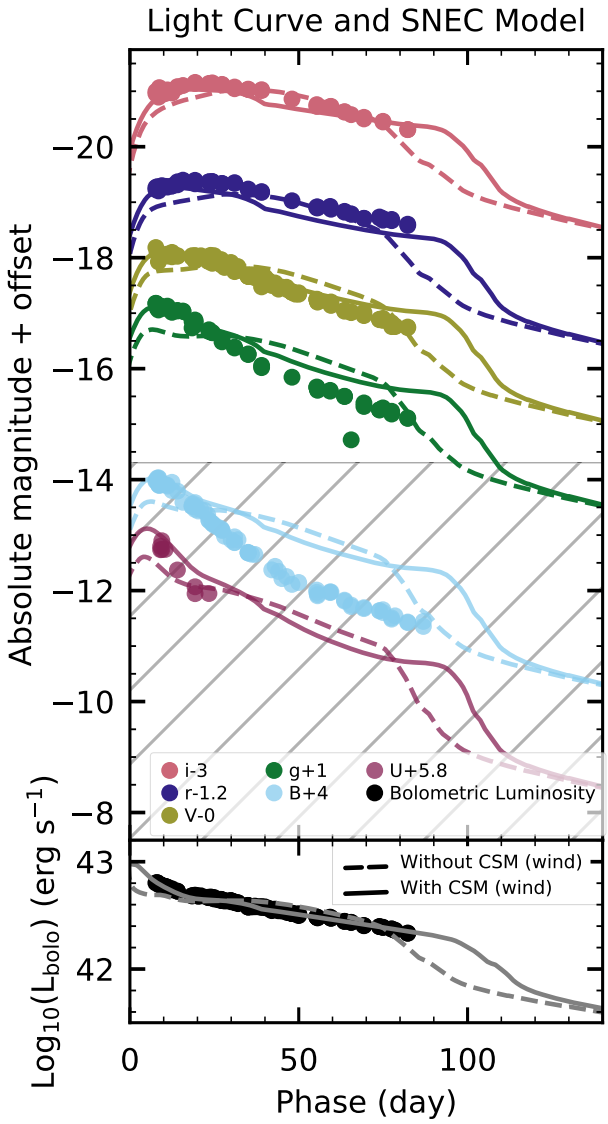

Figure 4.5 Top: the multi-band optical light curve of ASASSN-15oz. The observations are shown as circles and the best fit SNEC model is shown with and without CSM (solid and dashed lines, respectively). We require CSM to fit the light curve at early times. The blue filters are affected by line blanketing (U and V-band) and are thus not expected to be well approximated by the blackbody approximation used to convert the bolometric luminosity produced by the modeling into magnitudes in individual filters. For this reason we do not use these in the fit and have placed hatched lines over them. Line blanketing may also be responsible for the overestimate of the model flux in the g-band. Bottom: the bolometric luminosity of ASASSN-15oz plotted with the best model fit to the bolometric luminosity including CSM (solid line) and the best model without CSM (dashed line).

Towards a consistent picture of the SN explosion, we also verified that the parameters we found from the light curve modeling were in agreement with the interpretation of other observables. The high velocity derived from the spectroscopy is consistent with the large mass and explosion energy found by the light curve fitting. It is also compatible with the incomplete gamma-ray trapping, which is expected in SNe with high core velocities [Jerkstrand et al., 2011]. Figure 4.6 shows a comparison of the photospheric velocity of the best fit SNEC model to the observed photospheric velocity of ASASSN-15oz. Following Faran et al. [2014], we define the photospheric velocity as that of Fe II (λ5169). We use cachito feature, now identified as Si II (λ 6355), to trace the photosphere at early times. We note that while the Fe II (λ5169) is often used to characterize the photospheric velocity, it is not well understood where in the atmosphere line is being formed. Paxton et al. [2018] find that the Fe II (λ5169) line is originating above the photosphere at a specific value of Sobolev optical depth ($\tau_{\rm sob}$) (they find $\tau_{\rm sob} \sim 1$ fits the observations well). However, Hamuy [2001], in comparing the velocity derived from the Fe II (λ5169) line to the photospheric velocity in the Type II SN atmospheric models of Eastman et al. [1996], find a systematic offset for individual objects that is in different directions for different objects, leading to no average offset. While there is fair agreement between our model and observe velocity at early times, the model velocity is significantly lower than the observed velocity starting around day 25. Following Paxton et al. [2018], we adjust our model velocity to the value at $\tau_{\rm sob} = 1.0$. Figure 4.6 shows that this adjustment brings the SNEC velocities closer to the observed velocities. A more detailed discussion concerning the modeling of the minimum of the Fe II line is beyond the scope of this thesis.

According to the classical model by Chevalier [1982], the interaction of the SN ejecta with the surrounding wind leads to the formation of a cool dense shell between the forward and the reverse propagating shock waves. This shell is responsible for the X-ray emission from Type II SNe. In addition, an opaque shell can be formed in front of the forward shock wave, which may serve as an explanation of the narrow emission lines with broad wings seen in some interacting SNe [Chugai, 2001]. In our SNEC model, the CSM density is too high and the density drop between the envelope and the CSM is not sufficient to form a significantly over-dense shell between the forward and reverse shock waves. This is supported by Figure 4.7, where the interface between the RSG envelope and the CSM corresponds to the velocity coordinate of $\sim 4200\,{\rm km\,s^{-1}}$. In this

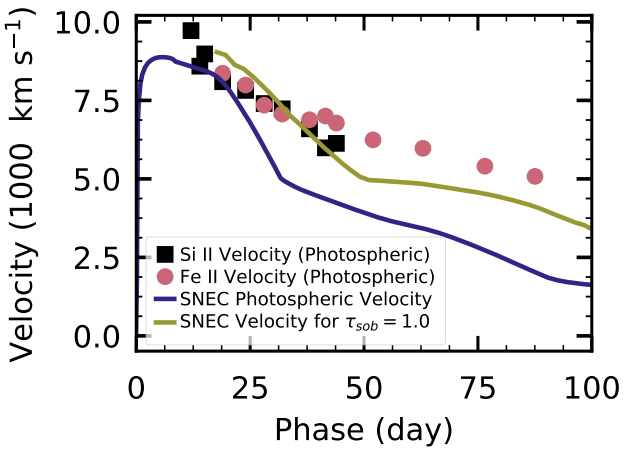

Figure 4.6 The model photospheric velocity computed by SNEC (indigo line) compared to the observed photospheric velocity (symbols) taken to be the velocity of the Si II (λ 6355) feature at early times (black squares) and Fe II (λ5169) feature at later times (pink circles). The model deviates from the observations around the time that the photosphere begins to recede into the ejecta. The model velocity at $\tau_{\rm sob} = 1$ is plotted in yellow. While this provides a better agreement with the observations, the model velocity evolution is still faster than the observed evolution.

model, the forward shock wave sweeps the CSM almost entirely before the breakout, and the opaque circumstellar shell ahead of the shock wave is not formed either.

On the other hand, if we were to consider a three component model, consisting of a RSG, a dense CSM and a regular low density stellar wind, like in Morozova et al. [2018], the thin cool dense shell would be formed at the interface between the dense CSM and the wind. In this scenario, the forward shock wave keeps propagating into the low density wind and generates radio emission. Since SNEC is not yet capable of handling the low density stellar wind, we have omitted it in our current simulations. However, we already know from the radio observations (Section 4.2.3) that the mass-loss rate of this wind in ASASSN-15oz is $\sim 0.9 - 9 \times 10^{-7}\, M_\odot\, {\rm yr}^{-1}$. Such low density wind would not have any significant influence on the optical light curve of the SN, which justifies using a two component model (RSG and dense CSM only) for the purpose of this section.

4.2.5. A Unified CSM Model for ASASSN-15oz. Having analyzed individual observations for CSM interaction, we now turn to finding a unified model. We derived mass-loss parameters from both the light curve modeling with SNEC and the modeling of radio observations. From the optical light curve we found a compact CSM with a density of K $= 4.0 \times 10^{18}$ g cm^{-1} extending

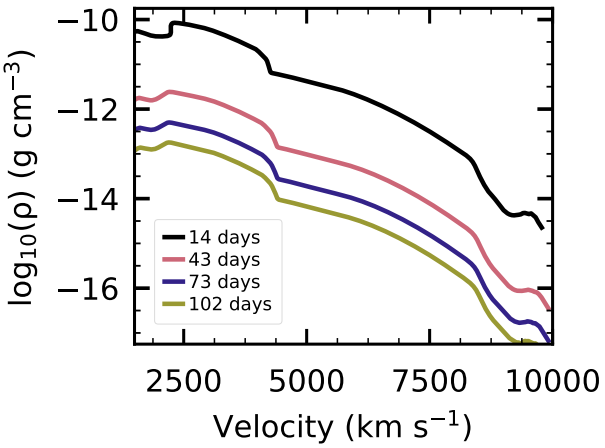

Figure 4.7 Density as a function of velocity in our best fit SNEC model at the free expansion stage. The interface between the RSG envelope and the CSM corresponds to the velocity value of $\sim 4200\,\mathrm{km\,s^{-1}}$. The kink in the velocity evolution at 5000 km s^{-1} is related to the fact that we do not attempt to artificially smooth the density step at the interface between the RSG model and the attached CSM. In reality, this interface will likely be smooth, but its exact shape will depend on the formation mechanism of the CSM, which is currently unknown. The mild increase in density at $\sim 2300\,\mathrm{km\,s^{-1}}$ is a result of the reverse shock wave reflected from this interface.

to a radius of R = 1800 $R_\odot$. Assuming a typical of RSG wind velocity between 10-100 km s^{-1}, the CSM density required to fit the optical component implies a mass-loss rate between 0.8-8.0 $M_\odot$ yr^{-1}. This is significantly higher than radio mass-loss rate, $10^{-6} - 10^{-7}$ $M_\odot$ yr^{-1}. While the mass-loss rate from the radio observations is consistent with typical RSG mass-loss rates of 10^{-4}-10^{-6} $M_\odot$ yr^{-1}, the optical mass-loss rate is consistent with some late stage mass-loss scenarios (e.g. Chugai 2001, Fuller 2017, Quataert and Shiode 2012, Shiode and Quataert 2014, Yaron et al. 2017). These discrepant values can be reconciled by considering the origin of the radiation we are observing. The excess luminosity seen in the optical light curve is due to radiation diffusion from the shocked CSM that is behind the forward shock and is only visible after shock breakout. The radio luminosity on the other hand, is created by the acceleration of electrons due to the shock's interaction with the CSM. It is therefore representative of the shock's location at the time of the observation. Our observations can then be explained by a long period of average mass loss, followed by a short period of extreme mass loss.

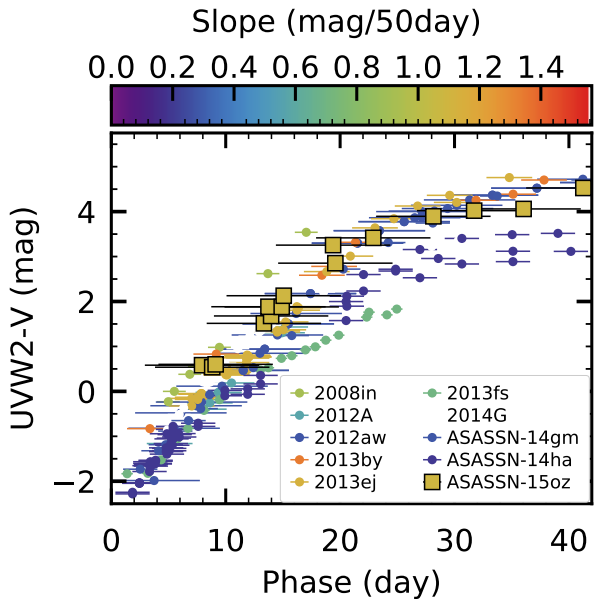

Figure 4.8 A comparison of the UV color of ASASSN-15oz to that of all other Type IIP/IIL SNe with *Swift* observations and s_{50V} measurements in SNDAVIS. Each point is colored by the s_{50V} slope, with shallower slopes in blue and steeper slopes in red. Based on this data, there is no relationship between UV excess and slope.

With this model in mind, we examine our UV and X-ray observations, in the context of other Type IIP/IIL SNe. Strongly interacting SNe remain UV bright throughout their interaction, implying that perhaps a UV excess would be observed for Type IIP/IIL SNe during the first 30 days, when the CSM has the greatest effect on the light curve. Furthermore, if in fact, the diversity in light curve shapes is due to mass loss and the interaction is strong enough to produce a UV excess, then those SNe with a steeper slope, should have lost more mass, and therefore should be more UV bright. We explore this by plotting *Swift* UV color, UVW2 - V, over the first 30 days of evolution for eight SNe in our database with *Swift* UVW2 and *V*-band photometry and s_{50V} measurements (Figure 4.8). The symbols for each SN are colored by the *V*-band slope at 50 days. Although this sample is small, a wide range of slopes are represented and no correlation between UV excess and slope is observed. We interpret this as an indication that the CSM interaction is not strong enough to produce UV excess. However, we cannot rule out the possibility that a correlation is disrupted by uncertainties in the extinction correction.

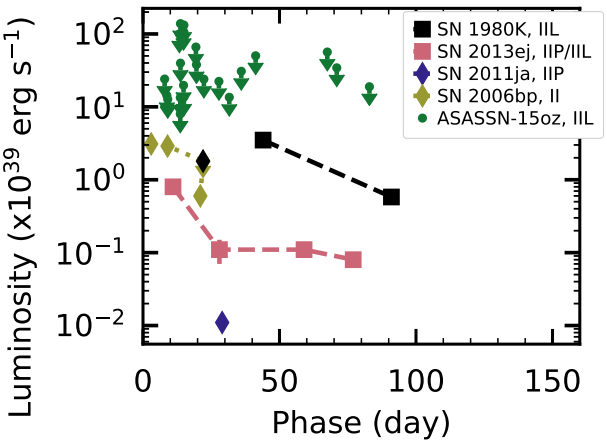

Figure 4.9 The X-ray luminosity of all published SNe found in the SNaX database. IIP-like SNe are shown with diamond symbols while IIL-like SNe are shown with square symbols and the upper limits as circles. All of the detections from IIP/IIL SNe are below the upper limits derived in this thesis, implying that deeper observations would be required to detect its X-ray flux.

Like the UV excess, X-rays from strongly interacting SNe are frequently observed. To gain more insight into the X-ray upper limit, we compare the upper limit of ASASSN-15oz with published X-ray observations of Type IIP/IIL SNe found in the SNaX database [Ross and Dwarkadas, 2017] (see Figure 4.9). We find our upper limits are above all of the detections and upper limits of Type IIP/IIL SNe in the database. This further suggests that deeper observations could be needed to detect the X-ray flux of ASASSN-15oz.

4.3. Conclusions

The observations described in this chapter reveal to that RSG mass loss is more complicated than the typical constant weak wind used in stellar evolution models. Both ASASSN-15oz and SN 2018ivc displayed evidence of periods of significant mass loss that influenced their light curves adding to the growing body of evidence that RSGs have eruptive outbursts. Furthermore, the detection of a weak stellar wind in the radio of ASASSN-15oz shows as well as the rapidly changing slope of the light curve of SN 2018ivc demonstrate that RSG mass loss is not constant. The early detection of ASASSN-15oz and SN 2018ivc, the high-cadence optical follow-up observations, and the UV, X-ray, and radio observations were all key to this characterization, demonstrating the need for more well studied SNe.

CHAPTER 5

Progenitors of SN 2018ivc and ASASSN-15oz

There is significant theoretical uncertainty in the final stages of massive star evolution (e.g. mass loss mechanisms, convection, binarity) which make it challenging to uniquely connect observed supernova (SN) types to their progenitor systems. The most comprehensive and trusted observational method to determine progenitor mass is to compare synthetic photometry of evolved massive stars from models such as KEPLER [Sukhbold et al., 2016, Woosley and Heger, 2007], MESA [Paxton et al., 2011, 2013, 2015, 2018], and GENEVA [Hirschi et al., 2004] to the photometry of a star, at the location of a SN, which has disappeared following the explosion. This method is known as direct detection and using it we have determined that the progenitors of Type II SNe are RSGs. In fact, since the first direct detection in 2001 [Smartt et al., 2001], a small but statistically significant catalog of 45 progenitors has been identified, including 13 detections of Type II SNe progenitors from RSG progenitors [Smartt et al., 2015]. Using this sample and a Salpeter initial mass function (IMF), Smartt et al. [2015] find the maximum mass of the sample from which this distribution was drawn to be 18.5^{+3}_{-4} $M_{\odot}$, well below the 30 $M_{\odot}$ predicted from stellar evolution theory.

A number of different theories have been proposed to explain the lack of high mass progenitors. One theory suggests that the higher mass SNe may form black holes either through direct collapse or fallback [Fryer, 1999, e.g.]. This theory is supported by the difficulty in producing successful explosions in stars with $M > 20$ $M_{\odot}$ where the core is less compact [Smartt et al., 2015]. The theoretical motivation for this mass limit varies. Most recently, [Sukhbold and Adams, 2020] proposed that energy transport in carbon core burning switches from convective to radiative between 16-20 $M_{\odot}$, leading to less compact cores which are more challenging to explode. According to their calculations only 8% of stars with $M>18M_{\odot}$ [Sukhbold et al., 2018]. In 2015, after seven years of searching, Gerke et al. [2015] detected a candidate failed SN with a progenitor mass of 25 $M_{\odot}$ [Adams et al., 2017]. However, using a method independent of progenitor determination, Strolger

et al. [2015] find that the number of observed core-collapse SNe per year per Mpc and the SN rate expected from star formation and stellar evolution are already in agreement (without an additional number of massive stars that directly form black holes) reinforcing the idea that there is a problem in our interpretation of the progenitor systems from direct detection observations.

Observationally, a few possible corrections to the direct detection method have been suggested to alleviate the tension between the predicted and observed progenitor masses. Walmswell and Eldridge [2012] propose that the luminosity of RSG progenitors is underestimated due to additional extinction from dust produced in RSG winds. With correction for circumstellar dust, they find an upper mass of 21^{+2}_{-1} $M_{\odot}$. Alternatively, Davies and Beasor [2018] suggest that there is a systematic error in the bolometric correction used to convert single-band flux to bolometric luminosity. This error is attributed to the evolution of RSGs to later spectral phases than those used in previous direct detection analyses. Reanalyzing the progenitors included in Smartt [2015], they find a maximum mass of 27 $M_{\odot}$, in excellent agreement with the theoretical predictions. These solutions show that the RSG problem maybe due to a bias in the the direct detection method that is mismatching SN explosions with their progenitor systems.

While direct detection has been the primary method to determine the progenitor of Type II SNe, the RSG problem demonstrates that its results may not be reliable. Additionally, it requires high-resolution imaging of the field prior to the SN explosion and that the SN be within 35 Mpc, the maximum distance at which single stars can be resolved. Recently, the community has developed the observational capabilities as well as the theoretical predictions required to determine the progenitor using light curve fitting and by measuring nucleosynthesis products in nebular spectra. These methods use independent, post-explosion observations and independent models to determine progenitor mass, providing a check on systematics that may be present in the direct detection method.

The linear light curve shape of Type IIL-like SNe may be an indication that these SNe originate from higher mass progenitors than Type IIP-like SNe. This is because if small hydrogen envelopes are responsible for the light curve shape, then Type IIL-like SNe are expected to have experienced more mass loss and mass loss increases with zero age main sequence mass (M_{ZAMS}) [Heger et al., 2003, Kasen and Woosley, 2009]. Observations that IIL-like SNe have shorter periods before falling

to the radioactive decay phase, are brighter, and have higher velocity ejecta support this hypothesis [Anderson et al., 2014, Faran et al., 2014, Gutiérrez et al., 2014, Patat et al., 1994, Sanders et al., 2015, Valenti et al., 2015, 2016]. However, with a sample of 12 SNe, Valenti et al. [2016] found that there is not a clear difference in the progenitor population of IIP-like and IIL-like SNe and more importantly, that the progenitors of IIL-like SNe are not above 17 $M_{\odot}$. With the small sample size of Valenti et al. [2016] and the acceptance of both the correlation between mass loss and $M_{\rm ZAMS}$ and the explanation of the Type IIL-like light curve shape as canonical theories it is prudent to continue to examine the progenitors of Type IIL-like SNe. This chapter details the progenitor masses determined for the Type IIL-like SNe: ASASSN-15oz and SN 2018ivc using direct detection, light curve modeling, population synthesis modeling, and nebular spectra modeling.

5.1. The Progenitor Mass of SN 2018ivc

5.1.1. SN 2018ivc Progenitor from HST Pre-Imaging. High-resolution images taken prior to explosion can be used to identify and characterize the properties of a SN progenitor [e.g. Crockett et al., 2011, Elias-Rosa et al., 2010, 2011, Fraser et al., 2010, 2011, 2014, Kilpatrick and Foley, 2018, Kochanek et al., 2012, 2017, Li et al., 2007, Mattila et al., 2008, Maund and Smartt, 2005, 2009, Maund et al., 2013, 2014, Smartt, 2009, Smartt et al., 2004, Tomasella et al., 2013, Van Dyk, 2017, Van Dyk et al., 2019]. We located pre-explosion *HST* observations in the Mikulski Archive for Space Telescopes (MAST) and analyzed them for the presence of a progenitor. The SN site is located in Advanced Camera for Surveys/Wide Field Channel (ACS/WFC) data in bands F658N and F814W from program GO-9788 (PI: L. Ho) and in F550M from GO-9503 (PI: N. Nagar), as well as Wide Field Planetary Camera (WFPC2) images in F606W from both GO-5479 (PI: M. Malkan) and GO-8597 (PI: M. Regan) and in F450W from GO-11128 (PI: D. Fisher); see Table 5.1.

To precisely pinpoint the SN location in the archival data, we obtained high spatial resolution *HST* images of the SN with the Wide Field Camera 3 (WFC3) on 2019 July 1. We identify 69 sources in common between between the F814W WFC3 image of the SN to the GO-9788 F814W ACS exposure and use these to identify the SN location in the pre-explosion ACS image. To do this, we randomly select 34 sources and use these to compute the astrometric transformation from

the WFC3 image to the ACS image the `PyRAF` task `geomap`. We then measure the location of the SN in the pre-explosion image using the `PyRAF` task `geoxytran` and the astrometric transformation from `geomap`. To understand the error introduced by the sources used to find the astrometric transformation, we calculate the root-mean-square (RMS) uncertainty of the 35 stars not used to determine the transformation. We repeat this process 1000 times and find the SN to be located at pixel $(3546.990 \pm 0.011 \pm 0.062,\ 4069.583 \pm 0.008 \pm 0.049)$ in the ACS F814W image, where the first uncertainty reported is the standard deviation of the measured SN location over the 1000 trials and the second uncertainty corresponds to the median RMS uncertainty of the stars not used to calculate the astrometric transformation. No source is detected within five sigma of this location, as indicated in Figure 5.1.

We then processed the individual archival FLC and C0F frames through `AstroDrizzle` [Hack et al., 2012] to flag cosmic-ray hits, and then extracted photometry from these frames using `Dolphot` [Dolphin, 2016, 2000]. Given that the progenitor is not detected in the pre-explosion *HST* images, we place upper limits on the progenitor detection which we list in Table 5.1.

We note in passing that, owing to the relative proximity of SN 2018ivc to the active nucleus of NGC 1068, the various pre-explosion data of the host galaxy obtained by the *Spitzer Space Telescope*, even at the shortest wavelength IRAC band at 3.6 μm, are of little value for progenitor identification, since the image of the nucleus was too luminous and effectively saturated the detectors. Given the comparatively low *Spitzer* spatial resolution, the pixels at the SN site were heavily affected by this saturation.

Table 5.1 *HST* Upper Limits to the SN 2018ivc Progenitor Detection

Date	Instrument	Filter	Apparent Mag Limit (3σ)	Absolute Mag Limit (3σ)	Program ID	PI
2007-08-16	WFPC2	F450W	> 25.8	> -6.2	GO-11128	D. Fisher
2003-01-08	ACS/WFC	F550M	> 25.0	> -6.5	GO-9503	N. Nagar
1994-12-03	WFPC2	F606W	> 25.0	> -6.4	GO-5479	M. Malkan
2001-06-30	WFPC2	F606W	> 25.4	> -6.0	GO-8597	M. Regan
2003-10-26	ACS/WFC	F658N	> 23.4	> -7.9	GO-9788	L. Ho
2003-10-26	ACS/WFC	F814W	> 24.4	> -6.5	GO-9788	L. Ho

Based on the upper limits we derive from the *HST* pre-explosion images (see Table 5.1 and Figure 5.2) and the fact that hydrogen is visible and strong throughout the spectroscopic evolution,

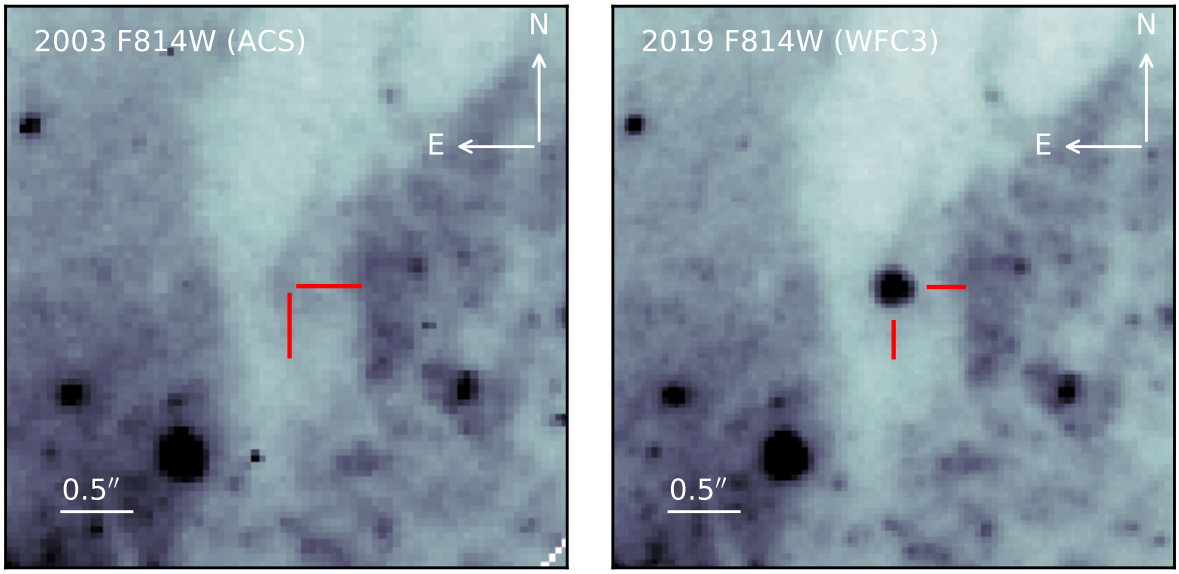

Figure 5.1 *Left:* Pre-explosion *HST* ACS/WFC image from 2003 Oct. 26 at F814W of NGC 1068 containing the site of SN 2018ivc. No source is identified at the SN location, indicated by the red ticks. *Right: HST* WFC3/UVIS image at F814W of SN 2018ivc, obtained on 2019 July 1. The SN is indicated with the red ticks.

we evaluate what we can infer about the progenitor. Referring to the single-star evolutionary tracks at solar metallicity from the MESA Isochrones & Stellar Tracks [MIST v1.2; Choi et al., 2016, Dotter, 2016, Paxton et al., 2011, 2013, 2015], we exclude stars whose photometry would exceed our upper limits or with less than 0.1 $M_\odot$ of hydrogen in the envelope. With these criteria we find we can eliminate all stars with initial masses between 9 $M_\odot$ and 48 $M_\odot$ and above 52 $M_\odot$ as the progenitor (see left panel of Figure 5.2). We conservatively include stars between 49 $M_\odot$ and 52 $M_\odot$ although we note that the largest hydrogen envelope mass in this range is 0.5 $M_\odot$, which could possibly be excluded with detailed spectroscopic modeling that is beyond the scope of this thesis. Additionally, we caution that this limit is highly dependent on the evolutionary models used. For instance, if we adopt the `STARS` models (Eggleton 1971, Eldridge and Tout 2004, Pols et al. 1995; on which the BPASS binary evolution models are based, e.g., Eldridge et al. 2017), we find that the hydrogen mass in the envelope drops below 0.1$M_\odot$ at a lower mass and redder SED, resulting in the exclusion of all stars with masses greater than 8 $M_\odot$ (see right panel of Figure 5.2).

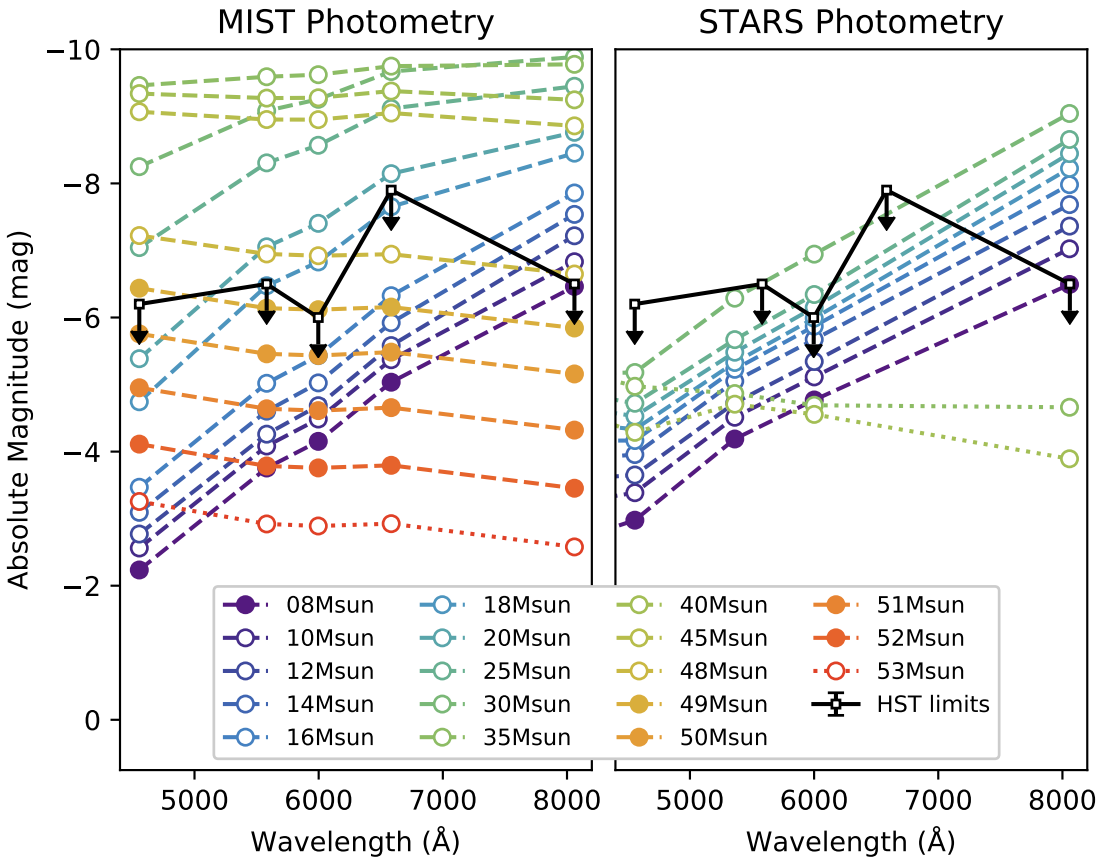

Figure 5.2 Upper limits on the detection, as given in Table 5.1, of the SN 2018ivc progenitor in archival *HST* images (black squares and arrows). In color are model SEDs derived from the endpoint of the solar-metallicity MIST [Choi et al., 2016, Dotter, 2016, Paxton et al., 2011, 2013, 2015] single-star evolutionary tracks (left) and the `STARS` models (Eggleton 1971, Eldridge and Tout 2004, Pols et al. 1995 (right) for masses spanning the range of allowed masses for each evolutionary model code. Allowed models are denoted with filled color circles. Models that are ruled out by the upper limits are marked with open circles and connected by a dashed line. Models that are ruled out by a lack of hydrogen in their envelope ($M_{\rm H,env} < 0.1$ M$_\odot$) are denoted with open circles and connected by a dotted line. The *HST* upper limits and strong hydrogen features in the spectra imply that that progenitor of SN 2018ivc, if single, was likely 8 M$_\odot$. The MIST models allow additional progenitors in the range 49-52 M$_\odot$, although these have small hydrogen envelopes which may not be able to produce the features seen in the spectra of SN 2018ivc.

The majority of massive stars form in binary systems [Sana et al., 2012]. For this reason, we also consider possible binary progenitor systems by examining the endpoints of the BPASS v2.2 models and the light from each combined system. Again, considering the *HST* upper limits and the mass of hydrogen in the envelope, we find a maximum progenitor mass of 11 M$_\odot$, with the

majority of progenitors between 8 $M_\odot$ and 9 $M_\odot$ (see Figure 5.3). Most progenitor systems are in a wide binary with log(Period[day]) = 2.75 for masses between 8 $M_\odot$ and 11 $M_\odot$ and a broader range of log(Period) (2.5-4) for an 8 $M_\odot$ progenitor. The few short-period progenitors occur when the secondary mass is much smaller than the primary mass ($M_2/M_1 \leq 0.2$; see Figure 5.4).

5.1.2. SN 2018ivc Progenitor Mass from the Surrounding H II Region. To better understand the nature of SN 2018ivc and its progenitor, we compare the host properties derived in Section 2.3 with those of all Type IIP/IIL SNe (85) and Type IIn SNe (16) from the PMAS/PPak Integral-field Supernova hosts COmpilation (PISCO) sample [Galbany et al., 2018][1]. The metallicity of the parent H II region of SN 2018ivc is near the median of the Type IIP/IIL SN distribution and slightly below the median of the Type IIn SN distribution (see the upper-right panel of Figure 2.6). Similarly, the EWH α falls near the median of both Type IIP/IIL SN and Type IIn SN distributions.

EWH α is an indicator of the age of the cluster. Assuming a Salpeter initial mass function (IMF) and an instantaneous burst of star formation, H II regions with younger stellar populations have larger EWH α. Using STARBURST99, a simple populations synthesis model, Kuncarayakti et al. [2013] derive a quantitative relationship between EWH α and the age of the stellar population . Assuming the SN progenitor was formed in this burst of star formation, the age of the stellar population is used to estimate the age of the SN progenitor, and therefore its mass. Using the EWH α derived from the parent H II region and Figure 1 from Kuncarayakti et al. [2013], we find the age of the progenitor of SN 2018ivc to be 6.75–7.75 Myr (depending on the slope and upper value of the IMF), corresponding to a progenitor mass of 25–28 $M_\odot$. We caution that this method is limited by our ability to isolate a single stellar population at this distance as well as simplifying assumptions made in mapping of the EWH α modeling to progenitor age (see Schady et al. 2019 for a detailed explanation). Specifically, the EWH α-age relation used assumes that massive stars are the ionizing source producing the H α emission, that we recover all of the photons ionizing the surrounding gas (i.e., there is no leakage), and that there are no binaries in the stellar population. The inclusion of these effects could yield an older age and therefore a lower mass progenitor, which is more consistent with the constraints from pre-explosion imaging.

[1]Updated with all new observations obtained through May 2019.

5.2. The Progenitor Mass of ASASSN-15oz

5.2.1. ASASSN-15oz Progenitor Mass from Nebular Spectra. Around 200 days the SN ejecta becomes optically transparent, revealing the inner core. At this time the SN enters the nebular phase, showing strong emission lines and no continuum (see Figure 5.5). Analysis of the spectra at this time can constrain the geometry of the explosion as well as the abundance of different elements. In particular, spectral modeling of this stage is a powerful tool to constrain the nature of the progenitor. Jerkstrand et al. [2012, 2014] have shown that the intensities of a few lines are sensitive to the M_{ZAMS} of the progenitor. Specifically, there is a tight monotonic correlation between the strength of the [OI] ($\lambda\lambda 6300, 6334$) line and the M_{ZAMS} of the progenitor. This is because [OI] is more isolated and less sensitive to the explosive nucleosynthesis of the SN than the other lines and thus reflects the oxygen abundance of the progenitor which has been shown to correlate well with progenitor mass [Woosley and Weaver, 1995].

Jerkstrand et al. [2014] modeled nebular spectra for 12, 15, 19, and 25 $M_{\odot}$ progenitors (M_{ZAMS}). Starting with the explosion models from Woosley and Heger [2007], the ejecta is divided into zones based on chemical composition and the evolution of the spectrum is found by modeling the gamma-ray transport and deposition, non-thermal electron degradation, NLTE ionization and excitation, and Monte Carlo radiative transfer.

Four nebular spectra of ASASSN-15oz were taken between day 228 (2016 Apr 11) and day 389 (2016-09-19). The first three spectra are high S/N and are use for modeling. In Figure 5.5 we compare these epochs to the different mass models, scaling the models to the observations over the full wavelength range. A zoom in on the [OI] line is displayed in the inset of each panel. We find the [OI] strength of ASASSN-15oz falls between the 15 and 19 $M_{\odot}$ models, consistent with the 17 $M_{\odot}$ found by modeling the light curve (see Section 4.2.4).

As a sanity check of the comparison between observations and synthetic spectra, we infer the ^{56}Ni mass from the scale factor we used to scale the models to the observations. Following Jerkstrand et al. [2018], the scaling combined with the equation for the luminosity of the cobalt decay (Equation 6 of Jerkstrand et al. 2012) yields the ^{56}Ni mass (assuming complete trapping):

$$\frac{F_{obs}}{F_{mod}} = \frac{d_{mod}^2}{d_{obs}^2} \frac{(M_{56,Ni})_{obs}}{(M_{56,Ni})_{mod}} exp\left(\frac{t_{mod} - t_{obs}}{111.4}\right) \tag{5.1}$$

where F_{obs} and F_{mod} are the observed and model fluxes, d_{obs} and d_{mod} the observed and model distances, $(M_{56,Ni})_{obs}$ and $(M_{56,Ni})_{mod}$ are the observed and model ^{56}Ni masses, and t_{obs} and t_{mod} are phases of the observation and the model. Using this relation, we average the ^{56}Ni mass found for each mass model to find an ^{56}Ni mass of 0.03 $M_{\odot}$ for day 228 (2016 Apr 11) and day 288 (2016 Jun 10) and 0.02 $M_{\odot}$ for day 340 (2016 Aug 03). These values are a factor of four smaller than our lower limit for the ^{56}Ni mass (see Section 3.2.1). This is due at least in part to the fact that the spectral synthesis modeling does not account for the incomplete gamma-ray trapping in ASASSN-15oz. The fact that several IIP/IIL SNe do not have complete trapping (see Section 3.5) should be taken into account in the future.

5.2.2. ASASSN-15oz Progenitor Mass from Light Curve Modeling. As described in Section 4.2.4, we built a grid of light curve using SNEC and varying progenitor mass, explosion energy, radial extent of circumstellar material (CSM), and CSM density. We find the best fit model to the multiband light curve and bolometric luminosity with and without CSM. In all cases, we find a progenitor mass of 17-18 $M_{\odot}$. The best fit light curves are compared to the data in Figure 4.5 and the best fit model parameters given in Table 4.2. Although there is a fair amount of degeneracy between the explosion energy and progenitor mass in the light curves produced, the progenitor mass derived from light curve modeling is in good agreement with that derived in the previous section for nebular spectra.

5.3. Conclusions

In this chapter we present the progenitor masses of ASASSN-15oz and SN 2018ivc each modeled using two different techniques. These SNe are strong candidates to have high mass progenitors as they are both Type IIL-like SNe. The progenitor masses derived for SN 2018ivc modeled with direct detection and population synthesis do not agree, with the direct detection mass at the low end of the RSG progenitor mass distribution and the mass derived from population synthesis at the upper end. Each of these methods has a number of caveats and it is unclear which is correct. The progenitor masses derived for ASASSN-15oz from light curve modeling and nebular spectra modeling are consistent, yielding an $\sim$17 $M_{\odot}$ progenitor which is intriguingly near the upper limit of those detected by direct detection.

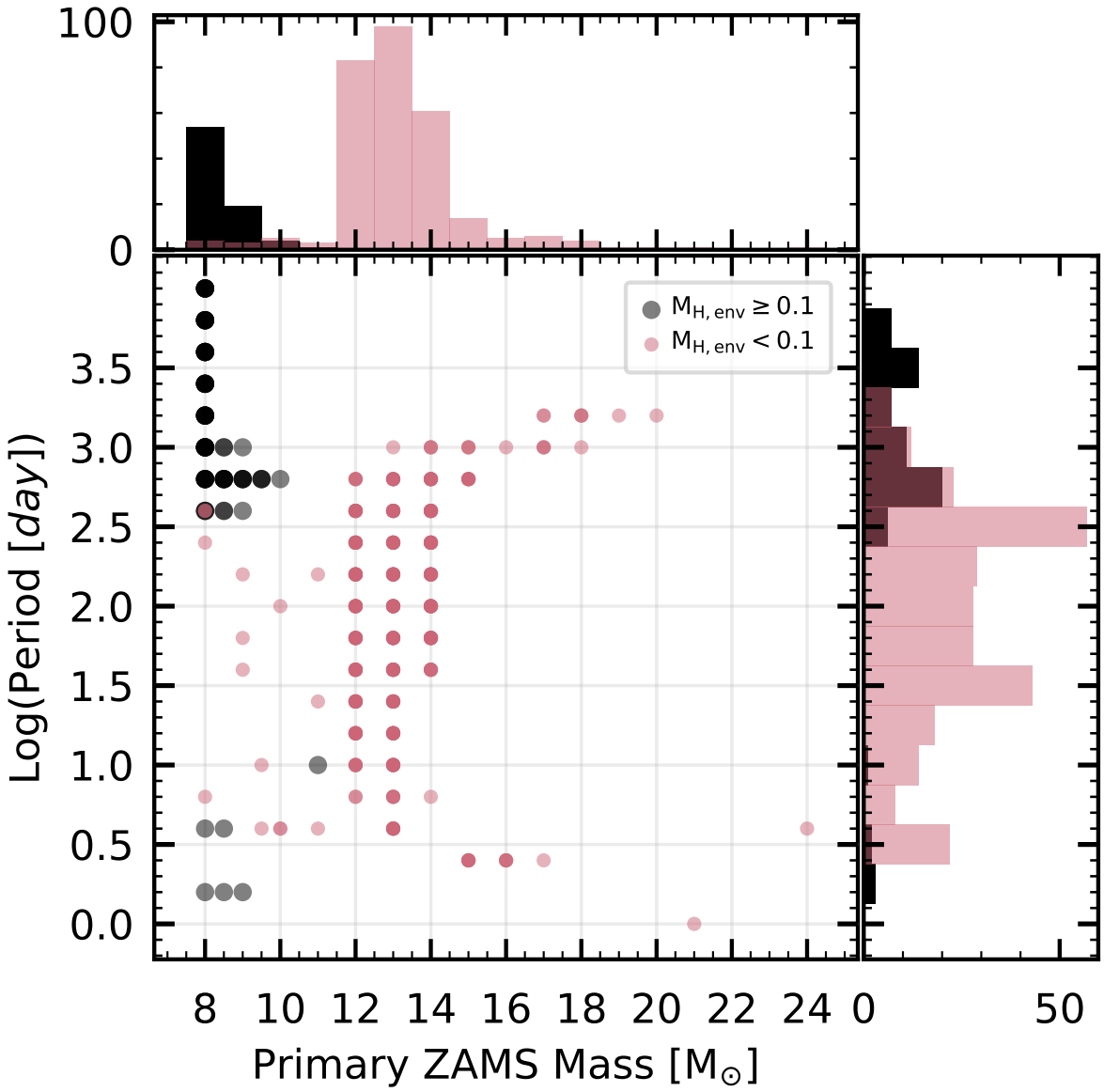

Figure 5.3 The range of progenitor masses and periods of the solar metallicity model binary systems from BPASS [Eldridge et al., 2017] that are allowed by the pre-explosion upper limits. Models that also contain more than 0.1 $M_\odot$ of hydrogen in their envelopes are marked as black circles, while models that contain less hydrogen are marked as pink points. The model parameters are marginalized over the ratio of the secondary to primary star mass (see Figure 5.4 for an animation of the three-dimensional distribution). The opacity of the markers indicates the density of models at a given location. The distribution of progenitor masses, further marginalized over the period, is shown in the top panel, with allowed progenitors in black and eliminated progenitors in pink. Similarly, the distribution of periods, further marginalized over progenitor mass, is shown in the right panel with the same color scheme. Consistent with the single stars, we find that the progenitor was less than 12 $M_\odot$ and most probably 8 $M_\odot$.

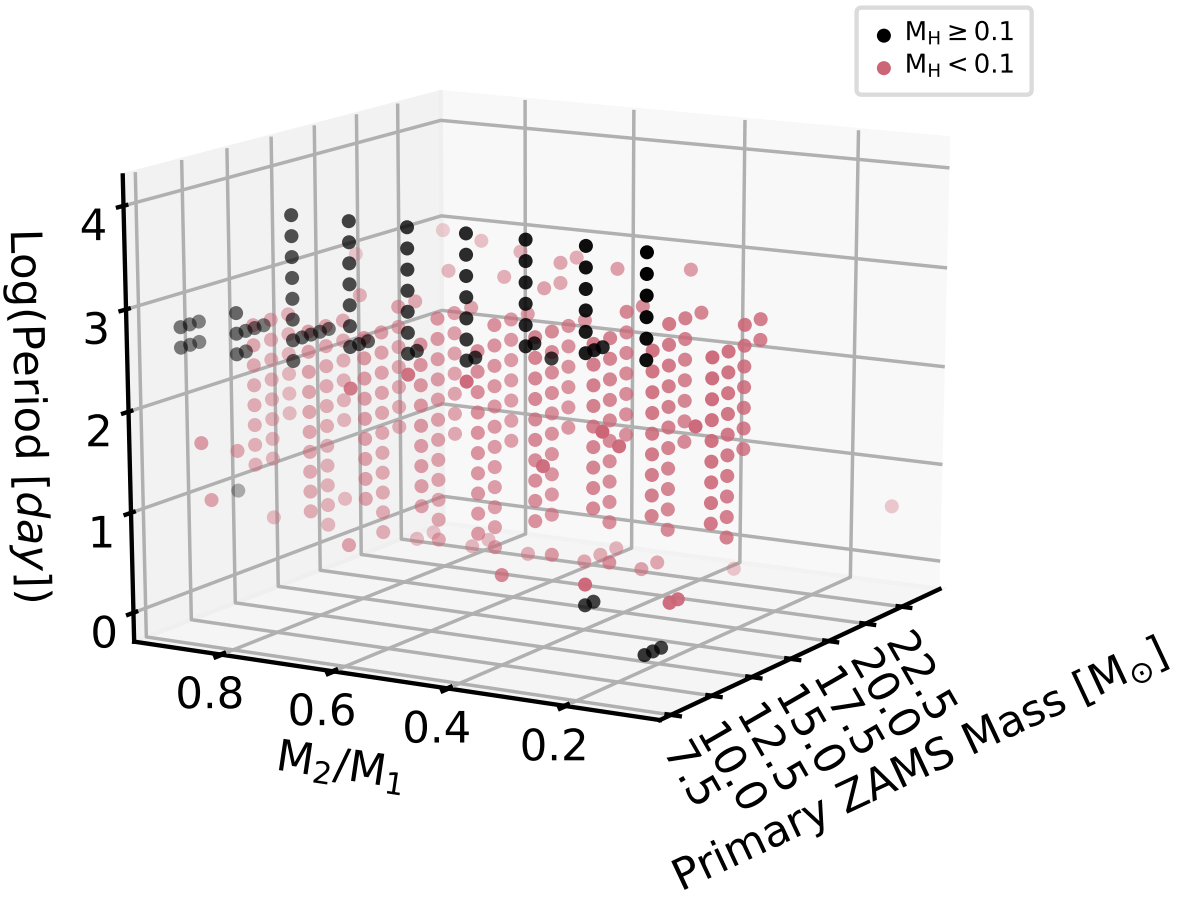

Figure 5.4 The range of progenitor mass, period, and mass ratio of the secondary to the primary star of the solar metallicity model binary systems from BPASS [Eldridge et al., 2017] that are allowed by the pre-explosion upper limits. Models that are allowed by both the *HST* upper limits and the hydrogen in their envelopes are shown in black, models that are ruled out are shown in pink. Most mass ratios are possible for allowed log(Period[days]) and progenitor masses, although there are 6 models that only occur at specific combinations of all three parameters.

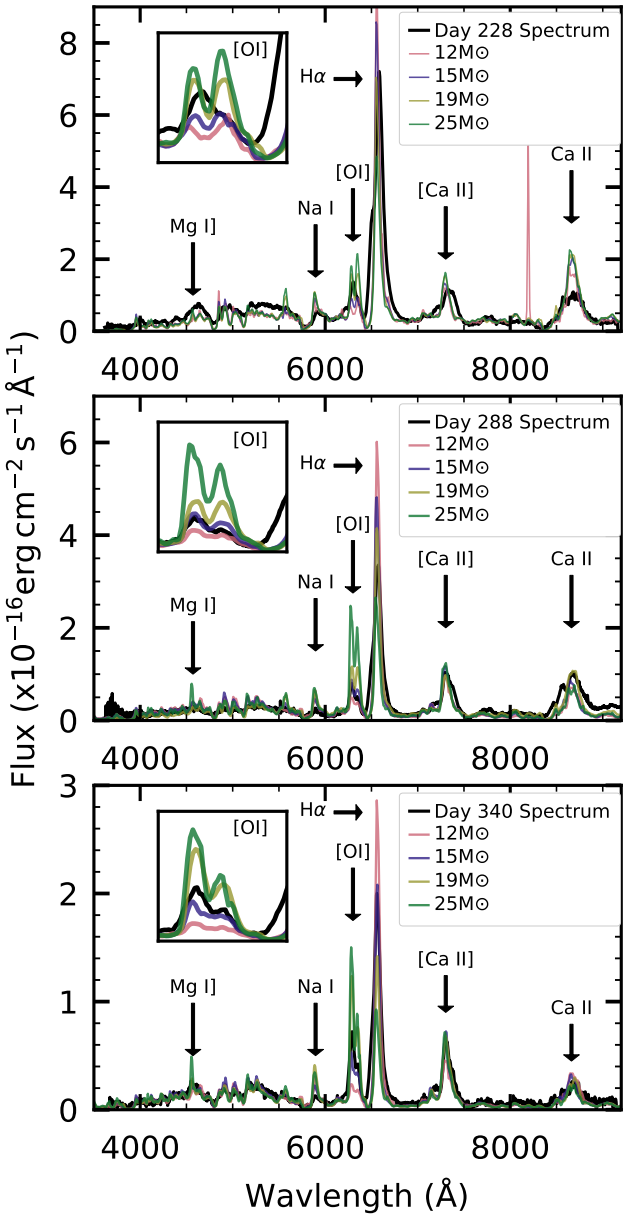

Figure 5.5 The nebular spectra of ASASSN-15oz from day 228 (2016 Apr 11; top), day 288 (2016 Jun 10; middle), and day 342 (2016 Aug 03; day 340; bottom) plotted with the scaled models of Jerkstrand et al. [2014] for M_{ZAMS} = 12, 15, 19, and 25 $M_{\odot}$. Most features in the observed spectra are well matched by the models. The inset shows the [O I] ($\lambda\lambda 6300, 6334$) doublet, the strength of which increases monotonically with progenitor mass. The [O I] flux falls between the 15 and 19 $M_{\odot}$ models, consistent with the 17 $M_{\odot}$ progenitor mass found using light curve modeling in Section 4.2.4.

CHAPTER 6

Progenitor Masses from Nebular Spectra

In Chapter 5, I showed how the nebular spectra of ASASSN-15oz could be compared to nebular models of Jerkstrand et al. [2012] to determine the mass of the progenitor. While it is useful to show that different methods of determining progenitor mass yield the same results, it is also important to show that for a sample of supernovae (SNe), no high mass progenitors are detected. While nebular spectra modeling can provide such a sample, collecting the observations for such a sample has been challenging as SNe fade by 3-5 magnitudes before reaching the nebular phase and so can only be observed if they are very nearby or with large telescopes. Over the last 45 years, SN by SN, a sample has slowly accumulated in the literature. In this final chapter, I collect these nebular spectra observations from the literature to construct a sample of SNe with progenitor masses, comparable in size to the direct detection sample analyzed in Smartt et al. [2015]

6.1. Comparing Observations to Models

Jerkstrand et al. [2012, 2014] showed the monotonic relationship between oxygen mass and progenitor mass. Theoretical predictions from first principles and simulations and observations show that oxygen formed during the star's life is dependent on the He core mass which is directly related to the progenitors $M_{\rm ZAMS}$ [Jerkstrand et al., 2014, Maguire et al., 2012, Thielemann et al., 1996, Woosley and Weaver, 1995]. Additionally, the oxygen mass is independent of the progenitor metallicity and explosion parameters [Woosley and Heger, 2007, Woosley and Weaver, 1995]. The final benefit of using oxygen is observational: the [OI] $\lambda\lambda 6300, 6364$Å is relatively isolated and the [O I] photons are not absorbed by other species in the outer ejecta [Jerkstrand et al., 2014]. Although different models consistently find the same trend of increasing oxygen luminosity with progenitor mass, we caution that there is still significant uncertainty in these calculations. Specifically, the amount of oxygen produced during stellar evolution depends on the poorly constrained parameters $^{15}{\rm C}(\alpha,\gamma)^{16}{\rm O}$ reaction rate, convection, mass loss, and rotation. Woosley and Weaver [1995] find

a maximum difference in M_O produced by different modeling groups to be 40%. In a more recent analysis, Dessart et al. [2021] find that the composition of the O/C shell can influence the strength of the [O I] lines by 25%. Nevertheless, comparisons of progenitor masses derived from nebular spectra and other methods have shown similar results giving us confidence in this method [Bostroem et al., 2019, Jerkstrand et al., 2011, 2012, 2014, 2015, Maguire et al., 2012, Szalai et al., 2019].

The oxygen mass (M_O) can be measured from the luminosity of the [OI] $\lambda\lambda 6300, 6364$Å. However, in addition to the amount of oxygen present, the [O I] luminosity is also determined by the gamma-ray luminosity from the radioactive decay of ^{56}Ni $\rightarrow$ ^{56}Co $\rightarrow$ ^{56}Fe which excites the oxygen-rich material in the ejecta [Elmhamdi et al., 2003, Maguire et al., 2010]. Quantitatively, this relationship is expressed as :

$$M_O = \frac{M_{ex}}{\eta} \frac{L_{6300}}{L_{^{56}Co}} \tag{6.1}$$

where M_{ex} is the mass of the material excited by gamma-rays, η is the efficiency of the transfer of energy from the gamma-rays into the [OI] emission, L_{6300} is the luminosity of the [OI] $\lambda\lambda 6300, 6364$Å, and $L_{^{56}Co}$ is the ^{56}Co luminosity Elmhamdi et al. [2003]. If one assumes that the mass of excited material and the efficiency are the same for all SNe, then the oxygen mass of different SNe can be compared using ratio of the oxygen luminosity to the ^{56}Co luminosity [Maguire et al., 2010]. This relationship allows us to quantify the comparison done in the previous chapter and extend the analysis to a sample of SNe.

6.2. ^{56}Co Luminosity

The radioactive decay ^{56}Ni $\rightarrow$ ^{56}Co $\rightarrow$ ^{56}Fe produces gamma-rays which are reprocessed in the SN ejecta, producing a characteristic linear decline in magnitude. While this occurs throughout the SN evolution, it becomes the primary source powering the light curve after the fall from plateau when hydrogen recombination is no longer contributing. The ^{56}Ni can therefore be measured from the light curve and used to characterize the ^{56}Co luminosity with the following equation [Jerkstrand et al., 2012]:

$$L_{^{56}\mathrm{Co}}(t) = 9.92 \times 10^{41} \frac{M_{^{56}\mathrm{Ni}}}{0.07\, M_\odot} \left(e^{-t/111.4\, d} - e^{-t/8.8\, d} \right) \mathrm{erg\ s^{-1}} \tag{6.2}$$

where t is days since explosion. Theoretical calculations connect the bolometric luminosity of a supernova to its $M_{^{56}Ni}$. However, it is rare that the full SED of a SN is observed such that the bolometric luminosity can be directly calculated. Most SNe are observed in two to five optical filters during their radioactive tail decline. One approach is to estimate the amount of flux missing from the observed filters and apply a bolometric correction to the observations. Alternately, as described in Section 3.2.1 and Bostroem et al. [2019], $M_{^{56}Ni}$ can be calculated directly by comparing the luminosity of the observed filters with that of SN 1987A in the same filters. We choose this later approach.

Another complication in the implementation of this method arises from the assumption of the complete trapping (and reprocessing) of gamma-rays by the SN ejecta. While this is not always the case, it is more likely to be true the earlier the SN is observed (after the fall from plateau). We therefore use photometry as close to the fall from plateau as possible to determine nickel mass. However, we caution that for SNe with incomplete trapping these values are lower limits.

The pseudo-bolometric luminosity is calculated by correcting the observed filters for both galactic and host extinction using the extinction law of Cardelli et al. [1989]. From the corrected filter magnitudes, the flux density is then calculated for each filter and linearly interpolated to the V band cadence when this filter available and bluest band available otherwise. The total flux is then derived by integrating the flux density at each central wavelength using the trapezoid rule. The flux density is assumed to be zero at edge of the end filters (e.g. central wavelength +/- band width) and integrated as such. The pseudo-bolometric luminosity is then calculated from the integrated flux using the distance modulus. Errors in pseudo-bolometric luminosity are derived using standard error propagation for errors in distance moduli, extinction, and apparent magnitude.

This method relies on the assumption that the SED of any type II SN is the same as that of SN 1987A during the nebular phase, allowing us to use as few as two filters to derive nickel mass. We test the validity of this assumption by comparing $M_{^{56}Ni}$ derived from the full SED with that derived using various subsets of filters for the SNe in our sample with broad wavelength coverage (SN 1999em: UBVRIJHK, SN 2004et: UBVRI, SN 2012aw: UBVRIJHKri, SN 2012ec: BVRIJHKri, and SN 2013ej: UBVRIJHKri). Figure 6.1 shows the pseudo-bolometric technique yields robust results, regardless of the optical filters used, as long as the filters are the same between

SN 1987A and the SN in question. This caveat proves challenging for modern SNe observed in

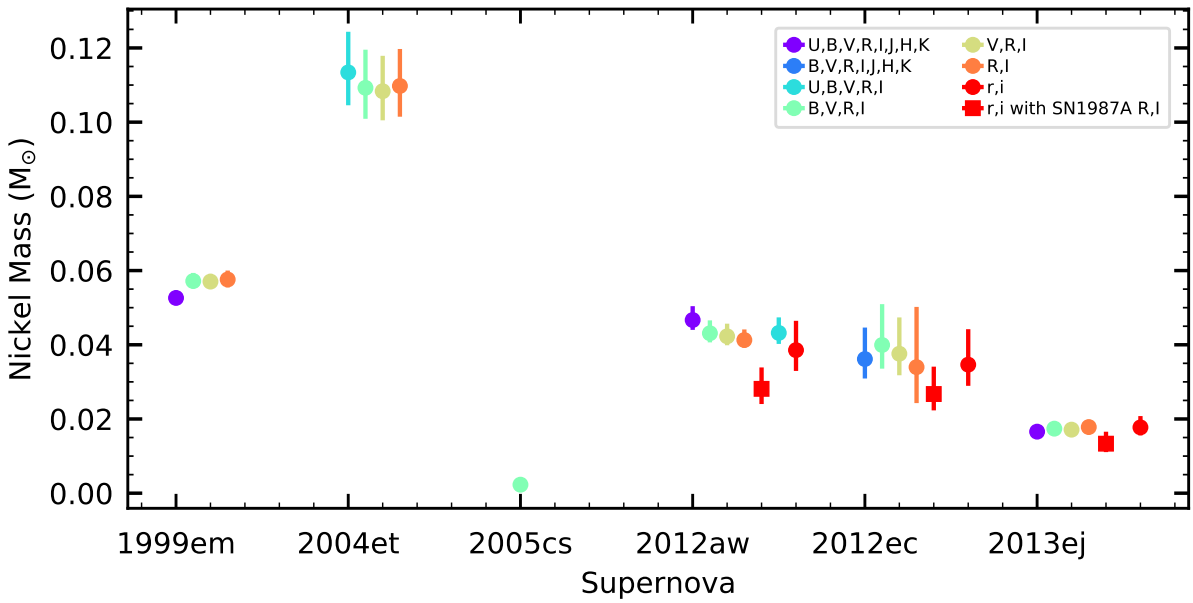

Figure 6.1 $M_{^{56}Ni}$ for different SNe measured from pseudo-bolometric luminosities calculated using different filters. Pseudo-bolometric luminosities calculated with the largest wavelength coverage are shown in purple and the smallest in orange and red. Circles represent measurements for which the same filters were used for the SN as for SN 1987A. The square symbol shows the measurement for each SN in r and i filters and SN 1987A in R and I filters. We find that we can robustly determine $M_{^{56}Ni}$, regardless of the filter combination used, provided that the same filters are used for SN 1987A. We also find that ^{56}Ni masses derived using our r- and i-band synthetic photometry of SN 1987A yields good agreement with other estimates using observed photometry.

Sloan filters rather than Landolt filters which were used for SN 1987A. For SNe with pseudo-bolometric light curves constructed from Sloan filters, we compute a pseudo-bolometric light curve for SN 1987A using Sloan filters in the following manner. Spectra of SN 1987A are flux calibrated to the Landolt photometry of SN 1987A. Then, synthetic Sloan and Landolt photometry is derived from these spectra and an s correction [Stritzinger et al., 2002] is derived relating B band and g band, R band and r band, I band and i band as a function of phase. This correction is smoothed with a cubic spline and applied to the observed B, R, and I-band photometry of SN 1987A to derive g, r, and i-band photometry, respectively. For the few SNe with observations in both systems, we find the nickel mass measured using the corrected Sloan pseudo-bolometric light curve to be consistent with that derived from Landolt filters.

6.3. [O I] Luminosity

The luminosity of the [OI] $\lambda\lambda 6300, 6364$Å can be used to measure of the oxygen mass. The measurement of this luminosity requires careful flux calibration of the spectra, definition of the continuum, and identification of the [O I] lines. In this section we describe the method used to analyze a sample of 112 spectra from 24 SNe taken from the literature. Details of the sample, including selection criteria are given in Section 6.4.

The quality of absolute flux calibration of spectra is highly variable across the literature. For this reason we scale all spectra to photometric observations taken after the fall from plateau. Different SNe have different photometric coverage in different filters, we therefore chose a single filter, as close to the [O I] doublet as possible, and perform a constant scaling. In order of preference, we use the following filters: r, R, i, I, V, and g, selecting the filter with photometric observations that extend past the spectroscopic observation and whose transmission function fully overlaps with the wavelength coverage of the spectrum. To avoid skipping filters whose coverage ends just before a spectroscopic observation, we allow filters with observations within 10 days of the spectroscopic observation. Once a filter is selected, if the spectroscopic observation falls between two photometric points, the photometry is linearly interpolated to the observation date. If the observation is outside of the photometry, a line is fit to a range of photometric observations and this is used to extrapolate the photometry to the observation date. Once the magnitude of the supernova has been determined at the phase of the spectroscopic observations, synthetic photometry is performed on the spectrum with PySynphot [STScI Development Team, 2013] and compared to the true photometry. The difference between the true and synthetic photometry is used to scale the flux. Spectra are then corrected for galactic and host extinction using the extinction law of Cardelli et al. [1989] with $R_V = 3.1$. Spectra are also shifted to rest wavelengths using the host redshift.

Previous studies [e.g. Jerkstrand et al., 2012, 2014, 2015, Valenti et al., 2016] have defined the [O I] doublet region to be between 6229.07 Å and 6435.64 Å (corresponding to a width of $3375 = 1.25 \times 2700$ km s^{-1} around the doublet). This region is shown in gray in the left panel of Figure 6.2. They defined the continuum as a straight line connecting the minimum flux in this region, on either side of the doublet. The continuum is shown in yellow in the left panel of Figure 6.2. The oxygen luminosity was then calculated from the difference of the integrated flux and the

integrated continuum between 6243.26 Å and 6421.31 Å (corresponding to a width of 2700 km s^{-1} on either side of the doublet). This region is shown in pink in the left panel of Figure 6.2. The values of 3375 km s^{-1} and 2700 km s^{-1} were chosen based on analysis of SN 2004et presented in Jerkstrand et al. [2012].

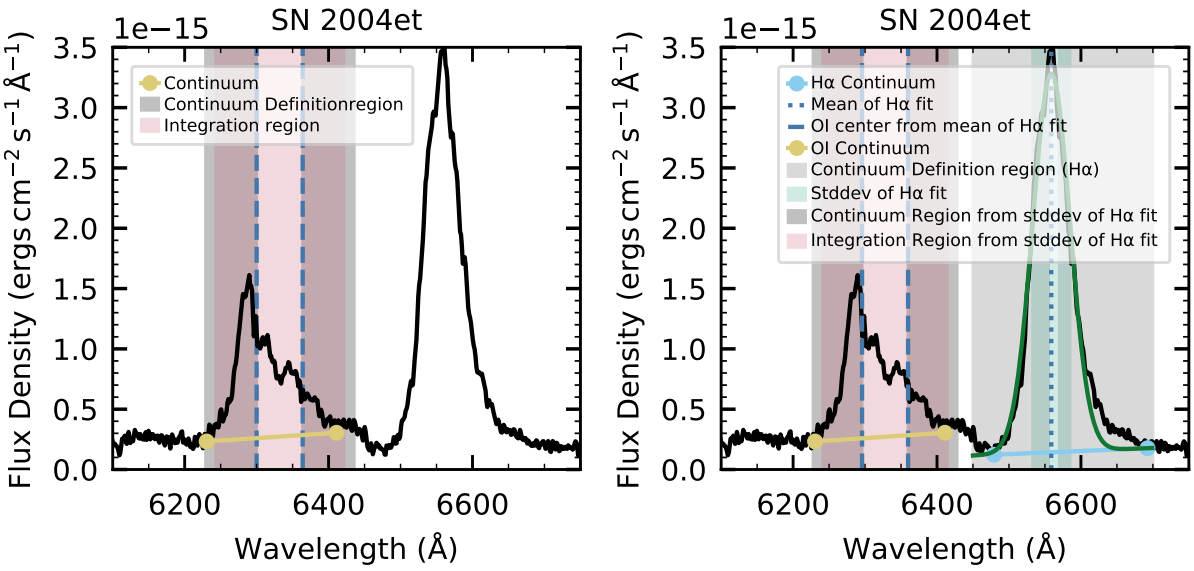

Figure 6.2 An example of previous and new continuum and integration region definitions. *Left:* The observed spectrum of SN 2004et from 2005-11-23, zoomed in on the [O I] doublet and H α line (black). This panel shows the way the continuum and integration regions were previously defined. The [O I] line centers are hard-coded to their rest wavelength values of 6300Å and 6364Å (blue dashed lines). This is clearly slightly offset from the actual peaks. The continuum on the left side is defined as the minimum between 6300 and $6300 - \frac{1.25\times2700}{c} \times 6300$. Similarly, on the right hand side, the continuum is defined as the minimum between 6364 and $6364 + \frac{1.25\times2700}{c} \times 6364$. These regions are shown in gray and the minimum is shown as a yellow circle. The continuum itself is the yellow line connecting these points. The integration region (pink) is defined in a similar manner as between $6300 - \frac{2700}{c} \times 6300$ and $6364 + \frac{2700}{c} \times 6364$. *Right:* This panel shows the new generalized the continuum and integration region definitions. As is seen when comparing the two panels, the regions equivalent for SN 2004et by design, but will vary depending on the width of the features in other spectra (see Figure 6.3). Similar to the [O I] continuum definition above, the H α continuum is defined as the minimum on either side of the peak between 6450Å and 6700Å (region: light gray, continuum: cyan). The fit to the H α line profile above this continuum is shown in green with the mean of the fit shown as a dotted blue line and the standard deviation of the fit shown as a shaded teal region. The [O I] line centers are defined as 263Å and 199Å from the mean of the H α fit and are shown as dashed blue lines. The continuum and integration regions are found in the same manner as the left panel except that $\frac{2700}{c} \times \lambda$ is replaced by $w = 2.1 * \sigma_{H_\alpha}$. The region used to find the continuum is shown in dark gray and the continuum itself in yellow. The integration region is shown in pink.

With a larger sample of SNe with varying velocities at different phases, this fixed integration value may define too large or small a region around the [O I] lines (see Figure 6.3). We generalize this definition to one that is based on the actual spectral features. While it would be ideal to use the [O I] lines themselves, these are often blended or have low signal-to-noise. However, we can easily fit H α which lies just redward of the [O I] doublet, is relatively isolated, and is generally the strongest feature in a nebular spectrum. Additionally, Maguire et al. [2010] find that the [O I] and H α lines have similar profiles. Using a similar methodology to that used previously for the [O I] line, we define the continuum around H α as a straight line connecting the minimum between 6450Å and the peak of the H α profile and the minimum between the peak and 6700Å. The continuum around H α is shown in cyan in the right panel of Figure 6.2. While all of the spectra analyzed have had the sky lines subtracted, this method may be sensitive to noise in the spectrum. By visually inspecting the continua and varying the definition of the continuum around H α, we find that this definition does not affect the final result. We then fit a single Gaussian on top of this fixed continuum to the region between 6450Å and 6700Å. The Gaussian fit is shown in green in the right panel of Figure 6.2. The peak of this fit (dotted blue line in the right panel of Figure 6.2) is used to define the peaks of the [O I] lines (dashed lines in the right panel of Figure 6.2).

As already mentioned, previous analyses used a hard-coded width derived from visual inspection of SN 2004et (2700 km s^{-1} on either side of the doublet). However, it is clear from the spectra in the sample that not all SNe have the same width lines. A generalized width prescription must rely on a general characterization of the line width, such as the standard deviation of a Gaussian fit to the lines, rather than a hard-coded value but should give the same result for SN 2004et. To ensure this consistency, we calculate a scaling factor (b) to map the standard deviation of the Gaussian fit to the width used in previous analyses for SN 2004et (e.g. for SN 2004et, $\frac{2700}{c} \times 6300 = b \times \sigma_{H_\alpha}$). Averaging over all SN 2004et spectra, we find a median scale factor of $b = 2.1$. We therefore define the [O I] region to be $w = 2.1\sigma_{H_\alpha}$ on either side of the [O I] doublet. The standard deviation of the H α fit is shown as a pink hatched region in the right panel of Figure 6.2. This region is used in the [O I] continuum (dark gray region in the right panel of Figure 6.2) and integration region (pink region in the right panel of Figure 6.2) definitions described above, replacing $\frac{2700}{c} \times \lambda$ with w. A visual inspection of the integrated region finds this generally improves the integrated region

or is similarly ambiguous to the previous method. Figure 6.3 demonstrates this, showing both the 2700 km s^{-1} width and the $2.1\sigma_{H_\alpha}$ width for SN 2004et for which there should be very little difference and SN 2015W for which the $2.1\sigma_{H_\alpha}$ width is a better characterization of the line width. In addition to a better description of the width of the doublet, the new method does a better job centering the integrated region on the features. Applying this new method to previously analyzed observations, we find that while individual observations may be shifted to higher or lower masses, it does not fundamentally alter any conclusions.

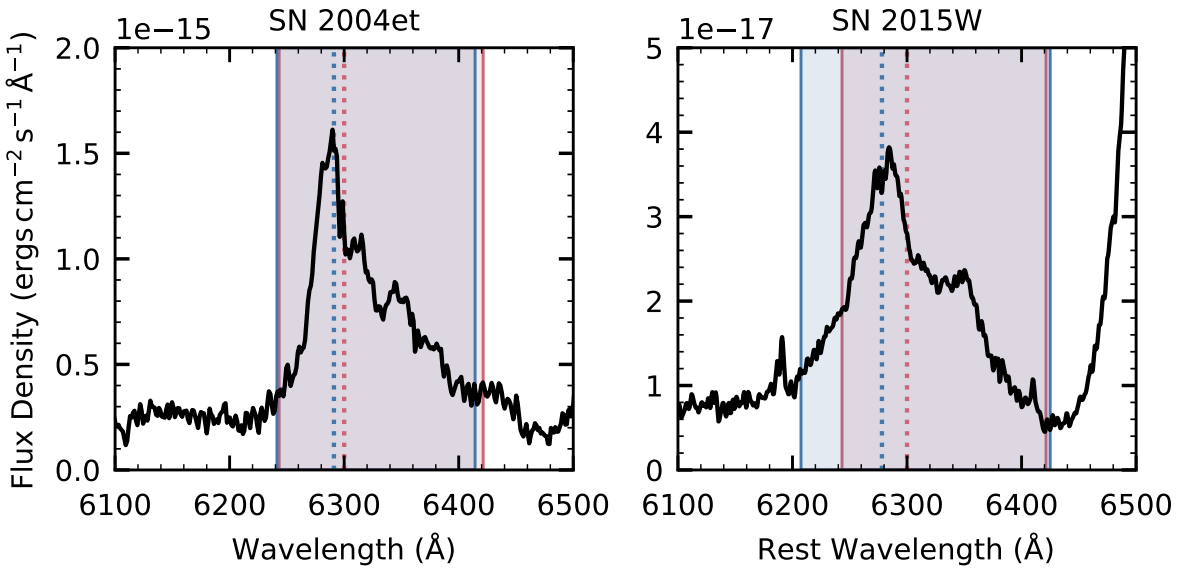

Figure 6.3 Two examples of the improved width definition of the [O I] doublet. *Left:* The observed spectrum of SN 2004et from 2005-11-23, zoomed in on the [O I] doublet (black). The region used to define the [O I] integrated flux in previous works, defined by 2700 km s^{-1}, is shown as a light pink shaded region between two solid pink lines. The [O I] region defined in this work as $2.1\sigma_{H_\alpha}$ is shown as a light blue shaded region outlined with solid blue lines. The region is centered on 6300 Å in the method of previous works which is shown in a dotted pink line and the new definition, based on the peak of H α is shown as a dotted blue line. *Right:* Same as for SN 2004et except for SN 2015W observed on 2015-10-10. By definition, the two regions are similar for SN 2004et and the [O I] feature is at 6300, 6364 Å. However, for SN 2015W, which shows a broader, blueshifted [O I] feature, the previous definition excludes the blue wing of the [O I] feature. The new definition both shifts the peak of the integrated region and expands it to include the full doublet.

6.4. Sample Selection and Analysis

The analysis described in the previous sections demonstrates the necessity of both spectroscopic and photometric observations during the radioactive tail phase. Additionally, this method uses the distance, extinction, and explosion date, although the ratio of the [O I] luminosity with the ^{56}Co luminosity alleviates most of the dependence of the results on distance and extinction. We search the literature for nebular spectra of SNe that also meet the following requirements:

- the explosion epoch is known to within 30 days
- observations in at least two filters after the fall from plateau
- observations taken between 200 and 525 days after explosion

We identify 24 SNe with 112 spectra and perform the analysis described above on each SN and spectrum. Appendix C gives observation details for each spectrum used. Host galaxy and SN properties are given in Tables 6.1 and 6.2 (respectively) and adopted from the following sources:

- *Host galaxies* were adopted from Silverman et al. [2017] Table A1 and the Transient Name Server [1].
- We use the host galaxy *redshift* from NED [2].
- The majority of *explosion epochs* are drawn from Silverman et al. [2017], Anderson et al. [2014], and Valenti et al. [2016]. SN 1997D is a low luminosity, low velocity, SN that was discovered at the end of the plateau and therefore the explosion epoch is uncertain. By comparing SN 1997D to the well constrained and very similar SN 1999br, Zampieri et al. [2003] determine that SN 1997D was discovered 90-100 days post explosion. Based on this, the explosion epoch in Table 6.2 is calculated as 95 days prior to the first observation.
- For *Milky Way extinction*, we calculate the $E(B-V)_{MW}$ values to be at the coordinates of the SN itself rather than the galaxy using the Schlafly and Finkbeiner [2011] values accessed through the NASA/IPAC Infrared Science Archive via astroquery [Ginsburg et al., 2019].
- NED *distances* can vary significantly with method used and H_0, we do not use the mean metric distance but choose the best methods in the following order: tip of the red giant

[1] `https://www.wis-tns.org`

[2] The NASA/IPAC Extragalactic Database (NED) is funded by the National Aeronautics and Space Administration and operated by the California Institute of Technology.

branch (TRGB), cepheid, surface brightness fluctuations, and Tully-Fisher (with a preference for NIR bands over optical). If no distance is available, the Hubble flow distance is used, including Virgo Infall with cosmological parameters from Planck Collaboration et al. [2016]

- *Host extinction* is adopted from the references given in Table 6.1. If only the total extinction is provided, the host extinction is calculated at the total - Galactic extinction.

Table 6.3 lists the ^{56}Ni masses derived for each SN along with the details of which filters and epochs were used. We compare the oxygen cobalt luminosity ratio to the oxygen cobalt luminosity ratio of the models of Jerkstrand et al. [2012] which are described in Section 5.2.1. The oxygen cobalt luminosity ratio for each spectrum is given in Appendix C. The model luminosities are computed using the same method as the nebular observations. We find no SNe with masses above 19 $M_\odot$, consistent with analysis of the progenitors of hydrogen-rich SNe using pre-explosion observations.

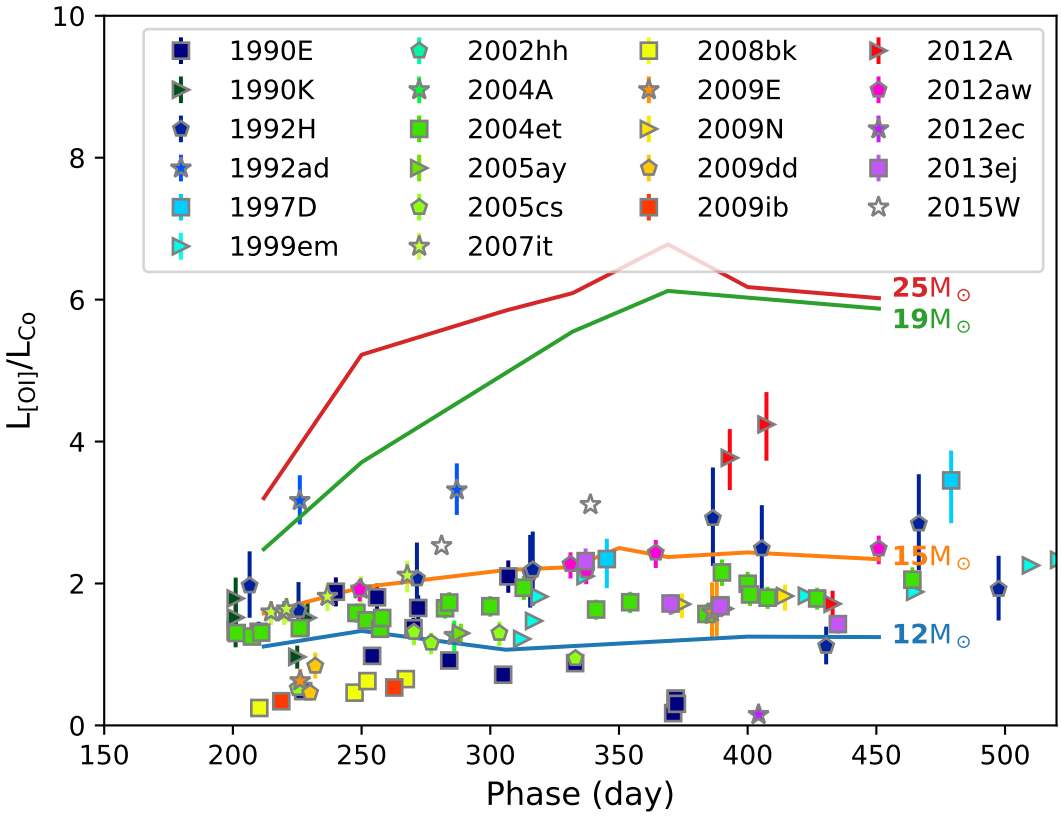

Figure 6.4 The ratio of oxygen to cobalt luminosity for a sample of 24 SNe and 4 models. Values derived from observed spectra are shown as colored points outlined in grey. Ratios derived from 12 (blue), 15 (orange), 19 (green), and 25 (red) $M_\odot$ models are shown as solid lines. The oxygen to cobalt ratio increases monotonically with progenitor mass and therefore can be used to evaluate the mass of a progenitor star from post-explosion observations. It is clear from this plot that although stars between 8 and 30 $M_\odot$ are expected to explode as type II SNe, we have not observed any progenitors above 19 $M_\odot$.

Table 6.1. Host Galaxy Properties for Nebular Spectra Sample

SN Name	RA	Dec	Host	Redshift	Distance Modulus	Type	Ref.	$E(B-V)_{host}$	Ref.
1988A	12:37:43.579	+11:48:19.69	NGC 4579	0.00506	31.09 (0.158)	SBF	14	0.085 (-)	5
1990E	02:39:28.500	-08:08:04.00	NGC 1035	0.00414	30.89 (0.450)	TF (I)	29	0.5 (0.1)	2
1990K	00:34:14.059	-27:47:46.72	NGC 150	0.00528	31.82 (0.450)	TF (I)	29	0.5 (-)	4
1991G	12:05:28.850	+50:32:11.69	NGC 4088	0.0052	30.64 (0.450)	TF (I)	29	0 (-)	3
1992H	13:56:22.200	+47:14:27.00	NGC 5377	0.00598	32.23 (0.450)	TF (I)	29	0.075 (0.06)	
1992ad	12:26:49.630	+08:52:38.39	NGC 4411	0.00426	31.09 (0.158)	SBF	14	- (-)	
1997D	04:11:01.000	-56:29:56.00	NGC 1536	0.00406	30.64 (0.800)	TF (B)	1	0 (-)	6
1999em	04:41:27.041	-02:51:45.22	NGC 1637	0.00239	30.34 (0.070)	Cepheid	8	0.1 (0.05)	8
2002hh	20:34:44.290	+60:07:18.98	NGC 6946	0.00013	29.44 (0.090)	TRGB	38	1.61 (-)	11
2004A	16:43:01.901	+36:50:12.52	NGC 6207	0.00284	30.94 (0.450)	TF (I)	29	0.06 (-)	17
2004et	20:35:25.330	+60:07:17.69	NGC 6946	0.00013	29.44 (0.090)	TRGB	38	0.1174 (0.07)	10
2005ay	11:52:48.070	+44:06:18.40	NGC 3938	0.0027	31.15 (0.400)	TF (B)	1	0.0817 (-)	12
2005cs	13:29:52.781	+47:10:35.69	NGC 5194	0.00154	29.39 (0.470)	TRGB	39	0.015 (-)	13
2006bp	11:53:55.740	+52:21:09.40	NGC 3953	0.00351	31.42 (0.450)	TF (I)	29	0.4 (-)	16
2007it	14:18:25.630	-43:22:53.80	NGC 5530	0.00398	30.33 (0.450)	TF (I)	29	0 (-)	18
2008bk	23:57:47.501	-32:33:24.01	NGC 7793	0.00077	27.89 (0.233)	TRGB	39	0 (0.016)	23
2008ex	19:20:28.680	+30:49:41.99	UGC 11428	0.01316	33.98 (0.150)	Hubble Flow	7	- (-)	
2009E	12:09:49.560	+58:50:50.32	NGC 4141	0.00633	33.22 (0.540)	TF (I)	29	0.02 (-)	19
2009N	12:31:09.470	-08:02:56.29	NGC 4487	0.00346	30.45 (0.540)	TF (I)	29	0.113 (0.019)	25
2009dd	12:05:34.099	+50:32:19.40	NGC 4088	0.00252	30.64 (0.450)	TF (I)	29	0.43 (-)	21
2009ib	04:17:39.919	-62:46:38.71	NGC 1559	0.00435	30.32 (0.450)	TF (I)	29	0.131 (0.025)	28
2012A	10:25:07.390	+17:09:14.62	NGC 3239	0.00251	29.53 (0.400)	TF (B)	1	0.009 (-0.006/+0.008)	22
2012aw	10:43:53.760	+11:40:17.90	NGC 3351	0.0026	29.84 (0.400)	TRGB	39	0.055 (0.014)	20
2012ec	02:45:59.880	-07:34:27.01	NGC 1084	0.00469	31.20 (0.450)	TF (I)	29	0.12 (+0.15/-0.12)	27
2013ej	01:36:48.161	+15:45:31.00	NGC 628	0.00219	29.68 (0.410)	TRGB	39	0 (0)	26
2015C	13:18:30.470	-14:36:44.60	IC 4221	0.00964	31.78 (0.540)	TF (I)	29	- (-)	
2015W	06:57:43.030	+13:34:45.70	UGC 3617	0.01329	33.83 (0.150)	Hubble Flow	7	0 (0)	30

Note. — (1) Tully and Fisher [1988], (2) Schmidt et al. [1993], (3) Blanton et al. [1995], (4) Cappellaro et al. [1995], (5) Clocchiatti et al. [1996], (6) Turatto et al. [1998], (7) Mould et al. [2000], (8) Leonard et al. [2003], (10) Li et al. [2005], (11) Pozzo et al. [2006], (12) Tsvetkov et al. [2006], (13) Baron et al. [2007], (14) Mei et al. [2007], (16) Dessart et al. [2008], (17) Gurugubelli et al. [2008], (18) Andrews et al. [2011], (19) Pastorello et al. [2012], (20) Van Dyk et al. [2012a], (21) Inserra et al. [2013], (22) Tomasella et al. [2013], (23) Anderson et al. [2014], (25) Takáts et al. [2014], (26) Valenti et al. [2014], (27) Barbarino et al. [2015], (28) Takáts et al. [2015], (29) Tully et al. [2016], (30) Valenti et al. [2016], (38) Anand et al. [2018], (39) Sabbi et al. [2018]

Table 6.2 Supernova Properties for the Nebular Spectra Analysis

SN Name	Explosion Epoch (MJD)	Ref.	$E(B-V)_{MW}$
1988A	47176.0 (2)	31,32	0.0346 (0.0009)
1990E	47935.0 (2)	31,2	0.0215 (0.0002)
1990K	48017.0 (5)	31,4	0.0123 (0.0003)
1991G	48279.5 (3)	3	0.0169 (0.0002)
1992H	48660.5 (3)	31,5	0.0148 (0.0009)
1992ad	48804.0 (2)	31,33	0.0229 (0.002)
1997D	50367.0 (40)	9	0.0166 (0.0014)
1999em	51476.0 (2)	31,34	0.0346 (0.0003)
2002hh	52576.0 (2)	31,11	0.2904 (0.0057)
2004A	53010.0 (3)	31,17	0.0131 (0.0002)
2004et	53270.0 (1)	31,10	0.2926 (0.0051)
2005ay	53453.0 (3)	31,12	0.0183 (0.0002)
2005cs	53549.0 (1)	31,35	0.0314 (0.0018)
2006bp	53834.0 (0.5)	15	0.0259 (0.0006)
2007it	54348.5 (1)	23,18	0.0994 (0.0016)
2008bk	54542.9 (6)	23,24	0.0169 (0.0004)
2008ex	54694.0 (2)	31,36	0.1971 (0.0026)
2009E	54832.0 (+2/-5)	19	0.0161 (0.0007)
2009N	54846.8 (5)	23,25	0.0182 (0.0007)
2009dd	54925.0 (5)	21	0.0169 (0.0002)
2009ib	55041.3 (3.1)	28	0.0257 (0.0002)
2012A	55933.0 (2)	31,22	0.0274 (0.0004)
2012aw	56003.0 (1)	31,37	0.0239 (0.0002)
2012ec	56143.0 (2)	31,27	0.0229 (0.0002)
2013ej	56496.95 (1)	26	0.0597 (0.0012)
2015C	57003.0 (19)	40	0.0692 (0.002)
2015W	57024.5 (10)	30	0.1181 (0.0023)

(2) Schmidt et al. [1993], (3) Blanton et al. [1995], (4) Cappellaro et al. [1995], (5) Clocchiatti et al. [1996], (9) Zampieri et al. [2003], (10) Li et al. [2005], (11) Pozzo et al. [2006], (12) Tsvetkov et al. [2006], (15) Immler et al. [2007], Quimby et al. [2007], (17) Gurugubelli et al. [2008], (18) Andrews et al. [2011], (19) Pastorello et al. [2012], (21) Inserra et al. [2013], (22) Tomasella et al. [2013], (23) Anderson et al. [2014], (24) Van Dyk et al. [2012b], (25) Takáts et al. [2014], (26) Valenti et al. [2014], (27) Barbarino et al. [2015], (28) Takáts et al. [2015], (30) Valenti et al. [2016], (31) Silverman et al. [2017], (32) Ruiz-Lapuente et al. [1990], (33) Liller et al. [1992], (34) Elmhamdi et al. [2003], (35) Pastorello et al. [2006], (36) Li and Filippenko [2008], (37) Bose et al. [2013], (40) de Jaeger et al. [2019]

6.5. Conclusions

In this chapter we analyzed a sample of 112 nebular spectra from 24 SNe to determine the masses of their progenitor stars. In addition to more than doubling the size of previous samples, this work also refines the calculation of the [O I] luminosity which is a critical component for deriving progenitor mass. We also calculate $M_{^{56}Ni}$ in a consistent way for all SNe in the sample, removing a potential source of scatter. Motivated by the lack of high mass progenitors observed in a sample of

Table 6.3 Ni Mass Table

Name	Ni Mass	Filters	JD (start)	JD (end)	Photometry Source
SN 1988A	0.08 (+0.006/-0.005)	B,V,R	2447340.0	2447380.0	1, 2, 3
SN 1988A	0.08 (+0.006/-0.005)	B,V,R	2447340.0	2447380.0	1, 2, 3
SN 1990E	0.06 (+0.008/-0.006)	B,V,R,I	2448080.0	2448140.0	4, 5, 3
SN 1990K	0.08 (+0.017/-0.012)	B,V,R	2448170.0	2448220.0	6, 3
SN 1991G	0.02 (+0.004/-0.003)	V,R,I	2448400.0	2448460.0	7
SN 1992H	0.14 (+0.041/-0.027)	B,V,R	2448860.0	2448960.0	8, 3
SN 1992ad	0.02 (+0.002/-0.002)	B,I	2449100.0	2449200.0	9
SN 1997D	0.00 (+0.001/-0.000)	B,V,R,I	2450490.0	2450570.0	10, 11, 3
SN 1999em	0.05 (+0.002/-0.001)	U,B,V,R,I,J,H,K	2451610.0	2451650.0	12, 13, 14, 15, 3, 16, 17, 9
SN 2002hh	0.02 (+0.002/-0.001)	V,R,I	2452730.0	2452880.0	18, 3
SN 2004A	0.02 (+0.005/-0.003)	B,V,R,I	2453150.0	2453230.0	19, 3
SN 2004et	0.11 (+0.011/-0.009)	U,B,V,R,I	2453410.0	2453440.0	20, 21, 3
SN 2005ay	0.03 (+0.003/-0.002)	B,V,R,I	2453570.0	2453700.0	22, 3, 17
SN 2005cs	0.00 (+0.000/-0.000)	B,V,R,I	2453690.0	2453750.0	23, 3
SN 2007it	0.08 (+0.011/-0.007)	B,V,R,I	2454480.0	2454550.0	24, 16
SN 2008bk	0.01 (+0.001/-0.001)	B,V,R,I	2454720.0	2454820.0	3, 25, 16
SN 2008ex	0.29 (+0.019/-0.016)	B,V	2454990.0	2455090.0	26, 27
SN 2009N	0.01 (+0.001/-0.001)	V,R,I	2454970.0	2455050.0	28
SN 2009dd	0.04 (+0.011/-0.007)	B,V,R,I	2455060.0	2455070.0	3, 29
SN 2009E	0.09 (+0.028/-0.018)	B,V,R,I	2454970.0	2455010.0	3, 30
SN 2009ib	0.02 (+0.004/-0.003)	B,V,R,I	2455190.0	2455230.0	31
SN 2012A	0.01 (+0.001/-0.001)	B,V,R,I	2456050.0	2456130.0	26, 32, 27
SN 2012aw	0.04 (+0.004/-0.003)	U,B,V,R,I	2456200.0	2456250.0	26, 33, 34, 35, 27
SN 2012ec	0.05 (+0.015/-0.008)	B,V	2456260.0	2456310.0	36
SN 2013ej	0.02 (+0.002/-0.001)	U,B,V,R,I,J,H	2456620.0	2456630.0	26, 37, 38, 27, 39
SN 2015W	0.04 (+0.002/-0.002)	r,i	2457150.0	2457320.0	40
SN 2015V	0.04 (+0.003/-0.002)	B,V,R,I	2457240.0	2457250.0	26, 27

(1) Ruiz-Lapuente et al. [1990], (2) Benetti et al. [1991], (3) Tsvetkov, D.Yu. and Pavlyuk, N.N. and Bartunov, O.S. and Pskovskii, Yu.P. [2010], (4) Schmidt et al. [1993], (5) Benetti et al. [1994], (6) Cappellaro et al. [1995], (7) Blanton et al. [1995], (8) Clocchiatti et al. [1996], (9) Galbany et al. [2016b], (10) Turatto et al. [1998], (11) Benetti et al. [2001], (12) Hamuy [2001], (13) Leonard et al. [2002], (14) Richardson et al. [2002], (15) Elmhamdi et al. [2003], (16) Anderson et al. [2014], (17) Faran et al. [2014], (18) Pozzo et al. [2006], (19) Tsvetkov [2008], (20) Sahu et al. [2006], (21) Maguire et al. [2010], (22) Tsvetkov et al. [2006], (23) Pastorello et al. [2009], (24) Andrews et al. [2011], (25) Van Dyk et al. [2012b], (26) Silverman et al. [2012], (27) de Jaeger et al. [2019], (28) Takáts et al. [2014], (29) Inserra et al. [2013], (30) Pastorello et al. [2012], (31) Takáts et al. [2015], (32) Tomasella et al. [2013], (33) Bose et al. [2013], (34) Dall'Ora et al. [2014], (35) Rubin et al. [2016], (36) Barbarino et al. [2015], (37) Huang et al. [2015], (38) Yuan et al. [2016], (39) Brown et al. [2014], (40) Valenti et al. [2016]

progenitor masses derived from pre-explosion observations, this work examines a statistical sample using independent observations and independent models. We constrain the progenitor masses of 24 SNe from the oxygen luminosity in nebular spectra. This completely independent method allows us to search for systematic effects in the pre-explosion analysis. With this sample we find no progenitors with masses over 19 $M_{\odot}$, reaching a similar conclusion to Smartt et al. [2015].

CHAPTER 7

Conclusions

This thesis examined the role of hydrogen-rich supernovae (SNe) in understanding mass loss and progenitor mass in RSGs. We search for interaction between the supernova ejecta and circumstellar material (CSM) in two type IIL-like SNe: SN 2018ivc [Bostroem et al., 2020] and ASASSN-15oz [Bostroem et al., 2019]. Type IIL-like SNe are thought to have small hydrogen envelopes, implying greater mass loss. This mass loss, if due to stellar winds, also implies that the progenitors of type IIL-like SNe are likely to be more massive than those of type IIP-like SNe, making theses SNe strong candidates for the missing high mass RSGs.

Observations from the X-ray through the radio shed light on the mass loss of the progenitors of SN 2018ivc and ASASSN-15oz. Although the mass loss of RSGs is generally characterized as a steady, weak wind which does not influence the light curve of type II SNe, we find interaction with material with different densities contributes to the light curve of SN 2018ivc. The light curve evidence is corroborated by a strong X-ray detection during a 10 day plateau in the light curve. Like SN 2018ivc, modeling of the light curve of ASASSN-15oz showed evidence for interaction with dense CSM immediately surrounding the star. However, radio observations showed that earlier in its history, the progenitor star had more prototypical mass loss. Taken together these two SNe point to a period of outbursts and/or eruptive mass loss in the final years of a RSG's lifetime that is typically associated with more massive stars.

Although stars between 8 and 30 $M_{\odot}$ are thought to explode as type II SNe, a sample of 45 SNe with pre-explosion observations reveals a maximum mass of 18.5 $M_{\odot}$. Both observational and theoretical proposals have been put forth to explain this dearth of high mass progenitors. Observational proposals have focused on a mechanism that would systematically decrease the derived pre-explosion luminosity and inferred progenitor mass. We take a different approach, deriving the progenitor masses of SN 2018ivc and ASASSN-15oz, both candidates for having massive progenitors due to their linearly declining light curves. For SN 2018ivc we find the most likely progenitor to be

an 8-12 $M_\odot$ RSG from pre-explosion observations regardless of whether single or binary evolution channels are considered. We also use the strength of H α emission from the surrounding H II region to measure the age of the surrounding stars and use this to indicate the age and therefore mass of the progenitor system. From this analysis, considering only single star evolution, we find a higher mass progenitor: 25-28 $M_\odot$.

We perform two different analyses on ASASSN-15oz to determine the progenitor mass. By modeling the optical light curve, we find a 17 $M_\odot$ progenitor. Comparing the [O I] luminosity of three spectroscopic observations taken more than 200 days after explosion to models, we find the progenitor falls between 15 and 19 $M_\odot$, consistent with the 17 $M_\odot$ found with light curve modeling. This agreement between analysis methods which rely on entirely different models, assumptions, and observations is encouraging that our analysis does not suffer from a systematic bias that shifts all progenitors to lower masses.

Finally, we extend the nebular spectra modeling we did for ASASSN-15oz to a sample of 112 spectra of 24 SNe. This increase sample size makes it more likely that our sample includes a high mass progenitor. Although some of these observations lie between 15 and 19 $M_\odot$, none of them exceed 19 $M_\odot$. The consistency of the progenitor mass upper limit between pre-explosion analyses and nebular spectra modeling forces us to look either for a systematic that effects both pre- and post-explosion observations, spectroscopy and photometry, and/or light curve and nebular spectra modeling or to accept this observational limit and agree on a theoretical explanation for it.

7.1. Future Work

Smartt et al. [2015] showed that assuming that all stars above 18 $M_\odot$ explode as SNe, for a sample of 30 SNe, there should be 13 SNe with progenitor masses above 18 $M_\odot$. However, it is possible that only a fraction of these stars explode as SNe [Sukhbold et al., 2016]. In this case, a larger sample size is required to confirm this theory and constrain the fraction of high-mass stars that explode. Over the last three years I have collected nebular spectra of an additional 30 SNe using the Keck and Gemini telescopes. These observations will be added to the literature sample, doubling the number of SNe with progenitor mass estimates. Depending on the fraction of stars above 18 $M_\odot$ that explode, this sample may detect the first high mass progenitor or an even larger

sample may be required. If this is the case, we will continue to apply for time on both the Keck and Gemini telescopes to build a larger sample.

An orthogonal approach, with the power to independently inform not just progenitor masses but broader progenitor and supernova properties, such as mass loss and explosion energy, is to model the light curves of a large sample of SNe. The SN community is currently collecting high quality, high cadence light curves of thousands of SNe per year. However, these light curves are currently modeled by creating individual grids for each SN, fixing as many parameters as possible. With this approach, it is already too computationally intensive to model all of SNe being discovered. As we enter the age of automated surveys, such as the Zwicky Transient Facility now and the Rubin Observatory Legacy Survey of Space and Time in the next few years, we need a general framework to automatically model the light curves produced by these surveys. In my post-doctoral work I will build such a tool, by first generating a grid of models using the Modules for Experiments in Stellar Astrophysics code [Paxton et al., 2018] to evolve the progenitor stars and the STELLA [Blinnikov and Bartunov, 2011, Blinnikov et al., 2006] code to explode them as supernovae. I will then create an interface that can be used by individuals and plugged into brokers to model the observed light curves of vanilla Type II SNe which may not be interesting alone but which when combined into a large sample can provide population level information about the final stages of stellar evolution for stars between 8-30 $M_{\odot}$.

APPENDIX A

Tables of Photometric and Spectroscopic Observations of SN 2018ivc

A.1. Tables of Observations SN 2018ivc

TABLE A.1. Log of Spectroscopic Observations of SN 2018ivc

Observation Date	MJD	Phase (day)	Telescope	Instrument	Wavelength Range (Å)	Exposure Time (s)	Resolution $\lambda/\Delta\lambda$
2018-11-24	58446.29	2.04	FTN	FLOYDS	3499-10000	2700	400-700
2018-11-24	58446.50	2.25	2.16m XLO	BFOSC	3852-8696	3000	250-800
2018-11-24	58446.70	2.45	2.4m LJT	YFOSC	3400-9100	1200	240
2018-11-24	58446.81	2.56	SALT	RSS	3494-9392	1793	600-2000
2018-11-25	58447.20	2.95	Gemini-S	FLAMINGOS-2	9852-18075	720	900
2018-11-25	58447.38	3.13	FTN	FLOYDS	3499-10000	1200	400-700
2018-11-25	58447.52	3.27	2.16m XLO	BFOSC	3852-8696	3300	250-800
2018-11-25	58447.60	3.35	HCT-IIA	HFOSC	3500-8998	1200	1200
2018-11-26	58448.57	4.32	2.16m XLO	BFOSC	3852-8697	3300	250-800
2018-11-27	58449.16	4.91	HET	lrs2	3640-10298	606	1140-1920
2018-11-27	58449.32	5.07	LBT	MODS	3290-5549	2400	1850-2300
2018-11-27	58449.32	5.07	LBT	MODS	5800-9572	2400	1850-2300
2018-11-27	58449.61	5.36	2.16m XLO	BFOSC	3853-8701	3300	250-800
2018-11-28	58450.23	5.98	FTN	FLOYDS	3499-10000	1200	400-700
2018-11-29	58451.25	7.00	Bok	SPOL	4001-7549	2400	430
2018-12-01	58453.40	9.15	FTN	FLOYDS	3499-10000	1200	400-700
2018-12-02	58454.00	9.75	Gemini-S	FLAMINGOS-2	9851-18077	1080	900
2018-12-03	58455.69	11.44	HCT-IIA	HFOSC	3500-8998	1200	1200
2018-12-04	58456.59	12.34	HCT-IIA	HFOSC	3500-8998	1200	1200
2018-12-05	58457.44	13.19	Keck I	LRIS	3136-10220	119	750-1475
2018-12-07	58459.20	14.95	Gemini-S	FLAMINGOS-2	9849-18077	1080	900

TABLE A.1. Log of Spectroscopic Observations of SN 2018ivc

Observation Date	MJD	Phase (day)	Telescope	Instrument	Wavelength Range (Å)	Exposure Time (s)	Resolution $\lambda/\Delta\lambda$
2018-12-07	58459.55	15.30	HCT-IIA	HFOSC	3500-8998	1800	1200
2018-12-08	58460.36	16.11	FTN	FLOYDS	3500-9999	1200	400-700
2018-12-10	58462.32	18.07	3.5m APO	DIS	3374-5607	2400	2450
2018-12-10	58462.32	18.07	3.5m APO	DIS	5263-9404	2400	3150
2018-12-11	58463.81	19.56	HCT-IIA	HFOSC	3500-8998	2400	1200
2018-12-13	58465.00	20.75	Gemini-S	FLAMINGOS-2	9850-18077	1440	900
2018-12-14	58466.30	22.05	MMT	Binospec	5072-7541	720	3590
2018-12-15	58467.76	23.51	HCT-IIA	HFOSC	3500-8998	2400	1200
2018-12-16	58468.65	24.40	HCT-IIA	HFOSC	3500-8998	2400	1200
2018-12-17	58469.23	24.98	FTN	FLOYDS	3500-10000	1800	400-700
2018-12-18	58470.51	26.26	2.16m XLO	BFOSC	4358-8690	2400	250-800
2018-12-19	58471.10	26.85	Gemini-S	FLAMINGOS-2	9852-18076	1800	900
2018-12-21	58473.15	28.90	SOAR	GHTS	3500-7000	780	1050
2018-12-21	58473.15	28.90	SOAR	GHTS	5000-9000	780	1050
2018-12-22	58474.35	30.10	FTN	FLOYDS	3499-9999	3600	400-700
2018-12-23	58475.21	30.96	FTN	FLOYDS	3499-9999	3600	400-700
2018-12-24	58476.63	32.38	HCT-IIA	HFOSC	3500-8998	2400	1200
2018-12-24	58476.78	32.53	HCT-IIA	HFOSC	3500-8998	1200	1200
2018-12-24	58476.85	32.60	SALT	RSS	6057-7010	2464	2200-5500
2018-12-26	58478.10	33.85	Gemini-S	FLAMINGOS-2	9849-18077	1800	900
2018-12-26	58478.48	34.23	FTS	FLOYDS	4800-10000	3600	400-700
2018-12-26	58478.83	34.58	SALT	RSS	3497-9393	2093	600-2000
2018-12-30	58482.49	38.24	FTS	FLOYDS	4800-9999	3600	400-700
2019-01-03	58486.30	42.05	FTN	FLOYDS	3500-10000	3600	400-700
2019-01-05	58488.00	43.75	Gemini-S	FLAMINGOS-2	9851-18075	1800	900
2019-01-06	58489.54	45.29	2.16m XLO	BFOSC	3851-8692	3600	250-800
2019-01-10	58493.33	49.08	FTN	FLOYDS	3499-10000	3600	400-700
2019-01-11	58494.30	50.05	Keck I	LRIS	3137-10197	420	750-1475
2019-01-13	58496.49	52.24	2.16m XLO	BFOSC	4095-8810	3000	250-800
2019-01-14	58497.10	52.85	Gemini-S	FLAMINGOS-2	9850-18079	2160	900

TABLE A.1. Log of Spectroscopic Observations of SN 2018ivc

Observation Date	MJD	Phase (day)	Telescope	Instrument	Wavelength Range (Å)	Exposure Time (s)	Resolution $\lambda/\Delta\lambda$
2019-01-22	58505.26	61.01	FTN	FLOYDS	3499-9999	3600	400-700
2019-01-28	58511.44	67.19	2.16m XLO	BFOSC	3869-8822	3600	250-800
2019-02-05	58519.25	75.00	Keck I	LRIS	3138-10244	1200	750-1475
2019-02-08	58522.13	77.88	MMT	Binospec	5062-7522	960	3590
2019-08-28	58723.59	279.34	Keck II	DEIMOS	4480-9510	1200	1875

TABLE A.2. Complete table of photometric observations of SN 2018ivc. Photometric measurements in Landolt and Swift filters are given in Vega magnitudes while measurements in Sloan filters are given in AB magnitudes.

Date-Obs	JD	Phase (day)	Apparent Magnitude (mag)	Apparent Magnitude Error (mag)	Filter	Source
2018-11-13	2458435.59	-9.16	<15.26	-1.0	Open	CTIO-Prompt5
2018-11-14	2458436.61	-8.14	<15.29	-1.0	Open	CTIO-Prompt5
2018-11-15	2458437.60	-7.15	<15.79	-1.0	Open	CTIO-Prompt5
2018-11-15	2458437.75	-7.00	<19.82	-1.0	g	ZTF
2018-11-15	2458437.81	-6.94	<20.16	-1.0	g	ZTF
2018-11-16	2458438.63	-6.12	<15.66	-1.0	Open	CTIO-Prompt5
2018-11-17	2458439.62	-5.13	<15.75	-1.0	Open	CTIO-Prompt5
2018-11-18	2458440.59	-4.16	<15.57	-1.0	Open	CTIO-Prompt5
2018-11-19	2458441.61	-3.14	<19.36	-1.0	Open	CTIO-Prompt5
2018-11-20	2458442.93	-1.82	<18.60	-1.0	o	ATLAS
2018-11-24	2458446.54	1.79	14.65	0.01	Open	CTIO-Prompt5
2018-11-24	2458446.55	1.80	14.66	0.01	Open	CTIO-Prompt5
2018-11-24	2458446.55	1.80	14.68	0.01	Open	CTIO-Prompt5
2018-11-24	2458446.56	1.81	14.63	0.01	Open	CTIO-Prompt5
2018-11-24	2458446.59	1.84	14.26	0.02	U	LCO LSC 1m
2018-11-24	2458446.59	1.84	14.35	0.02	U	LCO LSC 1m
2018-11-24	2458446.60	1.85	15.17	0.01	B	LCO LSC 1m
2018-11-24	2458446.60	1.85	15.17	0.01	B	LCO LSC 1m
2018-11-24	2458446.60	1.85	14.80	0.01	V	LCO LSC 1m
2018-11-24	2458446.61	1.86	14.88	0.01	V	LCO LSC 1m
2018-11-24	2458446.61	1.86	15.05	0.01	g	LCO LSC 1m
2018-11-24	2458446.61	1.86	14.96	0.01	g	LCO LSC 1m
2018-11-24	2458446.61	1.86	14.68	0.01	r	LCO LSC 1m
2018-11-24	2458446.62	1.87	14.65	0.04	i	LCO LSC 1m
2018-11-24	2458446.62	1.87	14.65	0.04	i	LCO LSC 1m
2018-11-24	2458446.62	1.87	14.68	0.02	r	LCO LSC 1m

Date-Obs	JD	Phase (Day)	Apparent Magnitude (mag)	Apparent Magnitude Error (mag)	Filter	Source
2018-11-24	2458446.64	1.89	14.61	0.01	Open	CTIO-Prompt5
2018-11-24	2458446.84	2.09	<17.83	-1.0	UVM2	Swift
2018-11-24	2458446.85	2.10	17.82	0.31	UVW1	Swift
2018-11-25	2458447.52	2.77	14.60	0.01	Open	CTIO-Prompt5
2018-11-25	2458447.53	2.78	14.60	0.01	Open	CTIO-Prompt5
2018-11-25	2458447.54	2.79	<18.04	-1.0	UVM2	Swift
2018-11-25	2458447.56	2.81	<18.08	-1.0	UVW2	Swift
2018-11-25	2458447.56	2.81	17.70	0.28	UVW1	Swift
2018-11-25	2458447.58	2.83	14.23	0.02	U	LCO LSC 1m
2018-11-25	2458447.58	2.83	14.20	0.03	U	LCO LSC 1m
2018-11-25	2458447.59	2.84	15.00	0.01	V	LCO LSC 1m
2018-11-25	2458447.59	2.84	15.13	0.01	B	LCO LSC 1m
2018-11-25	2458447.59	2.84	15.13	0.01	B	LCO LSC 1m
2018-11-25	2458447.60	2.85	14.76	0.02	r	LCO LSC 1m
2018-11-25	2458447.60	2.85	14.97	0.02	g	LCO LSC 1m
2018-11-25	2458447.60	2.85	14.93	0.02	g	LCO LSC 1m
2018-11-25	2458447.60	2.85	14.72	0.02	V	LCO LSC 1m
2018-11-25	2458447.61	2.86	14.49	0.05	i	LCO LSC 1m
2018-11-25	2458447.61	2.86	14.54	0.04	i	LCO LSC 1m
2018-11-25	2458447.61	2.86	14.73	0.03	r	LCO LSC 1m
2018-11-25	2458447.85	3.10	14.59	0.02	r	ZTF
2018-11-25	2458448.08	3.33	15.19	0.09	B	HCT
2018-11-25	2458448.08	3.33	14.58	0.06	R	HCT
2018-11-25	2458448.08	3.33	14.98	0.07	V	HCT
2018-11-25	2458448.08	3.33	14.30	0.06	I	HCT
2018-11-25	2458448.40	3.65	<17.95	-1.0	UVW2	Swift
2018-11-25	2458448.40	3.65	<18.17	-1.0	UVM2	Swift
2018-11-25	2458448.42	3.67	<17.91	-1.0	UVW1	Swift
2018-11-26	2458448.52	3.77	14.75	0.01	Open	CTIO-Prompt5
2018-11-26	2458448.53	3.78	14.74	0.01	Open	CTIO-Prompt5
2018-11-26	2458448.93	4.18	14.89	0.01	o	ATLAS
2018-11-26	2458449.36	4.61	15.07	0.03	U	LCO CPT 1m
2018-11-26	2458449.36	4.61	15.04	0.02	U	LCO CPT 1m
2018-11-26	2458449.36	4.61	15.68	0.02	B	LCO CPT 1m
2018-11-26	2458449.37	4.62	15.32	0.02	V	LCO CPT 1m
2018-11-26	2458449.37	4.62	15.52	0.02	g	LCO CPT 1m
2018-11-26	2458449.37	4.62	15.81	0.03	B	LCO CPT 1m
2018-11-26	2458449.37	4.62	15.28	0.02	V	LCO CPT 1m
2018-11-26	2458449.38	4.63	15.57	0.02	g	LCO CPT 1m
2018-11-26	2458449.38	4.63	14.71	0.04	i	LCO CPT 1m
2018-11-26	2458449.38	4.63	14.94	0.01	r	LCO CPT 1m
2018-11-26	2458449.38	4.63	14.94	0.02	r	LCO CPT 1m
2018-11-26	2458449.39	4.64	14.72	0.04	i	LCO CPT 1m
2018-11-27	2458449.53	4.78	14.90	0.01	Open	CTIO-Prompt5
2018-11-27	2458449.63	4.88	15.51	0.09	U	LCO LSC 1m

Date-Obs	JD	Phase (Day)	Apparent Magnitude (mag)	Apparent Magnitude Error (mag)	Filter	Source
2018-11-27	2458449.63	4.88	15.37	0.04	U	LCO LSC 1m
2018-11-27	2458449.64	4.89	15.76	0.01	B	LCO LSC 1m
2018-11-27	2458449.64	4.89	15.27	0.01	V	LCO LSC 1m
2018-11-27	2458449.64	4.89	15.25	0.01	V	LCO LSC 1m
2018-11-27	2458449.64	4.89	15.80	0.02	B	LCO LSC 1m
2018-11-27	2458449.65	4.90	15.11	0.04	r	LCO LSC 1m
2018-11-27	2458449.65	4.90	15.05	0.01	r	LCO LSC 1m
2018-11-27	2458449.66	4.91	14.81	0.04	i	LCO LSC 1m
2018-11-27	2458449.66	4.91	14.81	0.04	i	LCO LSC 1m
2018-11-27	2458450.02	5.27	14.76	0.01	Clear	Meckering-Prompt5
2018-11-27	2458450.06	5.31	14.96	0.01	Clear	Meckering-Prompt5
2018-11-27	2458450.14	5.39	14.50	0.09	I	HCT
2018-11-27	2458450.14	5.39	14.89	0.08	R	HCT
2018-11-27	2458450.14	5.39	15.29	0.09	V	HCT
2018-11-27	2458450.14	5.39	15.58	0.1	B	HCT
2018-11-27	2458450.34	5.59	15.28	0.03	U	LCO CPT 1m
2018-11-27	2458450.35	5.60	15.87	0.02	B	LCO CPT 1m
2018-11-27	2458450.35	5.60	15.25	0.03	U	LCO CPT 1m
2018-11-27	2458450.36	5.61	15.17	0.02	V	LCO CPT 1m
2018-11-27	2458450.36	5.61	15.14	0.03	r	LCO CPT 1m
2018-11-27	2458450.36	5.61	15.77	0.02	g	LCO CPT 1m
2018-11-27	2458450.36	5.61	15.62	0.02	g	LCO CPT 1m
2018-11-27	2458450.36	5.61	15.90	0.01	B	LCO CPT 1m
2018-11-27	2458450.36	5.61	15.18	0.02	V	LCO CPT 1m
2018-11-27	2458450.37	5.62	14.84	0.04	i	LCO CPT 1m
2018-11-27	2458450.37	5.62	15.16	0.03	r	LCO CPT 1m
2018-11-27	2458450.37	5.62	14.83	0.04	i	LCO CPT 1m
2018-11-28	2458450.52	5.77	15.03	0.01	Open	CTIO-Prompt5
2018-11-28	2458450.53	5.78	15.07	0.01	Open	CTIO-Prompt5
2018-11-28	2458450.57	5.82	15.89	0.03	U	LCO LSC 1m
2018-11-28	2458450.57	5.82	16.13	0.06	U	LCO LSC 1m
2018-11-28	2458450.58	5.83	15.71	0.02	g	LCO LSC 1m
2018-11-28	2458450.58	5.83	15.51	0.01	V	LCO LSC 1m
2018-11-28	2458450.59	5.84	14.89	0.05	i	LCO LSC 1m
2018-11-28	2458450.59	5.84	14.92	0.05	i	LCO LSC 1m
2018-11-28	2458450.59	5.84	15.13	0.03	r	LCO LSC 1m
2018-11-28	2458450.59	5.84	15.83	0.02	g	LCO LSC 1m
2018-11-28	2458450.73	5.98	15.96	0.29	U	LCO LSC 1m
2018-11-28	2458450.73	5.98	15.62	0.04	U	LCO LSC 1m
2018-11-28	2458450.74	5.99	15.46	0.02	V	LCO LSC 1m
2018-11-28	2458450.74	5.99	15.44	0.01	V	LCO LSC 1m
2018-11-28	2458450.74	5.99	15.97	0.02	B	LCO LSC 1m
2018-11-28	2458450.74	5.99	15.93	0.01	B	LCO LSC 1m
2018-11-28	2458450.74	5.99	15.87	0.02	g	LCO LSC 1m
2018-11-28	2458450.75	6.00	15.94	0.03	g	LCO LSC 1m

Date-Obs	JD	Phase (Day)	Apparent Magnitude (mag)	Apparent Magnitude Error (mag)	Filter	Source
2018-11-28	2458450.75	6.00	15.16	0.02	r	LCO LSC 1m
2018-11-28	2458450.75	6.00	15.13	0.02	r	LCO LSC 1m
2018-11-28	2458450.75	6.00	14.91	0.04	i	LCO LSC 1m
2018-11-28	2458450.75	6.00	14.91	0.04	i	LCO LSC 1m
2018-11-28	2458450.76	6.01	16.28	0.38	B	SLOTIS
2018-11-28	2458450.76	6.01	15.80	0.29	V	SLOTIS
2018-11-28	2458451.02	6.27	15.12	0.01	Clear	Meckering-Prompt5
2018-11-28	2458451.12	6.37	15.12	0.01	Clear	Meckering-Prompt5
2018-11-28	2458451.29	6.54	15.48	0.2	V	ST
2018-11-28	2458451.29	6.54	16.18	0.26	B	ST
2018-11-28	2458451.29	6.54	15.02	0.13	R	ST
2018-11-28	2458451.29	6.54	14.77	0.12	I	ST
2018-11-28	2458451.43	6.68	15.46	0.02	U	LCO CPT 1m
2018-11-28	2458451.43	6.68	15.53	0.02	U	LCO CPT 1m
2018-11-28	2458451.44	6.69	16.07	0.01	B	LCO CPT 1m
2018-11-28	2458451.44	6.69	15.97	0.01	B	LCO CPT 1m
2018-11-28	2458451.44	6.69	15.48	0.01	V	LCO CPT 1m
2018-11-28	2458451.44	6.69	15.52	0.01	V	LCO CPT 1m
2018-11-28	2458451.44	6.69	15.94	0.01	g	LCO CPT 1m
2018-11-28	2458451.45	6.70	15.94	0.01	g	LCO CPT 1m
2018-11-28	2458451.45	6.70	15.17	0.01	r	LCO CPT 1m
2018-11-28	2458451.45	6.70	15.19	0.01	r	LCO CPT 1m
2018-11-28	2458451.45	6.70	14.92	0.04	i	LCO CPT 1m
2018-11-28	2458451.45	6.70	14.91	0.04	i	LCO CPT 1m
2018-11-29	2458451.54	6.79	15.16	0.01	Open	CTIO-Prompt5
2018-11-29	2458451.64	6.89	15.77	0.09	U	LCO LSC 1m
2018-11-29	2458451.65	6.90	16.12	0.03	B	LCO LSC 1m
2018-11-29	2458451.65	6.90	15.86	0.09	U	LCO LSC 1m
2018-11-29	2458451.66	6.91	15.48	0.04	V	LCO LSC 1m
2018-11-29	2458451.67	6.92	14.98	0.05	i	LCO LSC 1m
2018-11-29	2458451.67	6.92	15.19	0.03	r	LCO LSC 1m
2018-11-29	2458451.67	6.92	14.99	0.04	i	LCO LSC 1m
2018-11-29	2458451.70	6.95	15.80	0.07	U	LCO LSC 1m
2018-11-29	2458451.71	6.96	15.28	0.11	V	SLOTIS
2018-11-29	2458451.71	6.96	15.43	0.04	U	LCO LSC 1m
2018-11-29	2458451.71	6.96	16.17	0.04	B	LCO LSC 1m
2018-11-29	2458451.71	6.96	15.02	0.11	R	SLOTIS
2018-11-29	2458451.72	6.97	15.92	0.02	B	LCO LSC 1m
2018-11-29	2458451.72	6.97	15.74	0.01	V	LCO LSC 1m
2018-11-29	2458451.72	6.97	15.83	0.02	g	LCO LSC 1m
2018-11-29	2458451.73	6.98	16.05	0.02	g	LCO LSC 1m
2018-11-29	2458451.73	6.98	14.96	0.04	i	LCO LSC 1m
2018-11-29	2458451.73	6.98	15.25	0.02	r	LCO LSC 1m
2018-11-29	2458452.02	7.27	15.15	0.01	Clear	Meckering-Prompt5
2018-11-29	2458452.12	7.37	14.43	0.26	I	DFOT

Date-Obs	JD	Phase (Day)	Apparent Magnitude (mag)	Apparent Magnitude Error (mag)	Filter	Source
2018-11-29	2458452.12	7.37	14.86	1.44	R	DFOT
2018-11-29	2458452.12	7.37	15.15	0.26	V	DFOT
2018-11-29	2458452.12	7.37	16.83	0.56	B	DFOT
2018-11-29	2458452.15	7.40	15.16	0.01	Clear	Meckering-Prompt5
2018-11-29	2458452.32	7.57	16.57	0.35	B	ST
2018-11-29	2458452.32	7.57	15.51	0.25	V	ST
2018-11-29	2458452.32	7.57	14.72	0.11	I	ST
2018-11-30	2458452.54	7.79	15.16	0.01	Open	CTIO-Prompt5
2018-11-30	2458453.18	8.43	15.24	0.01	Clear	Meckering-Prompt5
2018-11-30	2458453.21	8.46	15.21	0.01	Clear	Meckering-Prompt5
2018-11-30	2458453.21	8.46	15.24	0.01	Clear	Meckering-Prompt5
2018-12-01	2458453.54	8.79	15.18	0.01	Open	CTIO-Prompt5
2018-12-01	2458454.20	9.45	15.18	0.01	Clear	Meckering-Prompt5
2018-12-02	2458454.52	9.77	15.63	0.03	U	LCO LSC 1m
2018-12-02	2458454.53	9.78	15.66	0.03	U	LCO LSC 1m
2018-12-02	2458454.53	9.78	16.18	0.01	B	LCO LSC 1m
2018-12-02	2458454.54	9.79	15.65	0.01	V	LCO LSC 1m
2018-12-02	2458454.54	9.79	16.07	0.01	g	LCO LSC 1m
2018-12-02	2458454.54	9.79	15.19	0.01	Open	CTIO-Prompt5
2018-12-02	2458454.55	9.80	15.01	0.04	i	LCO LSC 1m
2018-12-02	2458454.55	9.80	15.27	0.02	r	LCO LSC 1m
2018-12-02	2458454.70	9.95	16.01	0.04	U	LCO LSC 1m
2018-12-02	2458454.71	9.96	16.18	0.01	B	LCO LSC 1m
2018-12-02	2458454.71	9.96	16.42	0.03	B	LCO LSC 1m
2018-12-02	2458454.71	9.96	15.62	0.01	V	LCO LSC 1m
2018-12-02	2458454.72	9.97	15.96	0.01	g	LCO LSC 1m
2018-12-02	2458454.72	9.97	15.22	0.02	r	LCO LSC 1m
2018-12-02	2458454.73	9.98	15.00	0.04	i	LCO LSC 1m
2018-12-02	2458455.02	10.27	15.14	0.01	Clear	Meckering-Prompt5
2018-12-02	2458455.21	10.46	15.16	0.01	Clear	Meckering-Prompt5
2018-12-03	2458455.54	10.79	15.23	0.01	Open	CTIO-Prompt5
2018-12-03	2458455.62	10.87	15.99	0.03	U	LCO LSC 1m
2018-12-03	2458455.63	10.88	16.21	0.01	B	LCO LSC 1m
2018-12-03	2458455.63	10.88	15.75	0.06	V	LCO LSC 1m
2018-12-03	2458455.64	10.89	15.22	0.02	r	LCO LSC 1m
2018-12-03	2458455.64	10.89	16.26	0.02	g	LCO LSC 1m
2018-12-03	2458455.65	10.90	15.02	0.04	i	LCO LSC 1m
2018-12-03	2458456.17	11.42	16.29	0.2	B	HCT
2018-12-03	2458456.17	11.42	14.81	0.16	I	HCT
2018-12-03	2458456.17	11.42	15.21	0.2	R	HCT
2018-12-03	2458456.17	11.42	15.72	0.17	V	HCT
2018-12-04	2458456.54	11.79	15.20	0.01	Open	CTIO-Prompt5
2018-12-04	2458456.72	11.97	15.09	0.03	r	ZTF
2018-12-04	2458456.73	11.98	15.74	0.18	V	Kuiper
2018-12-04	2458456.73	11.98	15.26	0.13	R	Kuiper

Date-Obs	JD	Phase (Day)	Apparent Magnitude (mag)	Apparent Magnitude Error (mag)	Filter	Source
2018-12-04	2458456.73	11.98	16.27	0.2	B	Kuiper
2018-12-04	2458456.75	12.00	15.12	0.03	r	ZTF
2018-12-04	2458457.02	12.27	15.13	0.01	Clear	Meckering-Prompt5
2018-12-04	2458457.12	12.37	14.63	0.08	I	HCT
2018-12-04	2458457.12	12.37	15.10	0.07	R	HCT
2018-12-04	2458457.12	12.37	15.69	0.12	V	HCT
2018-12-04	2458457.12	12.37	16.27	0.14	B	HCT
2018-12-04	2458457.32	12.57	16.27	0.11	U	LCO CPT 1m
2018-12-04	2458457.32	12.57	16.29	0.03	B	LCO CPT 1m
2018-12-04	2458457.33	12.58	15.87	0.04	V	LCO CPT 1m
2018-12-04	2458457.33	12.58	16.30	0.04	B	LCO CPT 1m
2018-12-04	2458457.33	12.58	15.95	0.06	V	LCO CPT 1m
2018-12-04	2458457.34	12.59	15.31	0.04	r	LCO CPT 1m
2018-12-04	2458457.34	12.59	15.09	0.04	i	LCO CPT 1m
2018-12-04	2458457.34	12.59	16.16	0.03	g	LCO CPT 1m
2018-12-04	2458457.34	12.59	15.00	0.04	i	LCO CPT 1m
2018-12-04	2458457.43	12.68	16.07	0.06	U	LCO CPT 1m
2018-12-04	2458457.44	12.69	16.21	0.1	U	LCO CPT 1m
2018-12-04	2458457.44	12.69	16.26	0.04	B	LCO CPT 1m
2018-12-04	2458457.44	12.69	16.49	0.03	B	LCO CPT 1m
2018-12-04	2458457.45	12.70	16.37	0.04	g	LCO CPT 1m
2018-12-04	2458457.45	12.70	16.33	0.04	g	LCO CPT 1m
2018-12-04	2458457.45	12.70	15.71	0.04	V	LCO CPT 1m
2018-12-04	2458457.45	12.70	15.63	0.05	V	LCO CPT 1m
2018-12-05	2458457.57	12.82	15.26	0.01	Open	CTIO-Prompt5
2018-12-05	2458458.03	13.28	15.17	0.01	Clear	Meckering-Prompt5
2018-12-05	2458458.04	13.29	15.23	0.01	Clear	Meckering-Prompt5
2018-12-05	2458458.43	13.68	16.68	0.09	U	LCO CPT 1m
2018-12-05	2458458.43	13.68	16.52	0.05	U	LCO CPT 1m
2018-12-05	2458458.44	13.69	15.88	0.05	V	LCO CPT 1m
2018-12-05	2458458.44	13.69	15.89	0.08	V	LCO CPT 1m
2018-12-05	2458458.45	13.70	15.01	0.04	i	LCO CPT 1m
2018-12-05	2458458.45	13.70	15.24	0.05	r	LCO CPT 1m
2018-12-06	2458458.54	13.79	15.21	0.01	Open	CTIO-Prompt5
2018-12-06	2458458.66	13.91	15.25	0.01	Open	CTIO-Prompt5
2018-12-06	2458459.02	14.27	15.20	0.01	Clear	Meckering-Prompt5
2018-12-06	2458459.24	14.49	16.13	0.16	B	HCT
2018-12-06	2458459.24	14.49	14.66	0.1	I	HCT
2018-12-06	2458459.24	14.49	15.61	0.14	V	HCT
2018-12-06	2458459.24	14.49	15.07	0.1	R	HCT
2018-12-07	2458460.09	15.34	16.52	0.57	B	HCT
2018-12-07	2458460.09	15.34	14.67	0.11	I	HCT
2018-12-07	2458460.09	15.34	15.98	0.52	V	HCT
2018-12-07	2458460.09	15.34	15.15	0.47	R	HCT
2018-12-08	2458460.61	15.86	15.23	0.01	Open	CTIO-Prompt5

Date-Obs	JD	Phase (Day)	Apparent Magnitude (mag)	Apparent Magnitude Error (mag)	Filter	Source
2018-12-08	2458460.65	15.90	16.47	0.01	B	LCO LSC 1m
2018-12-08	2458460.66	15.91	16.58	0.02	B	LCO LSC 1m
2018-12-08	2458461.01	16.26	15.27	0.01	Clear	Meckering-Prompt5
2018-12-09	2458461.53	16.78	15.26	0.01	Open	CTIO-Prompt5
2018-12-09	2458462.01	17.26	15.22	0.01	Clear	Meckering-Prompt5
2018-12-10	2458462.53	17.78	16.73	0.01	B	LCO LSC 1m
2018-12-10	2458462.53	17.78	16.48	0.06	U	LCO LSC 1m
2018-12-10	2458462.53	17.78	15.27	0.01	Open	CTIO-Prompt5
2018-12-10	2458462.53	17.78	16.48	0.04	U	LCO LSC 1m
2018-12-10	2458462.54	17.79	16.72	0.01	B	LCO LSC 1m
2018-12-10	2458462.54	17.79	15.76	0.01	V	LCO LSC 1m
2018-12-10	2458462.54	17.79	15.74	0.01	V	LCO LSC 1m
2018-12-10	2458462.54	17.79	16.48	0.01	g	LCO LSC 1m
2018-12-10	2458462.55	17.80	15.38	0.01	r	LCO LSC 1m
2018-12-10	2458462.55	17.80	15.28	0.01	r	LCO LSC 1m
2018-12-10	2458462.55	17.80	16.56	0.02	g	LCO LSC 1m
2018-12-10	2458462.55	17.80	15.07	0.04	i	LCO LSC 1m
2018-12-10	2458462.56	17.81	15.07	0.04	i	LCO LSC 1m
2018-12-10	2458462.76	18.01	16.25	0.04	g	ZTF
2018-12-10	2458462.77	18.02	15.18	0.02	r	ZTF
2018-12-10	2458462.91	18.16	<18.06	-1.0	UVM2	Swift
2018-12-10	2458462.91	18.16	<17.96	-1.0	UVW1	Swift
2018-12-10	2458463.01	18.26	15.28	0.01	Clear	Meckering-Prompt5
2018-12-11	2458463.53	18.78	15.25	0.01	Open	CTIO-Prompt5
2018-12-11	2458463.59	18.84	16.79	0.05	U	LCO LSC 1m
2018-12-11	2458463.60	18.85	16.75	0.1	U	LCO LSC 1m
2018-12-11	2458463.60	18.85	16.77	0.01	B	LCO LSC 1m
2018-12-11	2458463.60	18.85	16.84	0.01	B	LCO LSC 1m
2018-12-11	2458463.61	18.86	16.66	0.02	g	LCO LSC 1m
2018-12-11	2458463.61	18.86	16.63	0.02	g	LCO LSC 1m
2018-12-11	2458463.61	18.86	15.96	0.02	V	LCO LSC 1m
2018-12-11	2458463.61	18.86	15.96	0.02	V	LCO LSC 1m
2018-12-11	2458463.62	18.87	15.11	0.04	i	LCO LSC 1m
2018-12-11	2458463.62	18.87	15.11	0.04	i	LCO LSC 1m
2018-12-11	2458463.62	18.87	15.35	0.02	r	LCO LSC 1m
2018-12-11	2458463.62	18.87	15.28	0.02	r	LCO LSC 1m
2018-12-11	2458464.01	19.26	15.34	0.01	Clear	Meckering-Prompt5
2018-12-11	2458464.03	19.28	<17.59	-1.0	UVW1	Swift
2018-12-11	2458464.03	19.28	<18.08	-1.0	UVW2	Swift
2018-12-11	2458464.03	19.28	<18.14	-1.0	UVM2	Swift
2018-12-11	2458464.25	19.50	16.95	0.24	B	HCT
2018-12-11	2458464.25	19.50	15.20	0.11	R	HCT
2018-12-11	2458464.25	19.50	15.84	0.21	V	HCT
2018-12-11	2458464.25	19.50	14.77	0.09	I	HCT
2018-12-12	2458464.53	19.78	15.38	0.01	Open	CTIO-Prompt5

Date-Obs	JD	Phase (Day)	Apparent Magnitude (mag)	Apparent Magnitude Error (mag)	Filter	Source
2018-12-12	2458465.01	20.26	15.41	0.01	Clear	Meckering-Prompt5
2018-12-12	2458465.07	20.32	15.44	0.01	Clear	Meckering-Prompt5
2018-12-13	2458465.53	20.78	15.44	0.01	Open	CTIO-Prompt5
2018-12-13	2458466.01	21.26	15.48	0.01	Clear	Meckering-Prompt5
2018-12-14	2458466.53	21.78	15.68	0.02	Open	CTIO-Prompt5
2018-12-14	2458466.54	21.79	15.53	0.01	Open	CTIO-Prompt5
2018-12-14	2458466.73	21.98	15.40	0.03	r	ZTF
2018-12-14	2458466.78	22.03	16.59	0.1	g	ZTF
2018-12-14	2458467.01	22.26	15.56	0.01	Clear	Meckering-Prompt5
2018-12-14	2458467.16	22.41	15.71	0.65	I	DFOT
2018-12-14	2458467.16	22.41	15.93	0.89	R	DFOT
2018-12-15	2458467.53	22.78	15.65	0.02	Open	CTIO-Prompt5
2018-12-15	2458467.54	22.79	15.62	0.02	Open	CTIO-Prompt5
2018-12-15	2458467.66	22.91	17.32	0.08	U	LCO ELP 1m
2018-12-15	2458467.66	22.91	17.24	0.08	U	LCO ELP 1m
2018-12-15	2458467.67	22.92	17.39	0.02	B	LCO ELP 1m
2018-12-15	2458467.67	22.92	17.40	0.02	B	LCO ELP 1m
2018-12-15	2458467.67	22.92	16.27	0.01	V	LCO ELP 1m
2018-12-15	2458467.68	22.93	15.65	0.01	r	LCO ELP 1m
2018-12-15	2458467.68	22.93	17.17	0.02	g	LCO ELP 1m
2018-12-15	2458467.68	22.93	17.18	0.02	g	LCO ELP 1m
2018-12-15	2458467.68	22.93	16.26	0.01	V	LCO ELP 1m
2018-12-15	2458467.69	22.94	15.42	0.04	i	LCO ELP 1m
2018-12-15	2458467.69	22.94	15.41	0.04	i	LCO ELP 1m
2018-12-15	2458467.69	22.94	15.67	0.01	r	LCO ELP 1m
2018-12-15	2458468.01	23.26	16.25	0.17	V	HCT
2018-12-15	2458468.01	23.26	15.53	0.14	R	HCT
2018-12-15	2458468.01	23.26	15.09	0.08	I	HCT
2018-12-15	2458468.14	23.39	15.54	0.02	Clear	Meckering-Prompt5
2018-12-16	2458468.53	23.78	15.75	0.02	Open	CTIO-Prompt5
2018-12-16	2458469.18	24.43	16.47	0.2	V	HCT
2018-12-16	2458469.18	24.43	15.69	0.14	R	HCT
2018-12-16	2458469.18	24.43	15.24	0.13	I	HCT
2018-12-16	2458469.18	24.43	17.18	0.23	B	HCT
2018-12-17	2458469.53	24.78	15.82	0.02	Open	CTIO-Prompt5
2018-12-20	2458473.37	28.62	17.79	0.04	B	LCO CPT 1m
2018-12-20	2458473.37	28.62	17.70	0.04	B	LCO CPT 1m
2018-12-20	2458473.38	28.63	16.68	0.03	V	LCO CPT 1m
2018-12-20	2458473.38	28.63	16.67	0.03	V	LCO CPT 1m
2018-12-20	2458473.38	28.63	17.41	0.03	g	LCO CPT 1m
2018-12-20	2458473.38	28.63	16.01	0.03	r	LCO CPT 1m
2018-12-20	2458473.38	28.63	17.48	0.03	g	LCO CPT 1m
2018-12-20	2458473.39	28.64	16.05	0.03	r	LCO CPT 1m
2018-12-20	2458473.39	28.64	15.98	0.02	i	LCO CPT 1m
2018-12-20	2458473.39	28.64	16.00	0.02	i	LCO CPT 1m

Date-Obs	JD	Phase (Day)	Apparent Magnitude (mag)	Apparent Magnitude Error (mag)	Filter	Source
2018-12-21	2458473.53	28.78	16.01	0.03	Open	CTIO-Prompt5
2018-12-21	2458474.01	29.26	16.13	0.03	Clear	Meckering-Prompt5
2018-12-22	2458474.53	29.78	16.20	0.03	Open	CTIO-Prompt5
2018-12-22	2458475.01	30.26	16.15	0.03	Clear	Meckering-Prompt5
2018-12-22	2458475.33	30.58	17.20	0.13	U	LCO CPT 1m
2018-12-22	2458475.33	30.58	17.18	0.09	U	LCO CPT 1m
2018-12-22	2458475.34	30.59	17.82	0.04	B	LCO CPT 1m
2018-12-22	2458475.34	30.59	17.81	0.04	B	LCO CPT 1m
2018-12-22	2458475.34	30.59	16.81	0.03	V	LCO CPT 1m
2018-12-22	2458475.34	30.59	17.52	0.03	g	LCO CPT 1m
2018-12-22	2458475.34	30.59	16.77	0.02	V	LCO CPT 1m
2018-12-22	2458475.35	30.60	17.51	0.03	g	LCO CPT 1m
2018-12-22	2458475.35	30.60	16.10	0.02	r	LCO CPT 1m
2018-12-22	2458475.35	30.60	16.10	0.02	r	LCO CPT 1m
2018-12-22	2458475.35	30.60	16.03	0.02	i	LCO CPT 1m
2018-12-22	2458475.36	30.61	16.04	0.02	i	LCO CPT 1m
2018-12-23	2458475.53	30.78	16.21	0.03	Open	CTIO-Prompt5
2018-12-23	2458476.02	31.27	16.15	0.02	Clear	Meckering-Prompt5
2018-12-24	2458476.53	31.78	16.16	0.02	Open	CTIO-Prompt5
2018-12-24	2458477.02	32.27	16.30	0.03	Clear	Meckering-Prompt5
2018-12-24	2458477.09	32.34	16.24	0.02	Clear	Meckering-Prompt5
2018-12-24	2458477.34	32.59	17.19	0.06	U	LCO CPT 1m
2018-12-24	2458477.34	32.59	17.66	0.15	U	LCO CPT 1m
2018-12-24	2458477.35	32.60	17.68	0.04	B	LCO CPT 1m
2018-12-24	2458477.35	32.60	16.83	0.02	V	LCO CPT 1m
2018-12-24	2458477.35	32.60	17.69	0.04	B	LCO CPT 1m
2018-12-24	2458477.36	32.61	16.84	0.02	V	LCO CPT 1m
2018-12-24	2458477.36	32.61	16.09	0.03	r	LCO CPT 1m
2018-12-24	2458477.37	32.62	16.18	0.03	r	LCO CPT 1m
2018-12-24	2458477.37	32.62	16.08	0.04	i	LCO CPT 1m
2018-12-24	2458477.37	32.62	16.07	0.04	i	LCO CPT 1m
2018-12-25	2458477.53	32.78	16.18	0.02	Open	CTIO-Prompt5
2018-12-25	2458477.64	32.89	16.24	0.02	Open	CTIO-Prompt5
2018-12-25	2458477.73	32.98	17.91	0.18	U	LCO ELP 1m
2018-12-25	2458477.73	32.98	17.69	0.3	U	LCO ELP 1m
2018-12-25	2458477.74	32.99	17.80	0.04	B	LCO ELP 1m
2018-12-25	2458477.74	32.99	17.79	0.04	B	LCO ELP 1m
2018-12-25	2458477.74	32.99	16.95	0.03	V	LCO ELP 1m
2018-12-25	2458477.75	33.00	17.67	0.03	g	LCO ELP 1m
2018-12-25	2458477.75	33.00	17.67	0.03	g	LCO ELP 1m
2018-12-25	2458477.75	33.00	16.19	0.03	r	LCO ELP 1m
2018-12-25	2458477.75	33.00	16.16	0.03	r	LCO ELP 1m
2018-12-25	2458477.76	33.01	16.09	0.04	i	LCO ELP 1m
2018-12-25	2458477.76	33.01	16.12	0.04	i	LCO ELP 1m
2018-12-25	2458478.01	33.26	16.25	0.02	Clear	Meckering-Prompt5

Date-Obs	JD	Phase (Day)	Apparent Magnitude (mag)	Apparent Magnitude Error (mag)	Filter	Source
2018-12-26	2458478.53	33.78	16.20	0.02	Open	CTIO-Prompt5
2018-12-27	2458479.53	34.78	16.27	0.02	Open	CTIO-Prompt5
2018-12-27	2458479.59	34.84	17.98	0.03	B	LCO LSC 1m
2018-12-27	2458479.60	34.85	17.68	0.04	g	LCO LSC 1m
2018-12-27	2458479.60	34.85	17.12	0.03	V	LCO LSC 1m
2018-12-27	2458479.60	34.85	18.01	0.03	B	LCO LSC 1m
2018-12-27	2458479.60	34.85	17.11	0.03	V	LCO LSC 1m
2018-12-27	2458479.61	34.86	16.22	0.04	i	LCO LSC 1m
2018-12-27	2458479.61	34.86	16.23	0.04	r	LCO LSC 1m
2018-12-27	2458479.61	34.86	17.66	0.03	g	LCO LSC 1m
2018-12-27	2458479.61	34.86	16.24	0.04	r	LCO LSC 1m
2018-12-27	2458479.62	34.87	16.22	0.04	i	LCO LSC 1m
2018-12-27	2458480.02	35.27	16.25	0.02	Clear	Meckering-Prompt5
2018-12-28	2458480.53	35.78	16.22	0.03	Open	CTIO-Prompt5
2018-12-28	2458480.64	35.89	18.35	0.25	U	LCO ELP 1m
2018-12-28	2458480.65	35.90	17.83	0.17	U	LCO ELP 1m
2018-12-28	2458480.65	35.90	17.96	0.03	B	LCO ELP 1m
2018-12-28	2458480.65	35.90	17.93	0.03	B	LCO ELP 1m
2018-12-28	2458480.66	35.91	17.75	0.02	g	LCO ELP 1m
2018-12-28	2458480.66	35.91	17.05	0.04	V	LCO ELP 1m
2018-12-28	2458480.66	35.91	17.03	0.03	V	LCO ELP 1m
2018-12-28	2458480.67	35.92	16.31	0.03	r	LCO ELP 1m
2018-12-28	2458480.67	35.92	16.25	0.02	r	LCO ELP 1m
2018-12-28	2458480.67	35.92	16.23	0.04	i	LCO ELP 1m
2018-12-28	2458480.67	35.92	16.23	0.04	i	LCO ELP 1m
2018-12-28	2458481.02	36.27	16.29	0.02	Clear	Meckering-Prompt5
2018-12-28	2458481.25	36.50	16.77	0.06	V	ST
2018-12-28	2458481.25	36.50	15.97	0.06	R	ST
2018-12-29	2458481.53	36.78	16.29	0.03	Open	CTIO-Prompt5
2018-12-29	2458481.55	36.80	18.17	0.24	U	LCO LSC 1m
2018-12-29	2458481.56	36.81	17.88	0.02	B	LCO LSC 1m
2018-12-29	2458481.56	36.81	17.86	0.02	B	LCO LSC 1m
2018-12-29	2458481.56	36.81	17.84	0.46	U	LCO LSC 1m
2018-12-29	2458481.57	36.82	17.65	0.04	g	LCO LSC 1m
2018-12-29	2458481.57	36.82	17.06	0.02	V	LCO LSC 1m
2018-12-29	2458481.57	36.82	17.05	0.02	V	LCO LSC 1m
2018-12-29	2458481.57	36.82	17.67	0.03	g	LCO LSC 1m
2018-12-29	2458481.58	36.83	16.27	0.02	r	LCO LSC 1m
2018-12-29	2458481.58	36.83	16.26	0.02	r	LCO LSC 1m
2018-12-29	2458481.58	36.83	16.28	0.05	i	LCO LSC 1m
2018-12-29	2458481.58	36.83	16.28	0.05	i	LCO LSC 1m
2018-12-29	2458482.02	37.27	16.26	0.02	Clear	Meckering-Prompt5
2018-12-30	2458482.53	37.78	16.44	0.02	Open	CTIO-Prompt5
2018-12-30	2458482.60	37.85	16.12	0.02	Open	CTIO-Prompt5
2018-12-30	2458483.02	38.27	16.31	0.03	Clear	Meckering-Prompt5

Date-Obs	JD	Phase (Day)	Apparent Magnitude (mag)	Apparent Magnitude Error (mag)	Filter	Source
2018-12-31	2458483.54	38.79	16.32	0.03	Open	CTIO-Prompt5
2018-12-31	2458484.02	39.27	16.51	0.02	Clear	Meckering-Prompt5
2018-12-31	2458484.06	39.31	16.36	0.02	Clear	Meckering-Prompt5
2019-01-01	2458484.54	39.79	16.40	0.03	Open	CTIO-Prompt5
2019-01-01	2458485.02	40.27	16.39	0.02	Clear	Meckering-Prompt5
2019-01-02	2458485.54	40.79	16.30	0.03	Open	CTIO-Prompt5
2019-01-02	2458486.02	41.27	16.40	0.03	Clear	Meckering-Prompt5
2019-01-03	2458486.56	41.81	16.50	0.03	Open	CTIO-Prompt5
2019-01-03	2458487.02	42.27	16.58	0.03	Clear	Meckering-Prompt5
2019-01-03	2458487.13	42.38	17.74	1.56	B	ST
2019-01-03	2458487.13	42.38	15.86	0.86	R	ST
2019-01-03	2458487.13	42.38	17.09	1.29	V	ST
2019-01-03	2458487.31	42.56	18.22	0.1	B	LCO CPT 1m
2019-01-03	2458487.31	42.56	18.08	0.03	B	LCO CPT 1m
2019-01-03	2458487.32	42.57	17.09	0.04	V	LCO CPT 1m
2019-01-03	2458487.32	42.57	17.08	0.03	V	LCO CPT 1m
2019-01-03	2458487.32	42.57	17.81	0.03	g	LCO CPT 1m
2019-01-03	2458487.32	42.57	17.76	0.03	g	LCO CPT 1m
2019-01-03	2458487.33	42.58	16.56	0.02	r	LCO CPT 1m
2019-01-03	2458487.33	42.58	16.50	0.02	r	LCO CPT 1m
2019-01-03	2458487.33	42.58	16.52	0.04	i	LCO CPT 1m
2019-01-03	2458487.33	42.58	16.53	0.04	i	LCO CPT 1m
2019-01-04	2458487.54	42.79	16.39	0.03	Open	CTIO-Prompt5
2019-01-04	2458488.02	43.27	16.56	0.05	Clear	Meckering-Prompt5
2019-01-05	2458488.54	43.79	16.46	0.03	Open	CTIO-Prompt5
2019-01-05	2458489.04	44.29	16.73	0.03	Clear	Meckering-Prompt5
2019-01-06	2458489.54	44.79	16.67	0.04	Open	CTIO-Prompt5
2019-01-06	2458490.02	45.27	16.81	0.03	Clear	Meckering-Prompt5
2019-01-07	2458490.54	45.79	16.65	0.03	Open	CTIO-Prompt5
2019-01-07	2458490.95	46.20	18.42	0.1	B	LCO COJ 1m
2019-01-07	2458490.95	46.20	18.33	0.04	B	LCO COJ 1m
2019-01-07	2458490.96	46.21	17.42	0.04	V	LCO COJ 1m
2019-01-07	2458490.96	46.21	17.99	0.02	g	LCO COJ 1m
2019-01-07	2458490.96	46.21	17.43	0.03	V	LCO COJ 1m
2019-01-07	2458490.97	46.22	16.61	0.05	i	LCO COJ 1m
2019-01-07	2458490.97	46.22	16.68	0.05	i	LCO COJ 1m
2019-01-07	2458490.97	46.22	16.61	0.02	r	LCO COJ 1m
2019-01-07	2458490.97	46.22	16.58	0.02	r	LCO COJ 1m
2019-01-07	2458490.97	46.22	17.97	0.02	g	LCO COJ 1m
2019-01-07	2458491.02	46.27	16.78	0.05	Clear	Meckering-Prompt5
2019-01-08	2458491.54	46.79	16.68	0.04	Open	CTIO-Prompt5
2019-01-09	2458492.54	47.79	16.77	0.05	Open	CTIO-Prompt5
2019-01-09	2458493.02	48.27	16.75	0.03	Clear	Meckering-Prompt5
2019-01-10	2458493.54	48.79	16.80	0.05	Open	CTIO-Prompt5
2019-01-10	2458494.04	49.29	16.74	0.03	Clear	Meckering-Prompt5

Date-Obs	JD	Phase (Day)	Apparent Magnitude (mag)	Apparent Magnitude Error (mag)	Filter	Source
2019-01-11	2458494.54	49.79	17.02	0.05	Open	CTIO-Prompt5
2019-01-11	2458495.02	50.27	16.67	0.04	Clear	Meckering-Prompt5
2019-01-12	2458495.54	50.79	16.77	0.05	Open	CTIO-Prompt5
2019-01-12	2458495.59	50.84	18.83	0.05	B	LCO LSC 1m
2019-01-12	2458495.59	50.84	17.69	0.04	V	LCO LSC 1m
2019-01-12	2458495.59	50.84	18.76	0.06	B	LCO LSC 1m
2019-01-12	2458495.60	50.85	17.69	0.06	V	LCO LSC 1m
2019-01-12	2458495.60	50.85	18.44	0.05	g	LCO LSC 1m
2019-01-12	2458495.60	50.85	18.36	0.05	g	LCO LSC 1m
2019-01-12	2458495.61	50.86	16.91	0.03	r	LCO LSC 1m
2019-01-12	2458495.61	50.86	16.95	0.05	i	LCO LSC 1m
2019-01-12	2458495.61	50.86	16.91	0.04	r	LCO LSC 1m
2019-01-12	2458495.61	50.86	16.96	0.04	i	LCO LSC 1m
2019-01-12	2458496.05	51.30	17.08	0.04	Clear	Meckering-Prompt5
2019-01-13	2458496.54	51.79	16.85	0.05	Open	CTIO-Prompt5
2019-01-13	2458497.02	52.27	16.76	0.04	Clear	Meckering-Prompt5
2019-01-17	2458500.57	55.82	18.79	0.06	B	LCO LSC 1m
2019-01-17	2458500.58	55.83	18.77	0.06	B	LCO LSC 1m
2019-01-17	2458500.58	55.83	17.87	0.05	V	LCO LSC 1m
2019-01-17	2458500.58	55.83	17.97	0.05	V	LCO LSC 1m
2019-01-17	2458500.59	55.84	17.04	0.06	r	LCO LSC 1m
2019-01-17	2458500.59	55.84	18.51	0.04	g	LCO LSC 1m
2019-01-17	2458500.59	55.84	18.50	0.04	g	LCO LSC 1m
2019-01-17	2458500.60	55.85	17.12	0.06	r	LCO LSC 1m
2019-01-17	2458500.60	55.85	17.21	0.05	i	LCO LSC 1m
2019-01-17	2458500.60	55.85	17.17	0.05	i	LCO LSC 1m
2019-01-17	2458500.65	55.90	17.23	0.07	Open	CTIO-Prompt5
2019-01-17	2458501.02	56.27	17.12	0.06	Clear	Meckering-Prompt5
2019-01-18	2458501.53	56.78	17.20	0.06	Open	CTIO-Prompt5
2019-01-18	2458502.02	57.27	17.56	0.07	Clear	Meckering-Prompt5
2019-01-19	2458502.54	57.79	16.92	0.05	Open	CTIO-Prompt5
2019-01-19	2458503.03	58.28	17.41	0.07	Clear	Meckering-Prompt5
2019-01-20	2458503.53	58.78	16.93	0.06	Open	CTIO-Prompt5
2019-01-21	2458504.66	59.91	19.22	0.12	B	LCO ELP 1m
2019-01-21	2458504.66	59.91	19.28	0.11	B	LCO ELP 1m
2019-01-21	2458504.67	59.92	18.13	0.06	V	LCO ELP 1m
2019-01-21	2458504.67	59.92	18.23	0.06	V	LCO ELP 1m
2019-01-21	2458504.68	59.93	18.56	0.06	g	LCO ELP 1m
2019-01-21	2458504.68	59.93	17.09	0.03	r	LCO ELP 1m
2019-01-21	2458504.68	59.93	17.04	0.04	r	LCO ELP 1m
2019-01-21	2458504.68	59.93	17.27	0.05	i	LCO ELP 1m
2019-01-21	2458504.69	59.94	17.24	0.05	i	LCO ELP 1m
2019-01-22	2458505.54	60.79	16.98	0.05	Open	CTIO-Prompt5
2019-01-23	2458506.56	61.81	17.43	0.05	Open	CTIO-Prompt5
2019-01-24	2458507.54	62.79	17.16	0.05	Open	CTIO-Prompt5

Date-Obs	JD	Phase (Day)	Apparent Magnitude (mag)	Apparent Magnitude Error (mag)	Filter	Source
2019-01-24	2458508.02	63.27	17.47	0.06	Clear	Meckering-Prompt5
2019-01-25	2458508.54	63.79	17.13	0.05	Open	CTIO-Prompt5
2019-01-25	2458509.02	64.27	17.36	0.05	Clear	Meckering-Prompt5
2019-07-01	2458665.65	220.90	20.33	0.01	F555W	HST
2019-07-01	2458665.65	220.90	19.03	0.01	F814W	HST

APPENDIX B

Supplementary Materials for ASASSN-15oz Analysis

B.1. Line Identification and Fitting Details

For lines that are blended (but still showed partially isolated absorption troughs) we define the continuum as a straight line from the lowest side of the feature. After dividing by the continuum, we then simultaneously fit multiple 1D Gaussian profiles to the continuum normalized spectra. For blended features originating in the same part of the ejecta, we require that each component has the same width. We define the velocity of a feature as the minimum (mean) of the individual Gaussian profiles corresponding to that ion and the error as the standard deviation of the fit, representing the range of velocities present in the photosphere. An example of the multiple components and the combined fit is shown in the left panel of Figure B.1. For the Ca II NIR triplet we use the additional constraint of a fixed offset between the minima of the features.

Table B.1 The best parameters for the SYN++ fit. The Sobolev optical depth τ is modeled with an exponential profile with e-folding length, aux, minimum velocity, v_{min}, and maximum velocity, v_{max}. The temperature column is the Boltzmann excitation temperature. SYN++ models pure resonance scattering which is a poor approximation for the H α. For this reason we use the H β line to determine the hydrogen contribution to the fit. A separate fit is performed for H α and is listed separately in the table. We emphasize that this fit is used for line identification and not to derive ejecta properties.

Ion	log(τ)	v_{min}(kkm s^{-1})	v_{max}(kkm/s)	aux	Temperature (kK)
H I -α	0.06	0.1	40.0	2.0	10.0
H I - β	1.1	0.1	40.0	2.0	10.0
Na II	-0.5	0.1	40.0	1.0	10.0
O I	-0.8	0.1	40.0	1.0	10.0
Ca II	1.3	0.1	40.0	2.0	10.0
Sc II	0.1	0.1	40.0	1.0	10.0
Ti II	0.3	0.1	40.0	1.0	10.0
Fe I	0.3	0.1	40.0	1.0	10.0
Fe II	0.3	0.1	40.0	1.0	7.0
Ba I	0.0	0.1	40.0	1.0	10.0

For unblended lines, we perform the following steps to find the minimum and the standard deviation (following Silverman et al. 2012). We eliminate large noise spikes (e.g. from cosmic rays) using a Savitzky-Golay smoothing filter [Savitzky and Golay, 1964] with a quadratic function over a binsize of five pixels. For each line, a minimum and maximum wavelength is defined as well as a slope to account for the shifting of the feature over time as the ejecta slows. A slope is then fit to small bins over this wavelength range, starting with a binsize of five pixels and increasing until exactly three changes in slope are found (at either edge of the line and the line center). If the binsize reaches 40 percent of the feature size, no further attempt at fitting is made. The feature edges are confirmed by fitting a quadratic function to the region centered on each edge identified by the slope change with a width of 20 pixels for the FLOYDS spectra and five pixels for the EFOSC2 spectra. The edge is considered successfully found if the quadratic fit is concave down. The continuum is defined by a line though these end points. Finally, the velocity is found by fitting a cubic spline to the continuum subtracted flux between the edges using the flux errors as weights. An example of a feature with the continuum and spline fit is shown in the right panel of Figure B.1.

We use both methods to fit Na I (λ 5898) and H β (λ4861). For Na I, we find the spline fit does not characterize the minimum of the profile well and instead use the Gaussian minimum. The H β profile is contaminated by another feature (possibly Ti II) at later times, offsetting the minimum found using the spline fit. For this reason we prefer the Gaussian fit for H β as well. A comparison of the results of both fits for H β at early times finds them in good agreement, giving us confidence in the consistency of the two methods.

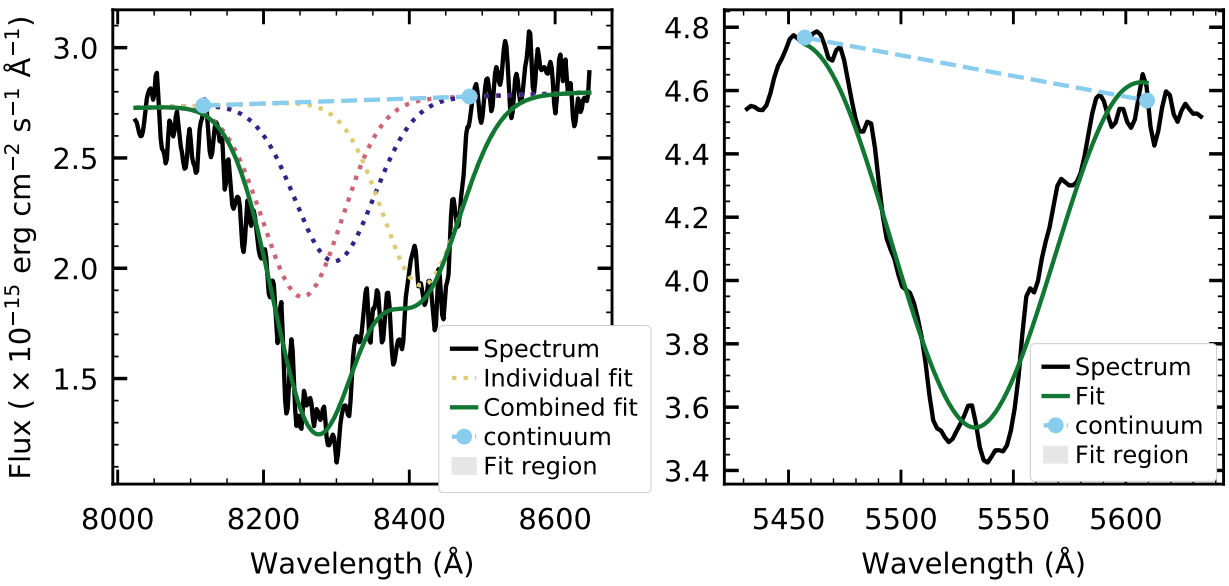

Figure B.1 An example of a fit to the multi-component Ca II NIR triplet (left) using multiple Gaussians and a single line fit (following Silverman et al. 2012, right) to the Sc II (λ5662) line. The observed spectrum is plotted in black. The continuum edges are marked with a cyan circle and the cyan dashed line connecting these points is used as the continuum. The Ca II NIR triplet fit is found by simultaneously fitting three Gaussians with the same standard deviation and mean offsets corresponding to the expected wavelength separation of the triplet. The individual Gaussians are plotting at as dotted lines and the combined fit is plotted as a solid green line. The minima of the individual Gaussians is used to find the velocity of each component. The Sc II feature is fit with a cubic spline. The minimum of the spline is used to find the Sc II velocity.

B.2. Tables of Observations

Table B.2 Spectroscopic Observations of ASASSN-15oz.

Date	JD	Phase (Day)	Observatory	Instrument
2015-09-04	2457270.0	8.0	LCO	FLOYDS
2015-09-05	2457270.7	8.7	Swift	UVOTA
2015-09-05	2457271.1	9.1	Swift	UVOTA
2015-09-05	2457270.6	8.6	NTT	SOFI
2015-09-06	2457272.0	10.0	LCO	FLOYDS
2015-09-07	2457273.0	11.0	LCO	FLOYDS
2015-09-10	2457275.7	13.7	Swift	UVOTA
2015-09-10	2457275.7	13.7	Swift	UVOTA
2015-09-11	2457277.0	15.0	LCO	FLOYDS
2015-09-11	2457276.9	14.9	Swift	UVOTA
2015-09-16	2457282.0	20.0	LCO	FLOYDS
2015-09-20	2457286.1	24.1	LCO	FLOYDS
2015-09-21	2457287.5	25.5	VLT	X-SHOOTER
2015-09-24	2457290.0	28.0	LCO	FLOYDS
2015-09-30	2457296.0	34.0	LCO	FLOYDS
2015-10-04	2457299.5	37.5	NTT	EFOSC
2015-10-05	2457300.5	38.5	NTT	SOFI
2015-10-06	2457301.9	39.9	LCO	FLOYDS
2015-10-10	2457305.7	43.7	IRTF	SpeX
2015-10-14	2457310.0	48.0	LCO	FLOYDS
2015-10-25	2457320.9	58.9	LCO	FLOYDS
2015-11-07	2457333.9	71.9	LCO	FLOYDS
2015-11-08	2457334.5	72.5	NTT	EFOSC
2015-11-19	2457345.5	83.5	NTT	EFOSC
2016-04-11	2457489.9	227.9	NTT	EFOSC
2016-04-11	2457489.9	227.9	NTT	EFOSC
2016-06-09	2457548.8	286.8	Gemini-S	GMOS
2016-06-10	2457549.7	287.7	Gemini-S	GMOS
2016-06-12	2457551.7	289.7	Gemini-S	GMOS
2016-08-03	2457603.7	341.7	NTT	EFOSC
2016-09-11*	2457642.6	380.6	NTT	EFOSC
2016-09-11*	2457642.6	380.6	NTT	EFOSC
2016-09-19	2457650.5	388.5	NTT	EFOSC
2017-09-20+	2458016.9	754.9	Swift	UVOTA

*No signal in data due to cloud cover

+ Template observation

TABLE B.3. Complete table of photometric observations of ASASSN-15oz. Photometric measurements in Landolt and Swift filters are given in Vega magnitudes while measurements in Sloan filters are given in AB magnitudes.

Date-Obs	JD	Phase (day)	Apparent Magnitude (mag)	Apparent Magnitude Error (mag)	Filter	Source
2015-09-04	2457269.68	7.68	14.6411	0.0175	B	LSC 1m
2015-09-04	2457269.68	7.68	14.6553	0.0176	B	LSC 1m
2015-09-04	2457269.69	7.69	14.3659	0.0174	V	LSC 1m
2015-09-04	2457269.69	7.69	14.425	0.0082	g	LSC 1m
2015-09-04	2457269.69	7.69	14.4249	0.0082	g	LSC 1m
2015-09-04	2457269.70	7.70	14.4914	0.0082	r	LSC 1m
2015-09-04	2457269.70	7.70	14.4529	0.0096	r	LSC 1m
2015-09-04	2457269.70	7.70	14.5113	0.0096	i	LSC 1m
2015-09-04	2457269.70	7.70	14.4716	0.0104	i	LSC 1m
2015-09-04	2457269.93	7.93	14.3038	0.0610591	uvw1	Swift
2015-09-04	2457269.93	7.93	14.0975	0.0544158	u	Swift
2015-09-04	2457269.93	7.93	14.7341	0.048288	b	Swift
2015-09-04	2457269.93	7.93	15.2638	0.074869	uvw2	Swift
2015-09-04	2457269.93	7.93	14.6812	0.0503335	v	Swift
2015-09-04	2457269.94	7.94	14.9059	0.0595927	uvm2	Swift
2015-09-04	2457270.09	8.09	14.5994	0.019	B	COJ 1m
2015-09-04	2457270.09	8.09	14.6363	0.0205	B	COJ 1m
2015-09-04	2457270.09	8.09	14.4606	0.0201	V	COJ 1m
2015-09-04	2457270.09	8.09	14.4612	0.0187	V	COJ 1m
2015-09-04	2457270.10	8.10	14.497	0.013	g	COJ 1m
2015-09-04	2457270.10	8.10	14.512	0.013	g	COJ 1m
2015-09-04	2457270.10	8.10	14.4388	0.0161	r	COJ 1m
2015-09-04	2457270.10	8.10	14.457	0.0096	r	COJ 1m
2015-09-04	2457270.10	8.10	14.4693	0.0124	i	COJ 1m
2015-09-04	2457270.11	8.11	14.466	0.0142	i	COJ 1m
2015-09-04	2457270.20	8.20	14.033	0.016	H	NTT

Date-Obs	JD	Phase (Day)	Apparent Magnitude (mag)	Apparent Magnitude Error (mag)	Filter	Source
2015-09-04	2457270.20	8.20	14.199	0.016	J	NTT
2015-09-04	2457270.20	8.20	13.883	0.017	K	NTT
2015-09-04	2457270.44	8.44	14.7131	0.0183	B	CPT 1m
2015-09-04	2457270.44	8.44	14.7129	0.0178	B	CPT 1m
2015-09-04	2457270.44	8.44	14.6226	0.0221	V	CPT 1m
2015-09-04	2457270.45	8.45	14.5121	0.0086	g	CPT 1m
2015-09-04	2457270.45	8.45	14.5443	0.0074	g	CPT 1m
2015-09-04	2457270.45	8.45	14.4967	0.0141	r	CPT 1m
2015-09-04	2457270.45	8.45	14.5153	0.0132	r	CPT 1m
2015-09-04	2457270.46	8.46	14.574	0.0157	i	CPT 1m
2015-09-04	2457270.46	8.46	14.6009	0.0195	B	CPT 1m
2015-09-04	2457270.47	8.47	14.5929	0.0192	B	CPT 1m
2015-09-05	2457270.68	8.68	14.7252	0.0179	B	LSC 1m
2015-09-05	2457270.68	8.68	14.7329	0.0182	B	LSC 1m
2015-09-05	2457270.69	8.69	14.4789	0.0177	V	LSC 1m
2015-09-05	2457270.69	8.69	14.5227	0.0088	g	LSC 1m
2015-09-05	2457270.70	8.70	14.4771	0.0101	r	LSC 1m
2015-09-05	2457270.70	8.70	14.4028	0.023	i	LSC 1m
2015-09-05	2457270.80	8.80	14.4123	0.0574254	uvw1	Swift
2015-09-05	2457270.82	8.82	15.2087	0.0806112	uvw2	Swift
2015-09-05	2457271.10	9.10	14.0899	0.1222	U	COJ 1m
2015-09-05	2457271.10	9.10	14.1519	0.1248	U	COJ 1m
2015-09-05	2457271.10	9.10	14.7151	0.0179	B	COJ 1m
2015-09-05	2457271.11	9.11	14.715	0.0182	B	COJ 1m
2015-09-05	2457271.11	9.11	14.5307	0.0183	V	COJ 1m
2015-09-05	2457271.11	9.11	14.5256	0.0183	V	COJ 1m
2015-09-05	2457271.11	9.11	14.4816	0.008	g	COJ 1m
2015-09-05	2457271.11	9.11	14.4754	0.0088	g	COJ 1m
2015-09-05	2457271.12	9.12	14.4523	0.0068	r	COJ 1m

Date-Obs	JD	Phase (Day)	Apparent Magnitude (mag)	Apparent Magnitude Error (mag)	Filter	Source
2015-09-05	2457271.12	9.12	14.4608	0.0079	r	COJ 1m
2015-09-05	2457271.12	9.12	15.2688	0.0756037	uvw2	Swift
2015-09-05	2457271.12	9.12	14.4994	0.0092	i	COJ 1m
2015-09-05	2457271.12	9.12	14.5392	0.0092	i	COJ 1m
2015-09-05	2457271.13	9.13	14.5207	0.0575286	uvw1	Swift
2015-09-05	2457271.45	9.45	13.9904	0.1758	U	CPT 1m
2015-09-05	2457271.45	9.45	14.147	0.0908	U	CPT 1m
2015-09-05	2457271.46	9.46	14.6927	0.0175	B	CPT 1m
2015-09-05	2457271.46	9.46	14.7138	0.0177	B	CPT 1m
2015-09-05	2457271.46	9.46	14.5085	0.0184	V	CPT 1m
2015-09-05	2457271.46	9.46	14.5195	0.0181	V	CPT 1m
2015-09-05	2457271.46	9.46	14.4962	0.0052	g	CPT 1m
2015-09-05	2457271.47	9.47	14.4868	0.0053	g	CPT 1m
2015-09-05	2457271.47	9.47	14.4208	0.0071	r	CPT 1m
2015-09-05	2457271.47	9.47	14.4337	0.0065	r	CPT 1m
2015-09-05	2457271.47	9.47	14.4526	0.0085	i	CPT 1m
2015-09-05	2457271.47	9.47	14.4714	0.0085	i	CPT 1m
2015-09-06	2457272.45	10.45	14.1467	0.1492	U	CPT 1m
2015-09-06	2457272.46	10.46	14.7158	0.0182	B	CPT 1m
2015-09-06	2457272.46	10.46	14.4953	0.0191	V	CPT 1m
2015-09-06	2457272.46	10.46	14.5095	0.0191	V	CPT 1m
2015-09-06	2457272.46	10.46	14.5105	0.0077	g	CPT 1m
2015-09-06	2457272.46	10.46	14.5089	0.0073	g	CPT 1m
2015-09-06	2457272.47	10.47	14.433	0.0069	r	CPT 1m
2015-09-06	2457272.47	10.47	14.4367	0.0068	r	CPT 1m
2015-09-06	2457272.47	10.47	14.5099	0.0092	i	CPT 1m
2015-09-07	2457273.09	11.09	14.7443	0.0134	B	COJ 1m
2015-09-07	2457273.09	11.09	14.7265	0.0133	B	COJ 1m
2015-09-07	2457273.09	11.09	14.519	0.0131	V	COJ 1m

Date-Obs	JD	Phase (Day)	Apparent Magnitude (mag)	Apparent Magnitude Error (mag)	Filter	Source
2015-09-07	2457273.10	11.10	14.4852	0.0126	V	COJ 1m
2015-09-07	2457273.10	11.10	14.501	0.0064	g	COJ 1m
2015-09-07	2457273.10	11.10	14.4756	0.0062	g	COJ 1m
2015-09-07	2457273.10	11.10	14.4458	0.0076	r	COJ 1m
2015-09-07	2457273.11	11.11	14.4439	0.009	i	COJ 1m
2015-09-07	2457273.11	11.11	14.463	0.009	i	COJ 1m
2015-09-08	2457274.43	12.43	14.513	0.0195	V	CPT 1m
2015-09-08	2457274.43	12.43	14.2065	0.0194	R	CPT 1m
2015-09-08	2457274.45	12.45	14.6746	0.0225	B	CPT 1m
2015-09-08	2457274.46	12.46	14.8226	0.0481	B	CPT 1m
2015-09-08	2457274.46	12.46	14.4539	0.0184	V	CPT 1m
2015-09-08	2457274.46	12.46	14.5327	0.0166	V	CPT 1m
2015-09-08	2457274.46	12.46	14.5717	0.008	g	CPT 1m
2015-09-08	2457274.46	12.46	14.5864	0.0089	g	CPT 1m
2015-09-08	2457274.47	12.47	14.4244	0.0094	r	CPT 1m
2015-09-08	2457274.47	12.47	14.4272	0.0088	r	CPT 1m
2015-09-08	2457274.47	12.47	14.4779	0.0101	i	CPT 1m
2015-09-08	2457274.47	12.47	14.4988	0.011	i	CPT 1m
2015-09-09	2457275.33	13.33	15.216	0.0753036	uvw1	Swift
2015-09-09	2457275.34	13.34	14.377	0.0636841	u	Swift
2015-09-09	2457275.34	13.34	14.9265	0.0579694	b	Swift
2015-09-09	2457275.34	13.34	16.132	0.0938217	uvw2	Swift
2015-09-09	2457275.34	13.34	14.6185	0.0671895	v	Swift
2015-09-09	2457275.34	13.34	16.0505	0.0821147	uvm2	Swift
2015-09-10	2457275.74	13.74	16.5027	0.118201	uvw2	Swift
2015-09-10	2457275.89	13.89	15.4385	0.0627936	uvw1	Swift
2015-09-10	2457275.96	13.96	15.4213	0.0598351	uvw1	Swift
2015-09-10	2457275.97	13.97	16.298	0.0858327	uvw2	Swift
2015-09-10	2457276.06	14.06	14.517	0.2662	U	COJ 1m

Date-Obs	JD	Phase (Day)	Apparent Magnitude (mag)	Apparent Magnitude Error (mag)	Filter	Source
2015-09-10	2457276.07	14.07	14.8337	0.0178	B	COJ 1m
2015-09-10	2457276.08	14.08	14.5227	0.0175	V	COJ 1m
2015-09-10	2457276.08	14.08	14.5121	0.0175	V	COJ 1m
2015-09-10	2457276.08	14.08	14.5534	0.0068	g	COJ 1m
2015-09-10	2457276.08	14.08	14.562	0.0068	g	COJ 1m
2015-09-10	2457276.08	14.08	14.4049	0.0072	r	COJ 1m
2015-09-10	2457276.09	14.09	14.3514	0.0068	r	COJ 1m
2015-09-10	2457276.09	14.09	14.3848	0.0084	i	COJ 1m
2015-09-10	2457276.09	14.09	14.3975	0.0092	i	COJ 1m
2015-09-11	2457276.88	14.88	14.7464	0.0495791	u	Swift
2015-09-11	2457276.90	14.90	16.5008	0.0980719	uvw2	Swift
2015-09-11	2457277.06	15.06	14.7949	0.0494715	u	Swift
2015-09-11	2457277.07	15.07	16.7502	0.0939673	uvw2	Swift
2015-09-12	2457277.70	15.70	15.0345	0.0189	B	LSC 1m
2015-09-12	2457277.70	15.70	14.5677	0.0065	g	LSC 1m
2015-09-12	2457277.71	15.71	14.5657	0.0066	g	LSC 1m
2015-09-12	2457277.71	15.71	14.3217	0.0094	r	LSC 1m
2015-09-12	2457277.71	15.71	14.3644	0.0095	i	LSC 1m
2015-09-14	2457280.41	18.41	15.1093	0.0224	B	CPT 1m
2015-09-14	2457280.41	18.41	15.1074	0.0249	B	CPT 1m
2015-09-14	2457280.41	18.41	14.5441	0.0201	V	CPT 1m
2015-09-14	2457280.41	18.41	14.5132	0.0656	V	CPT 1m
2015-09-14	2457280.41	18.41	14.8677	0.0705	g	CPT 1m
2015-09-14	2457280.42	18.42	14.7508	0.0167	g	CPT 1m
2015-09-14	2457280.45	18.45	15.0701	0.0399	B	CPT 1m
2015-09-15	2457281.27	19.27	15.1119	0.0205	B	CPT 1m
2015-09-15	2457281.27	19.27	15.1109	0.0217	B	CPT 1m
2015-09-15	2457281.27	19.27	14.553	0.0227	V	CPT 1m
2015-09-15	2457281.27	19.27	14.6043	0.0227	V	CPT 1m

Date-Obs	JD	Phase (Day)	Apparent Magnitude (mag)	Apparent Magnitude Error (mag)	Filter	Source
2015-09-15	2457281.27	19.27	14.7254	0.0168	g	CPT 1m
2015-09-15	2457281.28	19.28	14.7467	0.0181	g	CPT 1m
2015-09-15	2457281.28	19.28	14.3571	0.02	r	CPT 1m
2015-09-15	2457281.28	19.28	14.3245	0.02	r	CPT 1m
2015-09-15	2457281.28	19.28	14.3264	0.0143	i	CPT 1m
2015-09-15	2457281.29	19.29	14.8197	0.2312	U	CPT 1m
2015-09-15	2457281.30	19.30	14.944	0.1672	U	CPT 1m
2015-09-15	2457281.30	19.30	15.1623	0.0239	B	CPT 1m
2015-09-15	2457281.30	19.30	15.0406	0.0334	B	CPT 1m
2015-09-15	2457281.30	19.30	14.5597	0.024	V	CPT 1m
2015-09-15	2457281.31	19.31	14.5101	0.0255	V	CPT 1m
2015-09-15	2457281.31	19.31	14.819	0.0244	g	CPT 1m
2015-09-15	2457281.31	19.31	14.7758	0.0198	g	CPT 1m
2015-09-15	2457281.31	19.31	14.3684	0.0183	r	CPT 1m
2015-09-15	2457281.32	19.32	14.3869	0.0191	r	CPT 1m
2015-09-15	2457281.32	19.32	14.3086	0.0151	i	CPT 1m
2015-09-15	2457281.32	19.32	14.3229	0.0134	i	CPT 1m
2015-09-15	2457281.38	19.38	16.5715	0.0953889	uvw1	Swift
2015-09-15	2457281.38	19.38	15.3534	0.0701123	u	Swift
2015-09-15	2457281.38	19.38	15.3092	0.0570442	b	Swift
2015-09-15	2457281.39	19.39	17.8844	0.137142	uvw2	Swift
2015-09-15	2457281.39	19.39	14.6301	0.059278	v	Swift
2015-09-15	2457281.39	19.39	17.6966	0.17019	uvm2	Swift
2015-09-15	2457281.40	19.40	14.5587	0.0209	V	CPT 1m
2015-09-15	2457281.40	19.40	14.1453	0.0214	R	CPT 1m
2015-09-16	2457281.58	19.58	16.4064	0.084651	uvw1	Swift
2015-09-16	2457281.58	19.58	15.2617	0.0645454	u	Swift
2015-09-16	2457281.58	19.58	15.125	0.0522478	b	Swift
2015-09-16	2457281.58	19.58	17.4737	0.110691	uvw2	Swift

Date-Obs	JD	Phase (Day)	Apparent Magnitude (mag)	Apparent Magnitude Error (mag)	Filter	Source
2015-09-16	2457281.58	19.58	14.6206	0.0545996	v	Swift
2015-09-16	2457281.59	19.59	17.662	0.108057	uvm2	Swift
2015-09-16	2457282.24	20.24	14.5502	0.0177	V	CPT 1m
2015-09-16	2457282.25	20.25	14.5349	0.0181	V	CPT 1m
2015-09-16	2457282.25	20.25	14.2113	0.0182	R	CPT 1m
2015-09-16	2457282.25	20.25	15.1916	0.0198	B	CPT 1m
2015-09-17	2457283.04	21.04	14.515	0.0162	V	COJ 1m
2015-09-17	2457283.04	21.04	14.161	0.0172	R	COJ 1m
2015-09-17	2457283.05	21.05	15.1721	0.0205	B	COJ 1m
2015-09-18	2457283.95	21.95	14.0682	0.0331	R	COJ 2m
2015-09-18	2457283.95	21.95	13.833	0.0631	I	COJ 2m
2015-09-18	2457284.00	22.00	14.174	0.0278	R	COJ 1m
2015-09-18	2457284.00	22.00	15.1765	0.053	B	COJ 1m
2015-09-19	2457284.90	22.90	16.9926	0.0768775	uvw1	Swift
2015-09-19	2457284.90	22.90	15.6851	0.0581263	u	Swift
2015-09-19	2457284.90	22.90	15.382	0.0473402	b	Swift
2015-09-19	2457284.90	22.90	18.0879	0.100539	uvw2	Swift
2015-09-19	2457284.90	22.90	14.6721	0.0446836	v	Swift
2015-09-19	2457284.90	22.90	18.3948	0.0998688	uvm2	Swift
2015-09-19	2457285.03	23.03	14.6059	0.0176	V	COJ 1m
2015-09-19	2457285.03	23.03	14.162	0.0192	R	COJ 1m
2015-09-19	2457285.03	23.03	15.2618	0.0225	B	COJ 1m
2015-09-19	2457285.40	23.40	14.9415	0.3032	U	CPT 1m
2015-09-19	2457285.40	23.40	15.3585	0.0207	B	CPT 1m
2015-09-19	2457285.41	23.41	15.3612	0.0197	B	CPT 1m
2015-09-19	2457285.41	23.41	14.5985	0.0193	V	CPT 1m
2015-09-19	2457285.41	23.41	14.6202	0.0197	V	CPT 1m
2015-09-19	2457285.41	23.41	14.9018	0.0101	g	CPT 1m
2015-09-19	2457285.42	23.42	14.9322	0.009	g	CPT 1m

Date-Obs	JD	Phase (Day)	Apparent Magnitude (mag)	Apparent Magnitude Error (mag)	Filter	Source
2015-09-19	2457285.42	23.42	14.3516	0.013	r	CPT 1m
2015-09-19	2457285.42	23.42	14.3516	0.0079	r	CPT 1m
2015-09-19	2457285.42	23.42	14.3265	0.0085	i	CPT 1m
2015-09-20	2457285.90	23.90	14.5069	0.0628	V	COJ 2m
2015-09-20	2457285.90	23.90	14.1027	0.0328	R	COJ 2m
2015-09-20	2457285.90	23.90	13.8422	0.0572	I	COJ 2m
2015-09-20	2457286.38	24.38	15.4136	0.0183	B	CPT 1m
2015-09-20	2457286.38	24.38	15.4186	0.0182	B	CPT 1m
2015-09-20	2457286.38	24.38	14.6501	0.0193	V	CPT 1m
2015-09-20	2457286.38	24.38	14.6183	0.0186	V	CPT 1m
2015-09-20	2457286.39	24.39	14.954	0.0071	g	CPT 1m
2015-09-20	2457286.39	24.39	14.9531	0.0079	g	CPT 1m
2015-09-20	2457286.39	24.39	14.3507	0.009	r	CPT 1m
2015-09-20	2457286.39	24.39	14.3453	0.0083	r	CPT 1m
2015-09-20	2457286.39	24.39	14.3174	0.0098	i	CPT 1m
2015-09-20	2457286.40	24.40	14.326	0.0089	i	CPT 1m
2015-09-21	2457286.92	24.92	14.5126	0.0659	V	COJ 2m
2015-09-21	2457286.93	24.93	14.1012	0.0364	R	COJ 2m
2015-09-21	2457286.93	24.93	13.8606	0.0709	I	COJ 2m
2015-09-21	2457287.03	25.03	14.6238	0.0174	V	COJ 1m
2015-09-21	2457287.03	25.03	14.1973	0.0194	R	COJ 1m
2015-09-21	2457287.03	25.03	15.4518	0.0226	B	COJ 1m
2015-09-22	2457288.00	26.00	14.6066	0.0182	V	COJ 1m
2015-09-22	2457288.00	26.00	14.2242	0.018	R	COJ 1m
2015-09-22	2457288.00	26.00	15.4841	0.0243	B	COJ 1m
2015-09-23	2457288.74	26.74	14.6208	0.0586	V	OGG 2m
2015-09-23	2457288.74	26.74	14.139	0.0344	R	OGG 2m
2015-09-23	2457289.00	27.00	14.6765	0.0171	V	COJ 1m
2015-09-23	2457289.00	27.00	14.2441	0.0187	R	COJ 1m

Date-Obs	JD	Phase (Day)	Apparent Magnitude (mag)	Apparent Magnitude Error (mag)	Filter	Source
2015-09-23	2457289.00	27.00	15.5099	0.0232	B	COJ 1m
2015-09-23	2457289.02	27.02	14.5834	0.0685	V	COJ 2m
2015-09-23	2457289.02	27.02	14.1499	0.0328	R	COJ 2m
2015-09-23	2457289.02	27.02	13.8624	0.0577	I	COJ 2m
2015-09-23	2457289.27	27.27	15.5413	0.0213	B	CPT 1m
2015-09-23	2457289.28	27.28	15.5355	0.0203	B	CPT 1m
2015-09-23	2457289.28	27.28	14.6253	0.0194	V	CPT 1m
2015-09-23	2457289.28	27.28	14.6286	0.0203	V	CPT 1m
2015-09-23	2457289.28	27.28	15.119	0.0094	g	CPT 1m
2015-09-23	2457289.28	27.28	15.0629	0.0085	g	CPT 1m
2015-09-23	2457289.29	27.29	14.3842	0.0099	r	CPT 1m
2015-09-23	2457289.29	27.29	14.3805	0.0086	r	CPT 1m
2015-09-23	2457289.29	27.29	14.3528	0.0098	i	CPT 1m
2015-09-23	2457289.29	27.29	14.3446	0.0098	i	CPT 1m
2015-09-24	2457290.02	28.02	14.7245	0.0178	V	COJ 1m
2015-09-24	2457290.02	28.02	14.2069	0.0181	R	COJ 1m
2015-09-24	2457290.02	28.02	15.6466	0.026	B	COJ 1m
2015-09-24	2457290.15	28.15	17.5537	0.0880056	uvw1	Swift
2015-09-24	2457290.15	28.15	16.3027	0.064038	u	Swift
2015-09-24	2457290.15	28.15	15.6628	0.0481107	b	Swift
2015-09-24	2457290.15	28.15	18.6645	0.118147	uvw2	Swift
2015-09-24	2457290.15	28.15	14.7692	0.0447324	v	Swift
2015-09-24	2457290.16	28.16	19.0014	0.124085	uvm2	Swift
2015-09-25	2457290.88	28.88	14.6524	0.0756	V	COJ 2m
2015-09-25	2457290.88	28.88	14.197	0.0319	R	COJ 2m
2015-09-25	2457290.88	28.88	13.9036	0.0659	I	COJ 2m
2015-09-26	2457291.88	29.88	14.6824	0.0681	V	COJ 2m
2015-09-26	2457291.88	29.88	14.191	0.032	R	COJ 2m
2015-09-26	2457291.91	29.91	14.6355	0.0701	V	COJ 2m

Date-Obs	JD	Phase (Day)	Apparent Magnitude (mag)	Apparent Magnitude Error (mag)	Filter	Source
2015-09-26	2457291.91	29.91	14.6774	0.073	V	COJ 2m
2015-09-26	2457291.92	29.92	14.1658	0.0335	R	COJ 2m
2015-09-26	2457291.92	29.92	13.8629	0.0556	I	COJ 2m
2015-09-26	2457292.00	30.00	14.7224	0.0174	V	COJ 1m
2015-09-26	2457292.00	30.00	14.2434	0.0189	R	COJ 1m
2015-09-26	2457292.00	30.00	15.7146	0.0245	B	COJ 1m
2015-09-26	2457292.02	30.02	14.6623	0.0745	V	COJ 2m
2015-09-26	2457292.02	30.02	14.1934	0.0325	R	COJ 2m
2015-09-26	2457292.03	30.03	13.8559	0.0592	I	COJ 2m
2015-09-27	2457292.98	30.98	15.7575	0.0189	B	COJ 1m
2015-09-27	2457292.99	30.99	15.7618	0.0195	B	COJ 1m
2015-09-27	2457292.99	30.99	14.7305	0.0167	V	COJ 1m
2015-09-27	2457292.99	30.99	14.7305	0.0168	V	COJ 1m
2015-09-27	2457292.99	30.99	15.2137	0.0085	g	COJ 1m
2015-09-27	2457293.00	31.00	15.2293	0.0091	g	COJ 1m
2015-09-27	2457293.00	31.00	14.3795	0.008	r	COJ 1m
2015-09-27	2457293.00	31.00	14.3667	0.008	r	COJ 1m
2015-09-27	2457293.00	31.00	14.392	0.0096	i	COJ 1m
2015-09-27	2457293.00	31.00	14.4223	0.0088	i	COJ 1m
2015-09-27	2457293.01	31.01	14.7996	0.0179	V	COJ 1m
2015-09-27	2457293.01	31.01	14.214	0.0182	R	COJ 1m
2015-09-27	2457293.01	31.01	15.6575	0.0283	B	COJ 1m
2015-09-28	2457293.71	31.71	17.816	0.0959895	uvw1	Swift
2015-09-28	2457293.71	31.71	16.6479	0.0690434	u	Swift
2015-09-28	2457293.71	31.71	15.9235	0.0494111	b	Swift
2015-09-28	2457293.72	31.72	18.9344	0.13088	uvw2	Swift
2015-09-28	2457293.72	31.72	14.9131	0.0458542	v	Swift
2015-09-28	2457293.72	31.72	19.3185	0.142289	uvm2	Swift
2015-09-28	2457293.94	31.94	14.7084	0.0658	V	COJ 2m

Date-Obs	JD	Phase (Day)	Apparent Magnitude (mag)	Apparent Magnitude Error (mag)	Filter	Source
2015-09-28	2457293.94	31.94	14.2297	0.0334	R	COJ 2m
2015-09-28	2457293.94	31.94	13.9372	0.0681	I	COJ 2m
2015-09-28	2457294.01	32.01	14.7784	0.0182	V	COJ 1m
2015-09-28	2457294.01	32.01	14.2644	0.0193	R	COJ 1m
2015-09-28	2457294.01	32.01	15.7097	0.0269	B	COJ 1m
2015-09-28	2457294.02	32.02	14.7355	0.0698	V	COJ 2m
2015-09-28	2457294.02	32.02	14.1861	0.0345	R	COJ 2m
2015-09-28	2457294.02	32.02	13.9521	0.0647	I	COJ 2m
2015-10-01	2457296.91	34.91	14.8594	0.0712	V	COJ 2m
2015-10-01	2457296.92	34.92	14.2795	0.0319	R	COJ 2m
2015-10-01	2457296.92	34.92	13.9267	0.0597	I	COJ 2m
2015-10-01	2457297.00	35.00	15.9459	0.0212	B	COJ 1m
2015-10-01	2457297.00	35.00	14.8841	0.0161	V	COJ 1m
2015-10-01	2457297.00	35.00	14.862	0.068	V	COJ 2m
2015-10-01	2457297.00	35.00	14.2814	0.0318	R	COJ 2m
2015-10-01	2457297.00	35.00	14.3045	0.0173	R	COJ 1m
2015-10-01	2457297.00	35.00	13.9293	0.0627	I	COJ 2m
2015-10-01	2457297.00	35.00	14.0334	0.0229	I	COJ 1m
2015-10-01	2457297.01	35.01	15.9469	0.0209	B	COJ 1m
2015-10-01	2457297.01	35.01	14.8796	0.0171	V	COJ 1m
2015-10-01	2457297.02	35.02	15.9367	0.0191	B	COJ 1m
2015-10-01	2457297.02	35.02	14.3449	0.0186	R	COJ 1m
2015-10-01	2457297.02	35.02	14.0454	0.0232	I	COJ 1m
2015-10-01	2457297.02	35.02	15.9452	0.0191	B	COJ 1m
2015-10-01	2457297.02	35.02	14.8809	0.0156	V	COJ 1m
2015-10-01	2457297.02	35.02	14.8869	0.0153	V	COJ 1m
2015-10-01	2457297.02	35.02	15.3369	0.0073	g	COJ 1m
2015-10-01	2457297.03	35.03	15.3474	0.0074	g	COJ 1m
2015-10-01	2457297.03	35.03	14.4922	0.0072	r	COJ 1m

Date-Obs	JD	Phase (Day)	Apparent Magnitude (mag)	Apparent Magnitude Error (mag)	Filter	Source
2015-10-01	2457297.03	35.03	14.4821	0.006	r	COJ 1m
2015-10-01	2457297.03	35.03	14.4355	0.0079	i	COJ 1m
2015-10-01	2457297.03	35.03	14.4303	0.0087	i	COJ 1m
2015-10-02	2457298.00	36.00	15.9704	0.0198	B	COJ 1m
2015-10-02	2457298.00	36.00	14.8575	0.0169	V	COJ 1m
2015-10-02	2457298.00	36.00	14.3442	0.0181	R	COJ 1m
2015-10-02	2457298.01	36.01	14.0386	0.0248	I	COJ 1m
2015-10-02	2457298.02	36.02	13.9503	0.062	I	COJ 2m
2015-10-02	2457298.03	36.03	17.9368	0.109511	uvw1	Swift
2015-10-02	2457298.04	36.04	16.9781	0.08291	u	Swift
2015-10-02	2457298.04	36.04	16.0852	0.0525515	b	Swift
2015-10-02	2457298.04	36.04	19.1168	0.164704	uvw2	Swift
2015-10-02	2457298.07	36.07	15.0582	0.0602818	v	Swift
2015-10-02	2457298.07	36.07	19.623	0.276162	uvm2	Swift
2015-10-03	2457299.00	37.00	14.8704	0.0681	V	COJ 2m
2015-10-03	2457299.00	37.00	14.2832	0.0351	R	COJ 2m
2015-10-03	2457299.00	37.00	15.9744	0.0211	B	COJ 1m
2015-10-03	2457299.00	37.00	13.9815	0.062	I	COJ 2m
2015-10-03	2457299.01	37.01	14.9103	0.0176	V	COJ 1m
2015-10-03	2457299.01	37.01	14.3326	0.0202	R	COJ 1m
2015-10-03	2457299.01	37.01	14.0386	0.0242	I	COJ 1m
2015-10-04	2457300.00	38.00	14.9242	0.0662	V	COJ 2m
2015-10-04	2457300.00	38.00	14.2937	0.0337	R	COJ 2m
2015-10-04	2457300.00	38.00	14.0064	0.0636	I	COJ 2m
2015-10-04	2457300.00	38.00	14.3055	0.0769	R	COJ 1m
2015-10-04	2457300.01	38.01	14.0596	0.0256	I	COJ 1m
2015-10-04	2457300.11	38.11	13.613	0.009	H	NTT
2015-10-04	2457300.11	38.11	13.834	0.009	J	NTT
2015-10-04	2457300.11	38.11	13.446	0.012	K	NTT

Date-Obs	JD	Phase (Day)	Apparent Magnitude (mag)	Apparent Magnitude Error (mag)	Filter	Source
2015-10-05	2457301.00	39.00	15.0748	0.0269	V	COJ 1m
2015-10-05	2457301.00	39.00	15.5439	0.0181	g	COJ 1m
2015-10-05	2457301.00	39.00	15.5835	0.0182	g	COJ 1m
2015-10-05	2457301.00	39.00	14.8919	0.0653	V	COJ 2m
2015-10-05	2457301.00	39.00	14.3018	0.0342	R	COJ 2m
2015-10-05	2457301.00	39.00	14.5278	0.01	r	COJ 1m
2015-10-05	2457301.00	39.00	13.9848	0.061	I	COJ 2m
2015-10-05	2457301.00	39.00	14.5415	0.01	r	COJ 1m
2015-10-05	2457301.01	39.01	14.4404	0.0161	i	COJ 1m
2015-10-05	2457301.01	39.01	14.4549	0.0134	i	COJ 1m
2015-10-06	2457302.00	40.00	14.8997	0.0182	V	COJ 1m
2015-10-06	2457302.00	40.00	14.3496	0.0181	R	COJ 1m
2015-10-06	2457302.01	40.01	13.9175	0.0228	I	COJ 1m
2015-10-06	2457302.03	40.03	14.9431	0.0623	V	COJ 2m
2015-10-06	2457302.03	40.03	14.3357	0.0331	R	COJ 2m
2015-10-06	2457302.03	40.03	13.9981	0.06	I	COJ 2m
2015-10-07	2457303.00	41.00	14.9645	0.0296	V	COJ 1m
2015-10-07	2457303.00	41.00	14.9659	0.0742	V	COJ 2m
2015-10-07	2457303.00	41.00	14.3736	0.0342	R	COJ 2m
2015-10-07	2457303.26	41.26	19.5874	0.327179	uvw2	Swift
2015-10-07	2457303.26	41.26	15.0614	0.0684723	v	Swift
2015-10-07	2457303.26	41.26	19.8082	0.412167	uvm2	Swift
2015-10-07	2457303.29	41.29	18.333	0.156773	uvw1	Swift
2015-10-07	2457303.29	41.29	17.4491	0.119109	u	Swift
2015-10-07	2457303.29	41.29	16.2083	0.0651877	b	Swift
2015-10-08	2457304.00	42.00	15.0488	0.0767	V	COJ 2m
2015-10-08	2457304.00	42.00	14.3918	0.0321	R	COJ 2m
2015-10-08	2457304.00	42.00	14.0034	0.0586	I	COJ 2m
2015-10-08	2457304.01	42.01	14.108	0.0459	I	COJ 1m

Date-Obs	JD	Phase (Day)	Apparent Magnitude (mag)	Apparent Magnitude Error (mag)	Filter	Source
2015-10-08	2457304.01	42.01	16.2524	0.0247	B	COJ 1m
2015-10-08	2457304.01	42.01	15.0384	0.0168	V	COJ 1m
2015-10-08	2457304.01	42.01	14.463	0.018	R	COJ 1m
2015-10-08	2457304.01	42.01	14.1006	0.023	I	COJ 1m
2015-10-09	2457305.00	43.00	15.0051	0.0641	V	COJ 2m
2015-10-09	2457305.00	43.00	16.1896	0.0216	B	COJ 1m
2015-10-09	2457305.00	43.00	14.3475	0.0343	R	COJ 2m
2015-10-09	2457305.00	43.00	14.027	0.0611	I	COJ 2m
2015-10-09	2457305.00	43.00	15.0489	0.0159	V	COJ 1m
2015-10-09	2457305.01	43.01	14.4256	0.018	R	COJ 1m
2015-10-10	2457306.00	44.00	16.2807	0.0241	B	COJ 1m
2015-10-10	2457306.00	44.00	15.0728	0.0176	V	COJ 1m
2015-10-10	2457306.02	44.02	15.1156	0.0636	V	COJ 2m
2015-10-10	2457306.02	44.02	14.4153	0.0334	R	COJ 2m
2015-10-10	2457306.02	44.02	14.0404	0.0632	I	COJ 2m
2015-10-11	2457307.00	45.00	15.0803	0.0669	V	COJ 2m
2015-10-11	2457307.00	45.00	14.423	0.0337	R	COJ 2m
2015-10-11	2457307.00	45.00	14.0475	0.0607	I	COJ 2m
2015-10-11	2457307.01	45.01	16.4098	0.0199	B	COJ 1m
2015-10-11	2457307.02	45.02	13.998	0.0189	I	COJ 1m
2015-10-12	2457308.37	46.37	16.3729	0.0259	B	CPT 1m
2015-10-12	2457308.37	46.37	15.082	0.0164	V	CPT 1m
2015-10-12	2457308.38	46.38	14.4858	0.0174	R	CPT 1m
2015-10-13	2457308.89	46.89	15.1315	0.0683	V	COJ 2m
2015-10-13	2457308.89	46.89	14.4604	0.0333	R	COJ 2m
2015-10-13	2457308.89	46.89	14.0955	0.0579	I	COJ 2m
2015-10-14	2457309.89	47.89	15.1596	0.0725	V	COJ 2m
2015-10-14	2457309.89	47.89	14.491	0.0327	R	COJ 2m
2015-10-14	2457309.89	47.89	14.1281	0.0639	I	COJ 2m

Date-Obs	JD	Phase (Day)	Apparent Magnitude (mag)	Apparent Magnitude Error (mag)	Filter	Source
2015-10-14	2457309.99	47.99	16.5144	0.0216	B	COJ 1m
2015-10-14	2457310.00	48.00	15.1738	0.0207	V	COJ 1m
2015-10-14	2457310.00	48.00	15.1604	0.0186	V	COJ 1m
2015-10-14	2457310.00	48.00	15.7562	0.0095	g	COJ 1m
2015-10-14	2457310.01	48.01	14.6928	0.008	r	COJ 1m
2015-10-14	2457310.01	48.01	14.6082	0.0086	i	COJ 1m
2015-10-14	2457310.02	48.02	15.1733	0.0727	V	COJ 2m
2015-10-14	2457310.02	48.02	14.504	0.0315	R	COJ 2m
2015-10-14	2457310.02	48.02	14.0754	0.0795	I	COJ 2m
2015-10-15	2457311.00	49.00	15.2055	0.0772	V	COJ 2m
2015-10-15	2457311.01	49.01	14.4576	0.0353	R	COJ 2m
2015-10-15	2457311.01	49.01	14.1602	0.0692	I	COJ 2m
2015-10-16	2457311.98	49.98	16.4797	0.0246	B	COJ 1m
2015-10-16	2457311.98	49.98	15.2072	0.0171	V	COJ 1m
2015-10-16	2457311.99	49.99	14.5242	0.0193	R	COJ 1m
2015-10-16	2457311.99	49.99	14.2233	0.0237	I	COJ 1m
2015-10-16	2457312.00	50.00	15.1822	0.0628	V	COJ 2m
2015-10-16	2457312.01	50.01	14.4719	0.0334	R	COJ 2m
2015-10-16	2457312.01	50.01	14.0782	0.0576	I	COJ 2m
2015-10-21	2457317.33	55.33	16.6581	0.0254	B	CPT 1m
2015-10-21	2457317.33	55.33	16.6168	0.0283	B	CPT 1m
2015-10-21	2457317.34	55.34	15.2968	0.019	V	CPT 1m
2015-10-21	2457317.34	55.34	15.302	0.019	V	CPT 1m
2015-10-21	2457317.34	55.34	15.9408	0.0111	g	CPT 1m
2015-10-21	2457317.34	55.34	15.9331	0.011	g	CPT 1m
2015-10-21	2457317.35	55.35	14.8194	0.0085	r	CPT 1m
2015-10-21	2457317.35	55.35	14.8043	0.0087	r	CPT 1m
2015-10-21	2457317.35	55.35	14.7093	0.0109	i	CPT 1m
2015-10-21	2457317.35	55.35	14.7417	0.0092	i	CPT 1m

Date-Obs	JD	Phase (Day)	Apparent Magnitude (mag)	Apparent Magnitude Error (mag)	Filter	Source
2015-10-22	2457317.56	55.56	16.6969	0.0269	B	LSC 1m
2015-10-22	2457317.56	55.56	16.7196	0.0275	B	LSC 1m
2015-10-22	2457317.56	55.56	15.3492	0.0175	V	LSC 1m
2015-10-22	2457317.57	55.57	15.3416	0.0186	V	LSC 1m
2015-10-22	2457317.57	55.57	15.9796	0.0113	g	LSC 1m
2015-10-22	2457317.57	55.57	15.9918	0.0113	g	LSC 1m
2015-10-22	2457317.57	55.57	14.8206	0.0075	r	LSC 1m
2015-10-22	2457317.57	55.57	14.8053	0.0092	r	LSC 1m
2015-10-25	2457321.29	59.29	16.6622	0.0228	B	CPT 1m
2015-10-25	2457321.29	59.29	16.649	0.0221	B	CPT 1m
2015-10-25	2457321.30	59.30	15.3659	0.0197	V	CPT 1m
2015-10-25	2457321.30	59.30	15.374	0.0193	V	CPT 1m
2015-10-25	2457321.30	59.30	16.0071	0.0091	g	CPT 1m
2015-10-25	2457321.30	59.30	15.9937	0.0121	g	CPT 1m
2015-10-25	2457321.31	59.31	14.7951	0.0084	r	CPT 1m
2015-10-25	2457321.31	59.31	14.8208	0.0096	r	CPT 1m
2015-10-25	2457321.31	59.31	14.7448	0.0083	i	CPT 1m
2015-10-26	2457321.55	59.55	16.6516	0.0976	B	LSC 1m
2015-10-26	2457321.56	59.56	15.4091	0.0347	V	LSC 1m
2015-10-26	2457321.56	59.56	15.3474	0.0342	V	LSC 1m
2015-10-26	2457321.56	59.56	14.845	0.0179	r	LSC 1m
2015-10-26	2457321.57	59.57	14.7405	0.0319	i	LSC 1m
2015-10-30	2457325.55	63.55	16.815	0.0218	B	LSC 1m
2015-10-30	2457325.55	63.55	16.799	0.0212	B	LSC 1m
2015-10-30	2457325.56	63.56	15.5133	0.0166	V	LSC 1m
2015-10-30	2457325.56	63.56	15.4962	0.017	V	LSC 1m
2015-10-30	2457325.56	63.56	16.1001	0.0089	g	LSC 1m
2015-10-30	2457325.56	63.56	16.1033	0.0082	g	LSC 1m
2015-10-30	2457325.57	63.57	14.8984	0.0074	r	LSC 1m

Date-Obs	JD	Phase (Day)	Apparent Magnitude (mag)	Apparent Magnitude Error (mag)	Filter	Source
2015-10-30	2457325.57	63.57	14.8838	0.0074	r	LSC 1m
2015-10-30	2457325.57	63.57	14.8357	0.0089	i	LSC 1m
2015-10-30	2457325.57	63.57	14.8444	0.0089	i	LSC 1m
2015-11-01	2457327.52	65.52	16.9149	0.0235	B	LSC 1m
2015-11-01	2457327.52	65.52	16.8871	0.0234	B	LSC 1m
2015-11-01	2457327.52	65.52	15.5389	0.0172	V	LSC 1m
2015-11-01	2457327.52	65.52	15.5256	0.0172	V	LSC 1m
2015-11-01	2457327.53	65.53	16.8851	0.0248	g	LSC 1m
2015-11-01	2457327.53	65.53	14.9297	0.0069	r	LSC 1m
2015-11-01	2457327.53	65.53	14.9356	0.0067	r	LSC 1m
2015-11-01	2457327.54	65.54	14.8898	0.0092	i	LSC 1m
2015-11-03	2457329.52	67.52	15.6294	0.0881984	v	Swift
2015-11-03	2457329.52	67.52	20.0263	0.397107	uvm2	Swift
2015-11-03	2457329.61	67.61	18.9889	0.205934	uvw1	Swift
2015-11-03	2457329.61	67.61	18.5354	0.255097	u	Swift
2015-11-03	2457329.61	67.61	16.9809	0.0877446	b	Swift
2015-11-03	2457329.61	67.61	20.985	0.926686	uvw2	Swift
2015-11-04	2457331.29	69.29	16.9508	0.0249	B	CPT 1m
2015-11-04	2457331.30	69.30	16.9341	0.025	B	CPT 1m
2015-11-04	2457331.30	69.30	15.5346	0.0214	V	CPT 1m
2015-11-04	2457331.30	69.30	15.5924	0.0198	V	CPT 1m
2015-11-04	2457331.30	69.30	16.2199	0.0101	g	CPT 1m
2015-11-04	2457331.31	69.31	16.2832	0.0122	g	CPT 1m
2015-11-04	2457331.31	69.31	15.0094	0.011	r	CPT 1m
2015-11-04	2457331.31	69.31	15.0099	0.0094	r	CPT 1m
2015-11-04	2457331.31	69.31	14.9379	0.01	i	CPT 1m
2015-11-04	2457331.31	69.31	14.9664	0.0109	i	CPT 1m
2015-11-06	2457333.01	71.01	19.1299	0.232389	uvw1	Swift
2015-11-06	2457333.01	71.01	18.5821	0.227366	u	Swift

Date-Obs	JD	Phase (Day)	Apparent Magnitude (mag)	Apparent Magnitude Error (mag)	Filter	Source
2015-11-06	2457333.01	71.01	17.0693	0.0734797	b	Swift
2015-11-06	2457333.01	71.01	20.3651	0.37599	uvw2	Swift
2015-11-06	2457333.01	71.01	15.7718	0.0655467	v	Swift
2015-11-06	2457333.02	71.02	20.3922	0.320049	uvm2	Swift
2015-11-09	2457335.90	73.90	16.9873	0.0264	B	COJ 1m
2015-11-09	2457335.90	73.90	16.9925	0.0258	B	COJ 1m
2015-11-09	2457335.91	73.91	15.6589	0.0195	V	COJ 1m
2015-11-09	2457335.91	73.91	15.6664	0.0195	V	COJ 1m
2015-11-09	2457335.91	73.91	16.343	0.0119	g	COJ 1m
2015-11-09	2457335.91	73.91	16.3469	0.0106	g	COJ 1m
2015-11-09	2457335.92	73.92	14.9858	0.0078	r	COJ 1m
2015-11-09	2457335.92	73.92	15.0004	0.0079	r	COJ 1m
2015-11-10	2457336.92	74.92	16.9714	0.0247	B	COJ 1m
2015-11-10	2457336.92	74.92	17.0214	0.0254	B	COJ 1m
2015-11-10	2457336.93	74.93	15.6783	0.0201	V	COJ 1m
2015-11-10	2457336.93	74.93	15.6438	0.0206	V	COJ 1m
2015-11-10	2457336.93	74.93	16.3097	0.0107	g	COJ 1m
2015-11-10	2457336.93	74.93	16.3204	0.0108	g	COJ 1m
2015-11-10	2457336.94	74.94	15.0138	0.0104	r	COJ 1m
2015-11-10	2457336.94	74.94	15.0427	0.0086	r	COJ 1m
2015-11-10	2457336.94	74.94	15.0102	0.0113	i	COJ 1m
2015-11-10	2457336.94	74.94	15.0213	0.0113	i	COJ 1m
2015-11-13	2457339.51	77.51	17.1407	0.0255	B	LSC 1m
2015-11-13	2457339.52	77.52	17.1182	0.0262	B	LSC 1m
2015-11-13	2457339.52	77.52	15.7907	0.0177	V	LSC 1m
2015-11-13	2457339.52	77.52	15.7261	0.0194	V	LSC 1m
2015-11-13	2457339.52	77.52	16.4199	0.0114	g	LSC 1m
2015-11-13	2457339.52	77.52	16.3703	0.0103	g	LSC 1m
2015-11-13	2457339.53	77.53	15.0293	0.0113	r	LSC 1m

Date-Obs	JD	Phase (Day)	Apparent Magnitude (mag)	Apparent Magnitude Error (mag)	Filter	Source
2015-11-13	2457339.53	77.53	15.0512	0.0076	r	LSC 1m
2015-11-14	2457340.52	78.52	17.0814	0.0271	B	LSC 1m
2015-11-14	2457340.53	78.53	15.7803	0.0189	V	LSC 1m
2015-11-14	2457340.53	78.53	15.7904	0.019	V	LSC 1m
2015-11-17	2457344.27	82.27	16.4899	0.0142	g	CPT 1m
2015-11-17	2457344.27	82.27	16.4985	0.0153	g	CPT 1m
2015-11-17	2457344.27	82.27	17.1926	0.0318	B	CPT 1m
2015-11-17	2457344.27	82.27	15.1155	0.0131	r	CPT 1m
2015-11-17	2457344.27	82.27	17.2036	0.0387	B	CPT 1m
2015-11-17	2457344.27	82.27	15.137	0.0101	r	CPT 1m
2015-11-17	2457344.28	82.28	15.1596	0.0112	i	CPT 1m
2015-11-17	2457344.28	82.28	15.7994	0.0226	V	CPT 1m
2015-11-17	2457344.28	82.28	15.1587	0.0139	i	CPT 1m
2015-11-17	2457344.28	82.28	15.81	0.0226	V	CPT 1m
2015-11-18	2457345.04	83.04	19.5823	0.347677	uvw1	Swift
2015-11-18	2457345.04	83.04	20.097	0.952033	u	Swift
2015-11-18	2457345.04	83.04	17.2377	0.084596	b	Swift
2015-11-18	2457345.04	83.04	19.9466	0.291159	uvw2	Swift
2015-11-18	2457345.05	83.05	16.0324	0.0747309	v	Swift
2015-11-18	2457345.05	83.05	20.2633	0.301579	uvm2	Swift
2015-11-21	2457348.02	86.02	14.105	0.013	H	NTT
2015-11-21	2457348.02	86.02	14.225	0.013	J	NTT
2015-11-21	2457348.02	86.02	13.84	0.013	K	NTT
2015-11-22	2457348.91	86.91	17.2722	0.0643	B	COJ 1m
2015-11-22	2457348.91	86.91	17.1815	0.0543	B	COJ 1m
2016-02-27	2457446.27	184.27	19.6839	0.1956	g	COJ 1m
2016-02-27	2457446.27	184.27	17.5443	0.041	r	COJ 1m
2016-02-27	2457446.27	184.27	18.219	0.1371	i	COJ 1m
2016-02-27	2457446.28	184.28	17.8218	0.0934	i	COJ 1m

Date-Obs	JD	Phase (Day)	Apparent Magnitude (mag)	Apparent Magnitude Error (mag)	Filter	Source
2016-02-27	2457446.28	184.28	18.5598	0.128	V	COJ 1m
2016-02-27	2457446.28	184.28	18.6821	0.141	V	COJ 1m
2016-02-29	2457447.62	185.62	19.5147	0.2146	g	CPT 1m
2016-02-29	2457447.62	185.62	19.2656	0.1153	g	CPT 1m
2016-02-29	2457447.62	185.62	17.6414	0.0324	r	CPT 1m
2016-02-29	2457447.62	185.62	17.5973	0.0372	r	CPT 1m
2016-02-29	2457447.62	185.62	17.8761	0.0565	i	CPT 1m
2016-02-29	2457447.63	185.63	17.9711	0.0821	i	CPT 1m
2016-02-29	2457447.63	185.63	18.9092	0.151	V	CPT 1m
2016-03-03	2457451.27	189.27	19.7811	0.2962	B	COJ 1m
2016-03-03	2457451.27	189.27	18.8181	0.099	V	COJ 1m
2016-03-03	2457451.27	189.27	18.7776	0.1	V	COJ 1m
2016-03-04	2457451.61	189.61	17.699	0.0652	r	CPT 1m
2016-03-04	2457451.61	189.61	19.1904	0.2675	V	CPT 1m
2016-03-04	2457451.62	189.62	18.0481	0.1393	i	CPT 1m
2016-03-08	2457455.88	193.88	20.1824	0.1763	B	LSC 1m
2016-03-08	2457455.88	193.88	20.1263	0.1811	B	LSC 1m
2016-03-08	2457455.88	193.88	18.9387	0.0721	V	LSC 1m
2016-03-08	2457455.89	193.89	18.927	0.068	V	LSC 1m
2016-03-08	2457455.89	193.89	19.6032	0.0714	g	LSC 1m
2016-03-08	2457455.89	193.89	19.4178	0.0599	g	LSC 1m
2016-03-08	2457455.89	193.89	17.8001	0.0382	r	LSC 1m
2016-03-08	2457455.90	193.90	17.781	0.0363	r	LSC 1m
2016-03-08	2457455.90	193.90	18.1032	0.0581	i	LSC 1m
2016-03-08	2457455.90	193.90	18.1954	0.0659	i	LSC 1m
2016-03-09	2457456.87	194.87	20.0938	0.0606	B	LSC 1m
2016-03-09	2457456.88	194.88	20.245	0.0636	B	LSC 1m
2016-03-09	2457456.88	194.88	19.022	0.0347	V	LSC 1m
2016-03-09	2457456.88	194.88	18.9435	0.0277	V	LSC 1m

Date-Obs	JD	Phase (Day)	Apparent Magnitude (mag)	Apparent Magnitude Error (mag)	Filter	Source
2016-03-09	2457456.88	194.88	19.5712	0.0306	g	LSC 1m
2016-03-09	2457456.89	194.89	19.6401	0.0295	g	LSC 1m
2016-03-09	2457456.89	194.89	17.6705	0.0143	r	LSC 1m
2016-03-09	2457456.89	194.89	17.6684	0.0142	r	LSC 1m
2016-03-09	2457456.90	194.90	18.1059	0.0236	i	LSC 1m
2016-03-21	2457468.86	206.86	20.2362	0.1084	B	LSC 1m
2016-03-21	2457468.87	206.87	19.2252	0.051	V	LSC 1m
2016-03-21	2457468.87	206.87	19.2949	0.054	V	LSC 1m
2016-03-21	2457468.87	206.87	19.7965	0.0405	g	LSC 1m
2016-03-21	2457468.88	206.88	19.8266	0.0472	g	LSC 1m
2016-03-21	2457468.88	206.88	17.8812	0.0161	r	LSC 1m
2016-03-21	2457468.88	206.88	17.8783	0.0171	r	LSC 1m
2016-03-21	2457468.89	206.89	18.2893	0.0378	i	LSC 1m
2016-03-21	2457468.89	206.89	18.3295	0.033	i	LSC 1m
2016-04-02	2457480.78	218.78	20.5919	0.1455	B	LSC 1m
2016-04-02	2457480.79	218.79	20.3798	0.1181	B	LSC 1m
2016-04-02	2457480.79	218.79	19.3864	0.0579	V	LSC 1m
2016-04-02	2457480.79	218.79	19.3746	0.061	V	LSC 1m
2016-04-02	2457480.80	218.80	19.7984	0.0529	g	LSC 1m
2016-04-02	2457480.80	218.80	19.8997	0.063	g	LSC 1m
2016-04-02	2457480.81	218.81	18.0476	0.017	r	LSC 1m
2016-04-02	2457480.81	218.81	18.1067	0.018	r	LSC 1m
2016-04-02	2457480.82	218.82	18.5062	0.0359	i	LSC 1m
2016-04-02	2457480.82	218.82	18.5126	0.0426	i	LSC 1m
2016-04-13	2457491.85	229.85	20.4023	0.0811	B	LSC 1m
2016-04-13	2457491.86	229.86	20.7597	0.084	B	LSC 1m
2016-04-13	2457491.86	229.86	19.4889	0.0447	V	LSC 1m
2016-04-13	2457491.87	229.87	19.4739	0.0458	V	LSC 1m
2016-04-13	2457491.87	229.87	20.249	0.0441	g	LSC 1m

Date-Obs	JD	Phase (Day)	Apparent Magnitude (mag)	Apparent Magnitude Error (mag)	Filter	Source
2016-04-13	2457491.88	229.88	20.177	0.043	g	LSC 1m
2016-04-13	2457491.88	229.88	18.2857	0.017	r	LSC 1m
2016-04-13	2457491.88	229.88	18.2761	0.0153	r	LSC 1m
2016-04-13	2457491.89	229.89	18.7446	0.0292	i	LSC 1m
2016-04-13	2457491.89	229.89	18.6741	0.0264	i	LSC 1m
2016-04-16	2457494.88	232.88	20.9552	0.0889	B	LSC 1m
2016-04-16	2457494.88	232.88	20.8416	0.0753	B	LSC 1m
2016-04-16	2457494.89	232.89	19.5716	0.0297	V	LSC 1m
2016-04-16	2457494.89	232.89	19.6752	0.0387	V	LSC 1m
2016-04-16	2457494.89	232.89	20.1297	0.033	g	LSC 1m
2016-04-16	2457494.90	232.90	20.1588	0.0318	g	LSC 1m
2016-04-16	2457494.90	232.90	18.4662	0.0187	r	LSC 1m
2016-04-16	2457494.91	232.91	18.4905	0.0169	r	LSC 1m
2016-04-16	2457494.91	232.91	18.7707	0.0249	i	LSC 1m
2016-04-16	2457494.92	232.92	18.8137	0.0324	i	LSC 1m
2016-04-27	2457505.73	243.73	20.8433	0.245	B	LSC 1m
2016-04-27	2457505.74	243.74	20.7011	0.1787	B	LSC 1m
2016-04-27	2457505.74	243.74	19.9905	0.1207	V	LSC 1m
2016-04-27	2457505.75	243.75	19.902	0.0893	V	LSC 1m
2016-04-27	2457505.75	243.75	20.4106	0.1426	g	LSC 1m
2016-04-27	2457505.76	243.76	20.5091	0.1538	g	LSC 1m
2016-04-27	2457505.76	243.76	18.5246	0.0333	r	LSC 1m
2016-04-27	2457505.76	243.76	18.4269	0.0415	r	LSC 1m
2016-04-27	2457505.77	243.77	19.2402	0.085	i	LSC 1m
2016-04-27	2457505.77	243.77	19.024	0.0927	i	LSC 1m
2016-05-14	2457522.69	260.69	20.8839	0.1562	B	LSC 1m
2016-05-14	2457522.69	260.69	20.1439	0.1582	V	LSC 1m
2016-05-14	2457522.70	260.70	20.0693	0.1045	V	LSC 1m
2016-05-14	2457522.70	260.70	20.3288	0.082	g	LSC 1m

Date-Obs	JD	Phase (Day)	Apparent Magnitude (mag)	Apparent Magnitude Error (mag)	Filter	Source
2016-05-14	2457522.71	260.71	20.3613	0.063	g	LSC 1m
2016-05-14	2457522.71	260.71	18.6358	0.0251	r	LSC 1m
2016-05-14	2457522.72	260.72	18.669	0.023	r	LSC 1m
2016-05-14	2457522.72	260.72	19.2689	0.0465	i	LSC 1m
2016-05-14	2457522.72	260.72	19.1901	0.0378	i	LSC 1m
2016-06-09	2457548.82	286.82	21.5951	0.1884	B	LSC 1m
2016-06-09	2457548.83	286.83	21.4972	0.1543	B	LSC 1m
2016-06-09	2457548.83	286.83	20.4817	0.0802	V	LSC 1m
2016-06-09	2457548.84	286.84	20.3309	0.1268	V	LSC 1m
2016-06-10	2457549.86	287.86	21.7494	0.1455	B	LSC 1m
2016-06-10	2457549.86	287.86	21.7986	0.1953	B	LSC 1m
2016-06-10	2457549.87	287.87	20.3761	0.0762	V	LSC 1m
2016-06-10	2457549.87	287.87	20.3965	0.062	V	LSC 1m
2016-06-10	2457549.88	287.88	20.7123	0.0519	g	LSC 1m
2016-06-10	2457549.88	287.88	20.7157	0.0519	g	LSC 1m
2016-06-10	2457549.89	287.89	18.9864	0.0222	r	LSC 1m
2016-06-10	2457549.89	287.89	18.9985	0.0221	r	LSC 1m
2016-06-10	2457549.89	287.89	19.4022	0.0494	i	LSC 1m
2016-06-10	2457549.90	287.90	19.459	0.0446	i	LSC 1m
2016-07-06	2457575.78	313.78	21.0267	0.164	V	LSC 1m
2016-07-06	2457575.79	313.79	20.7467	0.09	V	LSC 1m
2016-07-06	2457575.79	313.79	21.2029	0.0824	g	LSC 1m
2016-07-06	2457575.79	313.79	21.3076	0.0779	g	LSC 1m
2016-07-06	2457575.80	313.80	19.488	0.0232	r	LSC 1m
2016-07-06	2457575.80	313.80	19.4685	0.0343	r	LSC 1m
2016-07-06	2457575.81	313.81	19.9025	0.0725	i	LSC 1m
2016-07-06	2457575.81	313.81	19.7482	0.0638	i	LSC 1m
2016-08-01	2457601.79	339.79	20.9252	0.211	V	LSC 1m
2016-08-01	2457601.80	339.80	21.1056	0.163	V	LSC 1m

Date-Obs	JD	Phase (Day)	Apparent Magnitude (mag)	Apparent Magnitude Error (mag)	Filter	Source
2016-08-01	2457601.80	339.80	21.5785	0.119	g	LSC 1m
2016-08-01	2457601.81	339.81	21.39	0.1078	g	LSC 1m
2016-08-01	2457601.81	339.81	19.744	0.0424	r	LSC 1m
2016-08-01	2457601.81	339.81	19.8065	0.0505	r	LSC 1m
2016-08-01	2457601.82	339.82	19.8546	0.084	i	LSC 1m
2016-08-01	2457601.82	339.82	20.0238	0.1013	i	LSC 1m
2016-08-27	2457628.29	366.29	21.6904	0.209	V	CPT 1m
2016-08-27	2457628.29	366.29	21.2635	0.166	V	CPT 1m
2016-08-27	2457628.30	366.30	21.362	0.0811	g	CPT 1m
2016-08-27	2457628.30	366.30	21.3729	0.1012	g	CPT 1m
2016-08-27	2457628.31	366.31	20.3302	0.0597	r	CPT 1m
2016-08-27	2457628.31	366.31	20.3289	0.0536	r	CPT 1m
2016-08-27	2457628.31	366.31	20.4718	0.0715	i	CPT 1m
2016-08-27	2457628.32	366.32	20.3308	0.0821	i	CPT 1m
2016-09-23	2457655.04	393.04	22.3121	0.335	V	COJ 1m
2016-09-23	2457655.04	393.04	21.8025	0.259	V	COJ 1m
2016-09-23	2457655.05	393.05	22.1532	0.1804	g	COJ 1m
2016-09-23	2457655.05	393.05	22.0526	0.1579	g	COJ 1m
2016-09-23	2457655.06	393.06	20.4515	0.0629	r	COJ 1m
2016-09-23	2457655.06	393.06	20.5789	0.069	r	COJ 1m
2016-09-23	2457655.06	393.06	20.8635	0.1216	i	COJ 1m
2016-09-23	2457655.07	393.07	20.8028	0.1206	i	COJ 1m
2016-09-26	2457658.03	396.03	22.2804	0.51	V	COJ 1m
2016-09-26	2457658.03	396.03	21.5522	0.246	V	COJ 1m
2016-09-26	2457658.04	396.04	21.6448	0.1918	g	COJ 1m
2016-09-26	2457658.04	396.04	21.3802	0.1514	g	COJ 1m
2016-09-26	2457658.05	396.05	20.5427	0.11	r	COJ 1m
2016-09-26	2457658.06	396.06	20.5842	0.1804	i	COJ 1m
2016-09-26	2457658.06	396.06	20.5119	0.1707	i	COJ 1m

Date-Obs	JD	Phase (Day)	Apparent Magnitude (mag)	Apparent Magnitude Error (mag)	Filter	Source
2016-09-27	2457658.98	396.98	21.7431	0.326	V	COJ 1m
2016-09-27	2457658.99	396.99	20.441	0.123	V	COJ 1m
2016-09-27	2457659.01	397.01	20.2102	0.0884	r	COJ 1m
2016-09-29	2457661.36	399.36	21.4259	0.32	V	CPT 1m
2016-09-29	2457661.36	399.36	21.6541	0.255	V	CPT 1m
2016-09-29	2457661.37	399.37	22.3209	0.2374	g	CPT 1m
2016-09-29	2457661.37	399.37	22.2199	0.5455	g	CPT 1m
2016-09-29	2457661.38	399.38	20.75	0.1491	r	CPT 1m
2016-09-29	2457661.38	399.38	20.6298	0.0948	r	CPT 1m
2016-09-29	2457661.39	399.39	20.9218	0.2325	i	CPT 1m
2016-09-29	2457661.39	399.39	20.6819	0.1544	i	CPT 1m
2016-10-01	2457663.37	401.37	20.9411	0.213	V	CPT 1m
2016-10-01	2457663.37	401.37	21.415	0.296	V	CPT 1m
2016-10-02	2457663.62	401.62	22.1463	0.254	V	LSC 1m
2016-10-02	2457663.62	401.62	21.793	0.195	V	LSC 1m
2016-10-02	2457663.63	401.63	22.2176	0.1896	g	LSC 1m
2016-10-02	2457663.63	401.63	22.4113	0.2366	g	LSC 1m
2016-10-02	2457663.64	401.64	20.738	0.1	r	LSC 1m
2016-10-02	2457663.64	401.64	20.7767	0.0908	r	LSC 1m
2016-10-02	2457663.65	401.65	21.3678	0.2874	i	LSC 1m
2016-10-02	2457663.65	401.65	20.8352	0.1495	i	LSC 1m
2017-09-17	2458014.40	752.40	21.7737	1.06044	uvw2	Swift
2017-09-17	2458014.41	752.41	21.3745	0.979387	uvw2	Swift
2017-09-20	2458017.16	755.16	21.3871	0.667885	u	Swift
2017-09-20	2458017.17	755.17	21.4974	0.997017	uvw2	Swift

APPENDIX C

Table of Spectroscopic Observations of Literature Sample Used in Nebular Spectra Analysis

C.1. Nebular Spectra Observations from the Literature

TABLE C.1. Table of Nebular Spectroscopic Observations drawn from the literature

Name	JD	Phase (day)	Exposure Time (s)	Instrument	Telescope	Reference	[OI]/Co Luminosity
1988A	2447623.50	447.00		EFOSC1	360 cm ESO	16, 33	$1.1^{+0.22}_{-0.08}$
1990E	2448145.50	210.00		b&c	182cm Ekar	8	$1.3^{+0.15}_{-0.14}$
1990E	2448162.81	227.31	1200.00	EFOSC	360 cm ESO	8	$0.5^{+0.05}_{-0.05}$
1990E	2448175.50	240.00	7200.00	b&c	182cm Ekar	8	$1.9^{+0.21}_{-0.20}$
1990E	2448189.61	254.11		FOS-2	WHT	2, 5	$1.0^{+0.11}_{-0.11}$
1990E	2448191.50	256.00	7200.00	b&c	182cm Ekar	8	$1.8^{+0.20}_{-0.19}$
1990E	2448205.67	270.17	3600.00	EMMI	NTT	8	$1.4^{+0.15}_{-0.15}$
1990E	2448207.50	272.00		MMT-Red	MMT	2, 6	$1.7^{+0.18}_{-0.18}$
1990E	2448219.56	284.06	1800.00	EFOSC1	360 cm ESO	8	$0.9^{+0.10}_{-0.10}$
1990E	2448240.50	305.00		b&c	182cm Ekar	8	$0.7^{+0.08}_{-0.08}$
1990E	2448242.50	307.00		UV Schmidt	Lick	7	$2.1^{+0.23}_{-0.23}$
1990E	2448268.47	332.97		FOS-1	WHT	2, 5	$0.9^{+0.10}_{-0.09}$
1990E	2448306.56	371.06		EFOSC	360 cm ESO	8	$0.2^{+0.02}_{-0.02}$
1990E	2448307.56	372.06		EFOSC	360 cm ESO	8	$0.4^{+0.04}_{-0.04}$
1990E	2448307.56	372.06		EFOSC	360 cm ESO	8	$0.4^{+0.04}_{-0.04}$
1990E	2448308.00	372.50	2400.00	EFOSC	360 cm ESO	8	$0.3^{+0.03}_{-0.03}$
1990K	2448218.55	201.05	1800.00	EFOSC1	360 cm ESO	23	$1.3^{+0.23}_{-0.22}$
1990K	2448218.58	201.08	3600.00	EFOSC1	360 cm ESO	23	$1.8^{+0.31}_{-0.29}$
1990K	2448218.60	201.10	3600.00	EFOSC1	360 cm ESO	23	$1.5^{+0.26}_{-0.25}$
1990K	2448242.50	225.00		UV Schmidt	Lick	1, 7	$1.0^{+0.17}_{-0.16}$
1990K	2448246.50	229.00	3000.00	EFOSC1	360 cm ESO	23	$1.5^{+0.26}_{-0.25}$
1991G	2448636.50	356.50		Red Channel Spectrograph	MMT	2, 28	$1.2^{+0.23}_{-0.23}$
1992H	2448867.50	206.50		Kast	Lick	1	$2.0^{+0.45}_{-0.48}$
1992H	2448886.50	225.50		Kast	Lick	21	$1.6^{+0.37}_{-0.40}$
1992H	2448932.50	271.50		b&c	182cm Ekar	20	$2.1^{+0.48}_{-0.51}$
1992H	2448976.50	315.50		unknown	unknown	16, 20	$2.2^{+0.50}_{-0.53}$
1992H	2448977.50	316.50	11700.00	b&c	182cm Ekar	20	$2.2^{+0.50}_{-0.54}$
1992H	2449047.50	386.50		Kast	Lick	21	$2.9^{+0.67}_{-0.72}$
1992H	2449066.50	405.50	10800.00	b&c	182cm Ekar	20	$2.5^{+0.57}_{-0.61}$
1992H	2449091.50	430.50		Kast	Lick	1	$1.1^{+0.26}_{-0.27}$

Name	JD	Phase (day)	Exposure Time (s)	Instrument	Telescope	Reference	[OI]/Co Luminosity
1992H	2449127.50	466.50		UV Schmidt	Lick	1	$2.8^{+0.65}_{-0.70}$
1992H	2449158.50	497.50		UV Schmidt	Lick	1	$1.9^{+0.44}_{-0.47}$
1992ad	2449030.50	226.00		Kast	Lick	1, 7	$3.2^{+0.34}_{-0.36}$
1992ad	2449091.50	287.00		Kast	Lick	1, 7	$3.3^{+0.35}_{-0.37}$
1997D	2450712.78	345.28	3600.00	EFOSC2	220 cm ESO	16, 25	$2.3^{+0.41}_{-0.29}$
1997D	2450846.56	479.06	300.00	EFOSC2	360 cm ESO	16, 25	$3.5^{+0.60}_{-0.42}$
1999em	2451788.88	312.38	600.00	EFOSC2	360 cm ESO	3	$1.2^{+0.04}_{-0.04}$
1999em	2451793.50	317.00	2100.00	Kast	Lick	2, 4	$1.5^{+0.05}_{-0.04}$
1999em	2451795.60	319.10	3120.00	AFOSC	182cm Ekar	3	$1.8^{+0.06}_{-0.05}$
1999em	2451813.50	337.00	2700.00	Kast	Lick	2, 4	$2.1^{+0.06}_{-0.06}$
1999em	2451867.50	391.00	1800.00	DFOSC	154 cm Danish	3	$1.6^{+0.05}_{-0.05}$
1999em	2451899.50	423.00		Kast	Lick	1, 2	$1.8^{+0.06}_{-0.05}$
1999em	2451941.57	465.07	1800.00	EFOSC2	360 cm ESO	3	$1.9^{+0.06}_{-0.05}$
1999em	2451986.56	510.06	2400.00	DFOSC	154 cm Danish	3	$2.3^{+0.07}_{-0.07}$
1999em	2451997.50	521.00	700.00	LRIS	Keck	2, 4	$2.3^{+0.07}_{-0.07}$
2002hh	2452805.00	228.50		ISIS	WHT	10, 9	$29.3^{+3.04}_{-2.67}$
2002hh	2452828.00	251.50		ALFOSC	NOT	10, 9	$34.5^{+3.57}_{-3.14}$
2002hh	2452914.67	338.17		Kast	Lick	11, 7	$13.2^{+1.37}_{-1.21}$
2002hh	2452972.72	396.22	400.00	LRIS	Keck	11, 7, 9	$46.3^{+4.79}_{-4.22}$
2002hh	2452973.00	396.50	900.00	Kast	Lick	10, 11	$37.4^{+3.87}_{-3.41}$
2004A	2453296.50	286.00		LRIS	Keck	1, 7	$1.3^{+0.22}_{-0.21}$
2004et	2453472.00	201.50	1800.00	Kast	Lick	11, 7	$1.3^{+0.11}_{-0.11}$
2004et	2453477.92	207.42	600.00	Kast	Lick	11, 7	$1.3^{+0.11}_{-0.11}$
2004et	2453481.50	211.00		HFOSC	HCT	15, 16	$1.3^{+0.12}_{-0.11}$
2004et	2453496.50	226.00		HFOSC	HCT	15, 16	$1.4^{+0.12}_{-0.12}$
2004et	2453518.50	248.00		HFOSC	HCT	15, 16	$1.6^{+0.14}_{-0.13}$
2004et	2453522.50	252.00		HFOSC	HCT	15, 16	$1.5^{+0.13}_{-0.13}$
2004et	2453527.70	257.20	1800.00	LRS	TNG	14	$1.4^{+0.12}_{-0.12}$
2004et	2453528.50	258.00		HFOSC	HCT	15, 16	$1.5^{+0.13}_{-0.13}$
2004et	2453552.93	282.43	1260.00	Kast	Lick	11, 7	$1.7^{+0.15}_{-0.14}$
2004et	2453554.56	284.06	300.00	AFOSC	182cm Ekar	14	$1.7^{+0.15}_{-0.15}$
2004et	2453570.50	300.00		HFOSC	HCT	15, 16	$1.7^{+0.15}_{-0.14}$
2004et	2453583.50	313.00		HFOSC	HCT	15, 16	$1.9^{+0.17}_{-0.16}$
2004et	2453611.62	341.12	3600.00	LRS	TNG	14	$1.6^{+0.14}_{-0.14}$
2004et	2453624.85	354.35	1500.00	LRIS	Keck	11, 7	$1.7^{+0.15}_{-0.15}$
2004et	2453654.47	383.97	3600.00	AFOSC	182cm Ekar	14	$1.6^{+0.14}_{-0.13}$
2004et	2453660.50	390.00		HFOSC	HCT	15, 16	$2.2^{+0.19}_{-0.18}$
2004et	2453670.50	400.00		HFOSC	HCT	15, 16	$2.0^{+0.18}_{-0.17}$
2004et	2453671.43	400.93	3600.00	AFOSC	182cm Ekar	14	$1.8^{+0.16}_{-0.16}$
2004et	2453678.25	407.75	2700.00	AFOSC	182cm Ekar	14	$1.8^{+0.16}_{-0.15}$
2004et	2453697.50	427.00		HFOSC	HCT	15, 16	$1.8^{+0.16}_{-0.15}$
2004et	2453734.50	464.00		HFOSC	HCT	15, 16	$2.1^{+0.18}_{-0.17}$
2005ay	2453742.08	288.58	2400.00	Kast	Lick	11, 7	$1.3^{+0.15}_{-0.13}$
2005cs	2453774.68	225.18	2700.00	AFOSC	182cm Ekar	13	$0.5^{+0.07}_{-0.06}$
2005cs	2453819.84	270.34		LRS	HET	13	$1.3^{+0.18}_{-0.16}$

Name	JD	Phase (day)	Exposure Time (s)	Instrument	Telescope	Reference	[OI]/Co Luminosity
2005cs	2453826.53	277.03	1800.01	ISIS	WHT	13	$1.2^{+0.16}_{-0.14}$
2005cs	2453853.03	303.53	604.00	LRIS	Keck	11, 7	$1.3^{+0.18}_{-0.16}$
2005cs	2453882.58	333.08	2700.00	DOLORES	TNG	13	$0.9^{+0.13}_{-0.12}$
2007it	2454563.84	214.84	600.01	WFCCD	250 Du Pont Telescope	22	$1.6^{+0.18}_{-0.15}$
2007it	2454568.87	219.87	600.01	WFCCD	250 Du Pont Telescope	22	$1.6^{+0.18}_{-0.15}$
2007it	2454569.81	220.81	900.01	WFCCD	250 Du Pont Telescope	22	$1.6^{+0.19}_{-0.16}$
2007it	2454585.76	236.76	600.01	WFCCD	250 Du Pont Telescope	22	$1.8^{+0.21}_{-0.18}$
2007it	2454598.72	249.72	600.01	WFCCD	250 Du Pont Telescope	22	$1.9^{+0.22}_{-0.18}$
2007it	2454616.75	267.75	600.00	b&c	250 Du Pont Telescope	22	$2.1^{+0.24}_{-0.20}$
2008bk	2454753.66	210.26	2700.00	EFOSC2	NTT	22	$0.2^{+0.03}_{-0.03}$
2008bk	2454790.69	247.29	1200.00	EFOSC2	NTT	22	$0.5^{+0.05}_{-0.05}$
2008bk	2454795.67	252.27	900.01	WFCCD	250 Du Pont Telescope	22	$0.6^{+0.07}_{-0.07}$
2008bk	2454810.58	267.18	1200.00	EFOSC2	NTT	22	$0.7^{+0.07}_{-0.07}$
2009E	2455058.50	226.00	7200.00	cafos	2.2m CAHA	2, 24	$0.6^{+0.16}_{-0.17}$
2009E	2455218.64	386.14	3600.00	ALFOSC	NOT	2, 24	$1.6^{+0.39}_{-0.42}$
2009E	2455220.50	388.00	3600.00	ALFOSC	NOT	2, 24	$1.7^{+0.41}_{-0.44}$
2009N	2455221.80	374.50		EFOSC2	NTT	2, 29	$1.7^{+0.19}_{-0.15}$
2009N	2455261.80	414.50		FORS2	VLT	2, 29	$1.8^{+0.21}_{-0.16}$
2009dd	2455155.50	230.00		nics	TNG	2, 30	$0.5^{+0.10}_{-0.10}$
2009dd	2455157.50	232.00		DOLORES	TNG	2, 30	$0.8^{+0.18}_{-0.19}$
2009ib	2455260.60	218.80		FORS2	VLT	2, 31	$0.3^{+0.06}_{-0.06}$
2009ib	2455304.50	262.70		EFOSC2	NTT	2, 31	$0.5^{+0.09}_{-0.09}$
2012A	2456326.56	393.06	3600.00	LRS	TNG	17, 18	$3.8^{+0.45}_{-0.41}$
2012A	2456340.80	407.30		Deimos	Keck	1, 7	$4.2^{+0.51}_{-0.46}$
2012A	2456366.50	433.00		LRS	HET	1, 2	$1.7^{+0.21}_{-0.18}$
2012aw	2456252.75	249.25	1800.00	ISIS	WHT	19	$1.9^{+0.17}_{-0.14}$
2012aw	2456334.66	331.16	1800.01	ISIS	WHT	19	$2.3^{+0.20}_{-0.17}$
2012aw	2456340.80	337.30		Deimos	Keck	1, 7	$2.2^{+0.19}_{-0.16}$
2012aw	2456367.80	364.30		LRS	HET	1, 2	$2.4^{+0.21}_{-0.18}$
2012aw	2456454.43	450.93	2700.00	ISIS	WHT	19	$2.5^{+0.22}_{-0.18}$
2012ec	2456547.72	404.22	1800.00	EFOSC2	NTT	2, 27	$0.2^{+0.04}_{-0.03}$
2013ej	2456834.50	337.05		Deimos	Keck	7	$2.3^{+0.21}_{-0.18}$
2013ej	2456867.50	370.05		LRIS	Keck	7	$1.7^{+0.16}_{-0.13}$
2013ej	2456886.80	389.35	2700.00	EFOSC2	NTT	26	$1.7^{+0.16}_{-0.13}$
2013ej	2456886.88	389.43	2700.00	EFOSC2	NTT	26	$1.7^{+0.16}_{-0.13}$
2013ej	2456932.50	435.05		Deimos	Keck	7	$1.4^{+0.13}_{-0.11}$
2015W	2457306.08	281.08	2400.00	LRIS	Keck	10	$2.5^{+0.14}_{-0.13}$
2015W	2457363.91	338.91	3800.00	GMOS-N	Gemini-N	10	$3.1^{+0.17}_{-0.16}$

Name	JD	Phase (day)	Exposure Time (s)	Instrument	Telescope	Reference	[OI]/Co Luminosity

(1) Elmhamdi et al. [2003], (2) Silverman et al. [2017], (3) Yaron and Gal-Yam [2012], (4) Leonard et al. [2002], (5) Gómez and López [2000], (6) Schmidt et al. [1993], (7) Benetti et al. [1994], (8) UC Berkeley SNDB, (9) Pozzo et al. [2006], (10) Valenti et al. [2016], (11) Faran et al. [2014], (12) Silverman et al. [2012], (13) Pastorello et al. [2009], (14) Maguire et al. [2010], (15) Sahu et al. [2006], (16) Richardson et al. [2001], (17) Tomasella priv. comm., (18) Tomasella et al. [2013], (19) Jerkstrand et al. [2014], (20) Filippenko [1997], (21) Clocchiatti et al. [1996], (22) Gutiérrez et al. [2017], (23) Cappellaro et al. [1995], (24) Pastorello et al. [2012], (25) Benetti et al. [2001], (26) Yuan et al. [2016], (27) Jerkstrand et al. [2015], (28) Blanton et al. [1995], (29) Maguire et al. [2012], (30) Inserra et al. [2013], (31) Takáts et al. [2015], (32) de Jaeger et al. [2019], (33) Turatto et al. [1993]

Bibliography

S. M. Adams, C. S. Kochanek, J. R. Gerke, K. Z. Stanek, and X. Dai. The search for failed supernovae with the Large Binocular Telescope: confirmation of a disappearing star. MNRAS, 468(4):4968–4981, July 2017. doi: 10.1093/mnras/stx816.

G. S. Anand, L. Rizzi, and R. B. Tully. A Robust Tip of the Red Giant Branch Distance to the Fireworks Galaxy (NGC 6946). AJ, 156(3):105, Sept. 2018. doi: 10.3847/1538-3881/aad3b2.

J. P. Anderson, S. González-Gaitán, M. Hamuy, C. P. Gutiérrez, M. D. Stritzinger, F. Olivares E., M. M. Phillips, S. Schulze, R. Antezana, L. Bolt, A. Campillay, S. Castellón, C. Contreras, T. de Jaeger, G. Folatelli, F. Förster, W. L. Freedman, L. González, E. Hsiao, W. Krzemiński, K. Krisciunas, J. Maza, P. McCarthy, N. I. Morrell, S. E. Persson, M. Roth, F. Salgado, N. B. Suntzeff, and J. Thomas-Osip. Characterizing the V-band Light-curves of Hydrogen-rich Type II Supernovae. ApJ, 786:67, May 2014. doi: 10.1088/0004-637X/786/1/67.

J. E. Andrews and N. Smith. Strong late-time circumstellar interaction in the peculiar supernova iPTF14hls. MNRAS, 477(1):74–79, Jun 2018. doi: 10.1093/mnras/sty584.

J. E. Andrews, J. S. Gallagher, G. C. Clayton, B. E. K. Sugerman, J. P. Chatelain, J. Clem, D. L. Welch, M. J. Barlow, B. Ercolano, J. Fabbri, R. Wesson, and M. Meixner. SN 2007od: A Type IIP Supernova with Circumstellar Interaction. ApJ, 715(1):541–549, May 2010. doi: 10.1088/0004-637X/715/1/541.

J. E. Andrews, B. E. K. Sugerman, G. C. Clayton, J. S. Gallagher, M. J. Barlow, J. Clem, B. Ercolano, J. Fabbri, M. Meixner, M. Otsuka, D. L. Welch, and R. Wesson. Photometric and Spectroscopic Evolution of the IIP SN 2007it to Day 944. ApJ, 731(1):47, Apr. 2011. doi: 10.1088/0004-637X/731/1/47.

J. E. Andrews, D. J. Sand, S. Valenti, N. Smith, R. Dastidar, D. K. Sahu, K. Misra, A. Singh, D. Hiramatsu, and P. J. Brown. SN 2017gmr: An energetic Type II-P supernova with asymmetries. *arXiv e-prints*, art. arXiv:1907.01013, Jul 2019.

I. Arcavi, A. Gal-Yam, S. B. Cenko, D. B. Fox, D. C. Leonard, D.-S. Moon, D. J. Sand, A. M. Soderberg, M. Kiewe, O. Yaron, A. B. Becker, R. Scheps, G. Birenbaum, D. Chamudot, and J. Zhou. Caltech Core-Collapse Project (CCCP) Observations of Type II Supernovae: Evidence for Three Distinct Photometric Subtypes. ApJ, 756:L30, Sept. 2012. doi: 10.1088/2041-8205/756/2/L30.

M. Asplund, N. Grevesse, A. J. Sauval, and P. Scott. The Chemical Composition of the Sun. ARA&A, 47(1):481–522, Sep 2009. doi: 10.1146/annurev.astro.46.060407.145222.

I. S. Balinskaia, K. V. Bychkov, and S. I. Neizvestnyi. The UBVR-photometry of the supernova in NGC 4321. A&A, 85:L19, May 1980.

C. Barbarino, M. Dall'Ora, M. T. Botticella, M. Della Valle, L. Zampieri, J. R. Maund, M. L. Pumo, A. Jerkstrand, S. Benetti, N. Elias-Rosa, M. Fraser, A. Gal-Yam, M. Hamuy, C. Inserra, C. Knapic, A. P. LaCluyze, M. Molinaro, P. Ochner, A. Pastorello, G. Pignata, D. E. Reichart, C. Ries, A. Riffeser, B. Schmidt, M. Schmidt, R. Smareglia, S. J. Smartt, K. Smith, J. Sollerman, M. Sullivan, L. Tomasella, M. Turatto, S. Valenti, O. Yaron, and D. Young. SN 2012ec: mass of the progenitor from PESSTO follow-up of the photospheric phase. MNRAS, 448(3):2312–2331, Apr. 2015. doi: 10.1093/mnras/stv106.

R. Barbon, F. Ciatti, L. Rosino, S. Ortolani, and P. Rafanelli. Spectra and light curves of three recent supernovae. A&A, 116:43–53, Dec. 1982.

E. Baron, D. Branch, and P. H. Hauschildt. Reddening, Abundances, and Line Formation in SNe II. ApJ, 662(2):1148–1155, June 2007. doi: 10.1086/517961.

S. Benetti, E. Cappellaro, and M. Turatto. Photometric and spectroscopic obseravtions of four supernovae. A&A, 247:410, July 1991.

S. Benetti, E. Cappellaro, M. Turatto, M. della Valle, P. A. Mazzali, and C. Gouiffes. The late evolution of the type II SN 1990E. A&A, 285:147–156, May 1994.

S. Benetti, M. Turatto, S. Balberg, L. Zampieri, S. L. Shapiro, E. Cappellaro, K. Nomoto, T. Nakamura, P. A. Mazzali, and F. Patat. The fading of supernova 1997D. MNRAS, 322(2):361–368, Apr. 2001. doi: 10.1046/j.1365-8711.2001.04122.x.

S. Benetti, N. N. Chugai, V. P. Utrobin, E. Cappellaro, F. Patat, A. Pastorello, M. Turatto, G. Cupani, R. Neuhäuser, N. Caldwell, G. Pignata, and L. Tomasella. The spectacular evolution

of Supernova 1996al over 15 yr: a low-energy explosion of a stripped massive star in a highly structured environment. MNRAS, 456:3296–3317, Mar. 2016. doi: 10.1093/mnras/stv2811.

M. C. Bersten, O. Benvenuto, and M. Hamuy. Hydrodynamical Models of Type II Plateau Supernovae. ApJ, 729(1):61, Mar. 2011. doi: 10.1088/0004-637X/729/1/61.

E. L. Blanton, B. P. Schmidt, R. P. Kirshner, C. H. Ford, F. R. Chromey, and W. Herbst. Observations of the Type II-P SN 1991G in NGC 4088. AJ, 110:2868, Dec. 1995. doi: 10.1086/117735.

S. I. Blinnikov and O. S. Bartunov. Non-equilibrium radiative transfer in supernova theory : models of linear type II supernovae. A&A, 273:106–122, June 1993.

S. I. Blinnikov and O. S. Bartunov. STELLA: Multi-group Radiation Hydrodynamics Code. ASCL, Aug 2011.

S. I. Blinnikov, F. K. Röpke, E. I. Sorokina, M. Gieseler, M. Reinecke, C. Travaglio, W. Hillebrand t, and M. Stritzinger. Theoretical light curves for deflagration models of type Ia supernova. A&A, 453(1):229–240, Jul 2006. doi: 10.1051/0004-6361:20054594.

S. Blondin and J. L. Tonry. Determining the Type, Redshift, and Age of a Supernova Spectrum. ApJ, 666:1024–1047, Sept. 2007. doi: 10.1086/520494.

S. Blondin and J. L. Tonry. SNID: Supernova Identification. Astrophysics Source Code Library, July 2011.

S. Bose, B. Kumar, F. Sutaria, B. Kumar, R. Roy, V. K. Bhatt, S. B. Pandey, H. C. Chandola, R. Sagar, K. Misra, and S. Chakraborti. Supernova 2012aw - a high-energy clone of archetypal Type IIP SN 1999em. MNRAS, 433(3):1871–1891, Aug. 2013. doi: 10.1093/mnras/stt864.

K. A. Bostroem, S. Valenti, A. Horesh, V. Morozova, N. P. M. Kuin, S. Wyatt, A. Jerkstrand, D. J. Sand, M. Lundquist, M. Smith, M. Sullivan, G. Hosseinzadeh, I. Arcavi, E. Callis, R. Cartier, A. Gal-Yam, L. Galbany, C. Gutiérrez, D. A. Howell, C. Inserra, E. Kankare, K. M. López, C. McCully, G. Pignata, A. L. Piro, Ó. Rodríguez, S. J. Smartt, K. W. Smith, O. Yaron, and D. R. Young. Signatures of circumstellar interaction in the Type IIL supernova ASASSN-15oz. MNRAS, 485(4):5120–5141, June 2019. doi: 10.1093/mnras/stz570.

K. A. Bostroem, S. Valenti, D. J. Sand, J. E. Andrews, S. D. Van Dyk, L. Galbany, D. Pooley, R. C. Amaro, N. Smith, S. Yang, G. C. Anupama, I. Arcavi, E. Baron, P. J. Brown, J. Burke, R. Cartier, D. Hiramatsu, R. Dastidar, J. M. DerKacy, Y. Dong, E. Egami, S. Ertel, A. V.

Filippenko, O. D. Fox, J. Haislip, G. Hosseinzadeh, D. A. Howell, A. Gangopadhyay, S. W. Jha, V. Kouprianov, B. Kumar, M. Lundquist, D. Milisavljevic, C. McCully, P. Milne, K. Misra, D. E. Reichart, D. K. Sahu, H. Sai, A. Singh, P. S. Smith, J. Vinko, X. Wang, Y. Wang, J. C. Wheeler, G. G. Williams, S. Wyatt, J. Zhang, and X. Zhang. Discovery and Rapid Follow-up Observations of the Unusual Type II SN 2018ivc in NGC 1068. ApJ, 895(1):31, May 2020. doi: 10.3847/1538-4357/ab8945.

A. A. Breeveld, P. A. Curran, E. A. Hoversten, S. Koch, W. Landsman, F. E. Marshall, M. J. Page, T. S. Poole, P. Roming, P. J. Smith, M. Still, V. Yershov, A. J. Blustin, P. J. Brown, C. Gronwall, S. T. Holland, N. P. M. Kuin, K. McGowan, S. Rosen, P. Boyd, P. Broos, M. Carter, M. M. Chester, B. Hancock, H. Huckle, S. Immler, M. Ivanushkina, T. Kennedy, K. O. Mason, A. N. Morgan, S. Oates, M. de Pasquale, P. Schady, M. Siegel, and D. vanden Berk. Further calibration of the Swift ultraviolet/optical telescope. MNRAS, 406:1687–1700, Aug. 2010. doi: 10.1111/j.1365-2966.2010.16832.x.

J. S. Brown, K. Z. Stanek, T. W. S. Holoien, C. S. Kochanek, G. Simonian, U. Basu, D. Godoy, J. F. Beacom, T. A. Thompson, B. J. Shappee, J. L. Prieto, D. Bersier, S. Dong, and J. Brimacombe. ASAS-SN Discovery of A Probable Bright Supernova in HIPASS J1919-33. *The Astronomer's Telegram*, 7989:1, Sept. 2015.

P. J. Brown, S. T. Holland, S. Immler, P. Milne, P. W. A. Roming, N. Gehrels, J. Nousek, N. Panagia, M. Still, and D. Vanden Berk. Ultraviolet Light Curves of Supernovae with the Swift Ultraviolet/Optical Telescope. AJ, 137:4517–4525, May 2009. doi: 10.1088/0004-6256/137/5/4517.

P. J. Brown, A. A. Breeveld, S. Holland, P. Kuin, and T. Pritchard. SOUSA: the Swift Optical/Ultraviolet Supernova Archive. Ap&SS, 354:89–96, nov 2014. doi: 10.1007/s10509-014-2059-8.

T. M. Brown, N. Baliber, F. B. Bianco, M. Bowman, B. Burleson, P. Conway, M. Crellin, É. Depagne, J. De Vera, B. Dilday, D. Dragomir, M. Dubberley, J. D. Eastman, M. Elphick, M. Falarski, S. Foale, M. Ford, B. J. Fulton, J. Garza, E. L. Gomez, M. Graham, R. Greene, B. Haldeman, E. Hawkins, B. Haworth, R. Haynes, M. Hidas, A. E. Hjelstrom, D. A. Howell, J. Hygelund, T. A. Lister, R. Lobdill, J. Martinez, D. S. Mullins, M. Norbury, J. Parrent,

R. Paulson, D. L. Petry, A. Pickles, V. Posner, W. E. Rosing, R. Ross, D. J. Sand, E. S. Saunders, J. Shobbrook, A. Shporer, R. A. Street, D. Thomas, Y. Tsapras, J. R. Tufts, S. Valenti, K. Vander Horst, Z. Walker, G. White, and M. Willis. Las Cumbres Observatory Global Telescope Network. *Publications of the Astronomical Society of the Pacific*, 125:1031, Sept. 2013. doi: 10.1086/673168.

G. Bruzual. Stellar Populations: High Spectral Resolution Libraries. Improved TP-AGB Treatment. In A. Vallenari, R. Tantalo, L. Portinari, and A. Moretti, editors, *From Stars to Galaxies: Building the Pieces to Build Up the Universe*, volume 374 of *Astronomical Society of the Pacific Conference Series*, page 303, Dec. 2007.

C. Bullivant, N. Smith, G. G. Williams, J. C. Mauerhan, J. E. Andrews, W.-F. Fong, C. Bilinski, C. D. Kilpatrick, P. A. Milne, O. D. Fox, S. B. Cenko, A. V. Filippenko, W. Zheng, P. L. Kelly, and K. I. Clubb. SN 2013fs and SN 2013fr: exploring the circumstellar-material diversity in Type II supernovae. MNRAS, 476:1497–1518, May 2018. doi: 10.1093/mnras/sty045.

R. J. Buta. Photometric observations of the bright type II supernova 1980k in NGC 6946. *Publications of the Astronomical Society of the Pacific*, 94:578–585, June 1982. doi: 10.1086/131026.

B. Buzzoni, B. Delabre, H. Dekker, S. Dodorico, D. Enard, P. Focardi, B. Gustafsson, W. Nees, J. Paureau, and R. Reiss. The ESO Faint Object Spectrograph and Camera (EFOSC). *The Messenger*, 38:9–13, Dec. 1984.

E. Cappellaro, I. J. Danziger, M. della Valle, C. Gouiffes, and M. Turatto. The bright linear type II SN 1990K. A&A, 293:723–732, Jan. 1995.

J. A. Cardelli, G. C. Clayton, and J. S. Mathis. The Relationship between Infrared, Optical, and Ultraviolet Extinction. ApJ, 345:245, Oct. 1989. doi: 10.1086/167900.

A. C. Carnall. SpectRes: A Fast Spectral Resampling Tool in Python. *arXiv e-prints*, art. arXiv:1705.05165, May 2017.

W. Cash. Parameter estimation in astronomy through application of the likelihood ratio. *The Astrophysical Journal*, 228:939–947, Mar 1979. doi: 10.1086/156922.

R. A. Chevalier. The radio and X-ray emission from type II supernovae. ApJ, 259:302–310, Aug. 1982. doi: 10.1086/160167.

R. A. Chevalier. Synchrotron Self-Absorption in Radio Supernovae. ApJ, 499:810–819, May 1998. doi: 10.1086/305676.

R. A. Chevalier and C. Fransson. Circumstellar Emission from Type Ib and Ic Supernovae. ApJ, 651:381–391, Nov. 2006. doi: 10.1086/507606.

M. J. Childress, B. E. Tucker, F. Yuan, R. Scalzo, A. Ruiter, I. Seitenzahl, B. Zhang, B. Schmidt, B. Anguiano, S. Aniyan, D. D. R. Bayliss, J. Bento, M. Bessell, F. Bian, R. Davies, M. Dopita, L. Fogarty, A. Fraser- McKelvie, K. Freeman, R. Kuruwita, A. M. Medling, S. J. Murphy, S. J. Murphy, M. Owers, F. Panther, S. M. Sweet, A. D. Thomas, and G. Zhou. The ANU WiFeS SuperNovA Programme (AWSNAP). *Publications of the Astronomical Society of Australia*, 33: e055, Nov. 2016. doi: 10.1017/pasa.2016.47.

J. Choi, A. Dotter, C. Conroy, M. Cantiello, B. Paxton, and B. D. Johnson. Mesa Isochrones and Stellar Tracks (MIST). I. Solar-scaled Models. ApJ, 823:102, June 2016. doi: 10.3847/0004-637X/823/2/102.

N. N. Chugai. Indications of a Superwind in the Lightcurves of Type-II Supernovae. Soviet Ast., 36:63, Feb. 1992.

N. N. Chugai. Broad emission lines from the opaque electron-scattering environment of SN 1998S. MNRAS, 326:1448–1454, Oct. 2001. doi: 10.1111/j.1365-2966.2001.04717.x.

N. N. Chugai, S. N. Fabrika, O. N. Sholukhova, V. P. Goranskij, P. K. Abolmasov, and V. V. Vlasyuk. Optical Observations of Type-IIP Supernova 2004dj: Evidence for Asymmetry of the 56Ni Ejecta. *Astronomy Letters*, 31:792–805, Dec. 2005. doi: 10.1134/1.2138766.

N. N. Chugai, R. A. Chevalier, and V. P. Utrobin. Optical Signatures of Circumstellar Interaction in Type IIP Supernovae. ApJ, 662:1136–1147, June 2007. doi: 10.1086/518160.

R. Cid Fernandes, A. Mateus, L. Sodré, G. Stasińska, and J. M. Gomes. Semi-empirical analysis of Sloan Digital Sky Survey galaxies - I. Spectral synthesis method. MNRAS, 358:363–378, Apr. 2005. doi: 10.1111/j.1365-2966.2005.08752.x.

A. Clocchiatti, S. Benetti, J. C. Wheeler, W. Wren, J. Boisseau, E. Cappellaro, M. Turatto, F. Patat, D. A. Swartz, R. P. Harkness, M. S. Brotherton, B. Wills, P. Hemenway, M. Cornell, M. Frueh, and M. B. Kaiser. A Study of SN 1992H in NGC 5377. AJ, 111:1286, Mar. 1996. doi: 10.1086/117874.

R. M. Crockett, S. J. Smartt, A. Pastorello, J. J. Eldridge, A. W. Stephens, J. R. Maund, and S. Mattila. On the nature of the progenitors of three Type II-P supernovae: 2004et, 2006my and 2006ov. MNRAS, 410(4):2767–2786, Feb. 2011. doi: 10.1111/j.1365-2966.2010.17652.x.

M. C. Cushing, W. D. Vacca, and J. T. Rayner. Spextool: A Spectral Extraction Package for SpeX, a 0.8-5.5 Micron Cross-Dispersed Spectrograph. *Publications of the Astronomical Society of the Pacific*, 116:362–376, Apr. 2004. doi: 10.1086/382907.

M. Dall'Ora, M. T. Botticella, M. L. Pumo, L. Zampieri, L. Tomasella, G. Pignata, A. J. Bayless, T. A. Pritchard, S. Taubenberger, R. Kotak, C. Inserra, M. Della Valle, E. Cappellaro, S. Benetti, S. Benitez, F. Bufano, N. Elias-Rosa, M. Fraser, J. B. Haislip, A. Harutyunyan, D. A. Howell, E. Y. Hsiao, T. Iijima, E. Kankare, P. Kuin, J. R. Maund, A. Morales-Garoffolo, N. Morrell, U. Munari, P. Ochner, A. Pastorello, F. Patat, M. M. Phillips, D. Reichart, P. W. A. Roming, A. Siviero, S. J. Smartt, J. Sollerman, F. Taddia, S. Valenti, and D. Wright. The Type IIP Supernova 2012aw in M95: Hydrodynamical Modeling of the Photospheric Phase from Accurate Spectrophotometric Monitoring. ApJ, 787(2):139, June 2014. doi: 10.1088/0004-637X/787/2/139.

B. Davies and E. R. Beasor. The initial masses of the red supergiant progenitors to Type II supernovae. MNRAS, 474:2116–2128, Feb. 2018. doi: 10.1093/mnras/stx2734.

T. de Jaeger, W. Zheng, B. E. Stahl, A. V. Filippenko, T. G. Brink, A. Bigley, K. Blanchard, P. K. Blanchard, J. Bradley, S. K. Cargill, C. Casper, S. B. Cenko, S. Channa, B. Y. Choi, K. I. Clubb, B. E. Cobb, D. Cohen, M. de Kouchkovsky, M. Ellison, E. Falcon, O. D. Fox, K. Fuller, M. Ganeshalingam, C. Gould, M. L. Graham, G. Halevi, K. T. Hayakawa, J. Hestenes, M. P. Hyland, B. Jeffers, N. Joubert, M. T. Kandrashoff, P. L. Kelly, H. Kim, M. Kim, S. Kumar, E. J. Leonard, G. Z. Li, T. B. Lowe, P. Lu, M. Mason, K. J. McAllister, J. C. Mauerhan, M. Modjaz, J. Molloy, D. A. Perley, K. Pina, D. Poznanski, T. W. Ross, I. Shivvers, J. M. Silverman, C. Soler, S. Stegman, S. Taylor, K. Tang, A. Wilkins, X. Wang, X. Wang, H. Yuk, S. Yunus, and K. D. Zhang. The Berkeley sample of Type II supernovae: BVRI light curves and spectroscopy of 55 SNe II. MNRAS, 490(2):2799–2821, Dec. 2019. doi: 10.1093/mnras/stz2714.

G. de Vaucouleurs, A. de Vaucouleurs, R. Buta, H. D. Ables, and A. V. Hewitt. The bright SN 1979 C in M 100. *Publications of the Astronomical Society of the Pacific*, 93:36–44, Feb. 1981.

doi: 10.1086/130772.

L. Dessart and D. J. Hillier. Quantitative spectroscopy of photospheric-phase type II supernovae. A&A, 437:667–685, July 2005. doi: 10.1051/0004-6361:20042525.

L. Dessart, S. Blondin, P. J. Brown, M. Hicken, D. J. Hillier, S. T. Holland, S. Immler, R. P. Kirshner, P. Milne, M. Modjaz, and P. W. A. Roming. Using Quantitative Spectroscopic Analysis to Determine the Properties and Distances of Type II Plateau Supernovae: SN 2005cs and SN 2006bp. ApJ, 675(1):644–669, Mar. 2008. doi: 10.1086/526451.

L. Dessart, D. J. Hillier, T. Sukhbold, S. Woosley, and H. T. Janka. The explosion of $9-29M_{\odot}$ stars as Type II supernovae : results from radiative-transfer modeling at one year after explosion. *arXiv e-prints*, art. arXiv:2105.13029, May 2021.

G. Dhungana, R. Kehoe, J. Vinko, J. M. Silverman, J. C. Wheeler, W. Zheng, G. H. Marion, O. D. Fox, C. Akerlof, B. I. Biro, T. Borkovits, S. B. Cenko, K. I. Clubb, A. V. Filippenko, F. V. Ferrante, C. A. Gibson, M. L. Graham, T. Hegedus, P. Kelly, J. Kelemen, W. H. Lee, G. Marschalko, L. Molnár, A. P. Nagy, A. Ordasi, A. Pal, K. Sarneczky, I. Shivvers, R. Szakats, T. Szalai, E. Szegedi-Elek, P. Székely, A. Szing, K. Takáts, and K. Vida. Extensive Spectroscopy and Photometry of the Type IIP Supernova 2013ej. ApJ, 822:6, May 2016. doi: 10.3847/0004-637X/822/1/6.

A. Dolphin. DOLPHOT: Stellar photometry. Astrophysics Source Code Library, Aug. 2016.

A. E. Dolphin. WFPC2 Stellar Photometry with HSTPHOT. PASP, 112(776):1383–1396, Oct 2000. doi: 10.1086/316630.

A. Dotter. MESA Isochrones and Stellar Tracks (MIST) 0: Methods for the Construction of Stellar Isochrones. ApJS, 222:8, Jan. 2016. doi: 10.3847/0067-0049/222/1/8.

R. G. Eastman, B. P. Schmidt, and R. Kirshner. The Atmospheres of Type II Supernovae and the Expanding Photosphere Method. ApJ, 466:911, Aug. 1996. doi: 10.1086/177563.

P. P. Eggleton. The evolution of low mass stars. MNRAS, 151:351, Jan 1971. doi: 10.1093/mnras/151.3.351.

M. Eichler, K. Nakamura, T. Takiwaki, T. Kuroda, K. Kotake, M. Hempel, R. Cabezón, M. Liebendörfer, and F. K. Thielemann. Nucleosynthesis in 2D core-collapse supernovae of 11.2 and 17.0 M progenitors: implications for Mo and Ru production. *Journal of Physics G*

Nuclear Physics, 45(1):014001, Jan. 2018. doi: 10.1088/1361-6471/aa8891.

J. J. Eldridge and C. A. Tout. The progenitors of core-collapse supernovae. MNRAS, 353(1):87–97, Sep 2004. doi: 10.1111/j.1365-2966.2004.08041.x.

J. J. Eldridge, E. R. Stanway, L. Xiao, L. A. S. McClelland , G. Taylor, M. Ng, S. M. L. Greis, and J. C. Bray. Binary Population and Spectral Synthesis Version 2.1: Construction, Observational Verification, and New Results. PASA, 34:e058, Nov 2017. doi: 10.1017/pasa.2017.51.

N. Elias-Rosa, S. D. Van Dyk, W. Li, A. A. Miller, J. M. Silverman, M. Ganeshalingam, A. F. Boden, M. M. Kasliwal, J. Vinkó, J.-C. Cuillandre, A. V. Filippenko, T. N. Steele, J. S. Bloom, C. V. Griffith, I. K. W. Kleiser, and R. J. Foley. The Massive Progenitor of the Type II-linear Supernova 2009kr. ApJ, 714(2):L254–L259, May 2010. doi: 10.1088/2041-8205/714/2/L254.

N. Elias-Rosa, S. D. Van Dyk, W. Li, J. M. Silverman, R. J. Foley, M. Ganeshalingam, J. C. Mauerhan, E. Kankare, S. Jha, A. V. Filippenko, J. E. Beckman, E. Berger, J.-C. Cuillandre, and N. Smith. The Massive Progenitor of the Possible Type II-Linear Supernova 2009hd in Messier 66. ApJ, 742(1):6, Nov. 2011. doi: 10.1088/0004-637X/742/1/6.

A. Elmhamdi, I. J. Danziger, N. Chugai, A. Pastorello, M. Turatto, E. Cappellaro, G. Altavilla, S. Benetti, F. Patat, and M. Salvo. Photometry and spectroscopy of the Type IIP SN 1999em from outburst to dust formation. MNRAS, 338:939–956, Feb. 2003. doi: 10.1046/j.1365-8711.2003.06150.x.

T. Faran, D. Poznanski, A. V. Filippenko, R. Chornock, R. J. Foley, M. Ganeshalingam, D. C. Leonard, W. Li, M. Modjaz, E. Nakar, F. J. D. Serduke, and J. M. Silverman. Photometric and spectroscopic properties of Type II-P supernovae. MNRAS, 442:844–861, July 2014. doi: 10.1093/mnras/stu955.

A. Fassia, W. P. S. Meikle, W. D. Vacca, S. N. Kemp, N. A. Walton, D. L. Pollacco, S. Smartt, A. Oscoz, A. Aragón-Salamanca, S. Bennett, T. G. Hawarden, A. Alonso, D. Alcalde, A. Pedrosa, J. Telting, M. J. Arevalo, H. J. Deeg, F. Garzón, A. Gómez-Roldán, G. Gómez, C. Gutiérrez, S. López, M. Rozas, M. Serra-Ricart, and M. R. Zapatero-Osorio. Optical and infrared photometry of the Type IIn SN 1998S: days 11-146. MNRAS, 318:1093–1104, Nov. 2000. doi: 10.1046/j.1365-8711.2000.03797.x.

J. W. Ferguson, D. R. Alexander, F. Allard, T. Barman, J. G. Bodnarik, P. H. Hauschildt, A. Heffner-Wong, and A. Tamanai. Low-Temperature Opacities. ApJ, 623:585–596, Apr. 2005. doi: 10.1086/428642.

A. V. Filippenko. The importance of atmospheric differential refraction in spectrophotometry. PASP, 94:715–721, Aug. 1982. doi: 10.1086/131052.

A. V. Filippenko. Optical Spectra of Supernovae. ARA&A, 35:309–355, Jan 1997. doi: 10.1146/annurev.astro.35.1.309.

E. L. Fitzpatrick. Correcting for the Effects of Interstellar Extinction. PASP, 111(755):63–75, Jan 1999. doi: 10.1086/316293.

R. J. Foley, E. Berger, O. Fox, E. M. Levesque, P. J. Challis, I. I. Ivans, J. E. Rhoads, and A. M. Soderberg. The Diversity of Massive Star Outbursts. I. Observations of SN2009ip, UGC 2773 OT2009-1, and Their Progenitors. ApJ, 732(1):32, May 2011. doi: 10.1088/0004-637X/732/1/32.

F. Förster, T. J. Moriya, J. C. Maureira, J. P. Anderson, S. Blinnikov, F. Bufano, G. Cabrera-Vives, A. Clocchiatti, T. de Jaeger, P. A. Estévez, L. Galbany, S. González-Gaitán, G. Gräfener, M. Hamuy, E. Y. Hsiao, P. Huentelemu, P. Huijse, H. Kuncarayakti, J. Martínez, G. Medina, F. Olivares E., G. Pignata, A. Razza, I. Reyes, J. San Martín, R. C. Smith, E. Vera, A. K. Vivas, A. de Ugarte Postigo, S.-C. Yoon, C. Ashall, M. Fraser, A. Gal-Yam, E. Kankare, L. Le Guillou, P. A. Mazzali, N. A. Walton, and D. R. Young. The delay of shock breakout due to circumstellar material evident in most type II supernovae. *Nature Astronomy*, Sept. 2018. doi: 10.1038/s41550-018-0563-4.

M. Fraser, K. Takáts, A. Pastorello, S. J. Smartt, S. Mattila, M. T. Botticella, S. Valenti, M. Ergon, J. Sollerman, I. Arcavi, S. Benetti, F. Bufano, R. M. Crockett, I. J. Danziger, A. Gal-Yam, J. R. Maund, S. Taubenberger, and M. Turatto. On the Progenitor and Early Evolution of the Type II Supernova 2009kr. ApJ, 714(2):L280–L284, May 2010. doi: 10.1088/2041-8205/714/2/L280.

M. Fraser, M. Ergon, J. J. Eldridge, S. Valenti, A. Pastorello, J. Sollerman, S. J. Smartt, I. Agnoletto, I. Arcavi, S. Benetti, M. T. Botticella, F. Bufano, A. Campillay, R. M. Crockett, A. Gal-Yam, E. Kankare, G. Leloudas, K. Maguire, S. Mattila, J. R. Maund, F. Salgado, A. Stephens, S. Taubenberger, and M. Turatto. SN 2009md: another faint supernova from a low-mass progenitor. MNRAS, 417(2):1417–1433, Oct. 2011. doi: 10.1111/j.1365-2966.2011.19370.x.

M. Fraser, J. R. Maund, S. J. Smartt, R. Kotak, A. Lawrence, A. Bruce, S. Valenti, F. Yuan, S. Benetti, T. W. Chen, A. Gal-Yam, C. Inserra, and D. R. Young. On the progenitor of the Type IIP SN 2013ej in M74. MNRAS, 439:L56–L60, Mar. 2014. doi: 10.1093/mnrasl/slt179.

P. Freeman, S. Doe, and A. Siemiginowska. Sherpa: a mission-independent data analysis application. In J.-L. Starck and F. D. Murtagh, editors, *Astronomical Data Analysis*, volume 4477 of *Society of Photo-Optical Instrumentation Engineers (SPIE) Conference Series*, pages 76–87, Nov 2001. doi: 10.1117/12.447161.

W. Freudling, M. Romaniello, D. M. Bramich, P. Ballester, V. Forchi, C. E. García-Dabló, S. Moehler, and M. J. Neeser. Automated data reduction workflows for astronomy. The ESO Reflex environment. A&A, 559:A96, Nov. 2013. doi: 10.1051/0004-6361/201322494.

A. Fruscione, J. C. McDowell, G. E. Allen, N. S. Brickhouse, D. J. Burke, J. E. Davis, N. Durham, M. Elvis, E. C. Galle, D. E. Harris, D. P. Huenemoerder, J. C. Houck, B. Ishibashi, M. Karovska, F. Nicastro, M. S. Noble, M. A. Nowak, F. A. Primini, A. Siemiginowska, R. K. Smith, and M. Wise. CIAO: Chandra's data analysis system. In *Society of Photo-Optical Instrumentation Engineers (SPIE) Conference Series*, volume 6270 of *Society of Photo-Optical Instrumentation Engineers (SPIE) Conference Series*, page 62701V, Jun 2006. doi: 10.1117/12.671760.

C. L. Fryer. Mass Limits For Black Hole Formation. ApJ, 522:413–418, Sept. 1999. doi: 10.1086/307647.

J. Fuller. Pre-supernova outbursts via wave heating in massive stars - I. Red supergiants. MNRAS, 470:1642–1656, Sept. 2017. doi: 10.1093/mnras/stx1314.

A. Gal-Yam, I. Arcavi, E. O. Ofek, S. Ben-Ami, S. B. Cenko, M. M. Kasliwal, Y. Cao, O. Yaron, D. Tal, J. M. Silverman, A. Horesh, A. De Cia, F. Taddia, J. Sollerman, D. Perley, P. M. Vreeswijk, S. R. Kulkarni, P. E. Nugent, A. V. Filippenko, and J. C. Wheeler. A Wolf-Rayet-like progenitor of SN 2013cu from spectral observations of a stellar wind. Nature, 509:471–474, May 2014. doi: 10.1038/nature13304.

L. Galbany, V. Stanishev, A. M. Mourão, M. Rodrigues, H. Flores, R. García-Benito, D. Mast, M. A. Mendoza, S. F. Sánchez, C. Badenes, J. Barrera-Ballesteros, J. Bland-Hawthorn, J. Falcón-Barroso, B. García-Lorenzo, J. M. Gomes, R. M. González Delgado, C. Kehrig, M. Lyubenova, A. R. López-Sánchez, A. de Lorenzo-Cáceres, R. A. Marino, S. Meidt, M. Mollá, P. Papaderos,

M. A. Pérez-Torres, F. F. Rosales-Ortega, and G. van de Ven. Nearby supernova host galaxies from the CALIFA Survey. I. Sample, data analysis, and correlation to star-forming regions. A&A, 572:A38, Dec. 2014. doi: 10.1051/0004-6361/201424717.

L. Galbany, J. P. Anderson, F. F. Rosales-Ortega, H. Kuncarayakti, T. Krühler, S. F. Sánchez, J. Falcón-Barroso, E. Pérez, J. C. Maureira, M. Hamuy, S. González-Gaitán, F. Förster, and V. Moral. Characterizing the environments of supernovae with MUSE. MNRAS, 455(4):4087–4099, Feb 2016a. doi: 10.1093/mnras/stv2620.

L. Galbany, M. Hamuy, M. M. Phillips, N. B. Suntzeff, J. Maza, T. de Jaeger, T. Moraga, S. González-Gaitán, K. Krisciunas, N. I. Morrell, J. Thomas-Osip, W. Krzeminski, L. González, R. Antezana, M. Wishnjewski, P. McCarthy, J. P. Anderson, C. P. Gutiérrez, M. Stritzinger, G. Folatelli, C. Anguita, G. Galaz, E. M. Green, C. Impey, Y.-C. Kim, S. Kirhakos, M. A. Malkan, J. S. Mulchaey, A. C. Phillips, A. Pizzella, C. F. Prosser, B. P. Schmidt, R. A. Schommer, W. Sherry, L.-G. Strolger, L. A. Wells, and G. M. Williger. UBVRIz Light Curves of 51 Type II Supernovae. AJ, 151:33, Feb. 2016b. doi: 10.3847/0004-6256/151/2/33.

L. Galbany, V. Stanishev, A. M. Mourão, M. Rodrigues, H. Flores, C. J. Walcher, S. F. Sánchez, R. García-Benito, D. Mast, C. Badenes, R. M. González Delgado, C. Kehrig, M. Lyubenova, R. A. Marino, M. Mollá, S. Meidt, E. Pérez, G. van de Ven, and J. M. Vílchez. Nearby supernova host galaxies from the CALIFA survey. II. Supernova environmental metallicity. A&A, 591:A48, June 2016c. doi: 10.1051/0004-6361/201528045.

L. Galbany, J. P. Anderson, S. F. Sánchez, H. Kuncarayakti, S. Pedraz, S. González-Gaitán, V. Stanishev, I. Domínguez, M. E. Moreno-Raya, W. M. Wood-Vasey, A. M. Mourão, K. A. Ponder, C. Badenes, M. Mollá, A. R. López-Sánchez, F. F. Rosales-Ortega, J. M. Vílchez, R. García-Benito, and R. A. Marino. PISCO: The PMAS/PPak Integral-field Supernova Hosts Compilation. ApJ, 855:107, Mar. 2018. doi: 10.3847/1538-4357/aaaf20.

N. Gehrels, G. Chincarini, P. Giommi, K. O. Mason, J. A. Nousek, A. A. Wells, N. E. White, S. D. Barthelmy, D. N. Burrows, L. R. Cominsky, K. C. Hurley, F. E. Marshall, P. Mészáros, P. W. A. Roming, L. Angelini, L. M. Barbier, T. Belloni, S. Campana, P. A. Caraveo, M. M. Chester, O. Citterio, T. L. Cline, M. S. Cropper, J. R. Cummings, A. J. Dean, E. D. Feigelson, E. E. Fenimore, D. A. Frail, A. S. Fruchter, G. P. Garmire, K. Gendreau, G. Ghisellini, J. Greiner, J. E.

Hill, S. D. Hunsberger, H. A. Krimm, S. R. Kulkarni, P. Kumar, F. Lebrun, N. M. Lloyd-Ronning, C. B. Markwardt, B. J. Mattson, R. F. Mushotzky, J. P. Norris, J. Osborne, B. Paczynski, D. M. Palmer, H. S. Park, A. M. Parsons, J. Paul, M. J. Rees, C. S. Reynolds, J. E. Rhoads, T. P. Sasseen, B. E. Schaefer, A. T. Short, A. P. Smale, I. A. Smith, L. Stella, G. Tagliaferri, T. Takahashi, M. Tashiro, L. K. Townsley, J. Tueller, M. J. L. Turner, M. Vietri, W. Voges, M. J. Ward, R. Willingale, F. M. Zerbi, and W. W. Zhang. The Swift Gamma-Ray Burst Mission. ApJ, 611(2):1005–1020, Aug 2004. doi: 10.1086/422091.

J. R. Gerke, C. S. Kochanek, and K. Z. Stanek. The search for failed supernovae with the Large Binocular Telescope: first candidates. MNRAS, 450(3):3289–3305, July 2015. doi: 10.1093/mnras/stv776.

S. Gezari, D. O. Jones, N. E. Sanders, A. M. Soderberg, T. Hung, S. Heinis, S. J. Smartt, A. Rest, D. Scolnic, R. Chornock, E. Berger, R. J. Foley, M. E. Huber, P. Price, C. W. Stubbs, A. G. Riess, R. P. Kirshner, K. Smith, W. M. Wood-Vasey, D. Schiminovich, D. C. Martin, W. S. Burgett, K. C. Chambers, H. Flewelling, N. Kaiser, J. L. Tonry, and R. Wainscoat. GALEX Detection of Shock Breakout in Type IIP Supernova PS1-13arp: Implications for the Progenitor Star Wind. ApJ, 804:28, May 2015. doi: 10.1088/0004-637X/804/1/28.

A. Ginsburg, B. M. Sipőcz, C. E. Brasseur, P. S. Cowperthwaite, M. W. Craig, C. Deil, J. Guillochon, G. Guzman, S. Liedtke, P. Lian Lim, K. E. Lockhart, M. Mommert, B. M. Morris, H. Norman, M. Parikh, M. V. Persson, T. P. Robitaille, J.-C. Segovia, L. P. Singer, E. J. Tollerud, M. de Val-Borro, I. Valtchanov, J. Woillez, Astroquery Collaboration, and a subset of astropy Collaboration. astroquery: An Astronomical Web-querying Package in Python. AJ, 157(3):98, Mar. 2019. doi: 10.3847/1538-3881/aafc33.

G. Gómez and R. López. The Canarias Database of Nearby Type II Supernovae. AJ, 120(1): 367–381, July 2000. doi: 10.1086/301419.

E. K. Grassberg, V. S. Imshennik, and D. K. Nadyozhin. On the Theory of the Light Curves of Supernovae. Ap&SS, 10:28–51, Jan. 1971. doi: 10.1007/BF00654604.

U. K. Gurugubelli, D. K. Sahu, G. C. Anupama, and N. K. Chakradhari. Photometric and spectroscopic evolution of type II-P supernova SN 2004A. *Bulletin of the Astronomical Society of India*, 36(2):79–97, Sept. 2008.

C. P. Gutiérrez, J. P. Anderson, M. Hamuy, S. González-Gaitán, G. Folatelli, N. I. Morrell, M. D. Stritzinger, M. M. Phillips, P. McCarthy, N. B. Suntzeff, and J. Thomas-Osip. H_α Spectral Diversity of Type II Supernovae: Correlations with Photometric Properties. ApJ, 786:L15, May 2014. doi: 10.1088/2041-8205/786/2/L15.

C. P. Gutiérrez, J. P. Anderson, M. Hamuy, N. Morrell, S. González-Gaitan, M. D. Stritzinger, M. M. Phillips, L. Galbany, G. Folatelli, L. Dessart, C. Contreras, M. Della Valle, W. L. Freedman, E. Y. Hsiao, K. Krisciunas, B. F. Madore, J. Maza, N. B. Suntzeff, J. L. Prieto, L. González, E. Cappellaro, M. Navarrete, A. Pizzella, M. T. Ruiz, R. C. Smith, and M. Turatto. Type II Supernova Spectral Diversity. I. Observations, Sample Characterization, and Spectral Line Evolution. ApJ, 850:89, Nov. 2017. doi: 10.3847/1538-4357/aa8f52.

C. P. Gutiérrez, J. P. Anderson, M. Sullivan, L. Dessart, S. González-Gaitan, L. Galbany, G. Dimitriadis, I. Arcavi, F. Bufano, T. W. Chen, M. Dennefeld, M. Gromadzki, J. B. Haislip, G. Hosseinzadeh, D. A. Howell, C. Inserra, E. Kankare, G. Leloudas, K. Maguire, C. McCully, N. Morrell, F. Olivares E, G. Pignata, D. E. Reichart, T. Reynolds, S. J. Smartt, J. Sollerman, F. Taddia, K. Takáts, G. Terreran, S. Valenti, and D. R. Young. Type II supernovae in low-luminosity host galaxies. MNRAS, 479:3232–3253, Sept. 2018. doi: 10.1093/mnras/sty1581.

W. J. Hack, N. Dencheva, A. S. Fruchter, A. Armstrong, R. Avila, S. Baggett, E. Bray, M. Droettboom, M. Dulude, S. Gonzaga, N. A. Grogin, V. Kozhurina-Platais, R. A. Lucas, J. Mack, J. MacKenty, L. Petro, N. Pirzkal, A. Rajan, L. J. Smith, C. Sontag, and L. Ubeda. AstroDrizzle: More than a New MultiDrizzle. In *American Astronomical Society Meeting Abstracts #220*, volume 220 of *American Astronomical Society Meeting Abstracts*, page 135.15, May 2012.

M. A. Hamuy. *Type II supernovae as distance indicators*. PhD thesis, The University of Arizona, 2001.

W. E. Harris. Transformation of HST WFC3/UVIS Filters to the Standard BVI System. AJ, 156 (6):296, Dec 2018. doi: 10.3847/1538-3881/aaedb8.

A. Heger, C. L. Fryer, S. E. Woosley, N. Langer, and D. H. Hartmann. How Massive Single Stars End Their Life. ApJ, 591:288–300, July 2003. doi: 10.1086/375341.

R. Hirschi. *Pre-supernova Evolution and Nucleosynthesis in Massive Stars and Their Stellar Wind Contribution*, page 1879. 2017. doi: 10.1007/978-3-319-21846-5_82.

R. Hirschi, G. Meynet, and A. Maeder. Stellar evolution with rotation. XII. Pre-supernova models. A&A, 425:649–670, Oct. 2004. doi: 10.1051/0004-6361:20041095.

I. M. Hook, I. Jørgensen, J. R. Allington-Smith, R. L. Davies, N. Metcalfe, R. G. Murowinski, and D. Crampton. The Gemini-North Multi-Object Spectrograph: Performance in Imaging, Long-Slit, and Multi-Object Spectroscopic Modes. PASP, 116:425–440, May 2004. doi: 10.1086/383624.

P. F. Hopkins, A. Wetzel, D. Kereš, C.-A. Faucher-Giguère, E. Quataert, M. Boylan-Kolchin, N. Murray, C. C. Hayward, and K. El-Badry. How to model supernovae in simulations of star and galaxy formation. MNRAS, 477(2):1578–1603, June 2018. doi: 10.1093/mnras/sty674.

A. Horesh, C. Stockdale, D. B. Fox, D. A. Frail, J. Carpenter, S. R. Kulkarni, E. O. Ofek, A. Gal-Yam, M. M. Kasliwal, I. Arcavi, R. Quimby, S. B. Cenko, P. E. Nugent, J. S. Bloom, N. M. Law, D. Poznanski, E. Gorbikov, D. Polishook, O. Yaron, S. Ryder, K. W. Weiler, F. Bauer, S. D. Van Dyk, S. Immler, N. Panagia, D. Pooley, and N. Kassim. An early and comprehensive millimetre and centimetre wave and X-ray study of SN 2011dh: a non-equipartition blast wave expanding into a massive stellar wind. MNRAS, 436:1258–1267, Dec. 2013. doi: 10.1093/mnras/stt1645.

G. Hosseinzadeh, S. Valenti, I. Arcavi, C. McCully, and D. A. Howell. FLOYDS Classification of ASASSN-15oz as a Young Type II Supernova and ASASSN-15os as a Few-Week-Old Type Ia Supernova. *The Astronomer's Telegram*, 7997:1, Sept. 2015.

G. Hosseinzadeh, S. Valenti, C. McCully, D. A. Howell, I. Arcavi, A. Jerkstrand, D. Guevel, L. Tartaglia, L. Rui, J. Mo, X. Wang, F. Huang, H. Song, T. Zhang, and K. Itagaki. Short-lived Circumstellar Interaction in the Low-luminosity Type IIP SN 2016bkv. ApJ, 861:63, July 2018. doi: 10.3847/1538-4357/aac5f6.

E. Y. Hsiao, M. M. Phillips, G. H. Marion, R. P. Kirshner, N. Morrell, D. J. Sand, C. R. Burns, C. Contreras, P. Hoeflich, M. D. Stritzinger, S. Valenti, J. P. Anderson, C. Ashall, C. Baltay, E. Baron, D. P. K. Banerjee, S. Davis, T. R. Diamond, G. Folatelli, W. L. Freedman, F. Förster, L. Galbany, C. Gall, S. González-Gaitán, A. Goobar, M. Hamuy, S. Holmbo, M. M. Kasliwal, K. Krisciunas, S. Kumar, C. Lidman, J. Lu, P. E. Nugent, S. Perlmutter, S. E. Persson, A. L. Piro, D. Rabinowitz, M. Roth, S. D. Ryder, B. P. Schmidt, M. Shahbandeh, N. B. Suntzeff, F. Taddia, S. Uddin, and L. Wang. Carnegie Supernova Project-II: The Near-infrared Spectroscopy Program.

PASP, 131(1):014002, Jan. 2019. doi: 10.1088/1538-3873/aae961.

F. Huang, X. Wang, J. Zhang, P. J. Brown, L. Zampieri, M. L. Pumo, T. Zhang, J. Chen, J. Mo, and X. Zhao. SN 2013ej in M74: A Luminous and Fast-declining Type II-P Supernova. ApJ, 807(1):59, July 2015. doi: 10.1088/0004-637X/807/1/59.

J. P. Huchra, M. S. Vogeley, and M. J. Geller. The CFA Redshift Survey: Data for the South Galactic CAP. ApJS, 121:287–368, Apr. 1999. doi: 10.1086/313194.

C. A. Iglesias and F. J. Rogers. Updated Opal Opacities. ApJ, 464:943, June 1996. doi: 10.1086/177381.

S. Immler, P. J. Brown, P. Milne, L. Dessart, P. A. Mazzali, W. Landsman, N. Gehrels, R. Petre, D. N. Burrows, J. A. Nousek, R. A. Chevalier, C. L. Williams, M. Koss, C. J. Stockdale, M. T. Kelley, K. W. Weiler, S. T. Holland, E. Pian, P. W. A. Roming, D. Pooley, K. Nomoto, J. Greiner, S. Campana, and A. M. Soderberg. X-Ray, UV, and Optical Observations of Supernova 2006bp with Swift: Detection of Early X-Ray Emission. ApJ, 664(1):435–442, July 2007. doi: 10.1086/518466.

C. Inserra, M. Turatto, A. Pastorello, S. Benetti, E. Cappellaro, M. L. Pumo, L. Zampieri, I. Agnoletto, F. Bufano, and M. T. Botticella. The Type IIP SN 2007od in UGC 12846: from a bright maximum to dust formation in the nebular phase. MNRAS, 417(1):261–279, Oct 2011. doi: 10.1111/j.1365-2966.2011.19128.x.

C. Inserra, A. Pastorello, M. Turatto, M. L. Pumo, S. Benetti, E. Cappellaro, M. T. Botticella, F. Bufano, N. Elias-Rosa, A. Harutyunyan, S. Taubenberger, S. Valenti, and L. Zampieri. Moderately luminous Type II supernovae. A&A, 555:A142, July 2013. doi: 10.1051/0004-6361/201220496.

A. Jerkstrand, C. Fransson, and C. Kozma. The ¡SUP¿44¡/SUP¿Ti-powered spectrum of SN 1987A. A&A, 530:A45, June 2011. doi: 10.1051/0004-6361/201015937.

A. Jerkstrand, C. Fransson, K. Maguire, S. Smartt, M. Ergon, and J. Spyromilio. The progenitor mass of the Type IIP supernova SN 2004et from late-time spectral modeling. A&A, 546:A28, Oct. 2012. doi: 10.1051/0004-6361/201219528.

A. Jerkstrand, S. J. Smartt, M. Fraser, C. Fransson, J. Sollerman, F. Taddia, and R. Kotak. The nebular spectra of SN 2012aw and constraints on stellar nucleosynthesis from oxygen emission

lines. MNRAS, 439:3694–3703, Apr. 2014. doi: 10.1093/mnras/stu221.

A. Jerkstrand, S. J. Smartt, J. Sollerman, C. Inserra, M. Fraser, J. Spyromilio, C. Fransson, T. W. Chen, C. Barbarino, M. Dall'Ora, M. T. Botticella, M. Della Valle, A. Gal-Yam, S. Valenti, K. Maguire, P. Mazzali, and L. Tomasella. Supersolar Ni/Fe production in the Type IIP SN 2012ec. MNRAS, 448(3):2482–2494, Apr. 2015. doi: 10.1093/mnras/stv087.

A. Jerkstrand, T. Ertl, H. T. Janka, E. Müller, T. Sukhbold, and S. E. Woosley. Emission line models for the lowest mass core-collapse supernovae - I. Case study of a 9 M¡SUB¿?¡/SUB¿ one-dimensional neutrino-driven explosion. MNRAS, 475:277–305, Mar. 2018. doi: 10.1093/mnras/stx2877.

P. M. W. Kalberla, W. B. Burton, D. Hartmann, E. M. Arnal, E. Bajaja, R. Morras, and W. G. L. Pöppel. The Leiden/Argentine/Bonn (LAB) Survey of Galactic HI. Final data release of the combined LDS and IAR surveys with improved stray- radiation corrections. A&A, 440:775–782, Sept. 2005. doi: 10.1051/0004-6361:20041864.

D. Kasen and S. E. Woosley. TYPE II SUPERNOVAE: MODEL LIGHT CURVES AND STANDARD CANDLE RELATIONSHIPS. *The Astrophysical Journal*, 703:2205–2216, 2009. doi: 10.1088/0004-637X/703/2/2205. URL `http://iopscience.iop.org/article/10.1088/0004-637X/703/2/2205/pdf`.

D. Khazov, O. Yaron, A. Gal-Yam, I. Manulis, A. Rubin, S. R. Kulkarni, I. Arcavi, M. M. Kasliwal, E. O. Ofek, Y. Cao, D. Perley, J. Sollerman, A. Horesh, M. Sullivan, A. V. Filippenko, P. E. Nugent, D. A. Howell, S. B. Cenko, J. M. Silverman, H. Ebeling, F. Taddia, J. Johansson, R. R. Laher, J. Surace, U. D. Rebbapragada, P. R. Wozniak, and T. Matheson. Flash Spectroscopy: Emission Lines from the Ionized Circumstellar Material around <10-day-old Type II Supernovae. ApJ, 818(1):3, Feb 2016. doi: 10.3847/0004-637X/818/1/3.

M. Kiewe, A. Gal-Yam, I. Arcavi, D. C. Leonard, J. Emilio Enriquez, S. B. Cenko, D. B. Fox, D.-S. Moon, D. J. Sand, A. M. Soderberg, and T. CCCP. Caltech Core-Collapse Project (CCCP) Observations of Type IIn Supernovae: Typical Properties and Implications for Their Progenitor Stars. ApJ, 744:10, Jan. 2012. doi: 10.1088/0004-637X/744/1/10.

C. D. Kilpatrick and R. J. Foley. The dusty progenitor star of the Type II supernova 2017eaw. MNRAS, 481(2):2536–2547, Dec. 2018. doi: 10.1093/mnras/sty2435.

C. Kobayashi, A. I. Karakas, and M. Lugaro. The Origin of Elements from Carbon to Uranium. *arXiv e-prints*, art. arXiv:2008.04660, Aug. 2020.

C. S. Kochanek, R. Khan, and X. Dai. On Absorption by Circumstellar Dust, with the Progenitor of SN 2012aw as a Case Study. ApJ, 759(1):20, Nov. 2012. doi: 10.1088/0004-637X/759/1/20.

C. S. Kochanek, M. Fraser, S. M. Adams, T. Sukhbold, J. L. Prieto, T. Müller, G. Bock, J. S. Brown, S. Dong, T. W. S. Holoien, R. Khan, B. J. Shappee, and K. Z. Stanek. Supernova progenitors, their variability and the Type IIP Supernova ASASSN-16fq in M66. MNRAS, 467 (3):3347–3360, May 2017. doi: 10.1093/mnras/stx291.

N. P. M. Kuin, W. Landsman, A. A. Breeveld, M. J. Page, H. Lamoureux, C. James, M. Mehdipour, M. Still, V. Yershov, P. J. Brown, M. Carter, K. O. Mason, T. Kennedy, F. Marshall, P. W. A. Roming, M. Siegel, S. Oates, P. J. Smith, and M. De Pasquale. Calibration of the Swift-UVOT ultraviolet and visible grisms. MNRAS, 449:2514–2538, May 2015. doi: 10.1093/mnras/stv408.

P. Kuin. UVOTPY: Swift UVOT grism data reduction. Astrophysics Source Code Library, Oct. 2014.

H. Kuncarayakti, M. Doi, G. Aldering, N. Arimoto, K. Maeda, T. Morokuma, R. Pereira, T. Usuda, and Y. Hashiba. Integral Field Spectroscopy of Supernova Explosion Sites: Constraining the Mass and Metallicity of the Progenitors. II. Type II-P and II-L Supernovae. AJ, 146(2):31, Aug 2013. doi: 10.1088/0004-6256/146/2/31.

D. C. Leonard, A. V. Filippenko, E. L. Gates, W. Li, R. G. Eastman, A. J. Barth, S. J. Bus, R. Chornock, A. L. Coil, S. Frink, C. A. Grady, A. W. Harris, M. A. Malkan, T. Matheson, A. Quirrenbach, and R. R. Treffers. The Distance to SN 1999em in NGC 1637 from the Expanding Photosphere Method. PASP, 114:35–64, Jan. 2002. doi: 10.1086/324785.

D. C. Leonard, S. M. Kanbur, C. C. Ngeow, and N. R. Tanvir. The Cepheid Distance to NGC 1637: A Direct Test of the Expanding Photosphere Method Distance to SN 1999em. ApJ, 594 (1):247–278, Sept. 2003. doi: 10.1086/376831.

E. M. Levesque. *Astrophysics of Red Supergiants*. 2514-3433. IOP Publishing, 2017. ISBN 978-0-7503-1329-2. doi: 10.1088/978-0-7503-1329-2. URL `http://dx.doi.org/10.1088/978-0-7503-1329-2`.

W. Li and A. V. Filippenko. Supernova 2008ex in UGC 11428. *Central Bureau Electronic Telegrams*, 1470:1, Aug. 2008.

W. Li, S. D. Van Dyk, A. V. Filippenko, and J.-C. Cuillandre. On the Progenitor of the Type II Supernova 2004et in NGC 6946. PASP, 117(828):121–131, Feb. 2005. doi: 10.1086/428278.

W. Li, X. Wang, S. D. Van Dyk, J.-C. Cuilland re, R. J. Foley, and A. V. Filippenko. On the Progenitors of Two Type II-P Supernovae in the Virgo Cluster. ApJ, 661(2):1013–1024, June 2007. doi: 10.1086/516747.

W. Li, J. Leaman, R. Chornock, A. V. Filippenko, D. Poznanski, M. Ganeshalingam, X. Wang, M. Modjaz, S. Jha, R. J. Foley, and N. Smith. Nearby supernova rates from the Lick Observatory Supernova Search - II. The observed luminosity functions and fractions of supernovae in a complete sample. MNRAS, 412:1441–1472, Apr. 2011. doi: 10.1111/j.1365-2966.2011.18160.x.

W. Liller, M. Adams, B. Wilson, P. Sventek, A. Hale, P. Camilleri, S. Pesci, and R. Evans. Supernova 1992ad in NGC 4411B. IAU Circ., 5570:3, July 1992.

Q. Z. Liu, J. Y. Hu, H. R. Hang, Y. L. Qiu, Z. X. Zhu, and Q. Y. Qiao. The supernova 1998S in NGC 3877: Another supernova with Wolf-Rayet star features in pre-maximum spectrum. *Astronomy and Astrophysics Supplement Series*, 144:219–225, June 2000. doi: 10.1051/aas:2000208.

R. López Fernández, R. Cid Fernandes, R. M. González Delgado, N. Vale Asari, E. Pérez, R. García-Benito, A. L. de Amorim, E. A. D. Lacerda, C. Cortijo-Ferrero, and S. F. Sánchez. Simultaneous spectroscopic and photometric analysis of galaxies with STARLIGHT: CALIFA+GALEX. MNRAS, 458:184–199, May 2016. doi: 10.1093/mnras/stw260.

Á. R. López-Sánchez, M. A. Dopita, L. J. Kewley, H. J. Zahid, D. C. Nicholls, and J. Scharwächter. Eliminating error in the chemical abundance scale for extragalactic H II regions. MNRAS, 426 (4):2630–2651, Nov 2012. doi: 10.1111/j.1365-2966.2012.21145.x.

K. Maguire, E. Di Carlo, S. J. Smartt, A. Pastorello, D. Y. Tsvetkov, S. Benetti, S. Spiro, A. A. Arkharov, G. Beccari, M. T. Botticella, E. Cappellaro, S. Cristallo, M. Dolci, N. Elias- Rosa, M. Fiaschi, D. Gorshanov, A. Harutyunyan, V. M. Larionov, H. Navasardyan, A. Pietrinferni, G. Raimondo, G. di Rico, S. Valenti, G. Valentini, and L. Zampieri. Optical and near-infrared coverage of SN 2004et: physical parameters and comparison with other Type IIP supernovae. MNRAS, 404:981–1004, May 2010. doi: 10.1111/j.1365-2966.2010.16332.x.

K. Maguire, A. Jerkstrand, S. J. Smartt, C. Fransson, A. Pastorello, S. Benetti, S. Valenti, F. Bufano, and G. Leloudas. Constraining the physical properties of Type II-Plateau supernovae using nebular phase spectra. MNRAS, 420(4):3451–3468, Mar. 2012. doi: 10.1111/j.1365-2966.2011.20276.x.

R. Margutti, D. Milisavljevic, A. M. Soderberg, R. Chornock, B. A. Zauderer, K. Murase, C. Guidorzi, N. E. Sanders, P. Kuin, C. Fransson, E. M. Levesque, P. Chandra, E. Berger, F. B. Bianco, P. J. Brown, P. Challis, E. Chatzopoulos, C. C. Cheung, C. Choi, L. Chomiuk, N. Chugai, C. Contreras, M. R. Drout, R. Fesen, R. J. Foley, W. Fong, A. S. Friedman, C. Gall, N. Gehrels, J. Hjorth, E. Hsiao, R. Kirshner, M. Im, G. Leloudas, R. Lunnan, G. H. Marion, J. Martin, N. Morrell, K. F. Neugent, N. Omodei, M. M. Phillips, A. Rest, J. M. Silverman, J. Strader, M. D. Stritzinger, T. Szalai, N. B. Utterback, J. Vinko, J. C. Wheeler, D. Arnett, S. Campana, R. Chevalier, A. Ginsburg, A. Kamble, P. W. A. Roming, T. Pritchard, and G. Stringfellow. A Panchromatic View of the Restless SN 2009ip Reveals the Explosive Ejection of a Massive Star Envelope. ApJ, 780(1):21, Jan 2014. doi: 10.1088/0004-637X/780/1/21.

S. Mattila, S. J. Smartt, J. J. Eldridge, J. R. Maund, R. M. Crockett, and I. J. Danziger. VLT Detection of a Red Supergiant Progenitor of the Type II-P Supernova 2008bk. ApJ, 688(2):L91, Dec. 2008. doi: 10.1086/595587.

J. C. Mauerhan, N. Smith, A. V. Filippenko, K. B. Blanchard, P. K. Blanchard, C. F. E. Casper, S. B. Cenko, K. I. Clubb, D. P. Cohen, K. L. Fuller, G. Z. Li, and J. M. Silverman. The unprecedented 2012 outburst of SN 2009ip: a luminous blue variable star becomes a true supernova. MNRAS, 430:1801–1810, Apr. 2013. doi: 10.1093/mnras/stt009.

J. C. Mauerhan, S. D. Van Dyk, J. Johansson, M. Hu, O. D. Fox, L. Wang, M. L. Graham, A. V. Filippenko, and I. Shivvers. Asphericity, Interaction, and Dust in the Type II-P/II-L Supernova 2013EJ in Messier 74. ApJ, 834:118, Jan. 2017. doi: 10.3847/1538-4357/834/2/118.

J. R. Maund and S. J. Smartt. Hubble Space Telescope imaging of the progenitor sites of six nearby core-collapse supernovae. MNRAS, 360(1):288–304, June 2005. doi: 10.1111/j.1365-2966.2005.09034.x.

J. R. Maund and S. J. Smartt. The Disappearance of the Progenitors of Supernovae 1993J and 2003gd. *Science*, 324(5926):486, Apr. 2009. doi: 10.1126/science.1170198.

J. R. Maund, M. Fraser, S. J. Smartt, M. T. Botticella, C. Barbarino, M. Childress, A. Gal-Yam, C. Inserra, G. Pignata, D. Reichart, B. Schmidt, J. Sollerman, F. Taddia, L. Tomasella, S. Valenti, and O. Yaron. Supernova 2012ec: identification of the progenitor and early monitoring with PESSTO. MNRAS, 431:L102–L106, Apr. 2013. doi: 10.1093/mnrasl/slt017.

J. R. Maund, E. Reilly, and S. Mattila. A late-time view of the progenitors of five Type IIP supernovae. MNRAS, 438(2):938–958, Feb. 2014. doi: 10.1093/mnras/stt2131.

N. Mauron and E. Josselin. The mass-loss rates of red supergiants and the de Jager prescription. A&A, 526:A156, Feb. 2011. doi: 10.1051/0004-6361/201013993.

S. Mei, J. P. Blakeslee, P. Côté, J. L. Tonry, M. J. West, L. Ferrarese, A. Jordán, E. W. Peng, A. Anthony, and D. Merritt. The ACS Virgo Cluster Survey. XIII. SBF Distance Catalog and the Three-dimensional Structure of the Virgo Cluster. ApJ, 655(1):144–162, Jan. 2007. doi: 10.1086/509598.

G. Meynet, V. Chomienne, S. Ekström, C. Georgy, A. Granada, J. Groh, A. Maeder, P. Eggenberger, E. Levesque, and P. Massey. Impact of mass-loss on the evolution and pre-supernova properties of red supergiants. A&A, 575:A60, Mar. 2015. doi: 10.1051/0004-6361/201424671.

T. J. Moriya, S.-C. Yoon, G. Gräfener, and S. I. Blinnikov. Immediate dense circumstellar environment of supernova progenitors caused by wind acceleration: its effect on supernova light curves. MNRAS, 469:L108–L112, July 2017. doi: 10.1093/mnrasl/slx056.

V. Morozova and J. M. Stone. Theoretical X-ray light curves of young SNe II: the example of SN 2013ej. *ArXiv e-prints*, art. arXiv:1804.07312, Apr. 2018.

V. Morozova, A. L. Piro, M. Renzo, C. D. Ott, D. Clausen, S. M. Couch, J. Ellis, and L. F. Roberts. Light Curves of Core-collapse Supernovae with Substantial Mass Loss Using the New Open-source SuperNova Explosion Code (SNEC). ApJ, 814:63, Nov. 2015. doi: 10.1088/0004-637X/814/1/63.

V. Morozova, A. L. Piro, and S. Valenti. Unifying Type II Supernova Light Curves with Dense Circumstellar Material. ApJ, 838:28, Mar. 2017. doi: 10.3847/1538-4357/aa6251.

V. Morozova, A. L. Piro, and S. Valenti. Measuring the Progenitor Masses and Dense Circumstellar Material of Type II Supernovae. ApJ, 858:15, May 2018. doi: 10.3847/1538-4357/aab9a6.

J. R. Mould, J. P. Huchra, W. L. Freedman, J. Kennicutt, Robert C., L. Ferrarese, H. C. Ford, B. K. Gibson, J. A. Graham, S. M. G. Hughes, G. D. Illingworth, D. D. Kelson, L. M. Macri,

B. F. Madore, S. Sakai, K. M. Sebo, N. A. Silbermann, and P. B. Stetson. The Hubble Space Telescope Key Project on the Extragalactic Distance Scale. XXVIII. Combining the Constraints on the Hubble Constant. ApJ, 529(2):786–794, Feb. 2000. doi: 10.1086/308304.

K. Mukai. Legacy 3. *Legacy 3*, page 21?31, 1993.

D. K. Nadyozhin. On the initial phase of interaction between expanding stellar envelopes and surrounding medium. Ap&SS, 112:225–249, May 1985. doi: 10.1007/BF00653506.

H. Nieuwenhuijzen and C. de Jager. Parametrization of stellar rates of mass loss as functions of the fundamental stellar parameters M, L, and R. A&A, 231:134–136, May 1990.

D. E. Osterbrock and G. J. Ferland. *Astrophysics of gaseous nebulae and active galactic nuclei*. University Science Books, 2006.

B. Paczynski. Models of X-ray bursters with radius expansion. ApJ, 267:315–321, Apr. 1983. doi: 10.1086/160870.

A. Pastorello, D. Sauer, S. Taubenberger, P. A. Mazzali, K. Nomoto, K. S. Kawabata, S. Benetti, N. Elias-Rosa, A. Harutyunyan, H. Navasardyan, L. Zampieri, T. Iijima, M. T. Botticella, G. di Rico, M. Del Principe, M. Dolci, S. Gagliardi, M. Ragni, and G. Valentini. SN 2005cs in M51 - I. The first month of evolution of a subluminous SN II plateau. MNRAS, 370(4):1752–1762, Aug. 2006. doi: 10.1111/j.1365-2966.2006.10587.x.

A. Pastorello, S. Valenti, L. Zampieri, H. Navasardyan, S. Taubenberger, S. J. Smartt, A. A. Arkharov, O. Bärnbantner, H. Barwig, S. Benetti, P. Birtwhistle, M. T. Botticella, E. Cappellaro, M. Del Principe, F. di Mille, G. di Rico, M. Dolci, N. Elias-Rosa, N. V. Efimova, M. Fiedler, A. Harutyunyan, P. A. Höflich, W. Kloehr, V. M. Larionov, V. Lorenzi, J. R. Maund, N. Napoleone, M. Ragni, M. Richmond, C. Ries, S. Spiro, S. Temporin, M. Turatto, and J. C. Wheeler. SN 2005cs in M51 - II. Complete evolution in the optical and the near-infrared. MNRAS, 394:2266–2282, Apr. 2009. doi: 10.1111/j.1365-2966.2009.14505.x.

A. Pastorello, M. L. Pumo, H. Navasardyan, L. Zampieri, M. Turatto, J. Sollerman, F. Taddia, E. Kankare, S. Mattila, J. Nicolas, E. Prosperi, A. San Segundo Delgado, S. Taubenberger, T. Boles, M. Bachini, S. Benetti, F. Bufano, E. Cappellaro, A. D. Cason, G. Cetrulo, M. Ergon, L. Germany, A. Harutyunyan, S. Howerton, G. M. Hurst, F. Patat, M. Stritzinger, L. G. Strolger, and W. Wells. SN 2009E: a faint clone of SN 1987A. A&A, 537:A141, Jan. 2012. doi: 10.1051/

0004-6361/201118112.

A. Pastorello, E. Cappellaro, C. Inserra, S. J. Smartt, G. Pignata, S. Benetti, S. Valenti, M. Fraser, K. Takáts, S. Benitez, M. T. Botticella, J. Brimacombe, F. Bufano, F. Cellier-Holzem, M. T. Costado, G. Cupani, I. Curtis, N. Elias-Rosa, M. Ergon, J. P. U. Fynbo, F. J. Hambsch, M. Hamuy, A. Harutyunyan, K. M. Ivarson, E. Kankare, J. C. Martin, R. Kotak, A. P. LaCluyze, K. Maguire, S. Mattila, J. Maza, M. McCrum, M. Miluzio, H. U. Norgaard-Nielsen, M. C. Nysewander, P. Ochner, Y. C. Pan, M. L. Pumo, D. E. Reichart, T. G. Tan, S. Taubenberger, L. Tomasella, M. Turatto, and D. Wright. Interacting Supernovae and Supernova Impostors: SN 2009ip, is this the End? ApJ, 767(1):1, Apr 2013. doi: 10.1088/0004-637X/767/1/1.

F. Patat, R. Barbon, E. Cappellaro, and M. Turatto. Light curves of type II supernovae. II. The analysis. A&A, 282:731–741, Feb. 1994.

B. Paxton, L. Bildsten, A. Dotter, F. Herwig, P. Lesaffre, and F. Timmes. Modules for Experiments in Stellar Astrophysics (MESA). ApJS, 192:3, Jan. 2011. doi: 10.1088/0067-0049/192/1/3.

B. Paxton, M. Cantiello, P. Arras, L. Bildsten, E. F. Brown, A. Dotter, C. Mankovich, M. H. Montgomery, D. Stello, F. X. Timmes, and R. Townsend. Modules for Experiments in Stellar Astrophysics (MESA): Planets, Oscillations, Rotation, and Massive Stars. ApJS, 208:4, Sept. 2013. doi: 10.1088/0067-0049/208/1/4.

B. Paxton, P. Marchant, J. Schwab, E. B. Bauer, L. Bildsten, M. Cantiello, L. Dessart, R. Farmer, H. Hu, N. Langer, R. H. D. Townsend, D. M. Townsley, and F. X. Timmes. Modules for Experiments in Stellar Astrophysics (MESA): Binaries, Pulsations, and Explosions. ApJS, 220: 15, Sept. 2015. doi: 10.1088/0067-0049/220/1/15.

B. Paxton, J. Schwab, E. B. Bauer, L. Bildsten, S. Blinnikov, P. Duffell, R. Farmer, J. A. Goldberg, P. Marchant, E. Sorokina, A. Thoul, R. H. D. Townsend, and F. X. Timmes. Modules for Experiments in Stellar Astrophysics (MESA): Convective Boundaries, Element Diffusion, and Massive Star Explosions. *The Astrophysical Journal Supplement Series*, 234:34, Feb. 2018. doi: 10.3847/1538-4365/aaa5a8.

M. Pettini and B. E. J. Pagel. [OIII]/[NII] as an abundance indicator at high redshift. MNRAS, 348:L59–L63, Mar. 2004. doi: 10.1111/j.1365-2966.2004.07591.x.

Planck Collaboration, P. A. R. Ade, N. Aghanim, M. Arnaud, M. Ashdown, J. Aumont, C. Baccigalupi, A. J. Banday, R. B. Barreiro, J. G. Bartlett, N. Bartolo, E. Battaner, R. Battye, K. Benabed, A. Benoît, A. Benoit-Lévy, J. P. Bernard, M. Bersanelli, P. Bielewicz, J. J. Bock, A. Bonaldi, L. Bonavera, J. R. Bond, J. Borrill, F. R. Bouchet, F. Boulanger, M. Bucher, C. Burigana, R. C. Butler, E. Calabrese, J. F. Cardoso, A. Catalano, A. Challinor, A. Chamballu, R. R. Chary, H. C. Chiang, J. Chluba, P. R. Christensen, S. Church, D. L. Clements, S. Colombi, L. P. L. Colombo, C. Combet, A. Coulais, B. P. Crill, A. Curto, F. Cuttaia, L. Danese, R. D. Davies, R. J. Davis, P. de Bernardis, A. de Rosa, G. de Zotti, J. Delabrouille, F. X. Désert, E. Di Valentino, C. Dickinson, J. M. Diego, K. Dolag, H. Dole, S. Donzelli, O. Doré, M. Douspis, A. Ducout, J. Dunkley, X. Dupac, G. Efstathiou, F. Elsner, T. A. Enßlin, H. K. Eriksen, M. Farhang, J. Fergusson, F. Finelli, O. Forni, M. Frailis, A. A. Fraisse, E. Franceschi, A. Frejsel, S. Galeotta, S. Galli, K. Ganga, C. Gauthier, M. Gerbino, T. Ghosh, M. Giard, Y. Giraud-Héraud, E. Giusarma, E. Gjerløw, J. González-Nuevo, K. M. Górski, S. Gratton, A. Gregorio, A. Gruppuso, J. E. Gudmundsson, J. Hamann, F. K. Hansen, D. Hanson, D. L. Harrison, G. Helou, S. Henrot-Versillé, C. Hernández-Monteagudo, D. Herranz, S. R. Hildebrandt, E. Hivon, M. Hobson, W. A. Holmes, A. Hornstrup, W. Hovest, Z. Huang, K. M. Huffenberger, G. Hurier, A. H. Jaffe, T. R. Jaffe, W. C. Jones, M. Juvela, E. Keihänen, R. Keskitalo, T. S. Kisner, R. Kneissl, J. Knoche, L. Knox, M. Kunz, H. Kurki-Suonio, G. Lagache, A. Lähteenmäki, J. M. Lamarre, A. Lasenby, M. Lattanzi, C. R. Lawrence, J. P. Leahy, R. Leonardi, J. Lesgourgues, F. Levrier, A. Lewis, M. Liguori, P. B. Lilje, M. Linden-Vørnle, M. López-Caniego, P. M. Lubin, J. F. Macías-Pérez, G. Maggio, D. Maino, N. Mandolesi, A. Mangilli, A. Marchini, M. Maris, P. G. Martin, M. Martinelli, E. Martínez-González, S. Masi, S. Matarrese, P. McGehee, P. R. Meinhold, A. Melchiorri, J. B. Melin, L. Mendes, A. Mennella, M. Migliaccio, M. Millea, S. Mitra, M. A. Miville-Deschênes, A. Moneti, L. Montier, G. Morgante, D. Mortlock, A. Moss, D. Munshi, J. A. Murphy, P. Naselsky, F. Nati, P. Natoli, C. B. Netterfield, H. U. Nørgaard-Nielsen, F. Noviello, D. Novikov, I. Novikov, C. A. Oxborrow, F. Paci, L. Pagano, F. Pajot, R. Paladini, D. Paoletti, B. Partridge, F. Pasian, G. Patanchon, T. J. Pearson, O. Perdereau, L. Perotto, F. Perrotta, V. Pettorino, F. Piacentini, M. Piat, E. Pierpaoli, D. Pietrobon, S. Plaszczynski, E. Pointecouteau, G. Polenta, L. Popa, G. W. Pratt, G. Prézeau, S. Prunet, J. L. Puget, J. P.

Rachen, W. T. Reach, R. Rebolo, M. Reinecke, M. Remazeilles, C. Renault, A. Renzi, I. Ristorcelli, G. Rocha, C. Rosset, M. Rossetti, G. Roudier, B. Rouillé d'Orfeuil, M. Rowan-Robinson, J. A. Rubiño-Martín, B. Rusholme, N. Said, V. Salvatelli, L. Salvati, M. Sandri, D. Santos, M. Savelainen, G. Savini, D. Scott, M. D. Seiffert, P. Serra, E. P. S. Shellard, L. D. Spencer, M. Spinelli, V. Stolyarov, R. Stompor, R. Sudiwala, R. Sunyaev, D. Sutton, A. S. Suur-Uski, J. F. Sygnet, J. A. Tauber, L. Terenzi, L. Toffolatti, M. Tomasi, M. Tristram, T. Trombetti, M. Tucci, J. Tuovinen, M. Türler, G. Umana, L. Valenziano, J. Valiviita, F. Van Tent, P. Vielva, F. Villa, L. A. Wade, B. D. Wandelt, I. K. Wehus, M. White, S. D. M. White, A. Wilkinson, D. Yvon, A. Zacchei, and A. Zonca. Planck 2015 results. XIII. Cosmological parameters. A&A, 594:A13, Sept. 2016. doi: 10.1051/0004-6361/201525830.

O. R. Pols, C. A. Tout, P. P. Eggleton, and Z. Han. Approximate input physics for stellar modelling. MNRAS, 274(3):964–974, Jun 1995. doi: 10.1093/mnras/274.3.964.

D. Poznanski, J. X. Prochaska, and J. S. Bloom. An empirical relation between sodium absorption and dust extinction. *Mon. Not. R. Astron. Soc*, 426:1465–1474, 2012. doi: 10.1111/j.1365-2966.2012.21796.x.

M. Pozzo, W. P. S. Meikle, A. Fassia, T. Geballe, P. Lundqvist, N. N. Chugai, and J. Sollerman. On the source of the late-time infrared luminosity of SN 1998S and other Type II supernovae. MNRAS, 352:457–477, Aug. 2004. doi: 10.1111/j.1365-2966.2004.07951.x.

M. Pozzo, W. P. S. Meikle, J. T. Rayner, R. D. Joseph, A. V. Filippenko, R. J. Foley, W. Li, S. Mattila, and J. Sollerman. Optical and infrared observations of the TypeIIP SN2002hh from days 3 to 397. MNRAS, 368(3):1169–1195, May 2006. doi: 10.1111/j.1365-2966.2006.10204.x.

T. P. Prabhu and G. C. Anupama. Science with Indian Astronomical Observatory, Hanle. In *Astronomical Society of India Conference Series*, volume 1 of *Astronomical Society of India Conference Series*, 2010.

E. Quataert and J. Shiode. Wave-driven mass loss in the last year of stellar evolution: setting the stage for the most luminous core-collapse supernovae. MNRAS, 423:L92–L96, June 2012. doi: 10.1111/j.1745-3933.2012.01264.x.

R. Quimby, P. Höflich, S. J. Kannappan, E. Rykoff, W. Rujopakarn, C. W. Akerlof, C. L. Gerardy, and J. C. Wheeler. SN 2005cg: Explosion Physics and Circumstellar Interaction of a Normal

Type Ia Supernova in a Low-Luminosity Host. *The Astrophysical Journal*, 636(1):400–405, Jan 2006. doi: 10.1086/498014.

R. M. Quimby, J. C. Wheeler, P. Höflich, C. W. Akerlof, P. J. Brown, and E. S. Rykoff. SN 2006bp: Probing the Shock Breakout of a Type II-P Supernova. ApJ, 666(2):1093–1107, Sept. 2007. doi: 10.1086/520532.

I. Rabinak and E. Waxman. The Early UV/Optical Emission from Core-collapse Supernovae. ApJ, 728(1):63, Feb. 2011. doi: 10.1088/0004-637X/728/1/63.

J. T. Rayner, D. W. Toomey, P. M. Onaka, A. J. Denault, W. E. Stahlberger, W. D. Vacca, M. C. Cushing, and S. Wang. SpeX: A Medium-Resolution 0.8-5.5 Micron Spectrograph and Imager for the NASA Infrared Telescope Facility. *Publications of the Astronomical Society of the Pacific*, 115:362–382, Mar. 2003. doi: 10.1086/367745.

D. Richardson, R. C. Thomas, D. Casebeer, Z. Blankenship, S. Ratowt, E. Baron, and D. Branch. SUSPECT - The Online Supernova Spectrum Database. In *American Astronomical Society Meeting Abstracts*, volume 199 of *American Astronomical Society Meeting Abstracts*, page 84.08, Dec. 2001.

D. Richardson, R. Thomas, D. Casebeer, D. Branch, and E. Baron. SUSPECT, The Online Supernova Spectrum Archive: Year Two. In *American Astronomical Society Meeting Abstracts*, volume 201 of *American Astronomical Society Meeting Abstracts*, page 56.09, Dec. 2002.

P. W. A. Roming, T. E. Kennedy, K. O. Mason, J. A. Nousek, L. Ahr, R. E. Bingham, P. S. Broos, M. J. Carter, B. K. Hancock, H. E. Huckle, S. D. Hunsberger, H. Kawakami, R. Killough, T. S. Koch, M. K. Mclelland, K. Smith, P. J. Smith, J. C. Soto, P. T. Boyd, A. A. Breeveld, S. T. Holland, M. Ivanushkina, M. S. Pryzby, M. D. Still, and J. Stock. The Swift Ultra-Violet/Optical Telescope. Space Sci. Rev., 120(3-4):95–142, oct 2005. doi: 10.1007/s11214-005-5095-4. URL `https://doi.org/10.1007%2Fs11214-005-5095-4`.

M. Ross and V. V. Dwarkadas. SNaX: A Database of Supernova X-Ray Light Curves. AJ, 153: 246, June 2017. doi: 10.3847/1538-3881/aa6d50.

A. Rubin and A. Gal-Yam. Unsupervised Clustering of Type II Supernova Light Curves. ApJ, 828: 111, Sept. 2016. doi: 10.3847/0004-637X/828/2/111.

A. Rubin, A. Gal-Yam, A. De Cia, A. Horesh, D. Khazov, E. O. Ofek, S. R. Kulkarni, I. Arcavi, I. Manulis, O. Yaron, P. Vreeswijk, M. M. Kasliwal, S. Ben-Ami, D. A. Perley, Y. Cao, S. B. Cenko, U. D. Rebbapragada, P. R. Woźniak, A. V. Filippenko, K. I. Clubb, P. E. Nugent, Y. C. Pan, C. Badenes, D. A. Howell, S. Valenti, D. Sand, J. Sollerman, J. Johansson, D. C. Leonard, J. C. Horst, S. F. Armen, J. M. Fedrow, R. M. Quimby, P. Mazzali, E. Pian, A. Sternberg, T. Matheson, M. Sullivan, K. Maguire, and S. Lazarevic. Type II Supernova Energetics and Comparison of Light Curves to Shock-cooling Models. ApJ, 820(1):33, Mar. 2016. doi: 10.3847/0004-637X/820/1/33.

P. Ruiz-Lapuente, M. Kidger, R. Lopez, and R. Canal. SN 1988A in M58: A Type II-P Supernova with a High Late-Time Luminosity. AJ, 100:782, Sept. 1990. doi: 10.1086/115559.

E. Sabbi, D. Calzetti, L. Ubeda, A. Adamo, M. Cignoni, D. Thilker, A. Aloisi, B. G. Elmegreen, D. M. Elmegreen, D. A. Gouliermis, E. K. Grebel, M. Messa, L. J. Smith, M. Tosi, A. Dolphin, J. E. Andrews, G. Ashworth, S. N. Bright, T. M. Brown, R. Chandar, C. Christian, G. C. Clayton, D. O. Cook, D. A. Dale, S. E. de Mink, C. Dobbs, A. S. Evans, M. Fumagalli, I. Gallagher, J. S., K. Grasha, A. Herrero, D. A. Hunter, K. E. Johnson, L. Kahre, R. C. Kennicutt, H. Kim, M. R. Krumholz, J. C. Lee, D. Lennon, C. Martin, P. Nair, A. Nota, G. Östlin, A. Pellerin, J. Prieto, M. W. Regan, J. E. Ryon, E. Sacchi, D. Schaerer, D. Schiminovich, F. Shabani, S. D. Van Dyk, R. Walterbos, B. C. Whitmore, and A. Wofford. The Resolved Stellar Populations in the LEGUS Galaxies1. ApJS, 235(1):23, Mar. 2018. doi: 10.3847/1538-4365/aaa8e5.

R. Sagar. Some new initiatives in optical astronomy at UPSO, Nainital. *Current Science*, 77: 643–652, Sep 1999.

R. Sagar, B. Kumar, A. Omar, and A. K. Pand ey. New optical telescope projects at Devasthal Observatory. In Proc. SPIE, volume 8444 of *Society of Photo-Optical Instrumentation Engineers (SPIE) Conference Series*, page 84441T, Sep 2012. doi: 10.1117/12.925634.

D. K. Sahu, G. C. Anupama, S. Srividya, and S. Muneer. Photometric and spectroscopic evolution of the Type IIP supernova SN 2004et. MNRAS, 372(3):1315–1324, Nov. 2006. doi: 10.1111/j.1365-2966.2006.10937.x.

H. Sana, S. E. de Mink, A. de Koter, N. Langer, C. J. Evans, M. Gieles, E. Gosset, R. G. Izzard, J. B. Le Bouquin, and F. R. N. Schneider. Binary Interaction Dominates the Evolution of Massive

Stars. *Science*, 337(6093):444, Jul 2012. doi: 10.1126/science.1223344.

S. F. Sánchez, F. F. Rosales-Ortega, R. A. Marino, J. Iglesias-Páramo, J. M. Vílchez, R. C. Kennicutt, A. I. Díaz, D. Mast, A. Monreal-Ibero, R. García-Benito, J. Bland-Hawthorn, E. Pérez, R. González Delgado, B. Husemann, Á. R. López-Sánchez, R. Cid Fernandes, C. Kehrig, C. J. Walcher, A. Gil de Paz, and S. Ellis. Integral field spectroscopy of a sample of nearby galaxies. II. Properties of the H ii regions. A&A, 546:A2, Oct. 2012. doi: 10.1051/0004-6361/201219578.

N. E. Sanders, A. M. Soderberg, S. Gezari, M. Betancourt, R. Chornock, E. Berger, R. J. Foley, P. Challis, M. Drout, R. P. Kirshner, R. Lunnan, G. H. Marion, R. Margutti, R. McKinnon, D. Milisavljevic, G. Narayan, A. Rest, E. Kankare, S. Mattila, S. J. Smartt, M. E. Huber, W. S. Burgett, P. W. Draper, K. W. Hodapp, N. Kaiser, R. P. Kudritzki, E. A. Magnier, N. Metcalfe, J. S. Morgan, P. A. Price, J. L. Tonry, R. J. Wainscoat, and C. Waters. Toward Characterization of the Type IIP Supernova Progenitor Population: A Statistical Sample of Light Curves from Pan-STARRS1. ApJ, 799:208, Feb. 2015. doi: 10.1088/0004-637X/799/2/208.

N. Sapir and E. Waxman. UV/Optical Emission from the Expanding Envelopes of Type II Supernovae. ApJ, 838(2):130, Apr. 2017. doi: 10.3847/1538-4357/aa64df.

A. Savitzky and M. J. E. Golay. Smoothing and differentiation of data by simplified least squares procedures. *Analytical Chemistry*, 36:1627–1639, 1964.

P. Schady, J. J. Eldridge, J. Anderson, T. W. Chen, L. Galbany, H. Kuncarayakti, and L. Xiao. The 50-100pc scale parent stellar populations of type II supernovae and limitations of single star evolution models. *arXiv e-prints*, art. arXiv:1907.12260, Jul 2019.

E. F. Schlafly and D. P. Finkbeiner. Measuring Reddening with Sloan Digital Sky Survey Stellar Spectra and Recalibrating SFD. ApJ, 737:103, Aug. 2011. doi: 10.1088/0004-637X/737/2/103.

E. M. Schlegel. On the Early Spectroscopic Distinction of Type II Supernovae. AJ, 111:1660, Apr. 1996. doi: 10.1086/117905.

B. P. Schmidt, R. P. Kirshner, R. Schild, B. Leibundgut, D. Jeffery, S. P. Willner, R. Peletier, A. I. Zabludoff, M. M. Phillips, N. B. Suntzeff, M. Hamuy, L. A. Wells, R. C. Smith, J. A. Baldwin, W. G. Weller, M. Navarette, L. Gonzalez, A. V. Filippenko, J. C. Shields, C. C. Steidel, S. Perlmutter, C. Pennypacker, C. K. Smith, A. C. Porter, T. A. Boroson, R. Stathakis, R. Cannon, J. Peters, E. Horine, K. C. Freeman, D. S. Womble, R. P. S. Stone, L. A. Marschall,

A. C. Phillips, A. Saha, and H. E. Bond. Photometric and Spectroscopic Observations of SN 1990E in NGC 1035 Observational Constraints for Models of Type II Supernovae. AJ, 105:2236, June 1993. doi: 10.1086/116602.

J. H. Shiode and E. Quataert. Setting the Stage for Circumstellar Interaction in Core-Collapse Supernovae. II. Wave-driven Mass Loss in Supernova Progenitors. ApJ, 780:96, Jan. 2014. doi: 10.1088/0004-637X/780/1/96.

J. M. Silverman, J. J. Kong, and A. V. Filippenko. Berkeley Supernova Ia Program - II. Initial analysis of spectra obtained near maximum brightness. MNRAS, 425:1819–1888, Sept. 2012. doi: 10.1111/j.1365-2966.2012.21269.x.

J. M. Silverman, S. Pickett, J. C. Wheeler, A. V. Filippenko, J. Vinkó, G. H. Marion, S. B. Cenko, R. Chornock, K. I. Clubb, R. J. Foley, M. L. Graham, P. L. Kelly, T. Matheson, and J. C. Shields. After the Fall: Late-Time Spectroscopy of Type IIP Supernovae. MNRAS, 467(1):369–411, May 2017. doi: 10.1093/mnras/stx058.

S. J. Smartt. Progenitors of Core-Collapse Supernovae. ARA&A, 47(1):63–106, Sept. 2009. doi: 10.1146/annurev-astro-082708-101737.

S. J. Smartt. Observational Constraints on the Progenitors of Core-Collapse Supernovae: The Case for Missing High-Mass Stars. *Publications of the Astronomical Society of Australia*, 32:e016, Apr 2015. doi: 10.1017/pasa.2015.17.

S. J. Smartt, G. F. Gilmore, N. Trentham, C. A. Tout, and C. M. Frayn. An Upper Mass Limit for the Progenitor of the Type II-P Supernova SN 1999gi. ApJ, 556:L29–L32, July 2001. doi: 10.1086/322868.

S. J. Smartt, J. R. Maund, M. A. Hendry, C. A. Tout, G. F. Gilmore, S. Mattila, and C. R. Benn. Detection of a Red Supergiant Progenitor Star of a Type II-Plateau Supernova. *Science*, 303 (5657):499–503, Jan. 2004. doi: 10.1126/science.1092967.

S. J. Smartt, S. Valenti, M. Fraser, C. Inserra, D. R. Young, M. Sullivan, A. Pastorello, S. Benetti, A. Gal-Yam, C. Knapic, M. Molinaro, R. Smareglia, K. W. Smith, S. Taubenberger, O. Yaron, J. P. Anderson, C. Ashall, C. Balland, C. Baltay, C. Barbarino, F. E. Bauer, S. Baumont, D. Bersier, N. Blagorodnova, S. Bongard, M. T. Botticella, F. Bufano, M. Bulla, E. Cappellaro, H. Campbell, F. Cellier-Holzem, T. W. Chen, M. J. Childress, A. Clocchiatti, C. Contreras,

M. Dall'Ora, J. Danziger, T. de Jaeger, A. De Cia, M. Della Valle, M. Dennefeld, N. Elias-Rosa, N. Elman, U. Feindt, M. Fleury, E. Gall, S. Gonzalez-Gaitan, L. Galbany, A. Morales Garoffolo, L. Greggio, L. L. Guillou, S. Hachinger, E. Hadjiyska, P. E. Hage, W. Hillebrandt, S. Hodgkin, E. Y. Hsiao, P. A. James, A. Jerkstrand, T. Kangas, E. Kankare, R. Kotak, M. Kromer, H. Kuncarayakti, G. Leloudas, P. Lundqvist, J. D. Lyman, I. M. Hook, K. Maguire, I. Manulis, S. J. Margheim, S. Mattila, J. R. Maund, P. A. Mazzali, M. McCrum, R. McKinnon, M. E. Moreno-Raya, M. Nicholl, P. Nugent, R. Pain, G. Pignata, M. M. Phillips, J. Polshaw, M. L. Pumo, D. Rabinowitz, E. Reilly, C. Romero-Cañizales, R. Scalzo, B. Schmidt, S. Schulze, S. Sim, J. Sollerman, F. Taddia, L. Tartaglia, G. Terreran, L. Tomasella, M. Turatto, E. Walker, N. A. Walton, L. Wyrzykowski, F. Yuan, and L. Zampieri. PESSTO: survey description and products from the first data release by the Public ESO Spectroscopic Survey of Transient Objects. A&A, 579:A40, July 2015. doi: 10.1051/0004-6361/201425237.

N. Smith, R. M. Humphreys, K. Davidson, R. D. Gehrz, M. T. Schuster, and J. Krautter. The Asymmetric Nebula Surrounding the Extreme Red Supergiant VY Canis Majoris. AJ, 121(2): 1111–1125, Feb. 2001. doi: 10.1086/318748.

N. Smith, S. B. Cenko, N. Butler, J. S. Bloom, M. M. Kasliwal, A. Horesh, S. R. Kulkarni, N. M. Law, P. E. Nugent, E. O. Ofek, D. Poznanski, R. M. Quimby, B. Sesar, S. Ben-Ami, I. Arcavi, A. Gal-Yam, D. Polishook, D. Xu, O. Yaron, D. A. Frail, and M. Sullivan. SN 2010jp (PTF10aaxi): a jet in a Type II supernova. *Monthly Notices of the Royal Astronomical Society*, 420(2):1135–1144, Feb 2012. doi: 10.1111/j.1365-2966.2011.20104.x.

N. Smith, J. C. Mauerhan, S. B. Cenko, M. M. Kasliwal, J. M. Silverman, A. V. Filippenko, A. Gal-Yam, K. I. Clubb, M. L. Graham, D. C. Leonard, J. C. Horst, G. G. Williams, J. E. Andrews, S. R. Kulkarni, P. Nugent, M. Sullivan, K. Maguire, D. Xu, and S. Ben-Ami. PTF11iqb: cool supergiant mass-loss that bridges the gap between Type IIn and normal supernovae. MNRAS, 449(2):1876–1896, May 2015. doi: 10.1093/mnras/stv354.

M. T. Smitka. TRUVOT: True Background Technique for the Swift UVOT Grisms. Astrophysics Source Code Library, Sept. 2015.

A. M. Soderberg, R. Margutti, B. A. Zauderer, M. Krauss, B. Katz, L. Chomiuk, J. A. Dittmann, E. Nakar, T. Sakamoto, N. Kawai, K. Hurley, S. Barthelmy, T. Toizumi, M. Morii, R. A. Chevalier, M. Gurwell, G. Petitpas, M. Rupen, K. D. Alexander, E. M. Levesque, C. Fransson, A. Brunthaler, M. F. Bietenholz, N. Chugai, J. Grindlay, A. Copete, V. Connaughton, M. Briggs, C. Meegan, A. von Kienlin, X. Zhang, A. Rau, S. Golenetskii, E. Mazets, and T. Cline. Panchromatic Observations of SN 2011dh Point to a Compact Progenitor Star. ApJ, 752:78, June 2012. doi: 10.1088/0004-637X/752/2/78.

S. Spiro, A. Pastorello, M. L. Pumo, L. Zampieri, M. Turatto, S. J. Smartt, S. Benetti, E. Cappellaro, S. Valenti, I. Agnoletto, G. Altavilla, T. Aoki, E. Brocato, E. M. Corsini, A. Di Cianno, N. Elias-Rosa, M. Hamuy, K. Enya, M. Fiaschi, G. Folatelli, S. Desidera, A. Harutyunyan, D. A. Howell, A. Kawka, Y. Kobayashi, B. Leibundgut, T. Minezaki, H. Navasardyan, K. Nomoto, S. Mattila, A. Pietrinferni, G. Pignata, G. Raimondo, M. Salvo, B. P. Schmidt, J. Sollerman, J. Spyromilio, S. Taubenberger, G. Valentini, S. Vennes, and Y. Yoshii. Low luminosity Type II supernovae - II. Pointing towards moderate mass precursors. MNRAS, 439:2873–2892, Apr. 2014. doi: 10.1093/mnras/stu156.

P. B. Stetson. DAOPHOT: A Computer Program for Crowded-Field Stellar Photometry. *Publications of the Astronomical Society of the Pacific*, 99:191, Mar. 1987. doi: 10.1086/131977.

M. Stritzinger, M. Hamuy, N. B. Suntzeff, R. C. Smith, M. M. Phillips, J. Maza, L. G. Strolger, R. Antezana, L. González, M. Wischnjewsky, P. Candia, J. Espinoza, D. González, C. Stubbs, A. C. Becker, E. P. Rubenstein, and G. Galaz. Optical Photometry of the Type Ia Supernova 1999ee and the Type Ib/c Supernova 1999ex in IC 5179. AJ, 124(4):2100–2117, Oct. 2002. doi: 10.1086/342544.

L.-G. Strolger, T. Dahlen, S. A. Rodney, O. Graur, A. G. Riess, C. McCully, S. Ravindranath, B. Mobasher, and A. K. Shahady. The Rate of Core Collapse Supernovae to Redshift 2.5 from the CANDELS and CLASH Supernova Surveys. ApJ, 813:93, Nov. 2015. doi: 10.1088/0004-637X/813/2/93.

STScI Development Team. pysynphot: Synthetic photometry software package, Mar. 2013.

T. Sukhbold and S. Adams. Missing red supergiants and carbon burning. MNRAS, 492(2):2578–2587, Feb. 2020. doi: 10.1093/mnras/staa059.

T. Sukhbold and S. E. Woosley. The Compactness of Presupernova Stellar Cores. ApJ, 783:10, Mar. 2014. doi: 10.1088/0004-637X/783/1/10.

T. Sukhbold, T. Ertl, S. E. Woosley, J. M. Brown, and H.-T. Janka. Core-collapse Supernovae from 9 to 120 Solar Masses Based on Neutrino-powered Explosions. ApJ, 821:38, Apr. 2016. doi: 10.3847/0004-637X/821/1/38.

T. Sukhbold, S. E. Woosley, and A. Heger. A High-resolution Study of Presupernova Core Structure. ApJ, 860(2):93, June 2018. doi: 10.3847/1538-4357/aac2da.

T. Szalai, J. Vinkó, R. Könyves-Tóth, A. P. Nagy, K. A. Bostroem, K. Sárneczky, P. J. Brown, O. Pejcha, A. Bódi, and B. Cseh. The Type II-P Supernova 2017eaw: From Explosion to the Nebular Phase. ApJ, 876(1):19, May 2019. doi: 10.3847/1538-4357/ab12d0.

K. Takáts, M. L. Pumo, N. Elias-Rosa, A. Pastorello, G. Pignata, E. Paillas, L. Zampieri, J. P. Anderson, J. Vinkó, S. Benetti, M. T. Botticella, F. Bufano, A. Campillay, R. Cartier, M. Ergon, G. Folatelli, R. J. Foley, F. Förster, M. Hamuy, V. P. Hentunen, E. Kankare, G. Leloudas, N. Morrell, M. Nissinen, M. M. Phillips, S. J. Smartt, M. Stritzinger, S. Taubenberger, S. Valenti, S. D. Van Dyk, J. B. Haislip, A. P. LaCluyze, J. P. Moore, and D. Reichart. SN 2009N: linking normal and subluminous Type II-P SNe. MNRAS, 438(1):368–387, Feb. 2014. doi: 10.1093/mnras/stt2203.

K. Takáts, G. Pignata, M. L. Pumo, E. Paillas, L. Zampieri, N. Elias-Rosa, S. Benetti, F. Bufano, E. Cappellaro, M. Ergon, M. Fraser, M. Hamuy, C. Inserra, E. Kankare, S. J. Smartt, M. D. Stritzinger, S. D. Van Dyk, J. B. Haislip, A. P. LaCluyze, J. P. Moore, and D. Reichart. SN 2009ib: a Type II-P supernova with an unusually long plateau. MNRAS, 450(3):3137–3154, July 2015. doi: 10.1093/mnras/stv857.

L. Tartaglia, D. J. Sand, S. Valenti, S. Wyatt, J. P. Anderson, I. Arcavi, C. Ashall, M. T. Botticella, R. Cartier, T.-W. Chen, A. Cikota, D. Coulter, M. Della Valle, R. J. Foley, A. Gal-Yam, L. Galbany, C. Gall, J. B. Haislip, J. Harmanen, G. Hosseinzadeh, D. A. Howell, E. Y. Hsiao, C. Inserra, S. W. Jha, E. Kankare, C. D. Kilpatrick, V. V. Kouprianov, H. Kuncarayakti, T. J. Maccarone, K. Maguire, S. Mattila, P. A. Mazzali, C. McCully, A. Melandri, N. Morrell, M. M. Phillips, G. Pignata, A. L. Piro, S. Prentice, D. E. Reichart, C. Rojas-Bravo, S. J. Smartt, K. W. Smith, J. Sollerman, M. D. Stritzinger, M. Sullivan, F. Taddia, and D. R. Young. The Early

Detection and Follow-up of the Highly Obscured Type II Supernova 2016ija/DLT16am. ApJ, 853:62, Jan. 2018. doi: 10.3847/1538-4357/aaa014.

G. Terreran, A. Jerkstrand, S. Benetti, S. J. Smartt, P. Ochner, L. Tomasella, D. A. Howell, A. Morales-Garoffolo, A. Harutyunyan, E. Kankare, I. Arcavi, E. Cappellaro, N. Elias-Rosa, G. Hosseinzadeh, T. Kangas, A. Pastorello, L. Tartaglia, M. Turatto, S. Valenti, P. Wiggins, and F. Yuan. The multifaceted Type II-L supernova 2014G from pre-maximum to nebular phase. MNRAS, 462:137–157, Oct. 2016. doi: 10.1093/mnras/stw1591.

F.-K. Thielemann, K. Nomoto, and M.-A. Hashimoto. Core-Collapse Supernovae and Their Ejecta. ApJ, 460:408, Mar. 1996. doi: 10.1086/176980.

F.-K. Thielemann, J. Isern, A. Perego, and P. von Ballmoos. Nucleosynthesis in Supernovae. Space Sci. Rev., 214(3):62, Apr. 2018. doi: 10.1007/s11214-018-0494-5.

R. C. Thomas. SYN++: Standalone SN spectrum synthesis. Astrophysics Source Code Library, Aug. 2013.

R. C. Thomas, P. E. Nugent, and J. C. Meza. SYNAPPS: Data-Driven Analysis for Supernova Spectroscopy. PASP, 123:237, Feb. 2011. doi: 10.1086/658673.

L. Tomasella, E. Cappellaro, M. Fraser, M. L. Pumo, A. Pastorello, G. Pignata, S. Benetti, F. Bufano, M. Dennefeld, A. Harutyunyan, T. Iijima, A. Jerkstrand, E. Kankare, R. Kotak, L. Magill, V. Nascimbeni, P. Ochner, A. Siviero, S. Smartt, J. Sollerman, V. Stanishev, F. Taddia, S. Taubenberger, M. Turatto, S. Valenti, D. E. Wright, and L. Zampieri. Comparison of progenitor mass estimates for the Type IIP SN 2012A. MNRAS, 434:1636–1657, Sept. 2013. doi: 10.1093/mnras/stt1130.

L. Tomasella, E. Cappellaro, M. L. Pumo, A. Jerkstrand, S. Benetti, N. Elias-Rosa, M. Fraser, C. Inserra, A. Pastorello, M. Turatto, J. P. Anderson, L. Galbany, C. P. Gutiérrez, E. Kankare, G. Pignata, G. Terreran, S. Valenti, C. Barbarino, F. E. Bauer, M. T. Botticella, T.-W. Chen, A. Gal-Yam, A. Harutyunyan, D. A. Howell, K. Maguire, A. Morales Garoffolo, P. Ochner, S. J. Smartt, S. Schulze, D. R. Young, and L. Zampieri. SNe 2013K and 2013am: observed and physical properties of two slow, normal Type IIP events. *MNRAS*, 475:1937–1959, 2018. doi: 10.1093/mnras/stx3220. URL `http://www.bosssupernova.com`.

D. Y. Tsvetkov. Observations of 14 Supernovae. *Peremennye Zvezdy*, 22:39, Jan. 1983.

D. Y. Tsvetkov. Photometric Observations of Two Type II-P Supernovae: Normal SN II-P2004A and Unusual SN 2004ek. *Peremennye Zvezdy*, 28(3):3, Mar. 2008.

D. Y. Tsvetkov, A. A. Volnova, A. P. Shulga, S. A. Korotkiy, A. Elmhamdi, I. J. Danziger, and M. V. Ereshko. Observations and analysis of two type IIP supernovae: the intrinsically faint object SN 2005cs and the ambiguous object SN 2005ay. A&A, 460(3):769–776, Dec. 2006. doi: 10.1051/0004-6361:20065704.

Tsvetkov, D.Yu. and Pavlyuk, N.N. and Bartunov, O.S. and Pskovskii, Yu.P. Sternberg Astronomical Institute Supernova Catalogue. http://www.sai.msu.su/sn/sncat/, 2010. Accessed via the Open Supernova Catalog.

R. B. Tully and J. R. Fisher. *Catalog of Nearby Galaxies*. 1988.

R. B. Tully, E. J. Shaya, I. D. Karachentsev, H. M. Courtois, D. D. Kocevski, L. Rizzi, and A. Peel. Our Peculiar Motion Away from the Local Void. ApJ, 676:184–205, Mar. 2008. doi: 10.1086/527428.

R. B. Tully, H. M. Courtois, and J. G. Sorce. Cosmicflows-3. AJ, 152(2):50, Aug. 2016. doi: 10.3847/0004-6256/152/2/50.

M. Turatto, E. Cappellaro, S. Benetti, and I. J. Danziger. Observations of type II plateau supernovae : SNe 1988A, 1988H, and 1989C. MNRAS, 265:471–485, Nov. 1993. doi: 10.1093/mnras/265.2.471.

M. Turatto, P. A. Mazzali, T. R. Young, K. Nomoto, K. Iwamoto, S. Benetti, E. Cappellaro, I. J. Danziger, D. F. de Mello, M. M. Phillips, N. B. Suntzeff, A. Clocchiatti, A. Piemonte, B. Leibundgut, R. Covarrubias, J. Maza, and J. Sollerman. The Peculiar Type II Supernova 1997D: A Case for a Very Low ^{56}Ni Mass. ApJ, 498(2):L129–L133, May 1998. doi: 10.1086/311324.

V. P. Utrobin and N. N. Chugai. Progenitor mass of the type IIP supernova 2005cs. A&A, 491: 507–513, Nov. 2008. doi: 10.1051/0004-6361:200810272.

V. P. Utrobin and N. N. Chugai. Luminous Type IIP SN 2013ej with high-velocity ^{56}Ni ejecta. MNRAS, 472:5004–5010, Dec. 2017. doi: 10.1093/mnras/stx2415.

W. D. Vacca, M. C. Cushing, and J. T. Rayner. A Method of Correcting Near-Infrared Spectra for Telluric Absorption. *Publications of the Astronomical Society of the Pacific*, 115:389–409, Mar.

2003. doi: 10.1086/346193.

S. Valenti, S. Benetti, E. Cappellaro, F. Patat, P. Mazzali, M. Turatto, K. Hurley, K. Maeda, A. Gal-Yam, R. J. Foley, A. V. Filippenko, A. Pastorello, P. Challis, F. Frontera, A. Harutyunyan, M. Iye, K. Kawabata, R. P. Kirshner, W. Li, Y. M. Lipkin, T. Matheson, K. Nomoto, E. O. Ofek, Y. Ohyama, E. Pian, D. Poznanski, M. Salvo, D. N. Sauer, B. P. Schmidt, A. Soderberg, and L. Zampieri. The broad-lined Type Ic supernova 2003jd. MNRAS, 383:1485–1500, Feb. 2008. doi: 10.1111/j.1365-2966.2007.12647.x.

S. Valenti, M. Fraser, S. Benetti, G. Pignata, J. Sollerman, C. Inserra, E. Cappellaro, A. Pastorello, S. J. Smartt, M. Ergon, M. T. Botticella, J. Brimacombe, F. Bufano, M. Crockett, I. Eder, D. Fugazza, J. B. Haislip, M. Hamuy, A. Harutyunyan, K. M. Ivarsen, E. Kankare, R. Kotak, A. P. Lacluyze, L. Magill, S. Mattila, J. Maza, P. A. Mazzali, D. E. Reichart, S. Taubenberger, M. Turatto, and L. Zampieri. SN 2009jf: a slow-evolving stripped-envelope core-collapse supernova. MNRAS, 416:3138–3159, Oct. 2011. doi: 10.1111/j.1365-2966.2011.19262.x.

S. Valenti, D. Sand, A. Pastorello, M. L. Graham, D. A. Howell, J. T. Parrent, L. Tomasella, P. Ochner, M. Fraser, S. Benetti, F. Yuan, S. J. Smartt, J. R. Maund, I. Arcavi, A. Gal-Yam, C. Inserra, and D. Young. The first month of evolution of the slow-rising Type IIP SN 2013ej in M74¡SUP¿?¡/SUP¿. MNRAS, 438:L101–L105, Feb. 2014. doi: 10.1093/mnrasl/slt171.

S. Valenti, D. Sand, M. Stritzinger, D. A. Howell, I. Arcavi, C. McCully, M. J. Childress, E. Y. Hsiao, C. Contreras, N. Morrell, M. M. Phillips, M. Gromadzki, R. P. Kirshner, and G. H. Marion. Supernova 2013by: a Type IIL supernova with a IIP-like light-curve drop$^{?}$. MNRAS, 448:2608–2616, Apr. 2015. doi: 10.1093/mnras/stv208.

S. Valenti, D. A. Howell, M. D. Stritzinger, M. L. Graham, G. Hosseinzadeh, I. Arcavi, L. Bildsten, A. Jerkstrand, C. McCully, A. Pastorello, A. L. Piro, D. Sand, S. J. Smartt, G. Terreran, C. Baltay, S. Benetti, P. Brown, A. V. Filippenko, M. Fraser, D. Rabinowitz, M. Sullivan, and F. Yuan. The diversity of Type II supernova versus the similarity in their progenitors. MNRAS, 459:3939–3962, July 2016. doi: 10.1093/mnras/stw870.

S. Valenti, D. J. Sand, and S. Wyatt. DLT40 Transient Discovery Report for 2018-11-24. *Transient Name Server Discovery Report*, 1816, Nov. 2018.

S. D. Van Dyk. The direct identification of core-collapse supernova progenitors. *Philosophical Transactions of the Royal Society of London Series A*, 375(2105):20160277, Sep 2017. doi: 10.1098/rsta.2016.0277.

S. D. Van Dyk, S. B. Cenko, D. Poznanski, I. Arcavi, A. Gal-Yam, A. V. Filippenko, K. Silverio, A. Stockton, J.-C. Cuillandre, G. W. Marcy, A. W. Howard, and H. Isaacson. The Red Supergiant Progenitor of Supernova 2012aw (PTF12bvh) in Messier 95. ApJ, 756(2):131, Sept. 2012a. doi: 10.1088/0004-637X/756/2/131.

S. D. Van Dyk, T. J. Davidge, N. Elias-Rosa, S. Taubenberger, W. Li, E. M. Levesque, S. Howerton, G. Pignata, N. Morrell, M. Hamuy, and A. V. Filippenko. Supernova 2008bk and Its Red Supergiant Progenitor. AJ, 143(1):19, Jan. 2012b. doi: 10.1088/0004-6256/143/1/19.

S. D. Van Dyk, W. Zheng, J. R. Maund, T. G. Brink, S. Srinivasan, J. E. Andrews, N. Smith, D. C. Leonard, V. Morozova, A. V. Filippenko, B. Conner, D. Milisavljevic, T. de Jaeger, K. S. Long, H. Isaacson, I. J. M. Crossfield, M. R. Kosiarek, A. W. Howard, O. D. Fox, P. L. Kelly, A. L. Piro, S. P. Littlefair, V. S. Dhillon, R. Wilson, T. Butterley, S. Yunus, S. Channa, B. T. Jeffers, E. Falcon, T. W. Ross, J. C. Hestenes, S. M. Stegman, K. Zhang, and S. Kumar. The Type II-plateau Supernova 2017eaw in NGC 6946 and Its Red Supergiant Progenitor. ApJ, 875 (2):136, Apr. 2019. doi: 10.3847/1538-4357/ab1136.

J. Vernet, H. Dekker, S. D'Odorico, L. Kaper, P. Kjaergaard, F. Hammer, S. Randich, F. Zerbi, P. J. Groot, J. Hjorth, I. Guinouard, R. Navarro, T. Adolfse, P. W. Albers, J. P. Amans, J. J. Andersen, M. I. Andersen, P. Binetruy, P. Bristow, R. Castillo, F. Chemla, L. Christensen, P. Conconi, R. Conzelmann, J. Dam, V. de Caprio, A. de Ugarte Postigo, B. Delabre, P. di Marcantonio, M. Downing, E. Elswijk, G. Finger, G. Fischer, H. Flores, P. François, P. Goldoni, L. Guglielmi, R. Haigron, H. Hanenburg, I. Hendriks, M. Horrobin, D. Horville, N. C. Jessen, F. Kerber, L. Kern, M. Kiekebusch, P. Kleszcz, J. Klougart, J. Kragt, H. H. Larsen, J. L. Lizon, C. Lucuix, V. Mainieri, R. Manuputy, C. Martayan, E. Mason, R. Mazzoleni, N. Michaelsen, A. Modigliani, S. Moehler, P. Møller, A. Norup Sørensen, P. Nørregaard, C. Péroux, F. Patat, E. Pena, J. Pragt, C. Reinero, F. Rigal, M. Riva, R. Roelfsema, F. Royer, G. Sacco, P. Santin, T. Schoenmaker, P. Spano, E. Sweers, R. Ter Horst, M. Tintori, N. Tromp, P. van Dael, H. van der Vliet, L. Venema, M. Vidali, J. Vinther, P. Vola, R. Winters, D. Wistisen, G. Wulterkens,

and A. Zacchei. X-shooter, the new wide band intermediate resolution spectrograph at the ESO Very Large Telescope. A&A, 536:A105, Dec. 2011. doi: 10.1051/0004-6361/201117752.

M. Vogelsberger, S. Genel, V. Springel, P. Torrey, D. Sijacki, D. Xu, G. Snyder, D. Nelson, and L. Hernquist. Introducing the Illustris Project: simulating the coevolution of dark and visible matter in the Universe. MNRAS, 444(2):1518–1547, Oct. 2014. doi: 10.1093/mnras/stu1536.

J. J. Walmswell and J. J. Eldridge. Circumstellar dust as a solution to the red supergiant supernova progenitor problem. MNRAS, 419:2054–2062, Jan. 2012. doi: 10.1111/j.1365-2966.2011.19860.x.

L. Wang, A. A. Dutton, G. S. Stinson, A. V. Macciò, C. Penzo, X. Kang, B. W. Keller, and J. Wadsley. NIHAO project - I. Reproducing the inefficiency of galaxy formation across cosmic time with a large sample of cosmological hydrodynamical simulations. MNRAS, 454(1):83–94, Nov. 2015. doi: 10.1093/mnras/stv1937.

T. A. Weaver, G. B. Zimmerman, and S. E. Woosley. Presupernova evolution of massive stars. ApJ, 225:1021–1029, Nov. 1978. doi: 10.1086/156569.

P. M. Weilbacher, O. Streicher, T. Urrutia, A. Pécontal-Rousset, A. Jarno, and R. Bacon. *The MUSE Data Reduction Pipeline: Status after Preliminary Acceptance Europe*, volume 485 of *Astronomical Society of the Pacific Conference Series*, page 451. 2014.

K. W. Weiler, N. Panagia, M. J. Montes, and R. A. Sramek. Radio Emission from Supernovae and Gamma-Ray Bursters. *Annual Review of Astronomy and Astrophysics*, 40:387–438, Jan. 2002. doi: 10.1146/annurev.astro.40.060401.093744.

S. Wellstein and N. Langer. Implications of massive close binaries for black hole formation and supernovae. A&A, 350:148–162, Oct. 1999.

G. G. Williams, P. A. Milne, H. S. Park, S. D. Barthelmy, D. H. Hartmann, A. Updike, and K. Hurley. The Robotic Super-LOTIS Telescope: Results & Future Plans. In M. Galassi, D. Palmer, and E. Fenimore, editors, *American Institute of Physics Conference Series*, volume 1000 of *American Institute of Physics Conference Series*, pages 535–538, May 2008. doi: 10.1063/1.2943525.

J. Wilms, A. Allen, and R. McCray. On the Absorption of X-Rays in the Interstellar Medium. *The Astrophysical Journal*, 542(2):914–924, Oct 2000. doi: 10.1086/317016.

S. E. Woosley and A. Heger. Nucleosynthesis and remnants in massive stars of solar metallicity. Phys. Rep., 442:269–283, Apr. 2007. doi: 10.1016/j.physrep.2007.02.009.

S. E. Woosley and A. Heger. The Remarkable Deaths of 9-11 Solar Mass Stars. ApJ, 810:34, Sept. 2015. doi: 10.1088/0004-637X/810/1/34.

S. E. Woosley and T. A. Weaver. The Evolution and Explosion of Massive Stars. II. Explosive Hydrodynamics and Nucleosynthesis. ApJS, 101:181, Nov. 1995. doi: 10.1086/192237.

S. E. Woosley, D. H. Hartmann, R. D. Hoffman, and W. C. Haxton. The nu -Process. ApJ, 356: 272, June 1990. doi: 10.1086/168839.

O. Yaron and A. Gal-Yam. WISeREP—An Interactive Supernova Data Repository. PASP, 124 (917):668, July 2012. doi: 10.1086/666656.

O. Yaron, D. A. Perley, A. Gal-Yam, J. H. Groh, A. Horesh, E. O. Ofek, S. R. Kulkarni, J. Sollerman, C. Fransson, A. Rubin, P. Szabo, N. Sapir, F. Taddia, S. B. Cenko, S. Valenti, I. Arcavi, D. A. Howell, M. M. Kasliwal, P. M. Vreeswijk, D. Khazov, O. D. Fox, Y. Cao, O. Gnat, P. L. Kelly, P. E. Nugent, A. V. Filippenko, R. R. Laher, P. R. Wozniak, W. H. Lee, U. D. Rebbapragada, K. Maguire, M. Sullivan, and M. T. Soumagnac. Confined dense circumstellar material surrounding a regular type II supernova. *Nature Physics*, 13:510–517, Feb. 2017. doi: 10.1038/nphys4025.

T. R. Young and D. Branch. Absolute Light Curves of Type II Supernovae. ApJ, 342:L79, July 1989. doi: 10.1086/185489.

F. Yuan, A. Jerkstrand, S. Valenti, J. Sollerman, I. R. Seitenzahl, A. Pastorello, S. Schulze, T. W. Chen, M. J. Childress, M. Fraser, C. Fremling, R. Kotak, A. J. Ruiter, B. P. Schmidt, S. J. Smartt, F. Taddia, G. Terreran, B. E. Tucker, C. Barbarino, S. Benetti, N. Elias-Rosa, A. Gal-Yam, D. A. Howell, C. Inserra, E. Kankare, M. Y. Lee, K. L. Li, K. Maguire, S. Margheim, A. Mehner, P. Ochner, M. Sullivan, L. Tomasella, and D. R. Young. 450 d of Type II SN 2013ej in optical and near-infrared. MNRAS, 461(2):2003–2018, Sept. 2016. doi: 10.1093/mnras/stw1419.

M. R. Zaghloul, M. A. Bourham, and J. M. Doster. Core-collapse Supernovae from 9 to 120 Solar Masses Based on Neutrino-powered Explosions. *JPhD*, 33:977, 2000.

L. Zampieri, A. Pastorello, M. Turatto, E. Cappellaro, S. Benetti, G. Altavilla, P. Mazzali, and M. Hamuy. Peculiar, low-luminosity Type II supernovae: low-energy explosions in massive

progenitors? MNRAS, 338(3):711–716, Jan. 2003. doi: 10.1046/j.1365-8711.2003.06082.x.

X. Zhang, J. Zhang, X. Wang, X. Wang, H. Sai, H. Lin, D. Xiang, L. Rui, Y. Wang, J. Zhang, T. Zhang, and H. Wang. Classification of SN 2018ivc (=DLT18aq) as a Young Type II Supernova. *The Astronomer's Telegram*, 12240:1, Nov 2018.